WRC RESEARCH REPORT NO. 148

TRANSPORT PROCESSES OF PARTICLES IN NON-DILUTE SUSPENSIONS IN TURBULENT WATER FLOW -- PHASE I: EXPERIMENTAL MEASUREMENTS

Barclay G. Jones, Professor of Nuclear and of Mechanical Engineering
John E. Gronager, Research Assistant, Nuclear Engineering

F I N A L R E P O R T
Project No. A-085-ILL.

This project was partially supported by the U.S. Department of the Interior in accordance with the Water Resources Research Act of 1964, P.L. 88-379, Agreement No. 14-34-001-8015.

UNIVERSITY OF ILLINOIS
WATER RESOURCES CENTER
2535 Hydrosystems Laboratory
Urbana, Illinois 61801

March, 1980

ABSTRACT

TRANSPORT PROCESSES OF PARTICLES IN NON-DILUTE SUSPENSIONS IN TURBULENT WATER FLOW -- PHASE I: EXPERIMENTAL MEASUREMENTS

Increased utilization of non-dilute, solid-fluid suspensions in transporting materials and in estimating the distribution of particles from atmospheric fallout, demands that the basic fluid-particle interactions be thoroughly understood. Our previous studies of such interactions were conducted on only dilute suspensions, where as this study has been conducted in the same vertical flows but with solid spherical particle suspensions with concentrations, ϕ, from 0 to 10 percent by volume, a range of practical interest to sedimentation and erosion as well as in slurry pipelines. Detailed experimental results of the particle-fluid relative mean and rms velocities as well as particle dispersion were obtained for two particle densities and several ϕ values. Both particle types showed a rapid rise of both relative mean and rms velocities as ϕ increased to about 1-2 percent and fell off gradually for higher ϕ values. Dispersion followed a similar behavior. The higher free fall velocity particles exhibited larger rms velocities and increased dispersion from the lighter, lower free fall velocity particles. Analytical models of the ϕ-dependence showed good agreement with the data, suggesting their use in engineering predictions.

Jones, Barclay G. and Gronager, John E.

TRANSPORT PROCESSES OF PARTICLES IN NON-DILUTE SUSPENSIONS IN TURBULENT WATER FLOW -- PHASE I: EXPERIMENTAL MEASUREMENTS

Research Report No. 148, Water Resources Center, University of Illinois March 1980, Urbana, IL 61801, 173 + xv pp.

KEY WORDS --- *turbulent transport/*dispersion/*sedimentation/*slurry/ turbulent flow/*particle suspension.

ACKNOWLEDGEMENT

Sponsorship of this research by the U.S. Department of Interior through the Office of Water Resources and Technology, the Water Resources Center at the University of Illinois at Urbana-Champaign, the Nuclear Engineering Program and the Department of Mechanical Engineering is gratefully acknowledged.

The participation of Dr. Charles Meek of Argonne National Laboratory and Roberaldo Souza of the University of Illinois is sincerely appreciated.

This report is in large part material directly presented in John E. Gronager's doctoral thesis, "Experimental Measurements of the Behavior of Non-Dilute Particle Suspensions in Turbulent Flow," Nuclear Engineering Program, University of Illinois at Urbana-Champaign, 1978.

TABLE OF CONTENTS

LIST OF FIGURES

LIST OF TABLES

NOMENCLATURE

a_j, b_j, c_j	=	coefficients of least square fit
a	=	particle radius
B	=	constant
C	=	constant
C_D	=	drag coefficient
C_l	=	defined by Equation 2.50
$cov(\tau j)$	=	autocovariance
d	=	distance between particles
e	=	voltage
E_f	=	energy spectra of fluid
E_p	=	energy spectra of particle
$f(\phi)$	=	free fall velocity of a particle at various ϕ
F*	=	momentum transfer coefficient
F_{d_i}	=	viscous drag
$F_d(n,a)$	=	viscous drag defined by Equation 2.4
F_i	=	external applied force
F_v	=	force of resistance
G_i	=	drag due to steady gravitational free fall
$\hat{i},\hat{j},\hat{k}$	=	unit vectors in x,y,z direction
M'	=	displaced fluid mass
n	=	number density
P	=	pressure
q_v	=	velocity potential
$Q(\omega)$	=	particle response function
r_{outer}	=	radius of outer sphere
Re_p	=	particle Reynolds number defined in Equation 2.38

$R(\tau)$ = autocorrelation

t = time

T_{f_z} = normalized fluid time integral

T_v = kinetic energy

T,U,V, = photomultiplier difference voltages

$\tilde{u}(w)$ = Fourier transform of u(t)

U_{f_i} = fluid velocity

U_{p_i} = particle velocity

V_c = carriage velocity

$V'^2_{Lat}(\phi)$ = averaged lateral particle velocity variance

V_{p_i} = particle fluctuating velocity

$\hat{V}'_{p,z}$ = defined as $(\overline{U}^2_{p,z} + V'^2_{p,z})^{1/2}$

V_{R_i} = relative velocity $(U_{f_i} - U_{p_i})$

W_p = instantaneous particle velocity used to define the p.d.f. in Equation 4.10

X = cartesian position

X^* = $\frac{X}{a}$

Z = axial position

Greek Symbols

$\alpha_k(\phi)$ = particle time parameter defined in Equation 2.67, 2.68 and 2.69

$\beta(\phi)$ = particle density parameter defined in Equation 2.48

$\gamma(\phi)$ = $2/3\,\gamma'(\phi)$

$\gamma'(\phi)$ = defined by Equation 2.36

δ_i = linear drag modified defined in Equation 2.55

ε = particle diffusion coefficient

$\eta(\phi)$ = virtual mass modified, Equation 2.24

θ = exponent in Equation 2.40 = .84

$\theta(\phi)$ = Basset term modifier

κ = particle parameter defined by Equation 2.97

λ = viscous drag modifier

μ = fluid viscosity

ν = kinetic fluid viscosity

ξ = particle parameter defined by Equation 2.95

π = constant

ρ = density

σ = standard deviation or error

τ_j = lag time

$\mathcal{J}$ = time integral scale

$\mathcal{J}_s$ = Stokian response time

ϕ = volume loading concentrations

$\chi(\phi)$ = arbitrary function of ϕ, for virtual mass modifier

ψ = particle parameter defined by Equation 2.96

ψ_v = stream function

ω = circular frequency

Subscripts and Superscripts

E = Eulerian frame of reference

f = fluid

i, j = cartesian tensor index notation, numerical index

L = Lagrangian frame

m = mean

max = maximum

M = pertaining to an ensemble of M runs

n = numerical index

o = zero reference condition

p	=	particle
Q	=	quiescent
r	=	radial direction
rms	=	root mean square
T	=	turbulent
z	=	axial direction
1,2,3	=	numerical index
primes	=	rms quantities
overbars	=	long time averages
overdot	=	a time derivation
θ	=	azimuthal direction
$\circledast$	=	complex conjugate of the argument

CHAPTER 1 INTRODUCTION AND BACKGROUND

1.1 Introduction

In many engineering disciplines, problems arise with regard to particulate matter suspended in turbulent fluids. For example, in nuclear reactor safety analysis, particles in turbulent suspension play an important role in post accident analysis; in the design of inertia and impingement filters, particle suspension characteristics help in assessing the efficiency of these filters; in erosion damage sustained by blades in steam turbines; in air and water pollution; in river sedimentation and in pneumatic conveying all of which encompass particles suspended in a turbulent environment. Unfortunately, due to the inherent complexity of transport in turbulent flows, a unified theory has not yet been realized.

In order to provide a fundamental understanding of the behavior of dilute turbulent particle suspensions, an experimental investigation was initiated by B.G. Jones (1966). Continued research by Shirazi (1967), Meek (1972) and Howard (1974) provided an analytical model, as well as experimental data, for particle behavior in very dilute turbulent suspension; where the particles' presence did not greatly alter the turbulent structure, nor did particle-particle interactions come into play. As a logical extension of the previous research this project was undertaken to examine the behavior of particles in a non-dilute turbulent suspension.

Two experimental objectives were selected; first, to modify the existing experimental facility, used by the previous investigators, to provide for the vastly increased inventory of particles without altering the

basic turbulent flow characteristics of the system (without particles present). This was done to enhance compatibility with previously obtained fluid and particle data.

Second, to measure various particle statistical quantities and their variation with respect to particle free fall velocity for a range of particle volume concentration, ϕ, from 0 to 10 percent and also to measure, or at least estimate, the fluids scales and intensity for similar concentration variations.

The analytic objectives of this research are twofold. First, to extend the previous model development by Meek (1972) to the case in which particle-particle hydrodynamic interactions must be considered, and secondly to relax the constraint of Stokesian particle behavior in order to incorporate high particle free fall Reynold's numbers.

1.2 Previous Analytical Work

The investigation of particle behavior has long been the subject of many investigations. The equation of motion for a single particle in a quiescent fluid was initially developed by Basset (1961), Bousinesq (1903) and Oseen (1927). Tchen (1947) extended the governing equation for the case of unsteady motion of the particle. Later, Corrsin and Lumley (1956) made a correction to Tchen's expression to include the proper pressure gradient effects applied to a particle in a turbulent flow field. Lumley (1957) pointed out the complexity of the equation by showing that the fluid velocity is to be evaluated at the yet unknown particle position. This has become known as the essential non-linearity of the governing equation.

The nature of the equation is one of a second order non-linear differential equation with the added complexity of Lumley's essential non-

linearity. As a result a closed form solution has not yet been realized. Some authors have solved simplified, linear approximations to the equation. In particular Hinze (1959), and Chao (1964) have solved the most complete equations. Chao's analysis technique was further employed by Meek and Jones (1973) in which statistical quantities of a particle in a turbulent fluid were predicted. In a recent renaissance of particle behavior literature, Reeks (1977) and Pismen and Nir (1978) have made particle turbulent calculations similar to Meek and Jones, but employing a very much simplified governing equation.

In all the above cited literature, the governing equations were restricted to very dilute suspensions, in which the particles did not interact with each other. As one moves onto the realm where the suspension becomes non-dilute, most of the research reported in the literature is concerned with the mean motion of a cloud of particles and a phenomenon often referred to as "hindered settling"; defined as the relatively slower free fall velocity for assemblages of particles.

Buyevich (1971) presented a generalized equation of motion for a particle in non-dilute suspension, but only considered the solution of the mean equation of motion for very high particle concentrations (Buyevich, 1972a, b).

Sedimentation of non-dilute suspensions was analyzed by Tam (1969) in which a formula for the drag exerted on a cloud of spherical particles in a quiescent fluid was derived. Tam made use of the point-force approximation, the essence of which was to replace the disturbance produced by a sphere with a point force, equal to the drag on the particle, at the center of the sphere. Tam obtained good agreement with experimental data he provided by Happel and Epstein (1954).

Batchelor (1972) looked at a similar problem for a sphere in a statistically homogeneous suspension. Batchelor assumed that the sphere's position took on a random distribution within the fluid. Batchelor's results, correct to first order in ϕ, determined the mean velocity of a cloud of particles as

$$\frac{f}{f_o} = (1. - 6.5\phi) \tag{1.1}$$

and where f_0 is the free fall velocity of a single spherical particle.

More recently Hinch (1977), in analyzing particle interactions in fluid suspensions, used an average equation technique in order to estimate the mean settling velocities and the drag force experienced by a cloud of particles. The basis of the average equation approach is to take the conservation laws and constitutive relations for each phase of the suspension and average over the ensemble of phases, hence producing a homogeneous phase of fluid and particle. The results show that the mean velocity of a suspended particle is

$$\frac{f}{f_o} = (1. - .66\phi) \tag{1.2}$$

which is very similar to Batchelor's result. The drag force calculation seems to fall short of the experimental results of Happel and Epstein and it isn't clear whether the difference is from the computation of a residual integral or from a more fundamental error.

1.3 Previous Experimental Work

Previous experimental investigations of particle behavior in turbulent suspensions have been limited to macroscopic studies in which bulk overall characteristics have been determined.

Kada and Hanratty (1960) showed the effects of solid particles on the

fluid turbulence for upward flow in a vertical pipe. The solid concentration levels varied from approximately 0.15 percent to 2.5 percent. Point source diffusion measurements indicated that the fluid diffusion rates were relatively unchanged until there was a sufficient slip velocity between the two phases and unless the particle concentration was large, (> 1%).

The mean settling velocity of particles in quiescent fluids was investigated by several authors. The results of Cheng and Schachaman (1955), and Me Nown and Lin (1952), as reported by Happel and Brenner (1973) show a relative decrease in the particle's velocity as the volume concentration (or loading) was increased. This phenomenon has been known as "hindered settling." Also reported by Happel and Brenner, was experimental data of Kaye and Boardman (1962) in which the particle velocity was seen to increase initially for low volume concentrations, then fall off rapidly at higher concentrations (> 3%). This was attributed to the formation of particle cluster which enhanced their free-fall.

Hino (1963) described Elata and Ippens (1961) experiment in which a suspension of solid particles, considered to be neutrally buoyant, was examined for volume loadings in the range of 15 and 25 percent. The experiments showed that the turbulent intensity increased as the volume loading was increased, but some doubt remains as to the sensitivity of the instrumentation employed due to a large spread in the data at similar particle concentrations.

CHAPTER 2 THEORY

2.1 Non-Dilute Particle Equation of Motion

Consider initially the Equation of Motion*** developed by Tchen (1947) for a particle suspended in a turbulent fluid field and in a sufficiently dilute suspension so as to ignore interactions between particles:

$$\frac{4\pi a^3}{3}\rho_p \dot{u}_{p_i} = \frac{4\pi a^3}{3}\rho_p F^*(\dot{u}_{f_i} - \dot{u}_{p_i}) - \frac{4\pi a^3}{3}\frac{\partial p}{\partial x_i} + \\ + \frac{2\pi a^3}{3}\rho(\dot{u}_{f_i} - \dot{u}_{p_i}) + 6a^2\sqrt{\pi\mu\rho}\int_{t_o}^{t}\frac{\dot{u}_{f_i} - \dot{u}_{p_i}}{(t-\tau)^{1/2}}\,d\tau + \\ + F_i \qquad (2.1)$$

where:

u_{p_i} : Particle Velocity

u_{f_i} : Fluid Velocity

ρ_p : Particle Density

ρ : Fluid Density

F^* : Momentum Transfer Coefficient

μ : Fluid Viscosity

p : Pressure

F_i : External Applied Force

$\cdot$: Convective Time Derivative With Respect to the Particle

a : Particle Radius

***This Equation of Motion is known as the B.B.O. Equation developed by Basset (1961), Boussinesque (1903), and Oseen (1927).

Basically Equation 2.1 is a force balance on a single particle taking into account the viscous drag due to unsteady motion and any applied potential force.

It is the intent of this chapter to expand Equation 2.1 for the case of a non-dilute or multiparticle suspension. This requires a careful look at the individual terms of the equation. Assumptions will be made throughout the development, as seem appropriate.

One of the more dominant terms of the equation of motion is the viscous drag term:

$$F_{D,i} = \frac{4\pi a^3}{3} \rho_p F^* (u_{f_i} - u_{p_i}) \tag{2.2}$$

where:

$$F^* = \frac{3}{8} C_D \frac{\rho}{\rho_p} a^{-1} | u_{f,i} - u_{p,i} | \tag{2.3}$$

It should be noted that C_D, the drag coefficient, is a function of the particles Reynolds number. In later sections various forms of C_D will be presented in order to model the drag over a wide range of particle Reynolds numbers.

In a multiparticle situation, motions of neighboring particles distort the fluid's behavior near a particle of interest. This is basically done through hydrodynamic interaction and depends on the number density of the particles and their characteristics dimensions. A modification of Equation 2.2 to account for particle-particle hydrodynamic interaction has historically taken the following form:

$$F_{D,i}(\eta, a) = F_{D_i} \lambda(\eta) \tag{2.4}$$

where $\lambda(n)$ modifies the viscous drag experienced by a single particle at a given number density, n. The number density is directly related to the volume fraction loading of particles, ϕ.

Substitution yields the modified viscous drag force as:

$$\frac{4\pi a^3}{3} \rho_p F^* (u_{fi} - u_{pi}) \lambda(\phi) \tag{2.5}$$

A functional form of $\lambda(\phi)$ was developed by Tam (1969) for the case of spherical particles of uniform size. Tam assumed that no direct collisions among particles occured. $\lambda(\phi)$ functional form is:

$$\lambda(\phi) = \frac{4 + 3\phi + 3(8\phi - 3\phi^2)^{1/2}}{(2 - 3\phi)^2} \tag{2.6}$$

Figure 2.1 shows $\lambda(\phi)$ for volume loading, zero to ten percent. It should be pointed out that Tam's results closely follow experimental results for particles falling in a quiescent fluid. Figure 2.2 shows a comparison of Tam's results and those of Happel and Epstein (1954).

The next term in Equation 2.1 is known as the pressure gradient force:

$$- \frac{4\pi a^3}{3} \frac{\partial P}{\partial x_i} \tag{2.7}$$

For very dilute suspensions, Corrsin and Lumley (1956) suggested that the pressure gradient take on the following form:

$$\frac{\partial P}{\partial x_i} = \mu \frac{\partial^2 u_{fi}}{\partial x_j^2} - \rho\left(\frac{\partial u_{fi}}{\partial t} + u_{fj} \frac{\partial u_{fi}}{\partial x_j}\right) \tag{2.8}$$

which is the Navier-Stokes Equation. Buyevich (1971) derived a modified Navier-Stokes Equation in which allowances were made for the volume fraction occupied by the particle; this is shown as:

$$\frac{\partial P}{\partial x_i} = \mu \frac{\partial^2 u_{fi}}{\partial x_j^2} - \rho(1-\phi)\left(\frac{\partial u_{fi}}{\partial t} + u_{fj} \frac{\partial u_{fi}}{\partial x_j}\right)^{\dagger} \tag{2.9}$$

---

†For none dilute concentrations μ should be replaced by an effective dynamic viscosity, the form of which is not yet well defined in the literature.

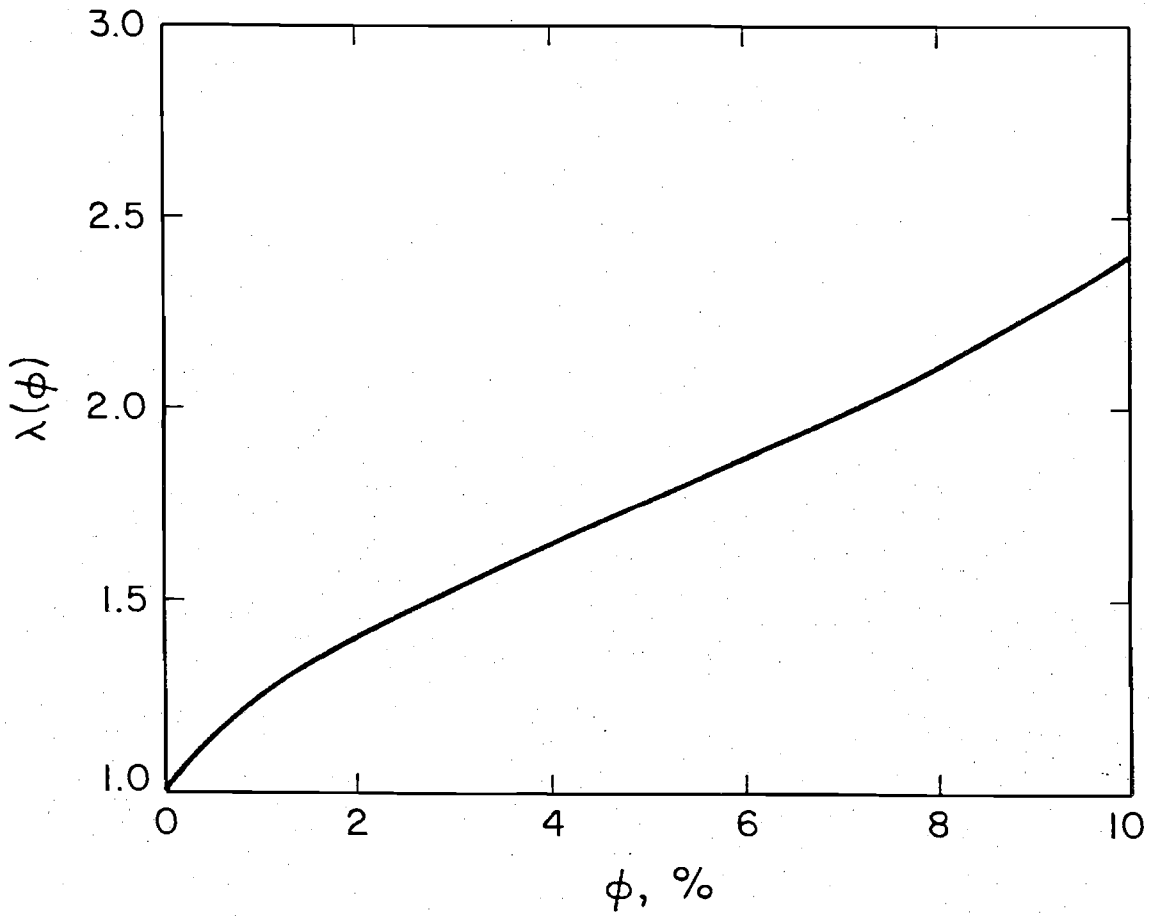

Figure 2.1 Tam's (1969) Prediction of $\lambda(\phi)$ at Various Volume Loadings ϕ,%

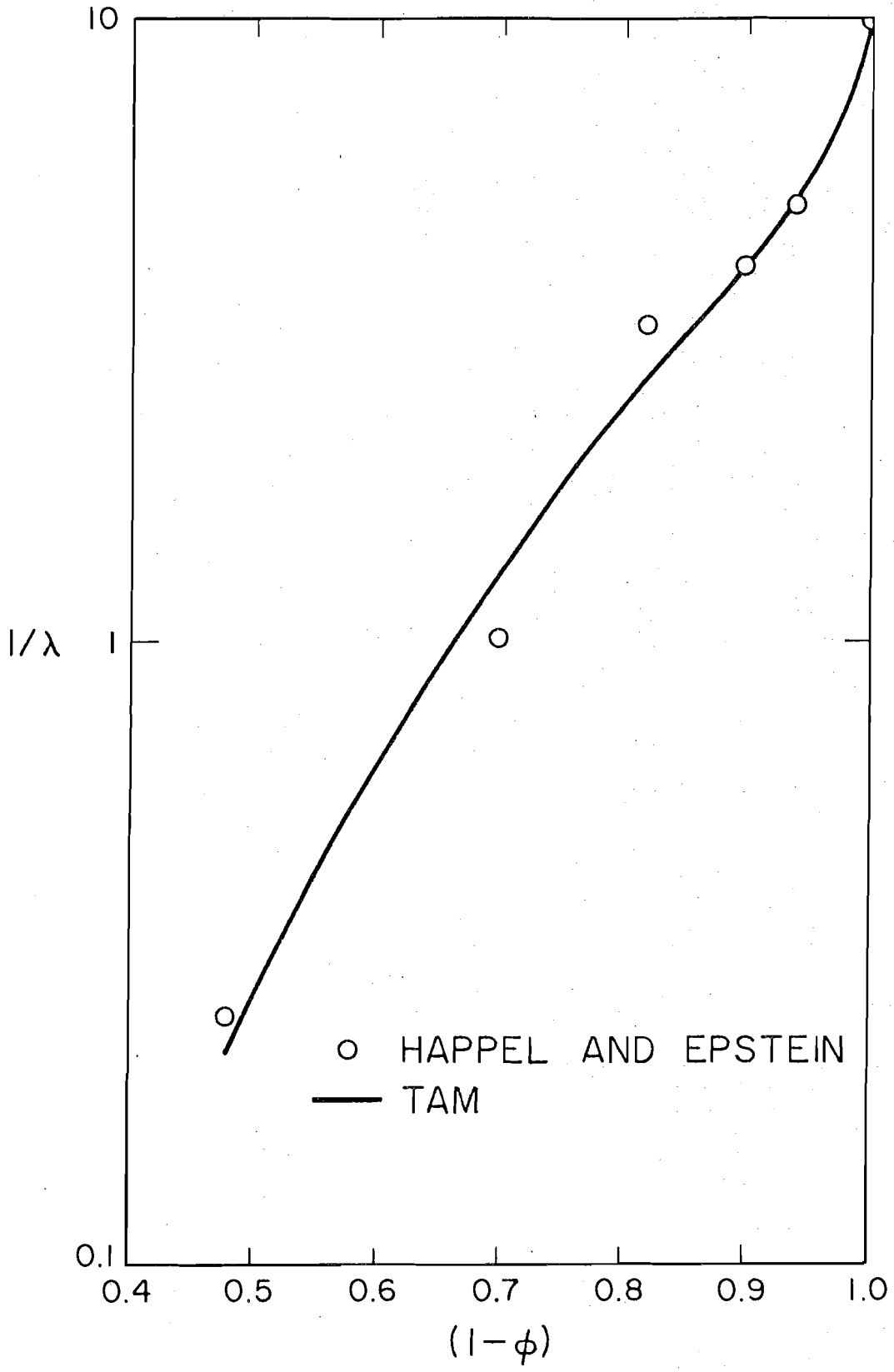

Figure 2.2 Comparison of Experimental Values of $\lambda(\phi)$ (Happel and Epstein (1954) and Tam's (1969) Theoretical Predictions)

Here once again ϕ is the volume fraction of particles. Substitution of Equation 2.9 into Equation 2.7 yields the modified pressure gradient term:

$$\frac{4\pi a^3}{3}\left[\mu \frac{\partial^2 u_{fi}}{\partial x_j^2} - \rho(1-\phi)\left(\frac{\partial u_{fi}}{\partial t} + u_{fj}\frac{\partial u_{fi}}{\partial x_j}\right)\right] \tag{2.10}$$

The third term is known as the virtual or apparent mass force, which is the force necessary to accelerate the fluid in contact with the particle.

Buyevich (1971) suggested that the virtual mass term be modified in the following manner

$$\frac{1}{2}\eta(\phi)\frac{4\pi a^3}{3}\rho\left(\dot{u}_{fi} - \dot{u}_{pi}\right) \tag{2.11}$$

Buyevich (1971) estimated $\eta(\phi)$ for spherical particles as:

$$\eta(\phi) = \frac{1+\left(\frac{\phi}{1+\phi}\right)\left[3 + \frac{2/3\ln\phi}{(1-\phi)}\right]}{1+\left(\frac{\phi}{1+\phi}\right)\left[1 + \frac{1/3\ln\phi}{(1-\phi)}\right]} \tag{2.12}$$

The function $\eta(\phi)$ is a slowly varying parameter of order unity, hence it provides a small change in the virtual mass force as the volume loading increases.

The next term in Equation 2.1 represents the force or drag due to unsteady motion of the particle. This term has been called the Basset term after A. B. Basset's (1961) work on particle drag.

The modification of the Basset term for the presence of other particles may take the following form:

$$6a^2\sqrt{\pi\mu\rho}\int_{t_o}^{t}\theta(\phi)\frac{\dot{u}_{fi} - \dot{u}_{pi}}{(t-\tau)^{1/2}}\,d\tau \tag{2.13}$$

where $\theta(\phi)$ is an unknown function of ϕ. Questions arise as to what effects other particles have on the response of a particle to an impulse force from the turbulent fluid. Buyevich indicates that $\theta(\phi)$ may be of order unity for volume loadings where particle interaction were not dominated by collisions with other particles.

The last term, F_i, is the force of an applied field, and unless the presence of additional material in the fluid alters the applied field, it will be assumed that F_i, is invariant with respect to ϕ, the volume loading.

Combining all of the above terms yields the equation of motion for a particle in a multiparticle suspension as:

$$\frac{4\pi a^3}{3}\rho_p \dot{u}_{p_i} = \frac{4\pi a^3}{3}\rho_p F^* \lambda(\phi)(u_{f_i} - u_{p_i}) - \frac{4\pi a^3}{3}\frac{\partial P(\phi)}{\partial x_i} + \tag{2.14}$$

$$+ \frac{4\pi a^3}{3}\frac{\eta(\phi)}{2}\rho(\dot{u}_{f_i} - \dot{u}_{p_i}) + 6a^2\sqrt{\pi\mu\rho}\int_{t_o}^{t}\theta(\phi)\frac{\dot{u}_{f_i} - \dot{u}_{p_i}}{(t-\tau)^{1/2}}\,d\tau + F_i$$

where $\frac{\partial P(\phi)}{\partial x_i}$ is defined by Equation 2.9. Note that the overdot is defined as the convective derivative:

$$\dot{} = \left(\frac{\partial}{\partial t} + u_{p_j}\frac{\partial}{\partial x_j}\right) \tag{2.15}$$

Equation 2.14 represents a non-linear second order equation with the additional stipulation, as Lumley (1957) points out, that the fluid velocity must be evaluated at the yet unknown particle position. This has become known as the "essential non-linearity."

The coefficients, $\lambda(\phi)$, $\eta(\phi)$, and $\theta(\phi)$ are bulk parameters that assume a linear relation with the equation of motion for a single particle.

This approach inherently states that the fluid's characteristics are those for the case in which a single particle is present and the parameters take into account the presence of other particles through hydrodynamical means.

A review of the assumptions indicates that:

1) No particle collisions are considered.

2) The particles are spherical and of a uniform size. This assumption may be dropped if Tam's solution is considered for a known particle size distribution.

Historically, certain physical assumptions are made to linearize the particles equation of motion in order to obtain a solution. The next section deals with these assumptions and produces a set of equations for further consideration.

2.2 Linearized Equation of Motion

Approximations are made in order to simplify the governing equation of motion. Once again the assumptions will be presented as deemed appropriate.

Starting with Equation 2.14 with Equation 2.9 substituted for the pressure gradient, we have:

$$\frac{4\pi a^3}{3}\rho_p \dot{u}_{pi} = \frac{4\pi a^3}{3}\rho_p F^* \lambda(\phi)(u_{fi} - u_{pi}) + \frac{4\pi a^3}{3}\rho(1-\phi)^* \\ * \left(\frac{\partial u_{fi}}{\partial t} + u_{fj}\frac{\partial u_{fi}}{\partial x_j}\right) - \frac{4\pi a^3}{3}\mu\frac{\partial^2 u_{fi}}{\partial x_j^2} + \eta(\phi)\frac{2\pi a^3}{3}\rho(\dot{u}_{fi} - \dot{u}_{pi}) + \\ + 6a^3\sqrt{\pi\mu\rho}\int_{t_0}^{t}\theta(\phi)\frac{\dot{u}_{fi} - \dot{u}_{pi}}{(t-\tau)^{1/2}}\,d\tau + F_i \qquad (2.16)$$

Noting that:

$$\frac{\partial u_{fi}}{\partial t} + u_{fj}\frac{\partial u_{fi}}{\partial x_j} = \dot{u}_{fi} + (u_{f_k} - u_{p_k})\frac{\partial u_{fi}}{\partial x_k} \qquad (2.17)$$

Equation 2.16 becomes:

$$\rho_p \dot{u}_p = \rho_p F^* \lambda(\phi)(u_{f_i} - u_{p_i}) + \rho(1-\phi)\left[\dot{u}_{f_i} + (u_{f_k} - u_{p_k})\frac{\partial u_{f_i}}{\partial x_k}\right] - \mu \frac{\partial^2 u_{f_i}}{\partial x_j^2} +$$

$$+ \frac{\eta(\phi)}{2}\rho(\dot{u}_{f_i} - \dot{u}_{p_i}) + \frac{9}{2}\sqrt{\frac{\mu\rho}{\pi a^2}}\int_{t_o}^{t} \theta(\phi)\, \frac{\dot{u}_{f_i} - \dot{u}_{p_i}}{(t-\tau)^{1/2}}\, d\tau + F_i' \qquad (2.18)$$

Hinze (1959) noted that the non-linearity is negligible if:

$$a\, \frac{\partial u_{f_i}}{\partial x_j^*} << 1 \qquad (2.19)$$

where $x^* = \frac{x}{a}$, thus if the particle is small as compared to the Taylor microscale, as Chao (1964) pointed out, this term is negligible. Furthermore, the equation becomes first order if the viscous term can be neglected, that is

$$u_{p_j}\frac{\partial u_{f_i}}{\partial x_j} >> \nu \frac{\partial^2 u_{f_i}}{\partial x_j^2} \quad \text{OR} \quad \frac{u_{p_j}\frac{\partial u_{f_i}}{\partial x_j}}{\nu \frac{\partial^2 u_{f_i}}{\partial x_j^2}} >> 1 \qquad (2.20)$$

which by the above assumption states:

$$\frac{u_{p_i}}{\frac{\partial^2 u_{f_i}}{\partial x_j^{*2}}} >> 1 \qquad (2.21)$$

This states once again that the particle must be very small as compared to the microscale. Thus:

$$\rho_p \dot{u}_{p_i} = \rho_p F^* \lambda(\phi)(u_{f_i} - u_{p_i}) + \left[\rho(1-\phi) + \frac{\eta(\phi)}{2}\right]\dot{u}_{f_i} - \frac{\eta(\phi)}{2}\rho \dot{u}_{p_i} +$$

$$+ \frac{9}{2}\sqrt{\frac{\mu\rho}{\pi a^2}}\int_{t_0}^{t} \theta(\phi)\,\frac{\dot{u}_{fi} - \dot{u}_{pi}}{(t-\tau)^{1/2}}\,d\tau + F_i' \qquad (2.22)$$

Meek (1972) had shown, that for particles whose density was within an order of magnitude of the fluid's density, the contribution of the Basset term toward statistical parameters, were negligible. This will be discussed further in Section 2.6. Thus, dropping the Basset term:

$$\left(\rho_p + \frac{\eta(\phi)}{2}\rho\right)\dot{u}_{pi} - \rho_p F^* \lambda(\phi)(u_{fi} - u_{pi}) - \rho\,\gamma'(\phi)\,\dot{u}_{fi} + F_i' = 0 \qquad (2.23)$$

Where:

$$\gamma'(\phi) = \left[1 - \phi + \frac{\eta(\phi)}{2}\right] \qquad (2.24)$$

$U_{p,i}$ can be expressed, for a particle with a finite free fall velocity as:

$$u_{pi} = V_{pi} + f\hat{K}$$

Where $V_{p,i}$ is the particle fluctuating velocity. Thus equation 2.35 becomes:

$$\left[\rho_p + \frac{\eta(\phi)}{2}\rho\right]\dot{V}_{pi} - \rho_p F^* \lambda(\phi)(u_{fi} - v_{pi}) - \rho\,\gamma'(\phi)\,\dot{u}_{fi} = 0 \qquad (2.25)$$

The above equation is linear only when F* is a constant. This is only the case when the particles are assumed Stokian (particles with Reynold's numbers less then one). For particle Reynold's numbers greater than one, the situation becomes non-linear. The next section will examine Equation 2.25 for various particle Reynold's numbers.

2.3 Linearized Equation of Motion at Various Particle Reynold's Numbers

The simplified equation of motion contains the particle's physical characteristics in the term F*. Reviewing Equation 2.3:

$$F^* = 3/8\, C_D \frac{\rho}{\rho_p} a^{-1} \left| u_{fi} - u_{pi} \right| \qquad (2.3)$$

The principle parameter is the drag coefficient, C_D. C_D is a function of the particle's Reynold's number, defined as follows:

$$Re_p = \frac{2a}{\nu} |u_{fi} - u_{Pi}| \qquad (2.26)$$

Figure 2.3 illustrates the behavior of the drag coefficient. There are three principle regions of behavior: Stokes Law, Intermediate Law and the Newton Law Region. A general description for each region is in order.

1) The Stokes Law or creeping flow region is defined for particle's Reynold's numbers less than one. The very nature of the functional form of C_D is linear, therefore most authors restrict the particle to reside within this region. The form of C_D is:

$$C_D = \frac{24}{Re_p} \qquad (2.27)$$

Substitution of C_D into Equation 2.3 yields a linear function of F*.

2) The Intermediate Law Region is defined for:

$$1 < Re_p < 400$$

Several investigators have estimated C_D analytically for R_{ep} less than ten, but only after a considerable amount of effort. The result seen in Figure 2.3 is based on experimental data. An approximate form of the curve is given by Ingebo (1956) as:

$$C_D = \frac{B}{Re_p^{\theta}} \qquad (2.28)$$

where B is a constant and θ an exponent less than one. If one substitutes Equation 2.26 into Equation 2.3:

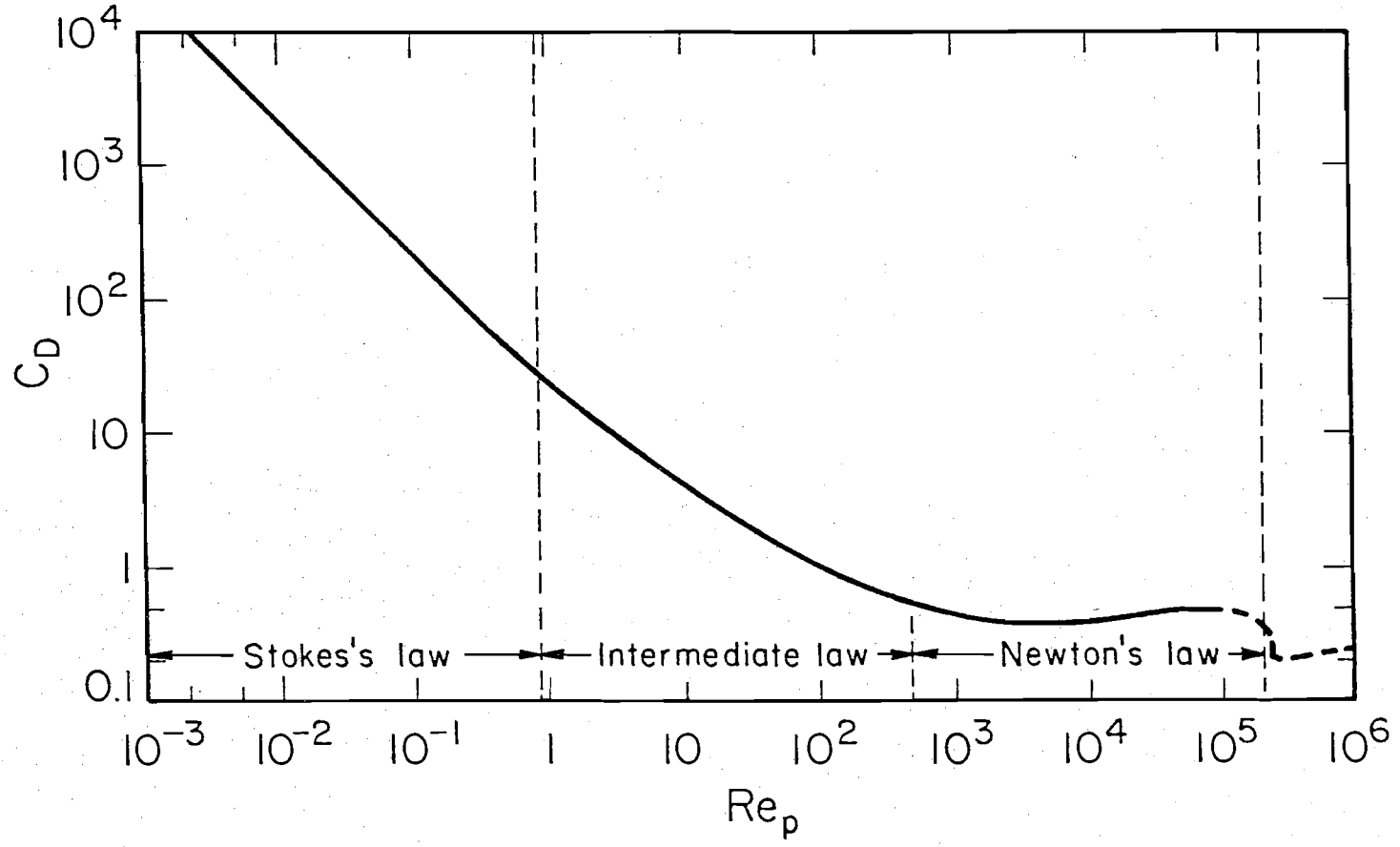

Figure 2.3 Drag Coefficient for Sphere Various Reynolds Number [Curve Taken from Bird, Steward and Lightfoot, "Transport Phenomena", John Wiley and Sons, New York, p. 192]

$$\lambda(\phi)\rho F^*(u_{fi}-u_{pi}) = C|u_{fi}-u_{pi}|^{1-\theta}(u_{fi}-u_{pi})\lambda(\phi)\rho \quad (2.29)$$

where C is constant, this result makes Equation 2.25 non-linear and in its present form is very troublesome to work with analytically.

3) The last region is known as Newton's Law Region. This should not be confused with Newton's Law of Motion or Viscosity. The Newton Region is defined for:

$$400 < Re_p < 10^5 \quad (2.30)$$

where the drag coefficient can be assumed constant, that is:

$$C_D = 0.44 \quad (2.31)$$

Substitution of C_D in F* results in:

$$\lambda(\phi)\rho_p F^*(u_{fi}-u_{pi}) = 3/8\, a^{-1}\rho\lambda(\phi) C_D |u_{Fi}-u_{Pi}|(u_{fi}-u_{pi}) \quad (2.32)$$

As before, this is non-linear and prevents an analytical solution to the equation of motion.

As pointed out before, most investigators assumed that the particle resides within the Stokes region, when in reality suspensions contain particles within the intermediate and Newton region. In order to present a complete multiparticle theory, three forms of the multiparticle linearized equation of motion will be presented. This includes an exact Stokian form and two approximate forms for the intermediate and Newton regions.

Let us consider first the Stokian drag form. Substitution of Equation 2.25 into Equation 2.3 yields

$$F^* = \frac{9\mu}{2a^2\rho_p} \tag{2.33}$$

Substitution into Equation 2.25 gives:

$$\dot{V}_{p,i} - \frac{3\nu}{a^2}\lambda(\phi)\beta(\phi)\left(U_{f_i} - V_{p_i}\right) - \beta(\phi)\,\gamma(\phi)\,\dot{U}_{f_i} = 0 \tag{2.34}$$

Here

$$\gamma(\phi) = \frac{2}{3}\gamma'(\phi) = \frac{2}{3}\left[(1-\phi) + \frac{\eta(\phi)}{2}\right] \tag{2.35}$$

$$\beta(\phi) = \frac{3\rho}{2\rho_p + \eta(\phi)\rho} \tag{2.36}$$

Equation 2.34 represents the Stokian multiparticle linearized equation of motion.

Consider now the intermediate region. Substituting Equation 2.28 into Equation 2.3 and then into Equation 2.23 yields:

$$\left[\rho_p + \frac{\eta(\phi)}{2}\rho\right]\dot{U}_{p_i} - \frac{9\nu}{2a^2}\lambda(\phi)\rho C_1\left|U_{f_i} - U_{p_i}\right|^{1-B}\left(U_{f_i} - U_{p_i}\right) - \rho\gamma'(\phi)\dot{U}_{f_i} + f_i = 0 \tag{2.37}$$

Where

$$C_1 = \left(\frac{B}{24}\right)\left(\frac{2a}{\nu}\right)^{1-B} \tag{2.38}$$

Linearization of this equation is reduced to an investigation of the second term in Equation 2.36 that is:

$$\frac{9\nu}{2a^2}\rho\lambda(\phi)C_1|u_{fi}-u_{pi}|^{1-\theta}(u_{fi}-u_{pi}) \tag{2.39}$$

Jones et al. (1973) investigated the above term without the presence of the multiparticle parameter $\lambda(\phi)$. By choosing the gravity force to act in the Z-direction, Jones expressed the relative velocity, V_R as:

$$V_{R_i} = u_{fi} - u_{pi} = V_{R_x}\hat{i} + V_{R_y}\hat{j} + (V_{R_z} - f)\hat{k} \tag{2.40}$$

and

$$|u_{fi} - u_{pi}|^{1-\theta} = (V_{R_x}^2 + V_{R_y}^2 + V_{R_z}^2 + f^2 - 2V_{R_z}f)^{(1-\theta)/2} \tag{2.41}$$

By expanding the above equations in a binomial series and taking a zero order consideration, Jones et al. determined that Equation 2.39 take the form:

$$\frac{9\nu}{2a^2}\rho\delta_i(u_{fi} - V_{pi}) + G_i \tag{2.42}$$

where G_i is the drag due to the steady gravitational free-fall and δ_i is defined as

$$\delta_i = C_1 Re_f^{1-\theta}[1, 1, (2-\theta)] \tag{2.43}$$

If one considers Ingebo's relation where B=27 and Q=.84, the δ_i becomes

$$\delta_i = 1.12\ R_f^{0.16}\ [1, 1, 1.16] \tag{2.44}$$

Where:

$$R_f = 2af/\nu \tag{2.45}$$

As Jones et al. points out, this drag modifier is limited to particle Reynold's numbers in the realm of $6 \leq R_{ep} \leq 400$ which is sufficiently large to accomodate the intermediate range. A comparison of Jones results to Ingebo's data is shown in Figure 2.4. Reasonably good results are indicated. Applying this technique to Equation 2.40 results in the following form of Equation 2.23:

$$\dot{V}_{P_i} - \frac{3\nu}{a^2}\,\delta_i\,\lambda(\phi)\,\beta(\phi)(u_{f_i} - V_{P_i}) - \beta(\phi)\,\gamma(\phi)\,\dot{u}_{f_i} = 0 \tag{2.46}$$

This represents the linearized equation of motion for the intermediate region.

Looking at the Newton law region, the drag coefficient is assumed to be constant. If we make use of the particle velocity definition:

$$u_{P_i} = V_{P_i} + f\hat{K} \tag{2.47}$$

Equation 2.3 becomes:

$$F^* = \frac{3}{8}\,\frac{C_D}{a}\,\frac{\rho}{\rho_P}\left[(u_{f_i} - V_{P_i} - f\hat{K})^2\right]^{1/2} = \frac{3}{8}\,\frac{C_D}{a}\,\frac{\rho}{\rho_P}\left[u_{f_x}^2 + \right.$$

$$+ u_{f_y}^2 + u_{f_z}^2 - 2\left(V_{P_x}u_{f_x} + V_{P_y}u_{f_y} + (V_{P_z} + f)u_{f_z}\right) +$$

$$\left. + V_{P_x}^2 + V_{P_y}^2 + V_{P_z}^2 + f^2 + 2fV_{P_z}\right]^{1/2} \tag{2.48}$$

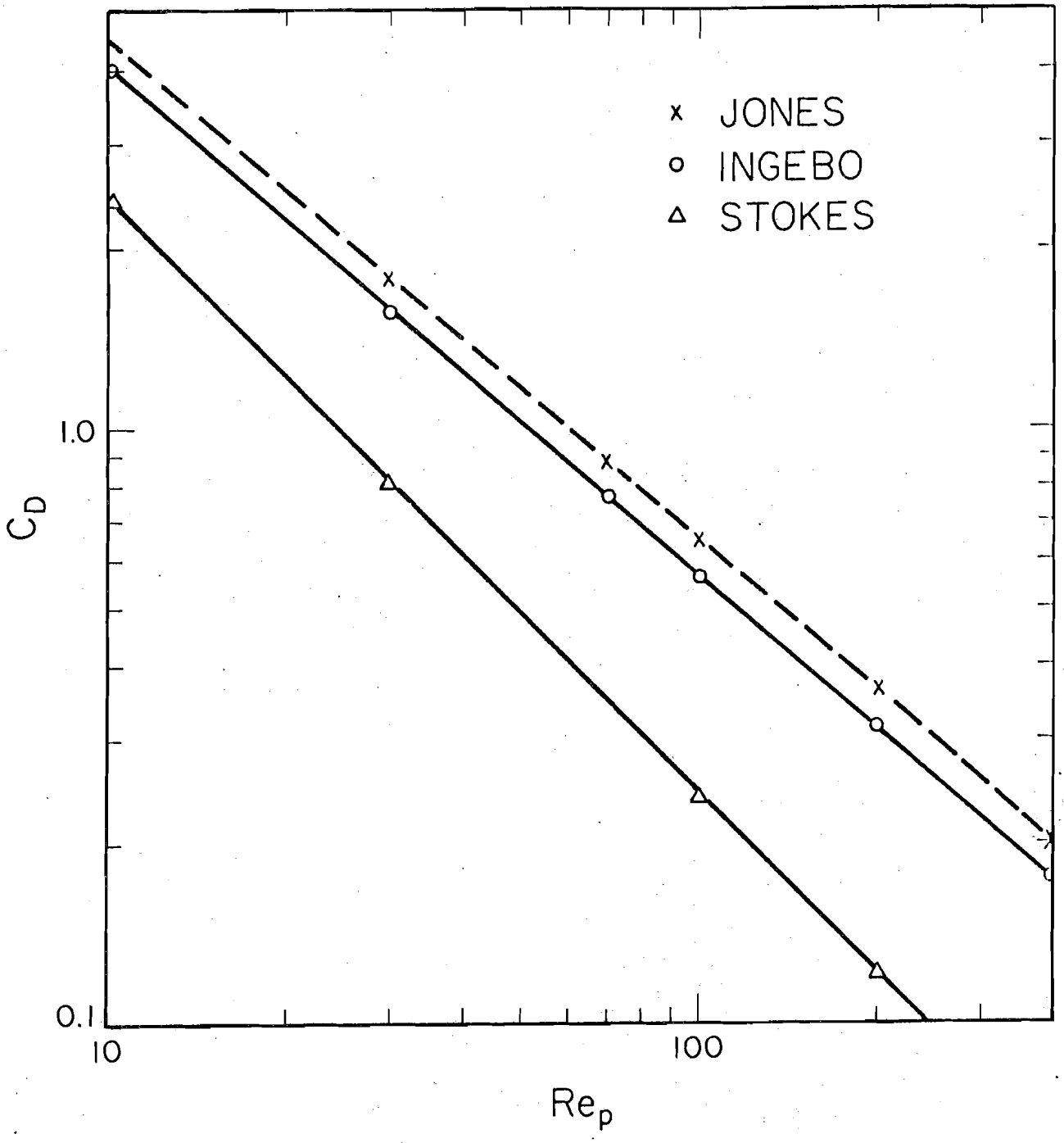

Figure 2.4 Comparison of Various Particle Drag Approximations

Taking note that:

$$V_p << f \tag{2.49}$$

and

$$V_p \simeq \mu_f \tag{2.50}$$

Thus, V_p^2, V_f^2 and $V_p U_f$ terms are much smaller as compared to other terms, therefore, they are neglected. Thus, Equation 2.48 becomes:

$$F^* = \frac{3}{8} \frac{C_D}{a} \frac{\rho}{\rho_p} \left[f^2 + 2f (V_{p_z} - \mu_{f_z}) \right]^{1/2} \tag{2.51}$$

Substitution into Equation 2.25 yields:

$$\left[\rho_p + \frac{\eta(\phi)}{2} \rho \right] \dot{V}_p - \frac{3}{8} \frac{C_D}{a} \rho \lambda(\phi) \left[f^2 + 2f(V_{p_z} - \mu_{f_z}) \right]^{1/2} (\mu_{f_i} -$$

$$- V_{p_i}) - \rho \gamma'(\phi) \dot{\mu}_f = 0 \tag{2.52}$$

Using the same order of magnitude evaluation as before reduces the above equation to:

$$\dot{V}_{p_i} - \frac{C_D f \lambda(\phi)}{2a} \beta(\phi) (\mu_{f_i} - V_{p_i}) - \beta(\phi) \gamma(\phi) \dot{\mu}_{f_i} = 0 \tag{2.53}$$

Equation 2.53 represents the linearized multiparticle equation for the Newton region.

Reviewing Equations 2.34, 2.46, and 2.53 indicates they follow a common form:

$$\dot{V}_p - \alpha_k(\phi)\,\beta(\phi)(u_{fi} - V_{pi}) - \beta(\phi)\,\gamma(\phi)\,\dot{u}_{fi} = 0 \qquad (2.54)$$

Where $\alpha_k(\phi)$ is a parameter, unique to each region, defined as

$$\alpha_N = (C_D f/2a)\,\lambda(\phi) \qquad (2.55)$$

$$\alpha_S = \frac{3\nu}{a^2}\,\lambda(\phi) \qquad (2.56)$$

$$\alpha_I = \frac{3\nu}{a^2}\,\delta_i\,\lambda(\phi) \qquad (2.57)$$

It should be noted that the viscous contributions in the Newton region is found within the drag coefficient.

Equation 2.54 is the multiparticle linearized equation of motion for particles of a wide range of particle Reynold's number.

With the linearized equation of motion, a solution will be demonstrated in the next section for the particle response function and statistical quantities.

2.4 Particle Response Function, Energy Spectra, Autocorrelation and Dispersion

In this section, the multiparticle equation of motion will be used to calculate statistical quantities, making use of the method described by Chao (1964).

Starting with the equation of motion:

$$\dot{V}_{p_i} - \alpha_k(\phi)\,\beta(\phi)(u_{fi} - V_{pi}) - \beta(\phi)\,\gamma(\phi)\,\dot{u}_{fi} = 0 \qquad (2.54)$$

Grouping the particle velocities on one side of the equality yields:

$$\dot{V}_{P_i} + \alpha_K(\phi)\beta(\phi)V_{P_i} = \beta(\phi)\gamma(\phi)\dot{U}_{f_i} + \alpha_K(\phi)\beta(\phi)U_{f_i} \qquad (2.58)$$

For convenience, we will drop subscript i and independent parameter ϕ.

If we defined the Fourier transforms in the following manner:

$$\tilde{U}_T(\omega) = \int_{-T}^{T} U(t)\, e^{-j\omega t}\, dt \qquad (2.59)$$

$$U(t) = \frac{1}{2\pi}\int_{-T}^{T} \tilde{U}_T(\omega)\, e^{-j\omega t}\, d\omega \qquad (2.60)$$

where $T \to \infty$. Applying the Fourier transform to Equation 2.58 yields

$$\frac{\tilde{V}_{P_T}}{\tilde{U}_{P_T}} = \frac{j\omega\beta\gamma + \alpha_K\beta}{j\omega + \alpha_K\beta} \qquad (2.61)$$

Chao defined the particle response function, $Q(\omega)$ as:

$$Q(\omega) = \frac{E_P(\omega)}{E_f(\omega)} = \frac{U_f'^2}{V_p'^2} \lim_{T\to\infty} \frac{\tilde{V}_{P_T}\tilde{V}_{P_T}^{\circledast}}{\tilde{U}_{f_T}\tilde{U}_{f_T}^{\circledast}} \qquad (2.62)$$

where $E_{p(\omega)}$: Energy spectra for the particle.

$E_f(\omega)$: Energy spectra for the fluid.

$V_p'(t)$: rms value of the particle velocity, $V_p(t)$.

$U_f'(t)$: rms value of the fluid velocity, $U_f(t)$.

$\circledast$: Indicate complex conjugate of the argument.

Substituting from Equation 2.61, the response function is to be:

$$Q(\omega) = \frac{U_f'^2}{V_p'^2}\left[\frac{1 + \gamma^2(\phi)\left(\frac{\omega}{\alpha_K(\phi)}\right)^2}{1 + \frac{1}{\beta^2(\phi)}\left(\frac{\omega}{\alpha_K(\phi)}\right)^2}\right] \qquad (2.63)$$

From the definition in Equation 2.62, the particle energy spectra is:

$$E_p(\omega) = Q(\omega) E_f(\omega) \tag{2.64}$$

Thus, if the fluid's energy spectra is known, the particle's energy can be determined through the particle response function. Hence, the problem reduces to obtain the energy spectra for the fluid.

The fluid energy spectra can be obtained from the fluid's Lagrangian autocorrelation by making use of a common technique in turbulence. The energy spectra can be determined from:

$$E_f(\omega) = \frac{2}{\pi}\int_0^\infty R_{f_z}(\tau)\cos(\omega\tau)\,d\tau \tag{2.65}$$

To determine the Lagrangian autocorrelation consider a particle as it falls through the fluid. The particle samples the fluid's behavior at a rate that is proportional to its velocity. With this in mind, the Lagrangian spatial correlation, defined as

$$R_{f_z}(z) = e^{-z/\Lambda_z} \tag{2.66}$$

where Λ_z is the Lagrangian spatial macroscale. Recalling that the spatial correlation is invariant with respect to translation in homogeneous, isotropic turbulence, we can express the spatial scale and its argument as:

$$z = \left[\left(V'^2_{p_z} + f^2\right)^{1/2}\tau\right]\hat{z} \tag{2.67}$$

$$\Lambda = \sigma'_{f_z}\mathcal{T}_{F_z} \tag{2.68}$$

Hence, we have a properly scaled Lagrangian time autocorrelation:

$$R_{f_z}(\tau) = e^{-(V'^2_{p_z} + f^2)^{1/2} \tau / \mathcal{J}_{F_z} u'_{f_z}} \tag{2.69}$$

It should be noted if the sampling particle is a "fluid particle", the above equation results in the familiar Lagrangian autocorrelation for a fluid:

$$R_{f_z}(\tau) = e^{-\tau / \mathcal{J}_{F_z}} \tag{2.70}$$

If we define:

$$T_{f_z} = \mathcal{J}_{F_z} / [(V'^2_{p_z} + f^2)/u'_{f_z}] \tag{2.71}$$

Then the axial Lagrangian fluid energy spectra is found to be:

$$E_{f_z}(\omega) = \frac{2}{\pi} \frac{T_{f_z}}{1 + (\omega T_{f_z})^2} \tag{2.72}$$

Since isotropy cannot be assumed for the particle of finite free-fall and size, the particles lateral autocorrelations must be determined from the fluids lateral autocorrelation. Making use of the isotropic behavior of the fluid:

$$R_{f_r}(\tau) = R_{f_\theta}(\tau) = R_{f_z}(\tau) + \frac{\tau}{2} \frac{dR_{f_z}(\tau)}{d\tau} \tag{2.73}$$

which results in:

$$R_{f_r}(\tau) = R_{f_\theta}(\tau) = [1 - (\tau / 2T_{f_z})] e^{-\tau / T_{f_z}} \tag{2.74}$$

and hence, the energy spectra yields:

$$E_{f_r}(\omega) = E_{f_\theta}(\omega) = \frac{T_{f_z}}{\pi} \frac{1 + 3(\omega T_{f_z})^2}{1 + (\omega T_{f_z})^2} \tag{2.75}$$

It should be noted that for $\omega = 0$ the ratio:

$$\frac{E_{f_z}(0)}{E_{f_r}(0)} = \frac{\mathcal{J}_{f_z}}{\mathcal{J}_{f_r}} = 2 \tag{2.76}$$

which is the case for isotropic turbulence. Substitution of the corresponding fluid energy spectra into Equation 2.64 produces particle spectra for the longitudinal and lateral directions:

$$E_{p_z}(\omega) = \frac{2}{\pi} \frac{u_f'^2}{V_p'^2} \frac{\left[1 + \gamma^2(\phi)\left(\frac{\omega}{\alpha_\kappa(\phi)}\right)^2\right] T_{f_z}}{\left[1 + \frac{1}{\beta^2(\phi)}\left(\frac{\omega}{\alpha_\kappa(\phi)}\right)^2\right]\left[1 + (\omega T_{f_z})^2\right]} \tag{2.77}$$

and

$$E_{p_r}(\omega) = E_{p_\theta}(\omega) = \frac{T_{f_z}}{\pi} \frac{u_{f_r}'^2}{V_{p_r}'^2} \frac{1 + \gamma^2(\phi)\left[\frac{\omega}{\alpha_\kappa(\phi)}\right]^2}{1 + \beta^{-2}(\phi)\left[\frac{\omega}{\alpha_\kappa(\phi)}\right]^2} \frac{1 + 3(\omega T_{f_z})^2}{1 + (\omega T_{f_z})^2} \tag{2.78}$$

The particle energy spectras can be transformed to represent the particle's autocorrelation and thus the particle's dispersion characteristics can be determined. Use of the classical definition for the autocorrelation transform gives:

$$R_{p_z}(\tau) = \int_0^\infty E_{p_z}(\omega) \cos(\omega\tau) d\tau \tag{2.79}$$

and

$$R_{P_{r,\theta}}(\tau) = \int_0^\infty E_{P_{r,\theta}}(\omega)\cos(\omega\tau)\,d\tau \tag{2.80}$$

Substitution of the respective energy spectra after integrating the auto-correlation is:

$$R_{P_z}(\tau) = \frac{U'^2_{f_z}}{V'^2_{P_z}} \cdot \frac{1}{1-\zeta^2}\left[(1-\zeta^2\psi^2)e^{-\tau/T_{f_z}} - \zeta(1-\psi^2)e^{-\tau/\zeta T_{f_z}}\right] \tag{2.81}$$

and

$$R_{P_r}(\tau) = \frac{U'^2_{f_c}}{V'^2_{P_r}} \frac{\zeta(\zeta^2-K^2)(1-3\zeta^2)e^{-\tau/T_{f_z}\zeta}}{2(1-\zeta^2)^2} +$$

$$+\left[\frac{2(1-2K^2)-\frac{\tau}{T_{f_z}}(1-K^2)}{2(1-\zeta^2)} + \frac{\zeta^2(1-K^2)}{(1-\zeta^2)^2}\right]e^{-\tau/T_{f_z}} \tag{2.82}$$

where:

$$\zeta = \frac{1}{\alpha_K(\phi)\beta(\phi)T_{f_z}} \tag{2.83}$$

$$\psi = \gamma(\phi)\beta(\phi) \tag{2.84}$$

$$K = \gamma(\phi)\beta(\phi)\zeta(\phi) \tag{2.85}$$

Noting for $R_p(0) = 1$

$$\frac{U_{fz}^{12}(\Phi)}{V_{pz}^{12}(\Phi)} = \frac{1+\mathfrak{z}(\Phi)}{1+\Psi^2(\Phi)\mathfrak{z}(\Phi)} \tag{2.86}$$

$$\frac{U_{fr}^{12}(\Phi)}{V_{pr}^{12}(\Phi)} = \frac{2(1-\mathfrak{z}^2)^2}{\mathfrak{z}(\mathfrak{z}^2-K^2)(1-3\mathfrak{z}^{-2})+2K^2(\mathfrak{z}^2-2)+2} \tag{2.87}$$

Through substitution, the final form of the autocorrelation is:

$$R_{p_z}(\tau) = \frac{1}{[1-\mathfrak{z}(\Phi)\Psi^2(\Phi)][1-\mathfrak{z}(\Phi)]}\left\{[1-[\mathfrak{z}(\Phi)\Psi(\Phi)]^2]e^{-\tau/T_{fz}} + \right.$$

$$\left. + \quad \mathfrak{z}(\Phi)[1-\Psi^2(\Phi)]e^{-\tau/\mathfrak{z}(\Phi)T_{fz}}\right\} \tag{2.88}$$

and

$$R_{p_r}(\tau) = R_{p_\theta}(\tau) = K_1 e^{-\tau/T_{fz}\mathfrak{z}(\Phi)} + K_2(\tau)e^{-\tau/T_{fz}} \tag{2.89}$$

where

$$K_1 = \frac{\mathfrak{z}(\mathfrak{z}^2-K^2)(1-3\mathfrak{z}^{-2})}{\mathfrak{z}(\mathfrak{z}^2-K^2)(1-3\mathfrak{z}^{-2})+2\mathfrak{z}^2K^2-4K^2+2} \tag{2.90}$$

$$K_2(\tau) = \frac{[2(1-2K^2)-(1-K^2)\tau/T_{fz}](1-\mathfrak{z}^2)+2\mathfrak{z}^2(1-K^2)}{\mathfrak{z}(\mathfrak{z}^2-K^2)(1-3\mathfrak{z}^{-2})+2\mathfrak{z}^2K^2-4K^2+2} \tag{2.91}$$

Thus, with the proper substitution, lateral and longitudinal autocorrelation for particles of various Reynold's numbers can be obtained. Taylor (1927) predicted the dispersion in a homogeneous isotropic turbulent flow field. Kanpe de Feriet (1939) expressed Taylor's results in the following form.

$$\overline{X_{P_i}^2(t)} = 2\,u_{P_i}'^2 \int_0^t (t-\tau)\, R_{P_i}(\tau)\, d\tau \qquad (2.92)$$

Through substitution and a considerable effort, the dispersions were found to be:

$$\overline{X_{P_z}^2(t)} = \frac{2\,u_{P_z}'^2}{[1-\psi(\phi)\,\mathfrak{z}(\phi)](1-\mathfrak{z})}\left\{[1-[\mathfrak{z}(\phi)\psi(\phi)]^2]\left[T_{f_z}t - T_{f_z}^2\left(1-e^{-t/T_{fz}}\right)\right] - \mathfrak{z}^2(\phi)[1-\psi^2(\phi)]\left[tT_{f_z} - \mathfrak{z}T_{f_z}^2\left[1-e^{-t/\mathfrak{z}(\phi)T_{f_z}}\right]\right]\right\} \qquad (2.93)$$

$$\overline{X_{P_r}^2(t)} = \overline{X_{P_\theta}^2(t)} = \frac{2\,u_P'^2}{\mathfrak{z}(\mathfrak{z}^2-K^2)(1-3\mathfrak{z}^{-2})+2\mathfrak{z}^2K^2-4K^2+2}\left\{\mathfrak{z}^2(\phi)T_{f_z}\left[\mathfrak{z}^2(\phi)-K^2(\phi)\right]\left[1-3\mathfrak{z}^{-2}(\phi)\right]\left[t-T_{f_z}\mathfrak{z}(\phi)\left[1-e^{-t/T_{f_z}\mathfrak{z}(\phi)}\right]\right]+\right.$$

$$+\ (K^2-1)(\mathfrak{z}^2-1)T_{f_z}\left[T_{f_z}\left(1-e^{-t/T_{f_z}}\right)-te^{-t/T_{f_z}}\right]+$$

$$\left.+\ (1+\mathfrak{z}^2+\mathfrak{z}^2K^2-3K^2)\left[tT_{f_z}-T_{f_z}^2\left(1-e^{-t/T_{f_z}}\right)\right]\right\} \qquad (2.94)$$

2.5 Discussion of Parameters

Several parameters have been defined in the development of the theory. Some of the parameters were defined for convenience while others are of importance. The primary parameters are $\alpha_k(\phi)$, $\beta(\phi)$ and $\xi(\phi)$.

The parameter $\alpha_k(\phi)$ defined in Equations 2.55, 2.56 and 2.57 contains the particle's physical characteristics, as well as the fluid's. The particle-fluid hydrodynamic effects are also included through the function, $\lambda(\phi)$.

If one rearranges the $\beta(\phi)$ in the following form:

$$\beta(\phi) = \frac{\rho + \rho/2}{\rho_p + \eta(\phi)\rho/2} \tag{2.95}$$

This can be seen as the ratio of the mass of a "fluid particle" plus its virtual mass to that of the particle's mass plus its modified virtual mass.

It is when the $\alpha_k(\phi)$, $\beta(\phi)$ terms are combined that one sees the importance of these parameters. ξ is defined by the Equation 2.83 as

$$\xi(\phi) = \frac{1}{\alpha_k(\phi)\beta(\phi)T_{fz}} \tag{2.83}$$

where $T_{f,z}$ is the properly scaled Lagrangian macroscale, as defined by Equation 2.71:

$$T_{fz} = \frac{\mathcal{J}_{F_z}}{(V_p'^2 + f^2)^{1/2}/\mu'_{f_z}} \tag{2.71}$$

Consider the case for Stokian particles, assuming very dilute suspension such as $\lambda(\phi)=1$, the Stokian response time is defined as:

$$\mathcal{J}_s = \frac{1}{\alpha\beta} \tag{2.96}$$

extending this to non-zero volume loadings:

$$\mathcal{J}_S(\Phi) = \frac{1}{\alpha_K(\Phi)\,\beta(\Phi)} \tag{2.97}$$

Thus becomes:

$$\mathcal{F}(\Phi) = \frac{\mathcal{J}_S(\Phi)}{T_{f_z}(\Phi)} \tag{2.98}$$

This can be regarded as the ratio of the particle response time to the time available to sample the local turbulent structure (or the time of fluid correlation).

This is applicable for each particle's Reynold's number region:

$$\mathcal{F}_I(\Phi) = \frac{\mathcal{J}_I(\Phi)}{T_{f_z}(\Phi)} \tag{2.99}$$

$$\mathcal{F}_N(\Phi) = \frac{\mathcal{J}_N(\Phi)}{T_{f_z}(\Phi)} \tag{2.100}$$

2.6 Discussion and Summary

The assumptions leading to the non-dilute particle equation of motion (Equation 2.14) are not overly restrictive. They are: that the particles are spheres and of uniform size, and that direct collisions between particles do not occur. A problem arises with the yet unknown function of $\theta(\phi)$, found in the Basset term, but as noted, it is of order unity and hence of little concern.

The assumptions leading to the linearization and simplification of the equation of motion require the particle to be very small as compared to the microscale of the turbulence, and that the Basset term can be ignored. Meek (1972) calculated the response function for the linearized equation of motion with Basset term (for very dilute suspensions). A comparison between Meek's response function and the response function calculated without the Basset term is shown in Figure 2.5. For particles of β's near 1, the simplified results are reasonably close to the general theory of Meek's. As the particle becomes very heavy with respect to the fluid, the Basset term predicts more information being transferred to the particle, hence it's importance becomes apparent. It is felt that the Basset term contribution, at β's close to unity, is not sufficiently large to warrant the additional complexity of the solution.

The linearized equation has been extended from Stokian restrictions to a wide range of non-Stokian behavior. This is an important addition due to the fact that most applications are of non-Stokian particles suspended in a fluid such as rivers and slurries.

The past work of Meek and Howard assumed incorrectly the isotropic behavior of particles with finite free-fall velocites. The approach taken in this development assumes that only the fluid is isotropic in behavior. Hence, lateral fluid autocorrelation was used to predict lateral particle behavior instead of applying isotropic relationships to the particles directly.

The parameter $\xi(\phi)$ discussed earlier can be thought of as the ratio of the amount of time a particle needs to respond to the eddy it resides within, to the time it resides within the eddy. This can simply be seen for a particle falling within the newton region of drag. Consider $T_{f,z}$ from Equation 2.71

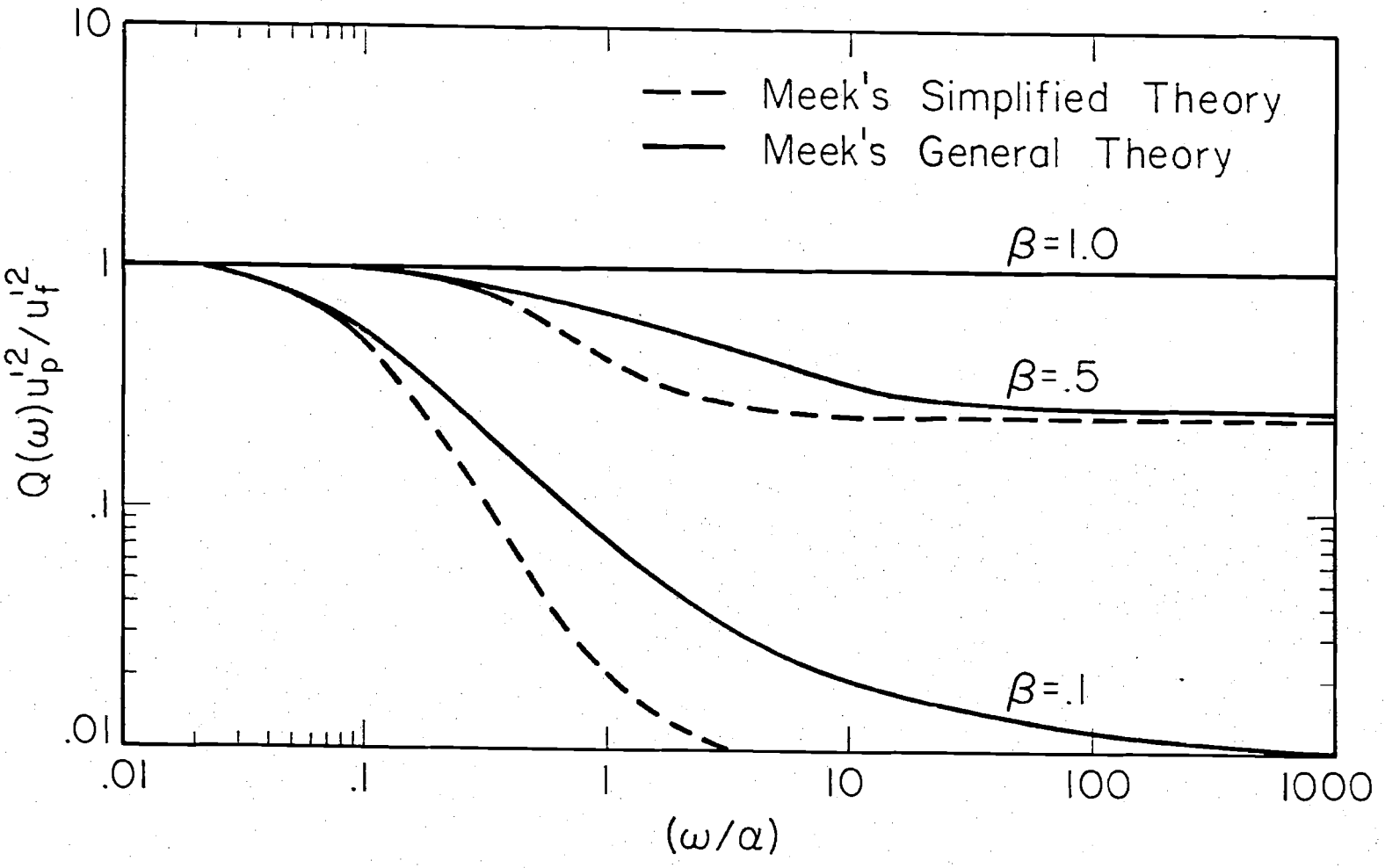

Figure 2.5 Particle Response Function, $Q(\omega)$, for Meek's (1972) Simplified and General Theory

$$T_{f_z} = \frac{\mathcal{T}_{f_z}}{(V_{p_z}'^2 + f^2)^{1/2}/U_{f_z}'} \tag{2.71}$$

Since $f >> U_p'$

$$T_{f_z} = \frac{\mathcal{T}_{f_z} U_{f_z}'}{f} = \frac{\Lambda}{f} \tag{2.101}$$

which states the time particle resides within an eddy of typical length Λ_z. If one substitutes Equation 2.101 into Equation 2.100:

$$\xi(\phi) = \frac{\mathcal{T}_N(\phi)}{\frac{\Lambda}{f}} \tag{2.102}$$

Thus $\xi(\phi)$ is the ratio of the particle response time to the time spent within an eddy. The particle response time is also a function of the volume loadings. This is expected. As the volume loading increases, the response time apparently decreases. This is due to the expected increase in the fluid intensities or amplitude, thus allowing the particle to sense larger impulses and hence appearing to respond in a shorter time.

In closing, the theory set forth here is capable of predicting the statistical quantities of particles within a turbulent fluid. Thus, if the theory proves to be valid, engineering predictions of particle behavior can be made for a variety of applications.

CHAPTER 3 EXPERIMENTAL FACILITIES

3.1 Experimental Loop Description

Experiments were conducted to measure fluid and particle statistical quantities in a turbulent environment. Fluid measurements were performed using standard anemometer techniques. Particle trajectories were investigated using the same method developed by Jones (1966) and improved upon by Shirazi (1967), Meek (1972) and Howard (1974). This consisted of tracking the trajectory of a radioactively tagged particle as it traverses through the test section. The tagged particle was tracked by a group of photomultiplier tubes mounted on a moving carriage, this system will be desribed in detail in Section 3.3.

The flow facility was initially designed and built by Jones (1966). Modifications were necessary to accommodate the non-dilute particle suspension flow. This section will be concerned with the description of the flow facility as modified for multiparticle measurements. The flow facility, shown in schematic form in Figure 3.1, provides a turbulent environment in which the behavior of the fluid, as well as that of the particles were investigated. The facility consists of two systems; the particle loop system and the supportive system, which maintained stable conditions within the particle loop.

The particle loop starts at the header tank, 30 feet above the datum. A slurry of particles exits from a perforated plate into a screened tube of 7 1/4 inches I.D. and of 4 inches in length. Within this mixing region, the particle slurry, jetting from the perforated plate, mixes with make-up water supplied to the header tank. From the screened tube, the particle suspension enters the inlet section of 7 1/4 I.D. and 11 feet in length. This provides a development length to insure a homogeneous mixture of

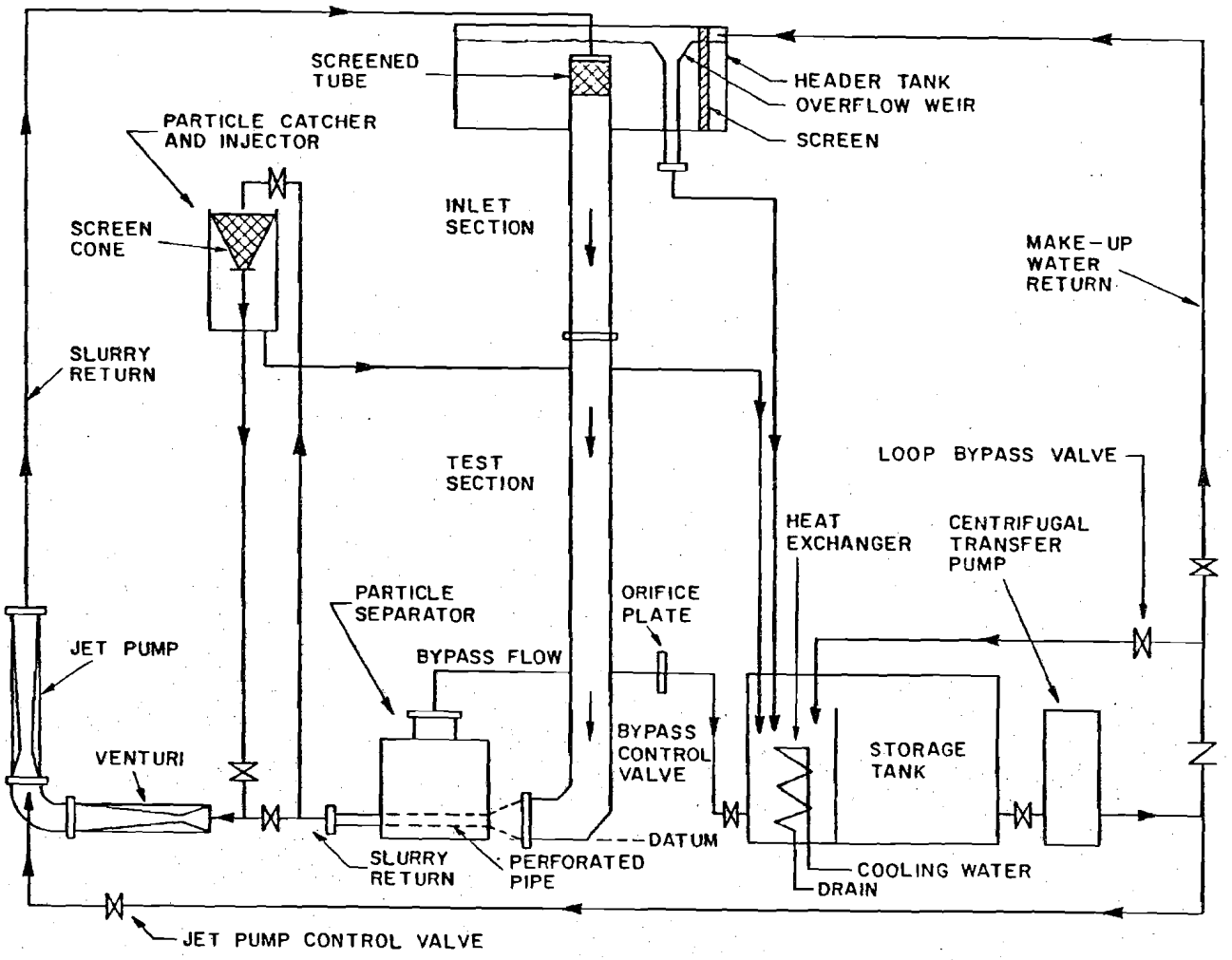

Figure 3.1 Schematic Form of Experimental Facilities Used for Fluid and Particle Measurements.

particles as well as fully developed turbulent flow. The homogeneous mixture of particles and water exits the inlet section into the vertical test section where the turbulent characteristics of the fluid and particle were measured.

The test section would be fitted with one of two 17 foot, 7 1/4 inch I.D. sections. Fluid measurements were conducted in an aluminum section with entry ports provided at several axial and radial positions, for which a detailed description could be found in Howard's thesis. For particle tracking, the aluminum section was replaced with a smooth, clear lucite tube with dimensions identical to the aluminum section. This provides a uniform track for the carriage to traverse down the test section.

At the base of the test section, a 90° elbow was fitted with a honeycomb of tubes to assure symmetry of the flow upstream of the elbow.

From the test section the particle suspension enters the particle separator; the purpose of which was to concentrate the particle suspension to a slurry of particles, originally the separator consisted of a 2 foot diameter circular tank with an 8 inch I.D. inlet, a 6 inch I.D. screened bypass outlet and a 3 inch I.D. slurry outlet. The operating performance proved to be poor due to dropout of particles within the separator. Hence a reducing 3 inch I.D. perforated pipe was fitted within the separator to provide a confined path for the particles, while allowing fluid to flow through the bypass. The particle slurry exited from the separator into a Venturi Flow Meter.

The Venturi Flow Meter was constructed of lucite, with an inlet of 3 inches I.D., a throat diameter of 1 inch and diverging with a 5° included angle to a 3 inch I.D. Calibration of the flow meter was performed using

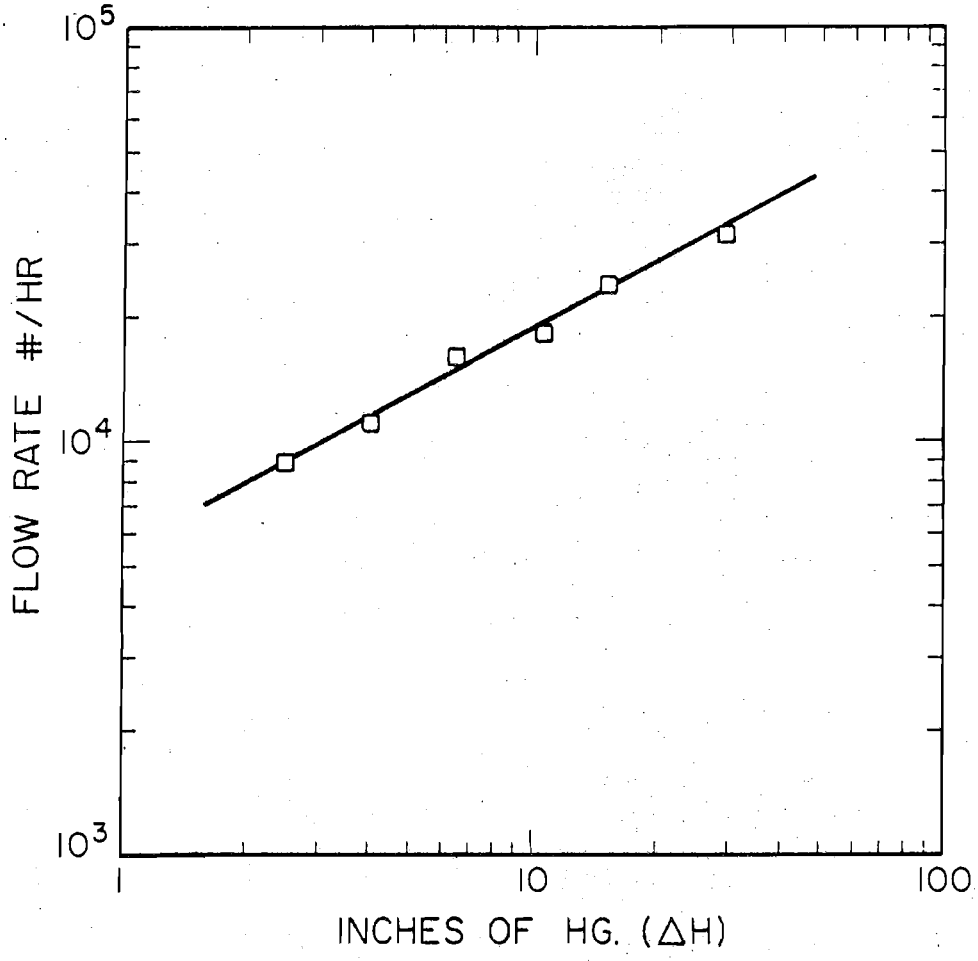

Figure 3.2 Calibration Curve for Venturi Flow Meter

a weigh tank. The results are shown in Figure 3.2. Because of the unavailability of a slurry weigh tank system, calibration was performed with no particles in suspension. The error, introduced by the presence of the particles, was calculated to be less than 5%, based on the physical observations of a no-slip condition between the particles and the fluid.

From the Venturi, the particle slurry enters the jet pump, to be returned to the header tank in order to re-enter the inlet section. The jet pump was selected for its ability to pump the slurry without crushing the particles. The pump was capable of pumping at a flow rate corresponding to a Reynolds number in excess of 50,000 within the test section. The Reynolds number maintained in the test section was 50,000 for all experiments.

It should be noted that the particles are initially introduced into the loop in a batch injection process, eventually distribute themselves equally throughout the closed loop. Typically the system requires approximately 10 minutes of operation to achieve a homogeneous mixture of particles throughout the test section. With the particles being continuously recycled through the test section, the inventory of particles is small and a stable environment is established for data acquisition for indefinite periods of time.

The support systems of the experimental facility have various functions. This includes injection and retrieval of particles, maintaining constant temperature, providing make-up water, and supplying pressure to drive the jet pump.

Bypass water exiting from the separator passes through a measuring orifice plate and enters the storage tank. The storage tank is capable

of holding the entire water inventory, approximately 750 gallons. The water is drawn through several baffles and down through a tubular heat exchanger within the storage tank. The temperature of the water can be regulated by passing hot or cold water through the tubular heat exchanger. The temperature within the system can be held constant, within ± 1°F, during the experiments. In all the experiments the water temperature was 80°F.

The water is drawn from the storage tank by an Ingersoll Rand Centrifugal Transfer pump (11.5 hp, 400 gpm at 90 foot head), which drives the jet pump and additionally provides the make-up water to the header tank.

In order to maintain a constant level within the header tank, an overflow weir was employed.

Since one of the particles was radioactive, it had to be removed from the system at the end of each day and placed in a shielded safe storage area. In order to accomplish this task, as well as change the relative loadings, a particle "Catcher-injector" was installed in the slurry return line. Referring to Figure 3.3, a stainless steel screen cone, with a trap door at its base was fitted with a 55 gallon steel drum, 18 feet above the datum. The base of the trap door lead, via a 2 inch I.D. p.v.c. pipe, to the particle slurry return line. Coming from the slurry return line a 2 inch I.D. p.v.c. pipe leads up through a butterfly valve to the top of the screened cone. Injection of particles was accomplished by filling the screen cone with a desired amount of particles, opening the trap door allowing particles to travel down to the slurry return line and being drawn to the header tank by the jet pump. Recovery of the particles was performed by closing the trap door and allowing the particle slurry to

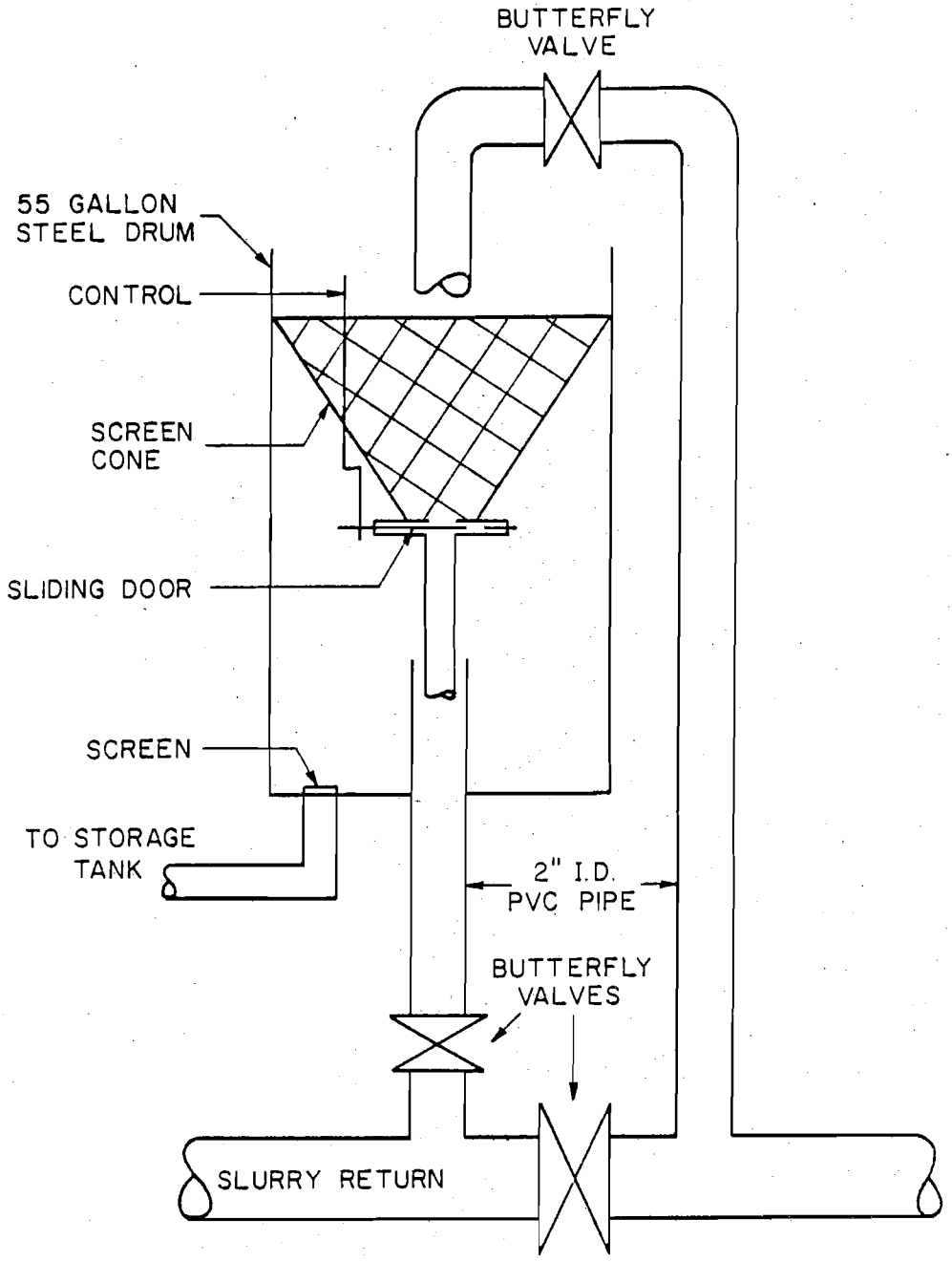

Figure 3.3 Schematic Diagram of the Particle "Catcher-Injector" Used to Load and Unload the Particle Inventory Into the Loop

travel up to the screen cone; excess water drained to the storage tank and the particles remained within the cone.

3.2 Fluid Data Acquisition and Analysis System

Standard anemometer techniques were used to obtain the fluid fluctuating velocity. A schematic diagram of the Electronic Data Acquisition System is shown in Figure 3.4.

Due to its rugged design it was felt that a conical probe would withstand direct collisions with particles, with a minimum amount of damage, hence a thermosystems 1230W conical sensor was employed. The sensor was mounted on a traversing mechanism, capable of sweeping across the diameter of the aluminum test section at various axial port locations. For a detailed description of the traversing device, consult Jones (1966) and Howard (1974).

The sensor was operated in the constant temperature mode by a Disa 55D01 anemometer. Linearization was performed by a Disa 55D10 Linearizer, with the proper exponent obtained from calibration experiment. The voltage signal from the Linearizer passes through a bandpass filter. The bandpass frequencies were 0.01 hz to 100 hz, this was done to eliminate the D.C. component of the signal, as well as, unwanted high frequency noise. Prior to the bandpass filter, an integrator in line with a D.V.M. was used to obtain the mean D.C. voltage, corresponding to a mean velocity measurement. Voltage rms measurements were made by a T.S.I. 1060 True R.M.S. meter.

A data switch was incorporated for providing a means of selecting a sine wave signal for calibration and experiment separation. The data were

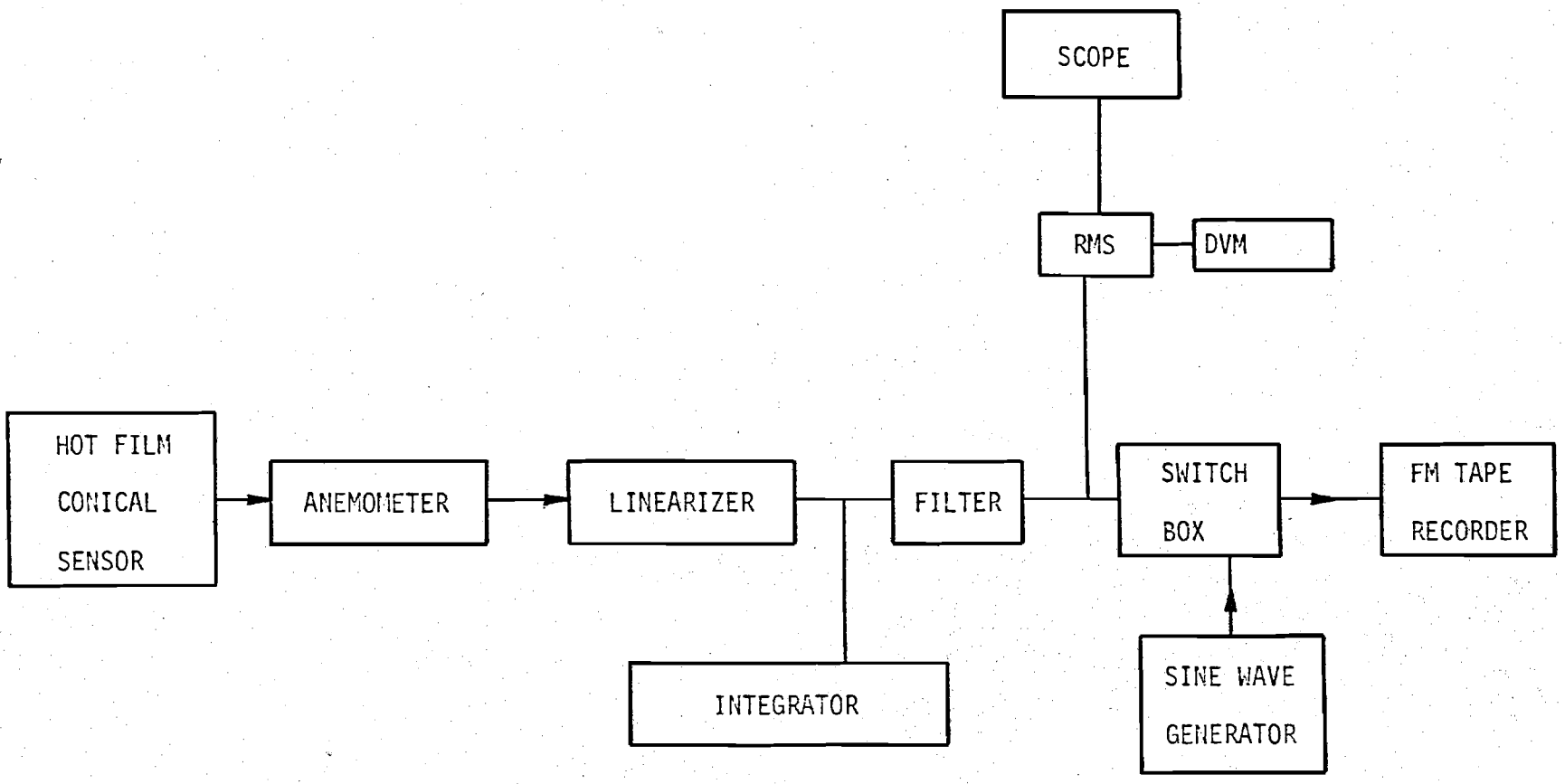

Figure 3.4 Fluid Data Acquisition System

recorded on analog tape by a Sangamon Model 3560 FM tape recorder, at a speed of 3.75 inches per second. Record lengths of ten minutes were recorded for most of the experiments. The long record length was necessary for a reasonable record length at a playback speed of 60 inches per second. By playing back to data at 60 ips the data's frequency spectra was artificially shifted up by a factor of 16. This was necessary in order to employ audio equipment in the data analysis.

Analysis of the data was performed offline using the analysis system shown in Figure 3.5. Voltage signals were played back in a 100 point correlator, Saicor Model 42; where autocorrelation functions were calculated. The data from the correlator was displayed graphically by a X-Y plotter, Houston Instruments Omnigraphic 2000 X-Y plotter. The numerical values of the autocorrelation obtained from the correlator by a microcomputer. This employed the 6800 Microprocessor L.S.I. chip, to interrogate the correlator for the voltage value of the 100 points plotted, perform a binary to B.C.D. conversion and display the values on a printer. Additional information, in the form of power spectra and macroscales was calculated from data obtained from the 100 point correlator.

3.3 Particle Data Acquisition and Analysis System

The objective of the Data Acquisition System was to provide continuous monitoring of the particle's velocity as it proceeded through the test section. This section will discuss in detail the data acquisition and analysis systems shown in Figure 3.6.

The original concept was provided by Jones (1966). Although his data were plagued with noise, he was able to show that the basic concept was

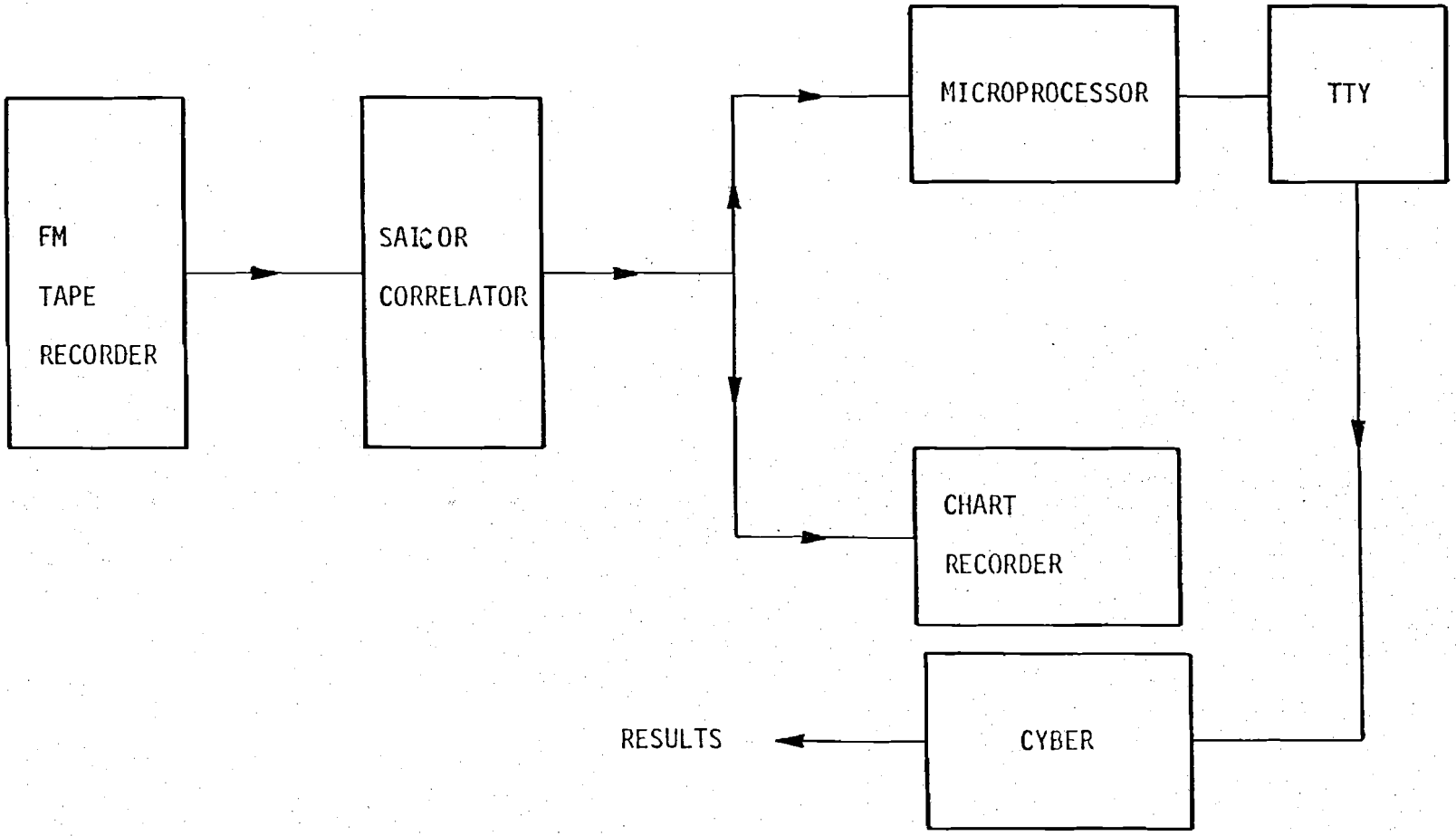

Figure 3.5 Fluid Analysis System

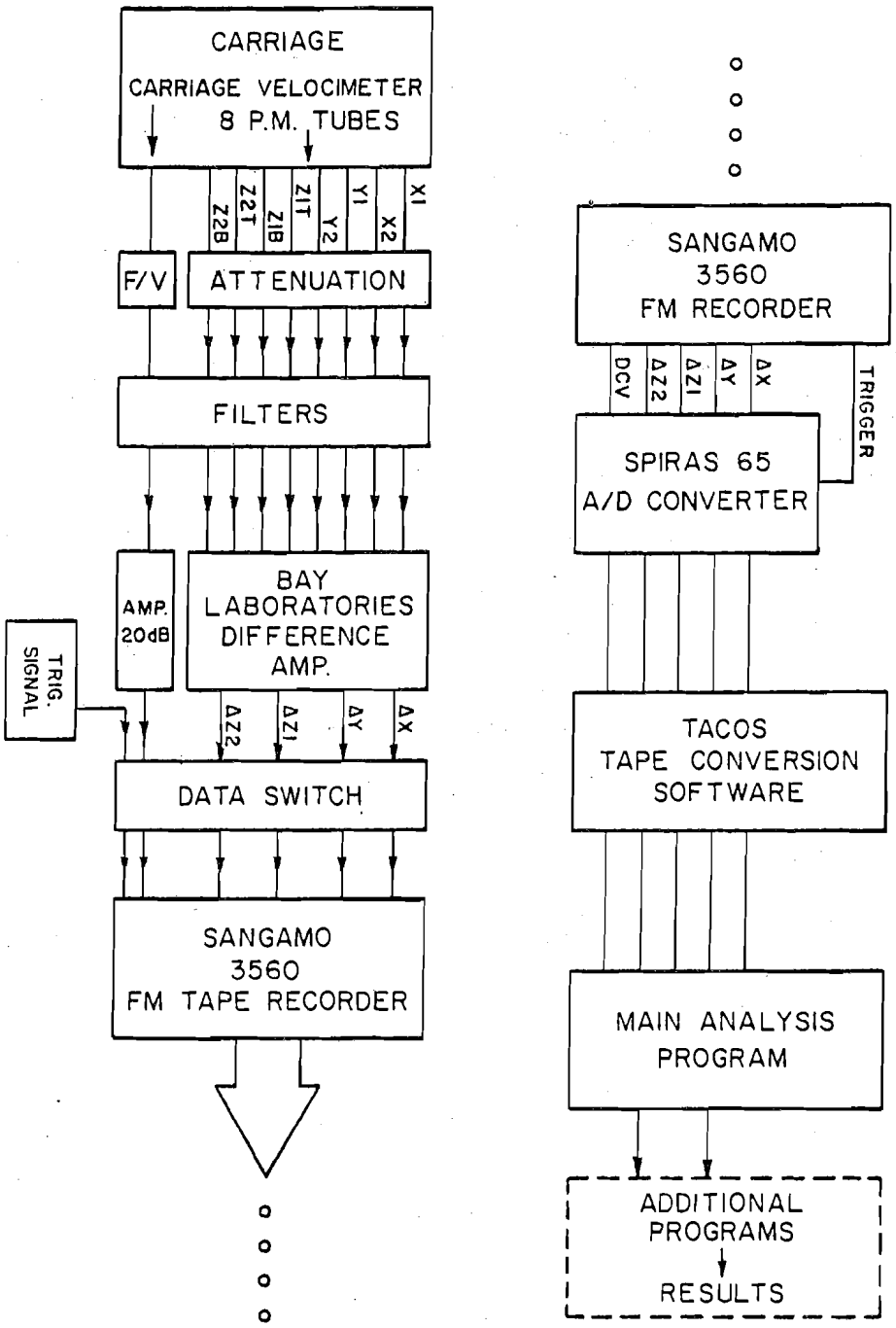

Figure 3.6 Particle Data Acquisition and Analysis Systems

workable. Improvements by Shirazi (1967), Meek (1972) and Howard (1974) eliminate most of the noise within the system, but uncertainties were still present and a complete overhaul of the Data Acquisition System was in order.

Referring to Figure 3.7, an aluminum carriage, which surrounds the lucite test section, traces a radioactively tagged particle as it navigates down the test section. Mounted on the carriage, as shown in Figure 3.8, are eight Harshaw Chemical Co. Gamma Ray Detectors. Each detector consists of a photomultiplier tube (RCA Model 6199) with a NaI crystal mount within a hermetically sealed aluminum shell. In addition, each detector was wrapped in Mμ metal to shield the detector from magnetic disturbances. Each of the electronic boxes contained the resistor network for the P.M. tubes. The P.M. tubes were operated at 800 volts from two well regulated power supplies. Depending upon the distance between the particle and the face of the detector, the output voltage varied from 0.0 volts to -8.00 volts. Typically a two hour warm-up period was necessary for stable operation.

The carriage was driven by a hydraulic system connected to the carriage via steel cables. Details of its operation may be found in Jones' thesis. The tracking capability of the carriage is due to a feedback circuit driven by the difference between the Z1T and Z1B signals; the carriage seeks to minimize the difference as the particle traverses the test section, causing the particle to be near the relative axial midplane of the carriage. The sensitivity of the feedback network may be adjusted to follow the particle closely or lowered to maintain a constant velocity. At either end of the test section, limit switches were provided to stop the carriage.

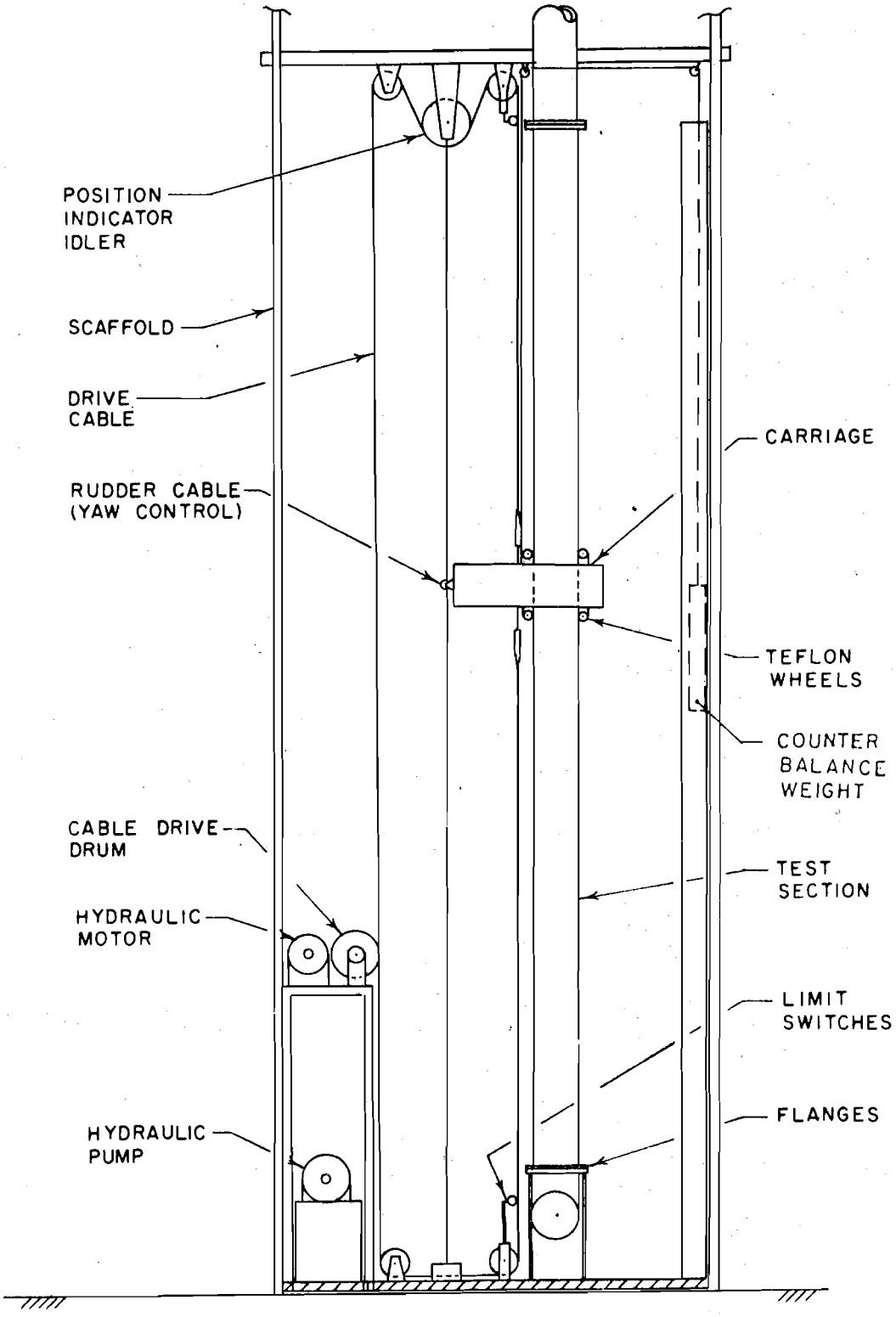

Figure 3.7 Carriage Support and Drive System

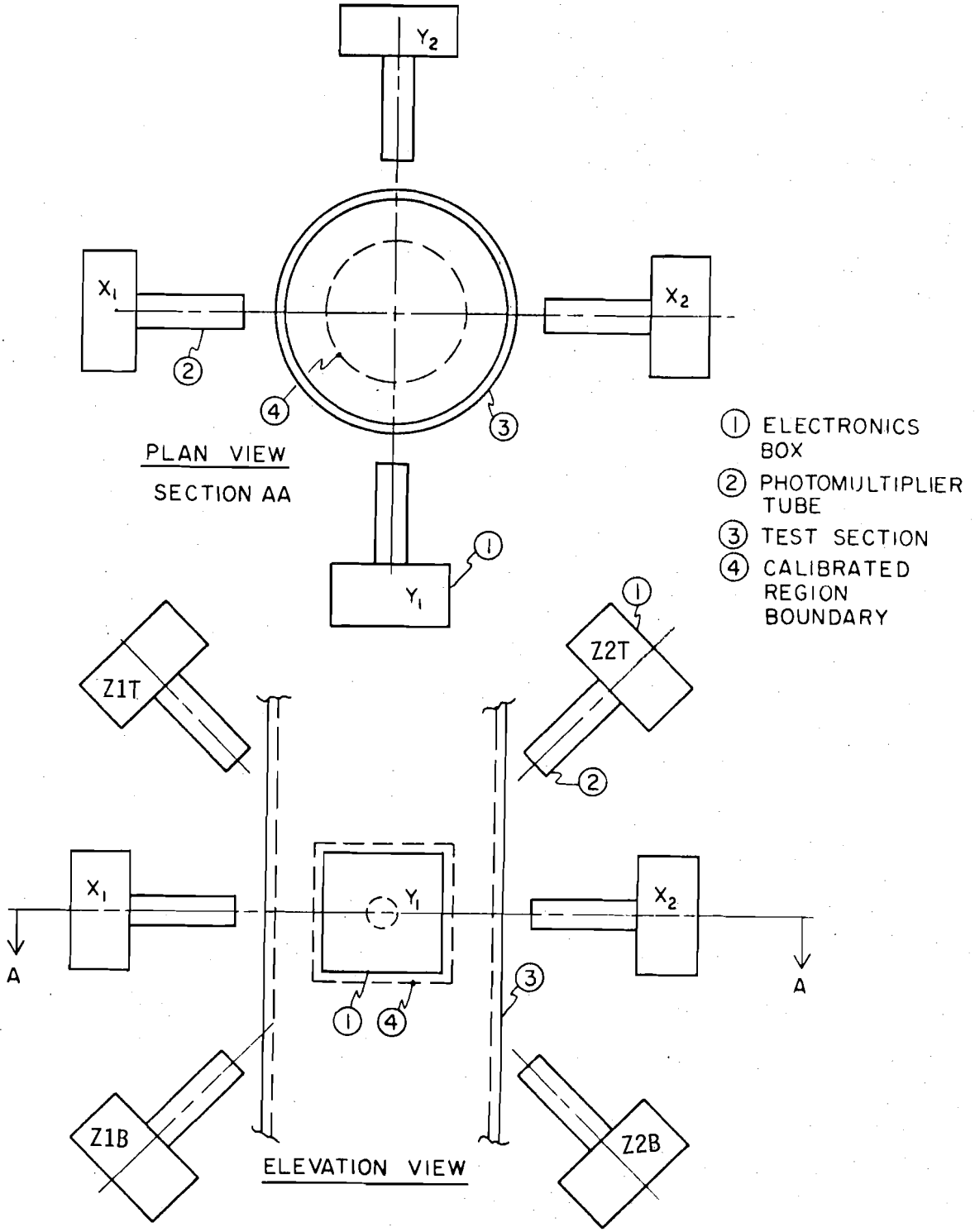

Figure 3.8 Schematic of Photomultiplier Geometry About Test Section

In past investigations, problems associated with the carriage velocimeter had hampered interpretation of the axial velocity data. The past system consisted of two potentiometers, 180° out of phase with respect to each other, driven by a common shaft from the idler pulley. As the carriage descended, a series of ramps were generated from which velocities were inferred. This method proved to be noisy from several points of view with reasonable filtering doing little to improve the data. Thus a new analog-digital hybrid velocimeter was developed. The hybrid velocimeter employed a timing wheel, shown in Figure 3.9, which contained 180 pairs of slots. As the timing wheel is spun, by the idler shaft, a light beam passes alternately through the timing slots striking the photoresistor and changing its resistance by 10,000 fold. The optics are of a simple nature as shown by Figure 3.10. The photoresistor is connected in the circuit shown in Figure 3.11. The first two stages provided a digital signal, the frequency of which was dependent on the angular velocity of the timing wheel, and hence the carriage's velocity. The digital, TTL compatible, signal is used to trigger a monostable. The monostable provides a 35 μsec pulse width at the given input rate. Conversion from the frequency domain to the voltage domain was provided by a linear frequency to voltage converter, Datel Model VFV-10K. A 10 Hz low pass filter was incorporated to remove residual ripple on the output D.C. signal. An amplifier with a gain of 20 db was used to provide a signal to the recorder. The linear relation between the voltage from the velocimeter and the carriage velocity is:

$$V_c = 9.416\, e_c \qquad (3.1)$$

Where V_c is carriage velocity in cm/sec and e_c is the velocimeter

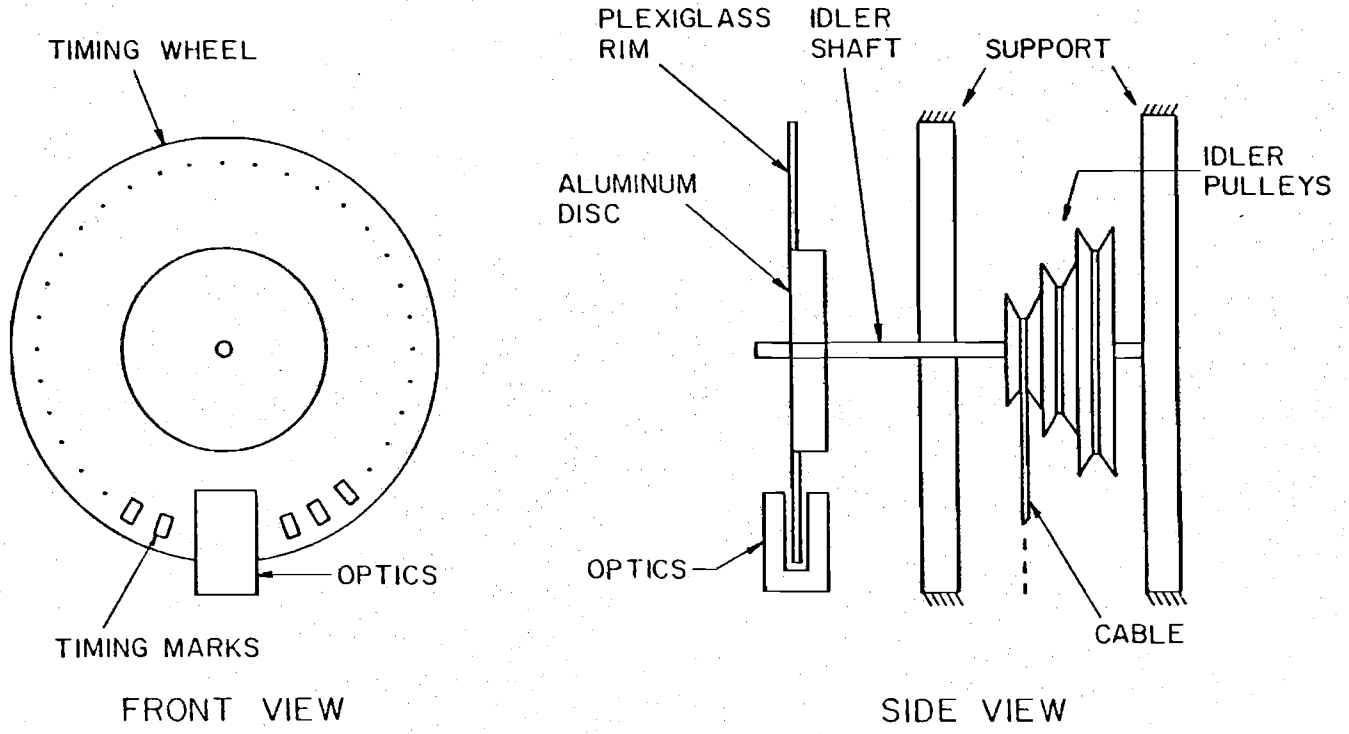

Figure 3.9 The Carriage Velocimeter's Timing Wheel

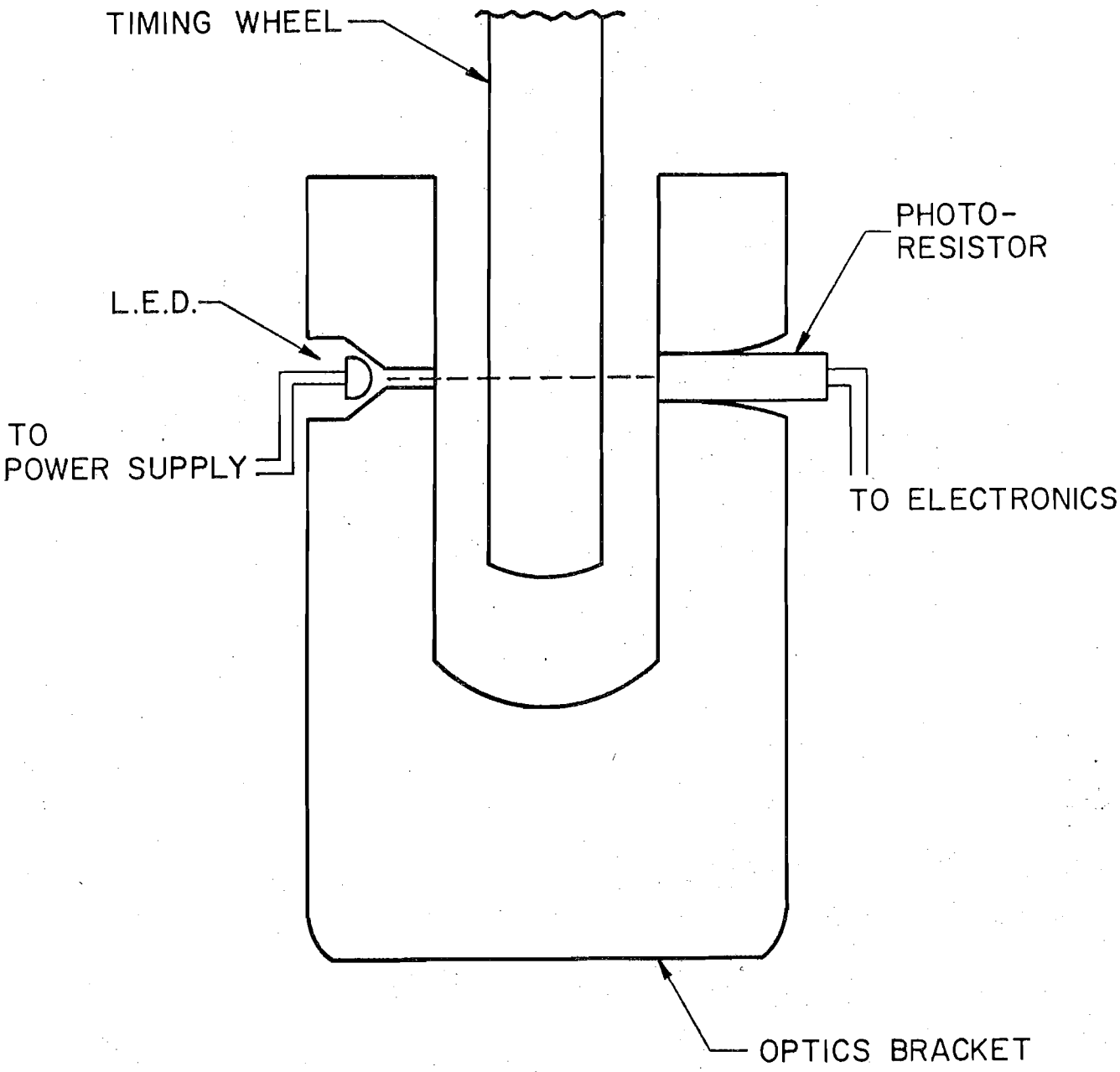

Figure 3.10 The Optics for the Carriage Velocimeter

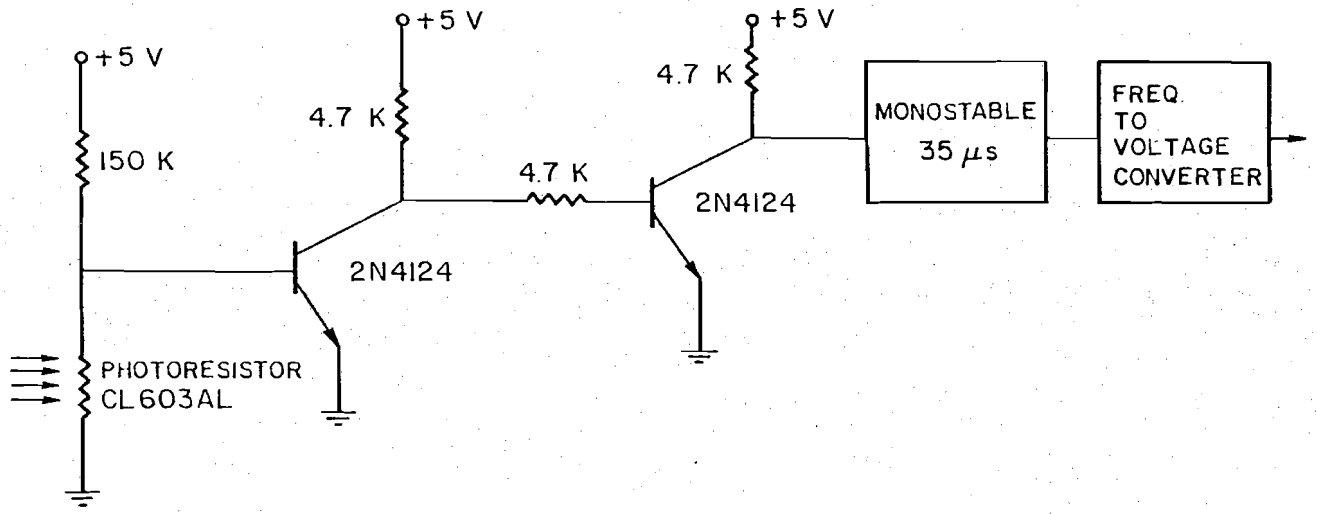

Figure 3.11 Schematic Diagram of Carriage Velocimeter Electronics

voltage. Experiments were conducted to confirm the velocimeter characteristics. The results indicated an error of less than 0.1%.

The carriage velocimeter voltage, along with the eight photomultiplier tube signals completes the initial stage of the Data Acquisition System. From the carriage, the 8 P.M. tube signals were fed into an attenuator in order to balance and calibrate the characteristics of the P.M. tubes. In order to remove the noise generated by the random decay of the radioactive source, pre-analysis filtering was provided by a third order, active low pass filter for each channel of data. The cutoff frequency was 100 Hz and the characteristics are shown in Figure 3.12. Figure 3.13 shows the attenuation and filtering circuit.

From the active filter the four pair of data channels are differenced by four Bay laboratories differencing amplifier such that the output were:

$$T = e_{x_2} - e_{x_1} \tag{3.2a}$$

$$U = e_{y_2} - e_{y_1} \tag{3.2b}$$

$$V_1 = e_{z1B} - e_{z1T} \tag{3.2c}$$

$$V_2 = e_{z2B} - e_{z2T} \tag{3.2d}$$

where e_{x_1} indicates the voltage from the x_1 P.M. tube and so on.

From the Bay Lab amplifiers the four differenced signals (T, U, V_1, V_2), the carriage velocimeter signal and a trigger signal were fed through a data switch to the Sangamo 3560 FM recorder. The recorder operated at 3.75 inches per second.

The four differenced voltages were used to determine the position of the particle within the test section. In order to assure that the particle experienced relatively homogeneous isotropic turbulence, only runs where

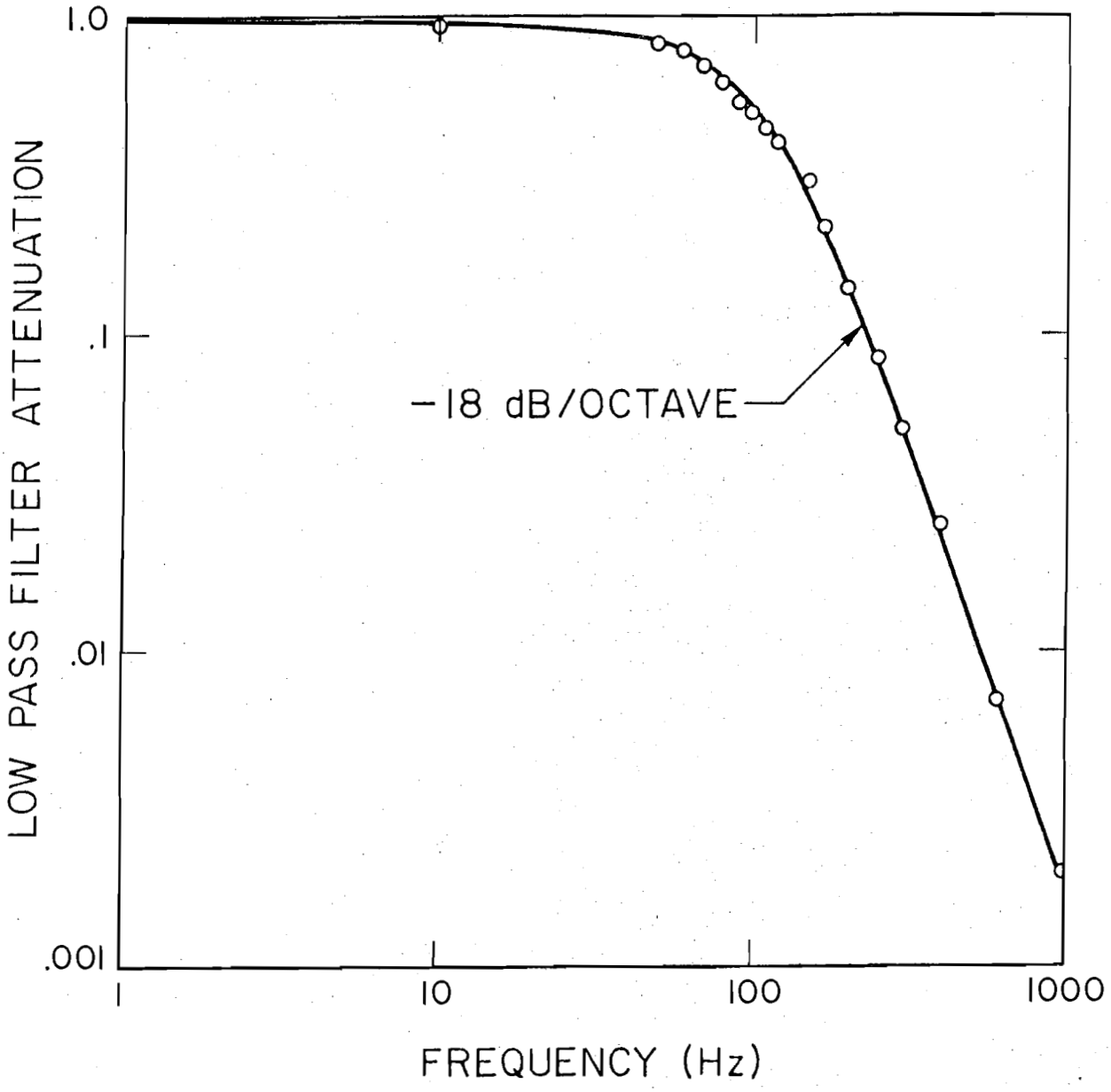

Figure 3.12 Characteristics of 3rd Order Active Filter With a Cutoff Frequency of 100 Hz

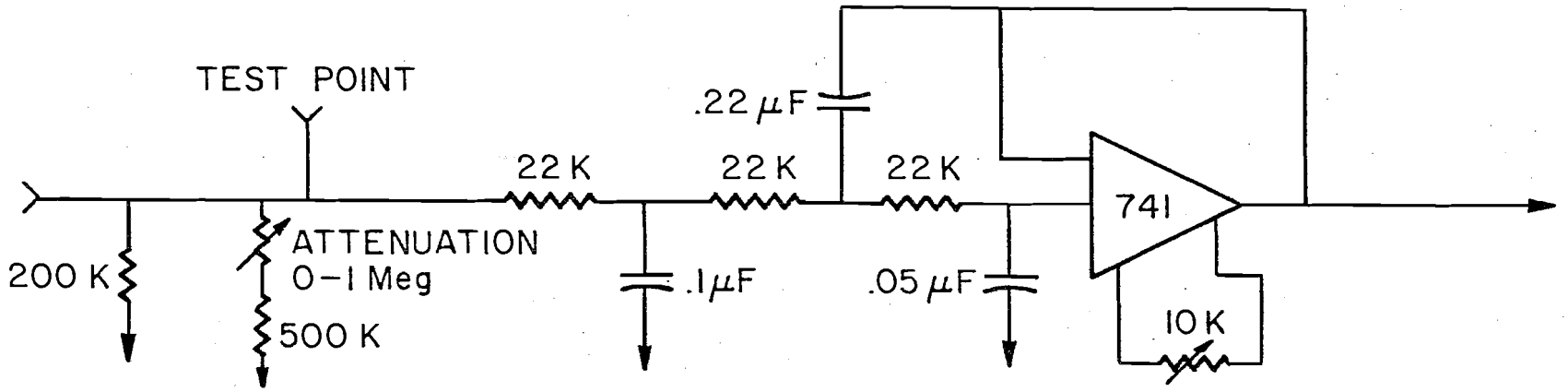

Figure 3.13 Schematic Diagram of the Electronics for the Attenuation and Filtering Circuits

the particle resided within the core region of the pipe were analyzed. A calibrated region, shown in Figure 3.8, was defined as a 14 cm by 14 cm right circular cylinder within the core region of the pipe. Calibration of the T, U, V_1, and V_2 voltages to absolute position was accomplished by placing a test source at over 1232 separate locations throughout the calibrated region. By summing the V_1 and V_2 voltages as:

$$V = V_1 + V_2 = e_{Z2B} + e_{Z1B} - e_{Z1T} - e_{Z2T} \tag{3.3}$$

it was found that T, U, and V provided a relatively linear relationship between position and voltage. This is demonstrated in Figure 3.14. The calibration data was fitted by a least squares technique, to a third order polynomial for the X, Y, Z directions. The functional form being:

$$\begin{aligned} X = {} & a_1 + a_2T + a_3T^2 + a_4T^3 + a_5U + a_6TU + \\ & + a_7T^2U + a_8U^2 + a_9TU^2 + a_{10}U^3 + a_{11}V + a_{12}TV + \\ & + a_{13}T^2V + a_{14}UV + a_{15}TUV + a_{16}U^2V + a_{17}V^2 + \\ & + a_{18}TV^2 + a_{19}UV^2 + a_{20}V^3 \end{aligned} \tag{3.4}$$

or:

$$X = f(a_j, T, U, V) \tag{3.5}$$

Similarly for the Y and Z directions:

$$Y = f(b_j, T, U, V) \tag{3.6}$$

$$Z = f(c_j, T, U, V) \tag{3.7}$$

With the recording of the analog signals, a permanent record was created for later digital analysis. To convert from the analog domain to the digital domain a Spiras 65 Analog-to-Digital converter was employed.

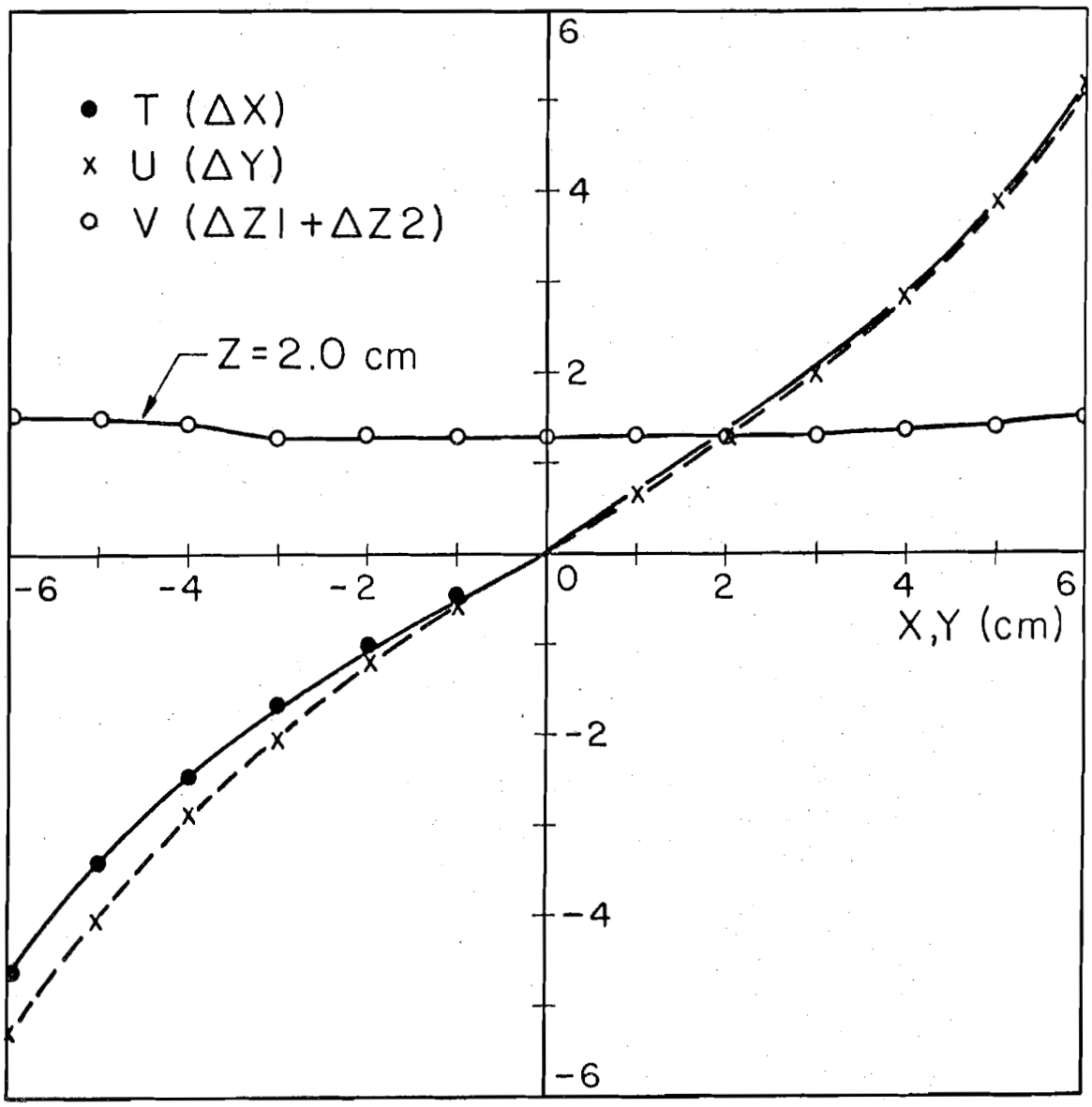

Figure 3.14 Calibration Signal Variation at the Plane Z = 2.0 cm

This unit digitized all 13 channels coming from the Sangamo 3560 at a rate of 1 millisecond between points. The 2 Byte, 16 bit words were recorded in 780 word blocks on a 9 channel digital tape.

The digital tapes created by the Spiras 65 were converted by a tape conversion program (TACOS). Conversion was necessary to improve the efficiency of the data handling and also to provide the proper normalization of the data. Normalization was performed by analyzing a zero signal and a 5.00 volt gain signal, from which the proper zero and gain constants were calculated. With the digital tapes from TACOS, statistical analysis could be performed by the main analysis program (MAP).

The main analysis program was the workhorse for particle analysis. MAP provided most of the statistical quantities for each run of data. Figure 3.15 shows a very simplified flow chart of Map/7. Once the data for a run has been read from the tape, a Gaussian digital low pass filter is applied to the data. The cutoff-frequency, F_{90}, for all of the analysis was 3 Hz. Figure 3.16 shows typical particle spectra, determined from autocorrelation data; obtained for experiment, with the characteristics of the filters also shown.

The filtered data, consisting of T, U, V and the carriage signal are converted to X, Y, Z positional data using equation 3.5, 3.6, and 3.7. The cartesian positions were then converted to cylindrical position as follows:

$$r_i = (x_i^2 + y_i^2)^{1/2} \tag{3.8}$$

$$\theta_i = \arctan(y_i/x_i) \tag{3.9}$$

$$z_i = z_i \tag{3.10}$$

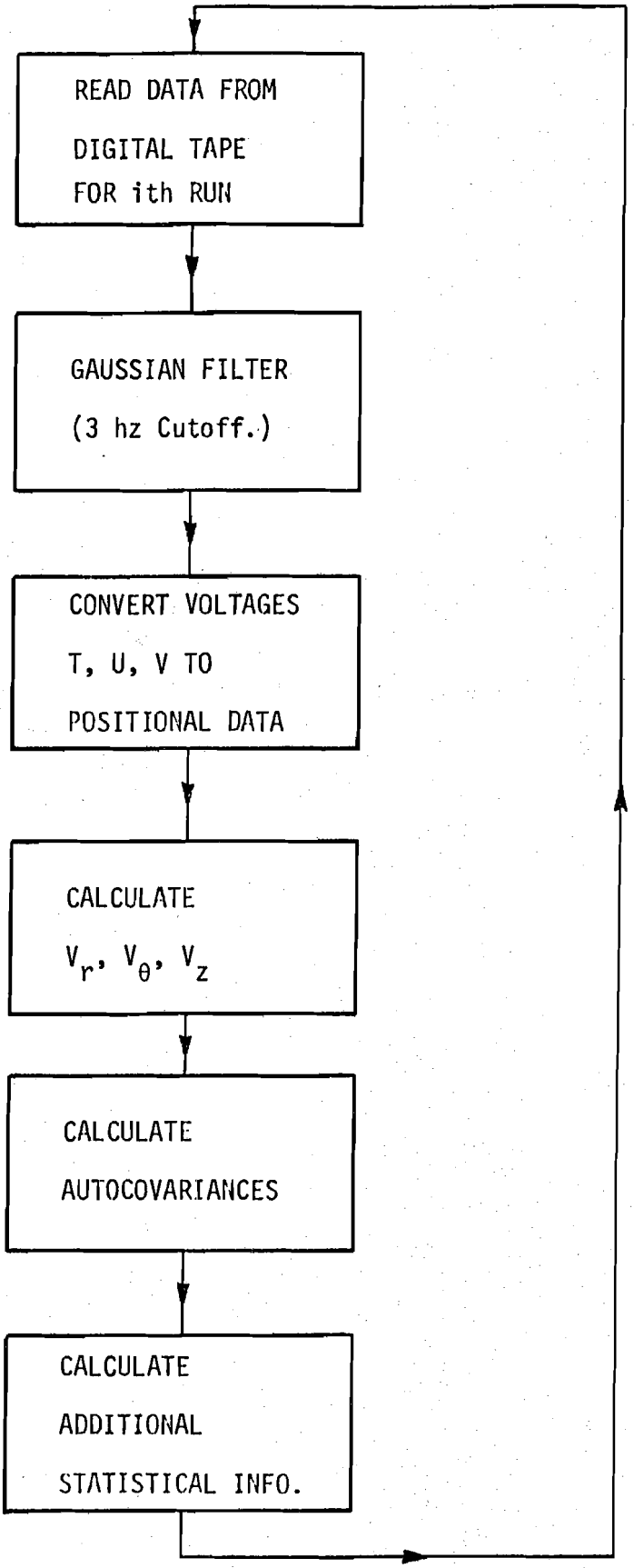

Figure 3.15 Simplified Flow Chart of Program MAP

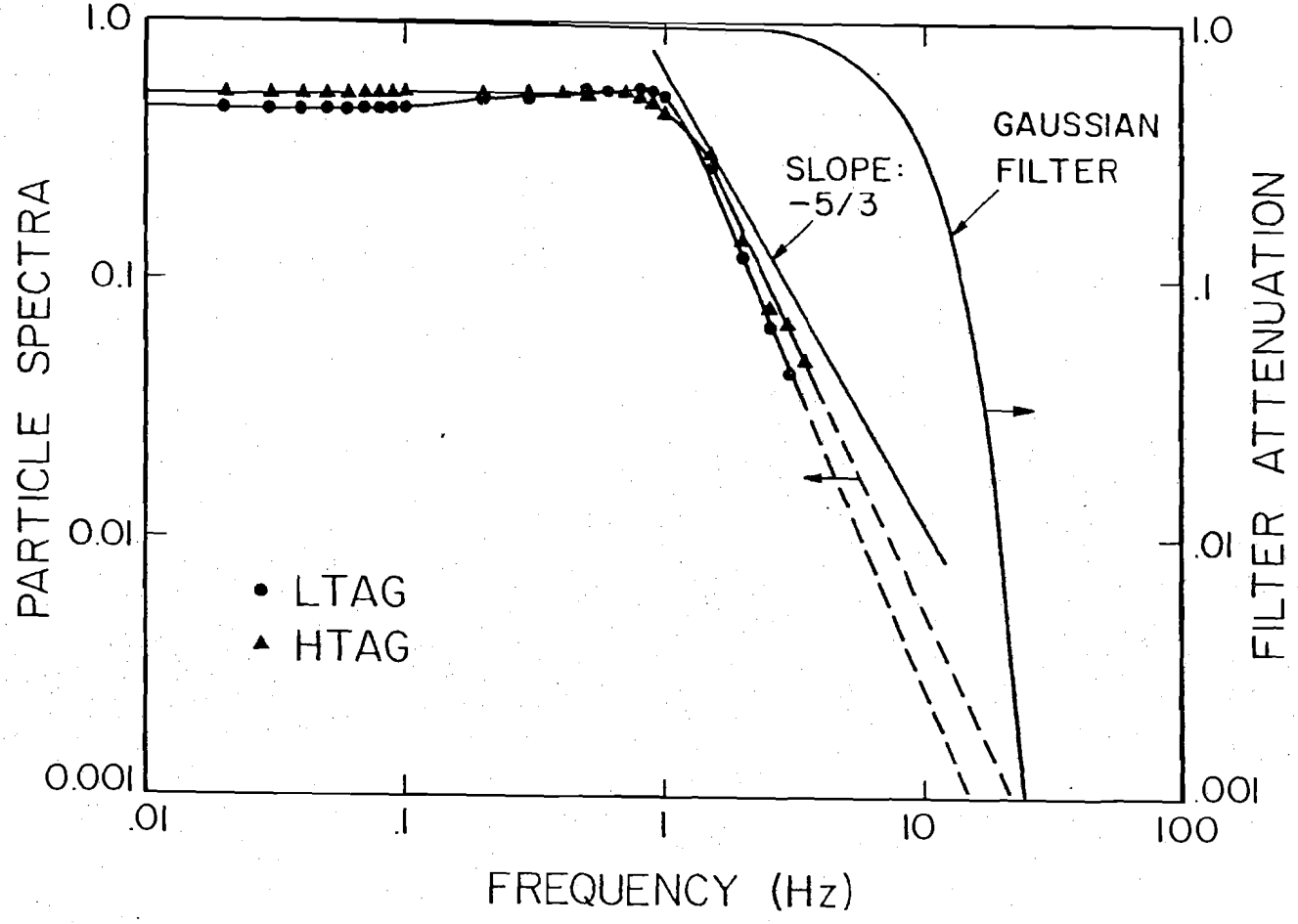

Figure 3.16 Comparison of Particle Spectra and Gaussian Filter Characteristics

The cylindrical velocities were inferred from the cylindrical positional data using the first order difference method. This is discussed in Appendix A.

The velocity autocovariances were calculated using the standard lagged products method:

$$\mathrm{cov}(\tau_j) = \frac{1}{N-j} \sum_{k=1}^{N-j} V(t_k)\, V(t_k + \tau_j) \qquad (3.11)$$

Additional statistical information such as the skewness, kurtosis, mean position and velocity, rms position and velocity, and the velocity probability density functions. A description of their caluclations can be found in Appendix A. Further analysis was provided by another program, ENSEMBLE; the details of which will be discussed in Appendix A.

3.4 Description and Fabrication of the Particles

The particles used for the experiment had to meet the following requirements:

1. The size and density had to be such that experimental data could be compared effectively with theory developed in Chapter 2.
2. The physical characteristics of the particle had to be such that they remained stable over the time of the experiments.
3. The impact strength of the particles had to be high due to the high velocity collision the particles experienced within the slurry return line.

4. Mass production of the particles was necessary due to the number of particles needed.

With a review of the available materials, two sets of particles were obtained from the Precision Plastic Ball company. The materials chosen were polystrene and acrylic plastics. The physical properties of which are listed in Table 1. The particles were fabricated by initially grinding of extruding material to the desired size, then several steps of polishing were performed to produce a smooth, spherical particle. The molding of particles by an injection molding machine did not produce quality particles, since usually air bubbles were intrained with the particles.

The radioactive source for "tagging" a particle was a nickel plated Cobalt-60 cylinder of 1 mm in diameter by 1 mm in height. Cobalt-60 was chosen because of its accessibility and relatively low solubility in water. Due to the large specific gravity of Co-60, NRC regulations, density of the plastic material, and current fabrication techniques, the size of the particle used was 0.476 cm. Howard (1974) estimated the Taylor microscale to be about 1.7 cm, hence the particle size met the requirements that they be less than the microscale of the turbulence. The tagged particle was constructed by taking a lighter density particle of identical size and drilling through a 0.03 undersize hole 3/4 of a particle diameter. Calculations yielded the amount of lead ballast necessary with the Co-60 to yield a tagged particle of identical characteristics. With the lead ballast added the Cobalt cylinder was press fitted into the hole, sealing the particle. Free-fall measurements, obtained by timing a particle falling down an 80 cm column of water, completed the verification of the fabrication. The particle was then soaked in an agitated water bath for 96 hours, resulting in no

Table 3.1 Physical Properties of Particles

Experiment	Density GM/cc	Diameter cm	Free Fall Velocity cm/sec	Approx. Weight mg	Reynolds Number	Water Absorption %
LTAG	1.05	.47625	7.26	59.4	413.0	0.03
HTAG	1.18	.47625	14.54	66.7	821.0	0.03

measurable difference in the density. A close watch of the density of the tagged particle was maintained throughout the experiments.

CHAPTER 4 EXPERIMENTAL MEASUREMENTS AND COMPARISON WITH THEORY

4.1 Fluid Measurements and Discussion

It is widely acknowledged that suspended matter modifies the turbulent structure of the residing fluid. To what extent a non-dilute volume loading changes the fluid's intensities and integral scales was of interest in the present experimental loop in order to provide input parameters for the theory developed in Chapter 2. Hence, an experimental investigation was initiated to quantitavely describe the fluid's characteristics at various non-dilute particle volume loadings.

Two separate series of experiments were performed: first, Eulerian velocity measurements were attempted with the use of a rugged conical anemometer; secondly, Lagrangian characteristics were to be estimated by tracking a neutrally buoyant particle circulating within the non-dilute suspensions.

A preliminary series of experiments was first conducted to determine to what extent the modification made to the system had on the loop's turbulent characteristics. Using the data acquisition system shown in Figure 3.4, the fluid's main velocity profile was measured. A conical probe was radially traversed across the test section. All the Eulerian measurements, referring to Figure 4.1, were made at port A, located 35 inches above the datum. The mean velocity data, normalized to centerline mean velocity, $\bar{U}_{f_t}$, is shown in Figure 4.2. Good agreement exists with the profile obtained by Howard (1974). The turbulent intensity defined as $U'_{f_{iz}}/U_{f_t}$, was measured in the same fashion as the mean velocity profile data. The results, shown in Figure 4.3, show good agreement with Howard's data. As a comparison, intensity measurements by Laufer (1954)

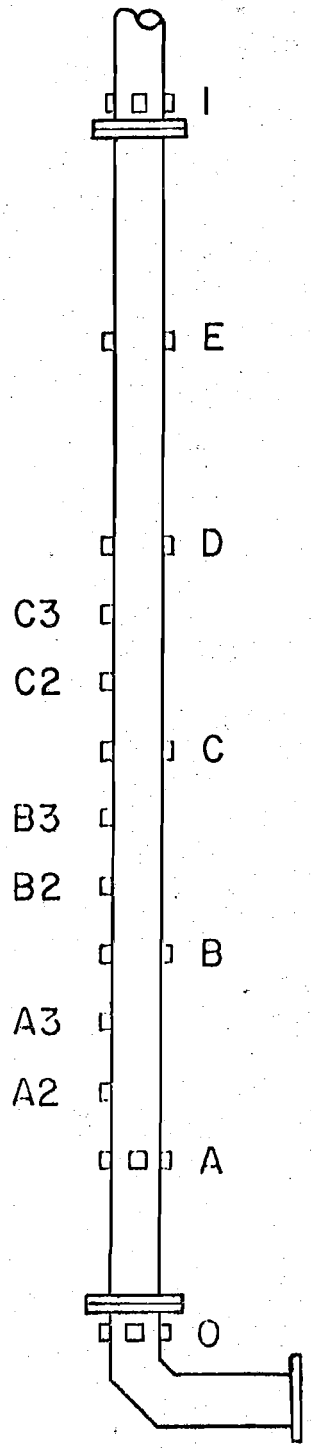

Figure 4.1 Test Section and Access Ports Used for Fluid Measurements

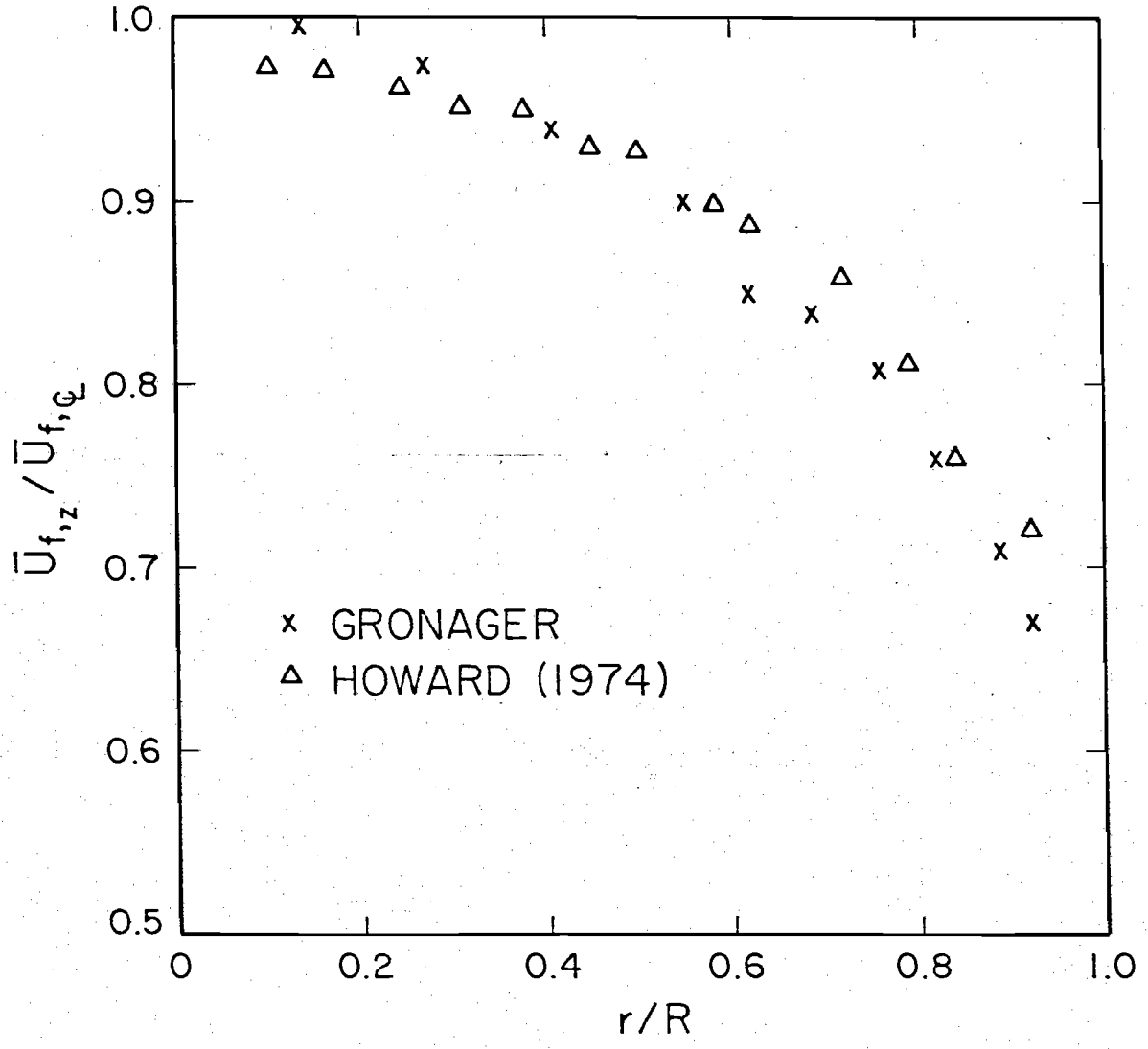

Figure 4.2 Fluid Mean Velocity Profile in a Pipe at Re = 50,000

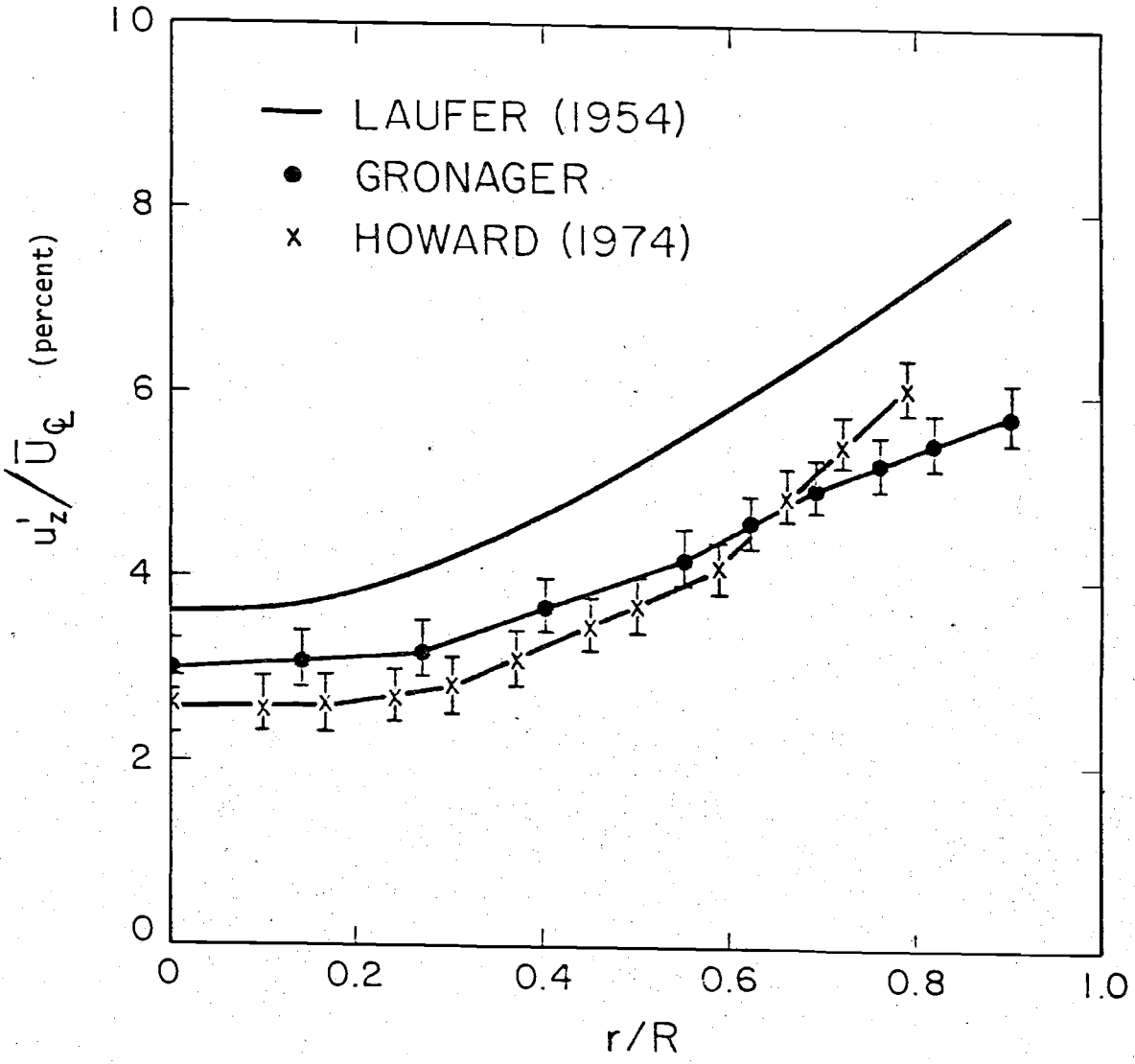

Figure 4.3 Turbulent Axial Intensity Profile in a Pipe at Re = 50,000

are also included. Relatively good agreement exists with Laufer's data. It should be pointed out that Laufer's results were originally normalized with the friction velocity, U_τ, and that some uncertainty is introduced in determining the centerline mean velocity from U_τ and the friction factor.

The fluid's fluctuating velocity was also recorded at several radial locations. Off-line analysis yielded the autocorrelation functions, R_{e_f}, shown in Figure 4.4. For each radial location, the time integral scale, $\mathcal{J}_E(r)$, defined as:

$$\mathcal{J} = \int_0^\infty R_{E_f}(\tau)\, d\tau \tag{4.1}$$

was determined. Referring to Figure 4.5, excellent agreement exists between Howard's data and that for this study.

After reviewing the mean velocity, intensity and integral scales profiles, one comes to the conclusion that the modifications to the flow system had a minimal effect on the Eulerian turbulent structures in the test section. As a result it would be expected that the convective properties, as measured by Howard, would not be significantly changed also.

Additional experiments were also conducted to confirm the particle suspension homogeneity. Particles, at the desired volume loading, were bulk loaded into the system. After approximately 10 minutes of operation the axial variation in the particle concentration appeared to be small from visual observations. With the use of an isokinetic particle sampler, shown in schematic form in Figure 4.6, radial traverses of the cross-section of the inlet section were made. The radial particle concentration profiles, for the particle volume loading, ϕ, equal to one, two and three percent are shown in Figure 4.7. As a whole, general agreement was observed between the

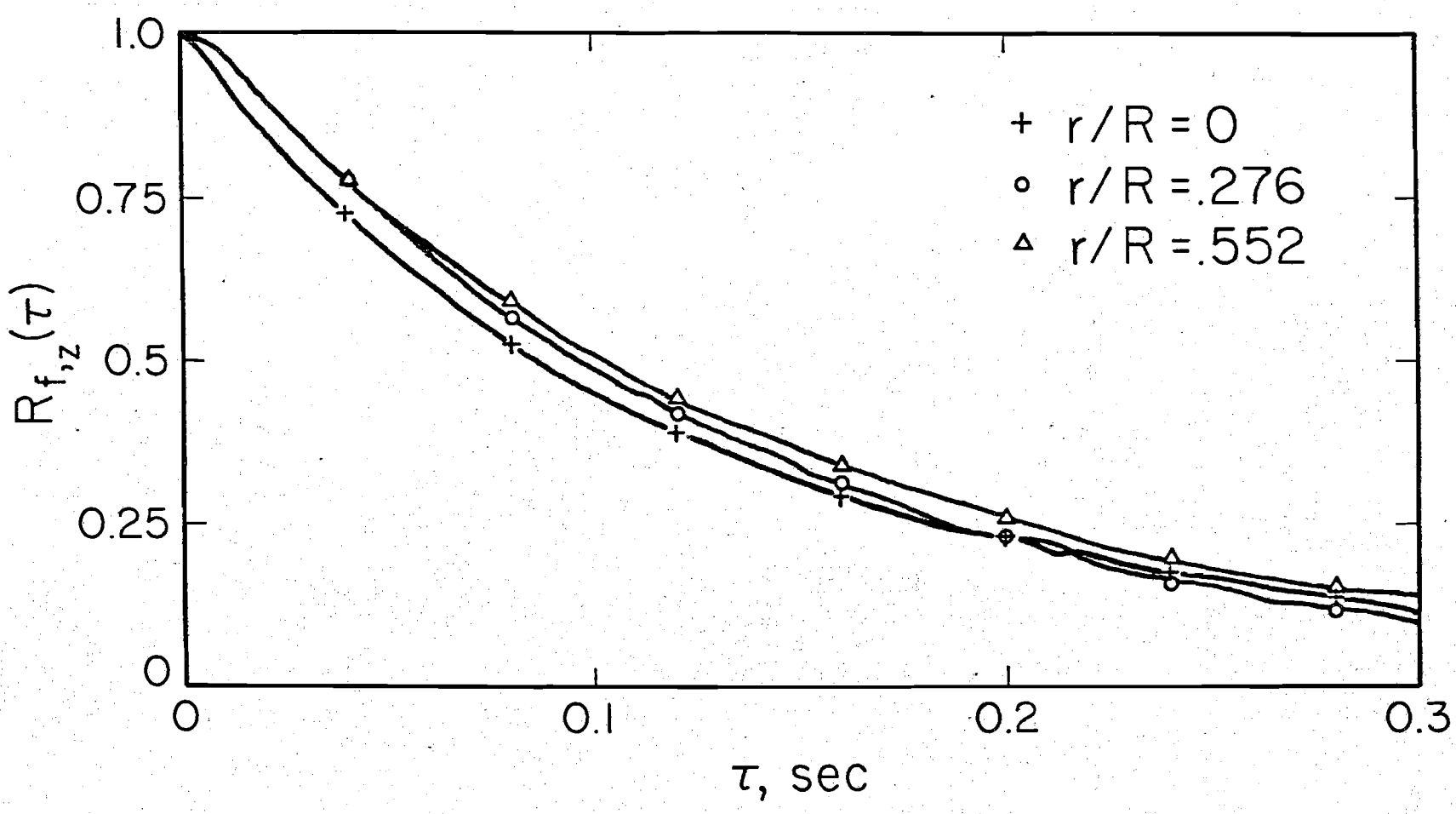

Figure 4.4 Fluid Velocity Autocorrelations at Selected Radi

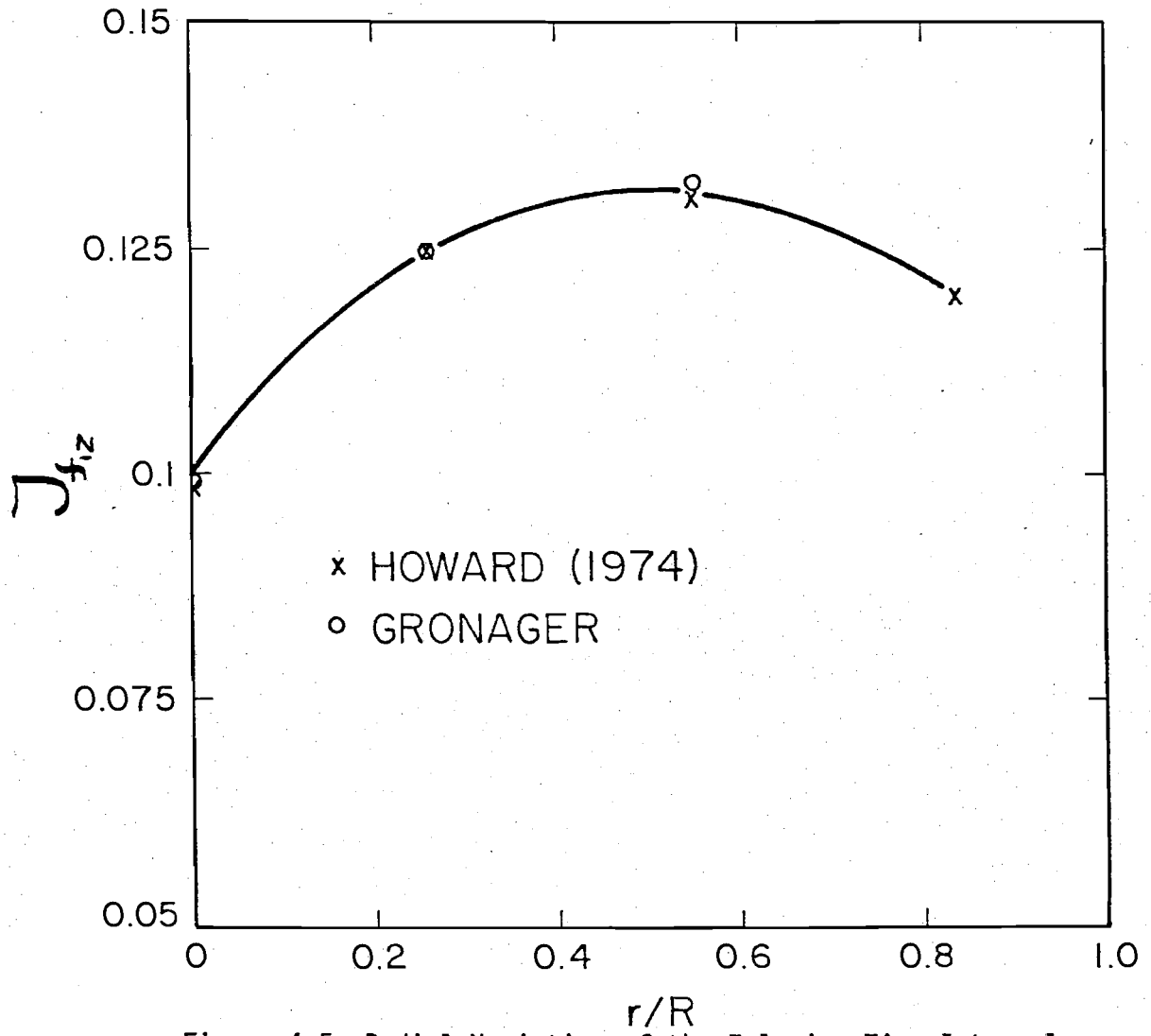

Figure 4.5 Radial Variation of the Eulerian Time Integral Scale $J_{f,z}$ Is a Pipe at Re = 50,000

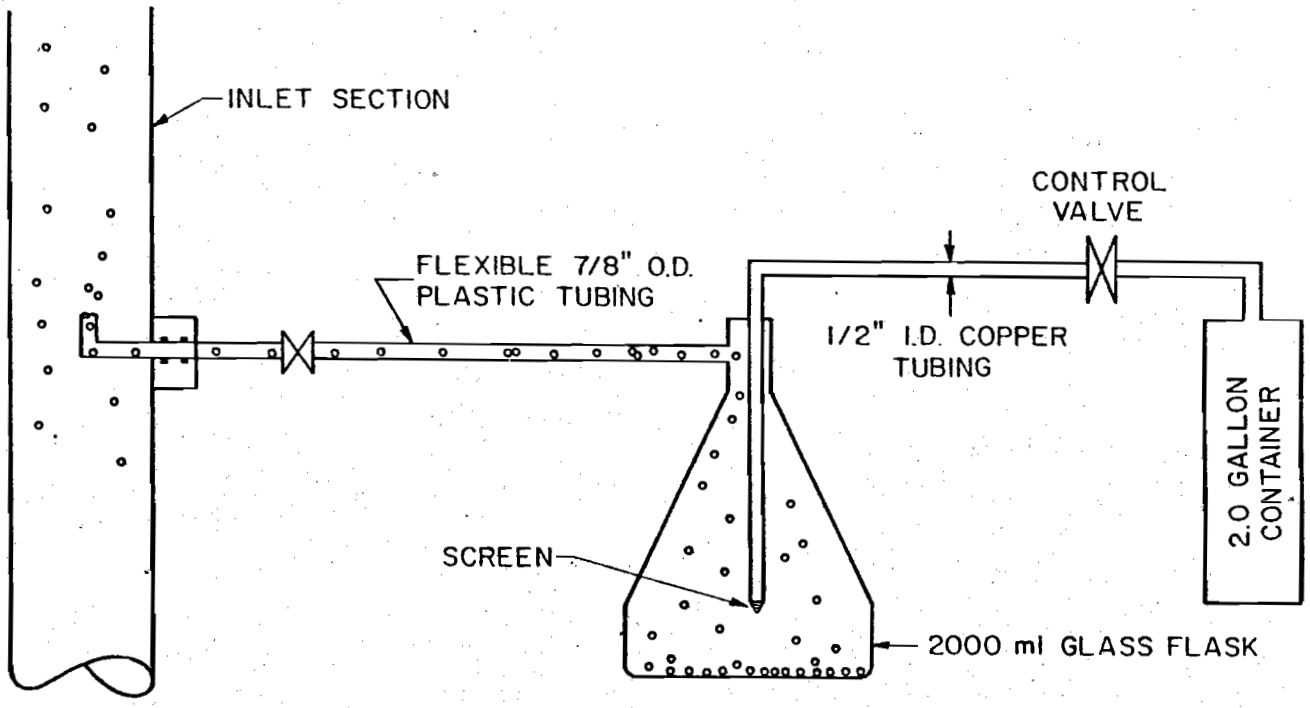

Figure 4.6 Isokinetic Particle Sampler

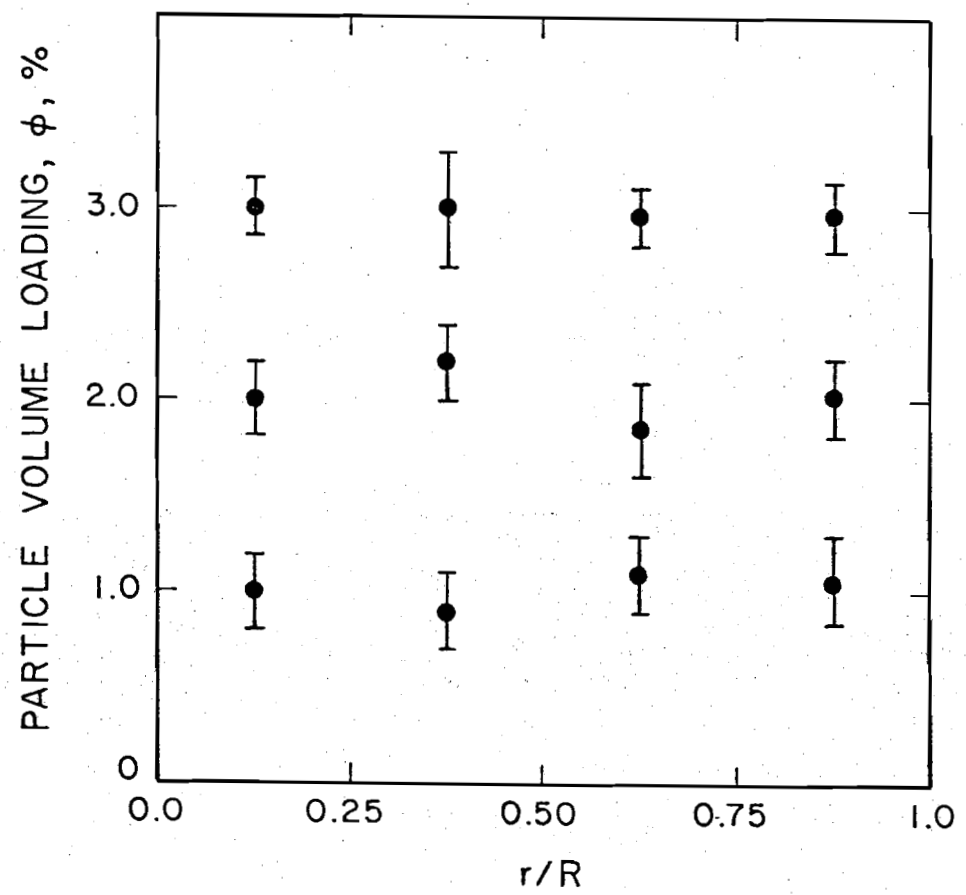

Figure 4.7 Radial Variation of the Particle Volume Concentration ϕ,%

calculated particle concentration and that which was observed by the sampler. Note, as the volume loading was increased from 3 percent, the sampler was prone to clogging. Based on visual observations of the system at higher volume loadings, no evidence was observed to indicate a deviation from the previous linear loading behavior.

With the completion of the zero particle loading data, and the suspension characteristics, the fluid investigation was directed toward the characteristics of the turbulent fluid structure for non-dilute particle volume loadings. Fluid measurements were made for volume loadings of 1, 2 and 3 percent. The rugged conical probe was placed at the centerline of the pipe and for each volume loading, the fluctuating signal was recorded. Off-line analysis provided the statistical quantities of the recorded signals. Initial results indicated larger mean and rms voltages than previously observed when $\phi = 0$. A signal intensity S', was defined as

$$S' = e_{rms}/e_{mean} \qquad (4.2)$$

where e_{rms}, e_{mean} are the rms and mean linearized signals from the anemometer, respectively. A comparison of the signal intensities at various ϕ is shown in Figure 4.8. S' is seen to increase sharply from ϕ equal to 0 to ϕ equal 2 percent. It then tends to level off at the higher volume loadings. This large increase in the intensity is believed to be due to particle interaction with the probe. As shown in Figure 4.9.

The effects of particle collisions and near misses with the probe cause large disturbances in the signal. The rate of occurrence of the interactions was proportional to the volume loading and appeared as a higher rms voltage. This was observed until the point was reached where the interactions were so

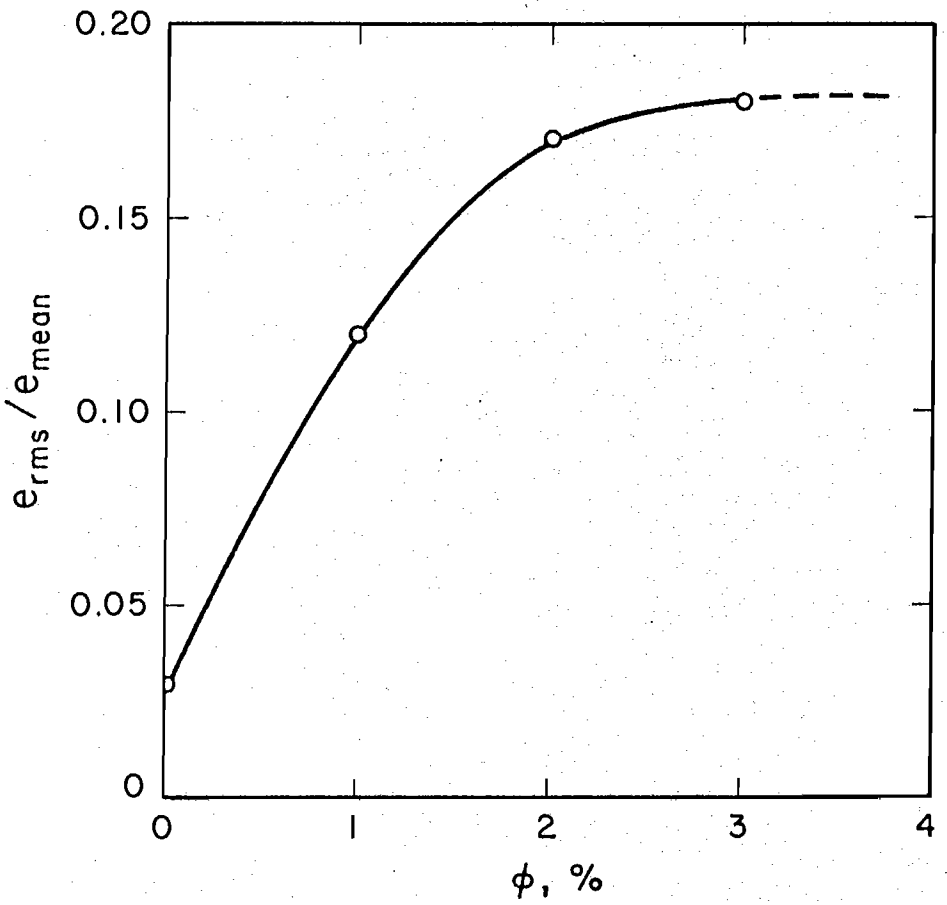

Figure 4.8 Anemometer Signal Intensities for Various Particle Loadings

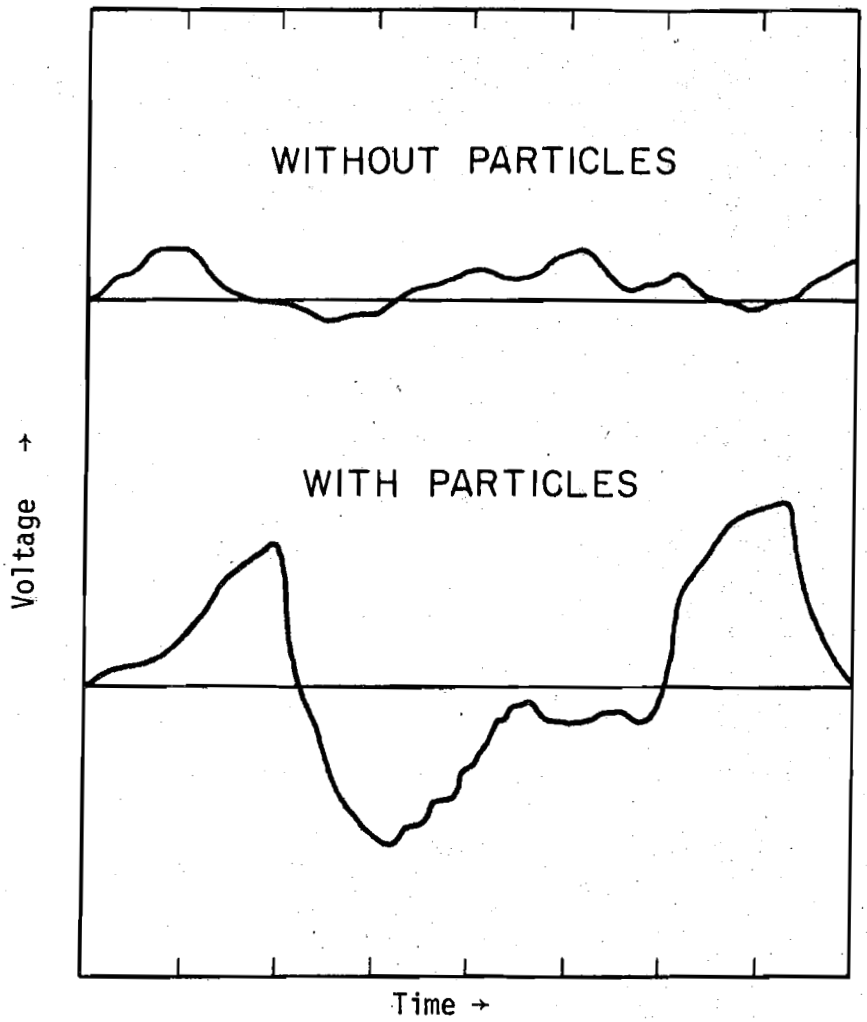

Figure 4.9 Typical Anemometer Signals with and Without Particles Present in the Test Section

numerous that the probe's output was saturated by them. (As indicated for ϕ = 3 percent.) The autocorrelation functions, shown in Figure 4.10, indicate a rapid loss of correlation for ϕ equal 1, 2 and 3 percent. Simultaneous visual observations of the anemometer signal and the proximity of the particles to the sensor showed strong correlation. It is not clear that the signal can be interpreted as a true measure of the fluid's turbulent velocity. Therefore, caution must be exercised in utilizing the anemometer results for the fluid turbulence. It is suggested that only after direct comparison with neutrally buoyant particle data should the anemometer results be accepted as true measurements of the fluid turbulence. As discussed below, this was not accomplished in these studies.

With the uncertainty of measuring the Eulerian characteristics of the fluid for non-dilute suspensions, the experimental investigation turned to estimating the fluid's Lagrangian characteristics from the earlier work of Howard. A comparison was made between the tagged particle's axial integral time scale and that of the fluid's convective integral time scale at various particle free fall velocities. As shown in Figure 4.11, good agreement was found between the experimental scale ratio $\mathcal{J}_{p,z}/\mathcal{J}_{f,z}$ and the theoretical predictions. This indicated that for very small free fall velocity, the particle's scale measurements approached that of the fluid's. Thus, if one was consistent with the theory's assumptions of very small particles, a tagged neutrally buoyant particle could be used as a Lagrangian "probe" to estimate the fluid's behavior. With this in mind, experiments were conducted in which a tagged particle's trajectories were recorded at various volume loadings.

Several 3mm particles were constructed by molding expandable polystyrene plastic in which a radioactive Co-60 source was placed. For a detailed

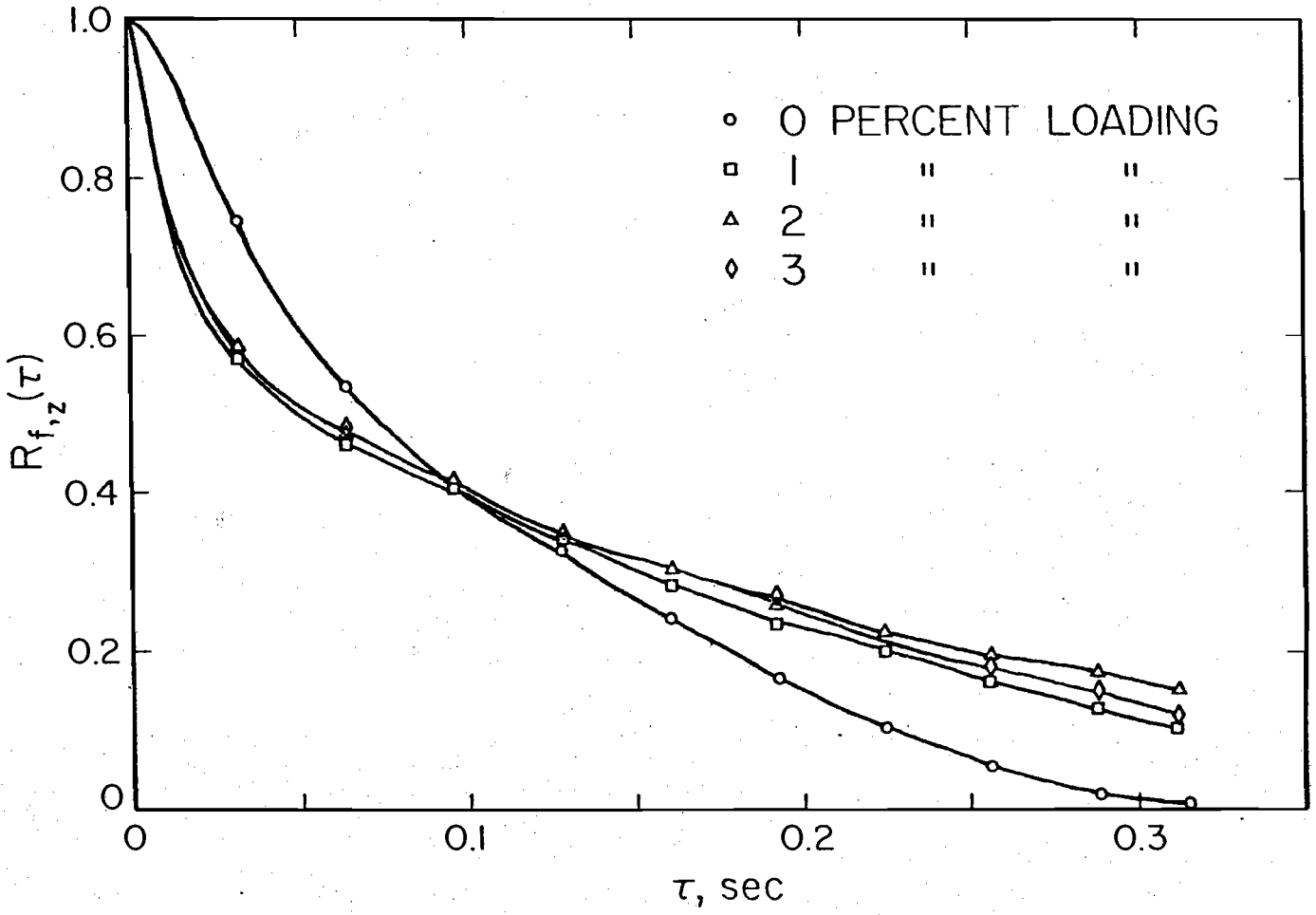

Figure 4.10 Anemometer Signal Autocorrelation for Various Particle Volume Loading ϕ,%

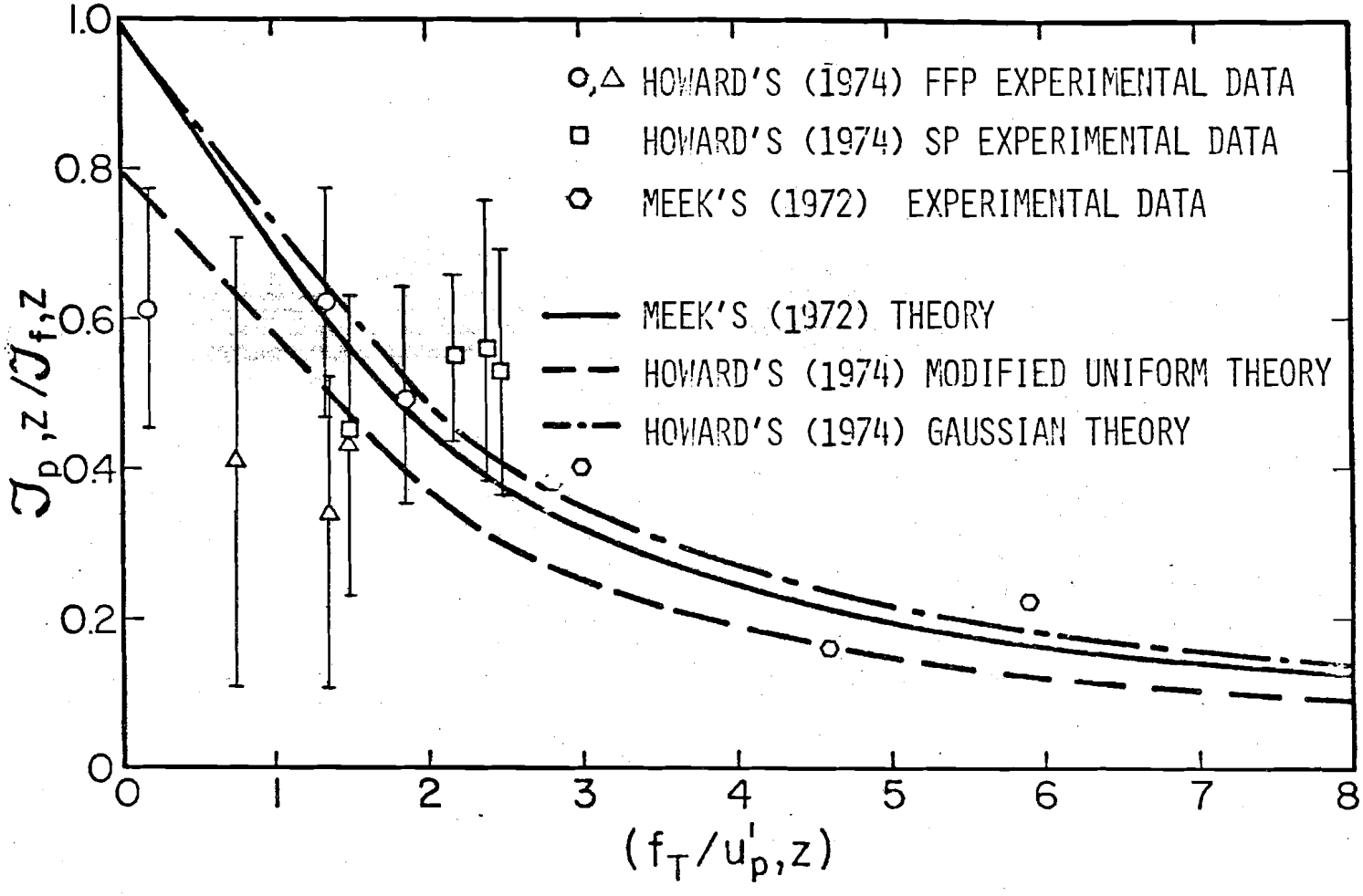

Figure 4.11 Howard's (1974) Comparison of Experimental Scale Ratios $\mathcal{J}_{p,z}/\mathcal{J}_{f,z}$ with Theoretical Predictions

description, consult Howard's thesis. Unfortunately, the particle was not able to withstand the highly agitated environment imposed by the jet pump. Most of the particles showed damage after several passes through the loop, and in one case a particle was destroyed. Several techniques were advanced toward making the particle's outer surface harder. This includes applying various epoxy resins, paints and even encapsulation of the particle within an epoxy macrosphere. This resulted in stronger particles, but still an unsatisfactory performance. As a result, a larger 4mm particle made of polypropylene was used to construct a low free-fall velocity particle. The particle's construction was similar to the technique described in Chapter 3. This particle exhibited excellent stability of its physical properties over many hours of operation in the loop. The free fall velocity in quiescent water was 2.05 cm/sec., with a Reynold's number of 94.2.

Experiments were performed using the particle data acquisition system shown in Figure 3.6. Initially, experiments were run with only the tagged polypropylene particle in the loop. This was to provide data for a direct comparison with the fluid structure reported by Howard. The experimental investigation moved on to loading the system with 1 and 2 percent volume fraction of the heavy (ρ = 1.18) particles. During the data recording, an oscilloscope was used to display the four different voltages from the differential amplifiers. From the relative level of the signals of the X-Y plane, and that for the carriage velocity, it was observed for most of the 220 runs recorded that the tagged particle was located near the wall of the pipe. Upon close visual observation, it was found that the slower moving tagged particle underwent a constant bombardment from the bulk particles. The tagged particle eventually migrated to the wall, where it experienced

less collisions and a relatively lower fluid velocity. Occasionally, the particle was swept away from the wall region, but returned rapidly to it. This behavior resulted in an insufficient amount of data for the particle in the core region to provide adequate analysis.

In light of the results described above, unsuccessful attempts were made to define the fluid's structure in the presence of the particles. Thus, without in-house measurements, the investigation turned to examining the theoretical and experimental information reported in the literature.

Hinze (1972) indicated several effects that discrete particle's suspension have on the fluid turbulent structure. This included an: effect due to the wakes of the particle moving with respect to the fluid, thus modifying the energy-spectra of the fluid in the wave number range corresponding to the particle's dimension and effects due to the decreased volume of the fluid with the presence of particles, on the turbulent intensity, integral scales and viscous dissipation of the fluid. Hinze showed that particles modified the fluid spectra at the relatively higher wave numbers. This implied, according to Hinze, a higher energy-dissipation rate within the fluid. This was supported by Owen (1969) in which he demonstrated a direct proportionality between energy dissipation and the particle volume loading. Experimental work by Kada and Hanratty (1960) supported Owen's work by reporting a linear relationship between energy dissipation and particle volume loading.

The other turbulent characteristics of interest, the intensity of integral scale, and eddy-diffusion coefficients don't enjoy the same support between theory and experiment. Hino (1963) showed for neutrally buoyant particles that the intensity of the fluid increased with the presence of particles. This seemed to agree satisfactorily with experimental results,

as reported by Hino, for Elata and Ippen (1961). Elata and Ippen's data was for higher loading of approximately 15% and 25%, showing changes of 10-15 percent in the intensity. Hino also predicted for heavy particles a continued decrease in the intensity as volume loading increased. Owen on the other hand, showed a decrease in the fluid intensity for all particle densities. The only available experimental intensity observations of heavy particles was by Kada (1960). He showed a general increase in the intensity as volume loading increased. Hino also reported that the integral scales decreased, for all cases of particle density, as the volume loading increased. No experimental evidence was found to support his prediction. Owen and Hino agree qualitatively that a decrease of the eddy-diffusion coefficient should occur for increased particle loading. But Kada and Hanratty showed a large increase in the eddy diffusion for particles of high free-fall velocity with respect to the fluid, and small effects for low relative free-fall velocity particles.

As one can see, the experimental evidence and the theories themselves are not in general agreement with each other.

This is due in part to the different systems under consideration. Kada and Hanratty's experiment was conducted in an upwardly flowing vertical pipe, Owen's predictions were based on a horizontal pipe, and Hino, an open channel flow. A general conclusion cannot be drawn, at this point, as to the turbulent characteristics of the fluid in the present system. Further discussion will be presented in the next section, as to estimates of the fluid turbulent properties.

4.2 Particle Measurements and Comparison with Theory

Two series of experiments were conducted to investigate the behavior of particles in a non-dilute turbulent suspension. The first set of experiments (HTAG series) consisted of spherical particles, of uniform size (0.476 cm diameter) with a specific gravity of 1.18. The second series consisted of similar size particles with a specific gravity of 1.05. The density differences were provided to investigate the free-fall effects at various particle volume loadings. The physical properties of the particles are shown in Table 3.1. As was the case for both experiments, the particle volume loading, ϕ, ranged from single particle circulation (i.e., ϕ =0) to a bulk particle volume loading of 10 percent. The volume loadings investigated for each series are shown in Table 4.1.

The mean and rms positions of the tagged particle, at various volume loadings, is shown in Table 4.1. As one can see, the HTAG series particle was generally found at a radial position of approximately 3.0 cm, where as the LTAG series particle was found at a somewhat larger radial position. The mean axial position for a given run was strongly dependent upon the adjustable feedback characteristics of the carriage tracking circuits. It was found that the carriage exhibited its best tracking performance when the particle's position was in the upper half of the calibrated region (refer to Figure 3.8). This is evident from the number of runs resulting from the analysis of the LTAG series. Fewer runs were rejected because of the carriages inability to lock onto the particle's trajectory. This was accomplished by increasing the feedback tracking sensitivity. The rms positions are the standard deviation about the mean position. Generally, the results are as expected for the physical system in which the particle's position is constrained to reside within the calibrated region.

Table 4.1 Mean and rms Positions

Volume Loading Series	Number of Runs HTAG	LTAG	Mean Position $\overline{r}$ HTAG	LTAG	$\overline{\theta}$ HTAG	LTAG	$\overline{Z}_{wrc}$ HTAG	LTAG	rms Position r' HTAG	LTAG	θ' HTAG	LTAG	Z' HTAG	LTAG
0	16	21	3.158	3.668	3.07	3.50	3.115	-2.245	0.789	0.708	0.988	1.308	0.532	0.695
0.5	38	9	3.838	4.378	3.50	4.33	-0.255	-0.795	0.922	0.888	0.325	0.388	0.962	0.494
1.0	19	23	3.318	2.628	3.15	3.33	1.295	-1.765	1.096	1.458	1.004	0.908	1.062	0.723
2.0	15	25	2.898	5.488	2.76	2.83	-1.095	-2.115	1.103	2.268	0.908	1.028	1.442	0.962
3.0	14		2.888		3.18		0.785		1.166		1.038		1.392	
4.0	16	24	3.168	5.258	2.50	2.90	-0.205	-1.185	1.125	2.238	0.908	1.088	1.301	0.827
5.0	9	22	2.918	3.398	2.64	3.39	1.025	-1.585	1.135	0.828	1.068	0.884	1.302	0.884
6.0	0	17		6.424		3.00		-0.487		1.828		0.738		0.740
10.0	13	33	2.798	4.278	3.08	3.14	0.347	-0.051	1.264	2.598	0.776	0.988	1.062	0.560

The mean and rms velocity data for both series of experiments are shown in Table 4.2. An initial look at the radial and azimuthal mean velocities show them to be nearly zero, with no apparent volume loading dependency, as would be expected in a vertical pipe flow. On the other hand, the axial mean velocity, $\overline{U}_{p,z}(\phi)$, indicates significant effects of increasing the volume loading. The general trend of $U_{p,z}(\phi)/U_{p,z}(0)$ is demonstrated in Figure 4.12. Note the initial increase for low volume loading, followed by a gradual decrease as ϕ is increased. Several models to predict the volume loading behavior on the mean particle velocity are included in Figure 4.12. It can be shown from Equation 2.23, that for steady state case:

$$-\rho_p F^* \lambda(\phi) f(\phi) + g\rho_p = 0 \tag{4.3}$$

Recalling that $F^* = g/f(0)$, we find:

$$\frac{f(\phi)}{f(0)} = \frac{1}{\lambda(\phi)} \tag{4.4}$$

Poor agreement is found from comparing Tam's (1969) functional form (equation 2.6) with the experimental data. Similar results are found for a model developed by Batchelor (1972), where $\lambda(\phi)$ was given by:

$$\lambda(\phi) = 1./(1. - 6.55\phi) \tag{4.5}$$

In both cases, the predicted behavior for hindered settling, fails to show the initial increase in the particle mean velocity. The third model shown in Figure 4.12 combines two effects of particle settling; the hindered settling demonstrated by Batchelor, and the reduced drag experienced by binary particle interaction. If one considers the classic solution to the

Table 4.2 Mean and rms Velocities

Series	Volume Loading	MEAN VELOCITY $\overline{U}_{p_r}$		$\overline{U}_{p_\theta}$		$\overline{U}_{p_z}$		RMS VELOCITY V'_{p_r}		V'_{p_θ}		V'_{p_z}	
		HTAG	LTAG	HTAG	LTAG	HTAG	LTAG	HTAG	LTAG	HTAG	LTAG	HTAG	LTAG
	0.0	0.047	0.008	0.079	0.271	13.21	5.70	1.12	1.06	1.09	1.15	1.28	1.40
	0.5	0.013	0.089	-0.063	0.000	14.13	6.77	2.13	1.39	2.21	1.36	3.50	2.14
	1.0	-0.139	-0.035	0.213	0.199	14.76	6.00	2.59	1.29	2.79	1.43	3.38	2.07
	2.0	0.065	-0.113	0.078	0.104	13.67	5.72	2.84	1.44	3.26	1.51	3.89	2.47
	3.0	-0.124		-0.060		14.28		2.96		3.07		3.90	
	4.0	-0.031	-0.069	-0.32	-0.95	12.31	5.15	3.07	1.37	3.23	1.50	3.98	2.47
	5.0	0.014	0.049	-0.088	0.057	12.04	3.73	2.70	1.36	2.96	1.42	4.00	2.78
	6.0		0.070		0.062		4.68		1.25		1.34		2.18
	10.0	-0.089	0.015	-0.08	0.128	11.12	3.027	2.28	1.19	2.53	1.19	3.89	2.17

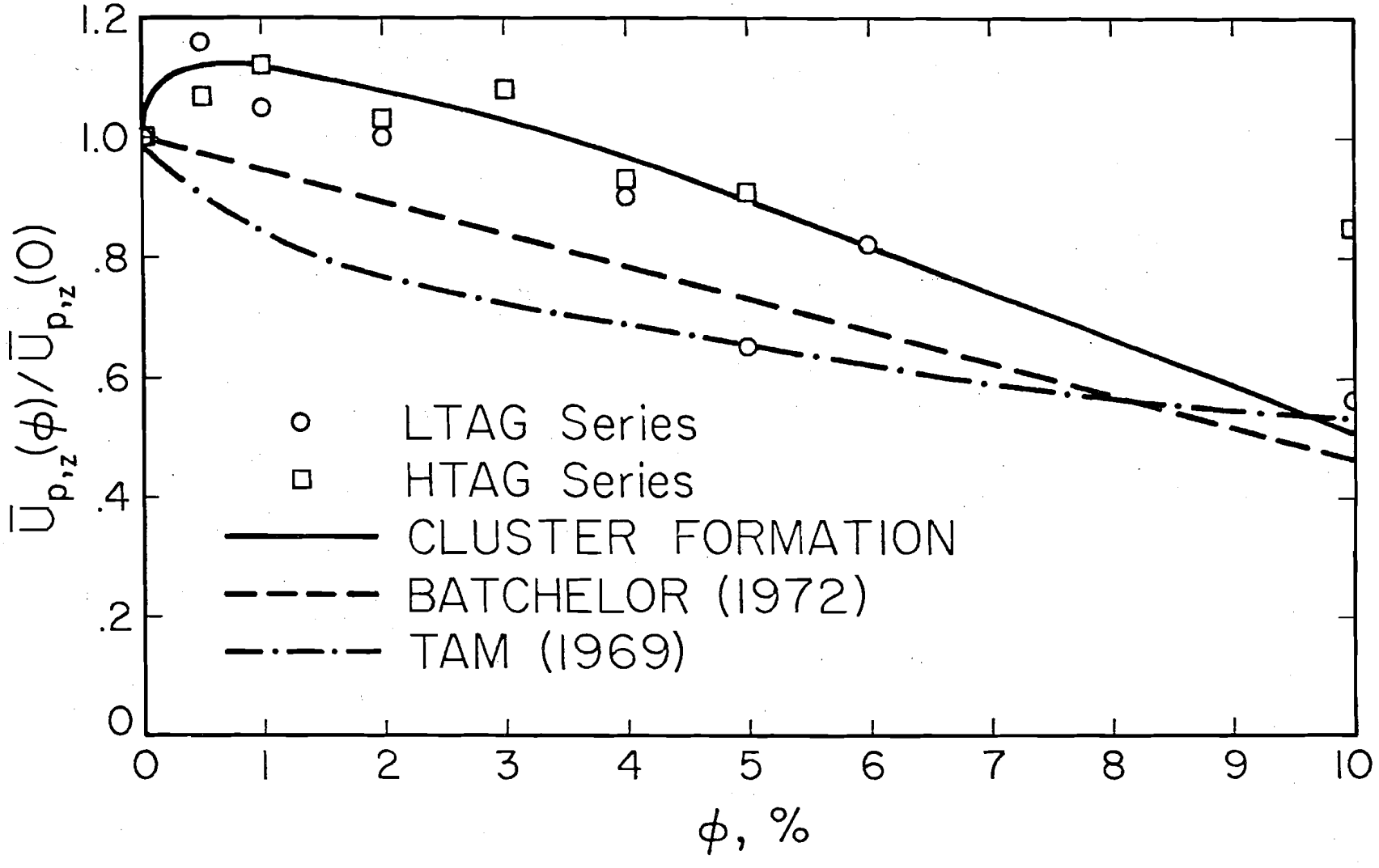

Figure 4.12 Relative Particle Mean Velocity, $\bar{U}_{p,z}(\phi)/\bar{U}_{p,z}(0)$, at Various Volume Loading in Turbulent Flow

problem of two spheres, aligned in the direction of the flow, one finds that the particles experience a reduction in their drag as the distance between them decreases. A reasonable approximation of the drag reduction was shown by Milne-Thomson (1960) to be:

$$\lambda' = 1./[1. + 3/2(a/d)] \tag{4.6}$$

where d is the average distance between particles and a is the radius. If one assumes a uniform spacing between particles such that:

$$d = a\sqrt[3]{\frac{4\pi}{3\phi}} \quad ; \quad \phi > 0$$

then Equation 4.6 becomes

$$\lambda' = 1./\left[1. + 3/2\left(\frac{4\pi}{3\phi}\right)^{-1/3}\right] \tag{4.7}$$

If we combine the hindered settling term, we obtain the following expression for $\lambda(\phi)$.

$$\lambda''(\ ) = \frac{1.}{(1.-6.55\phi)\left[1. + 3/2\left(\frac{4\pi}{3\phi}\right)^{-1/3}\right]} \quad ; \quad \phi > 0 \tag{4.8}$$

Applying Equation 4.8 to Equation 4.4 obtain the upper curve shown in 4.12. As one can see, reasonable good agreement exists with the experimental data.

The general phenomena, shown in Figure 4.12, has been observed by Kaye and Boardman (1962) (as reported by Happel and Brenner, 1973) as shown in Figure 4.13. In their experiments a considerable amount of particle cluster formation was observed. It has been well established that clusters of particles will settle at a faster rate than the same number of particles that are uniformly distributed. In the present study, cluster formations

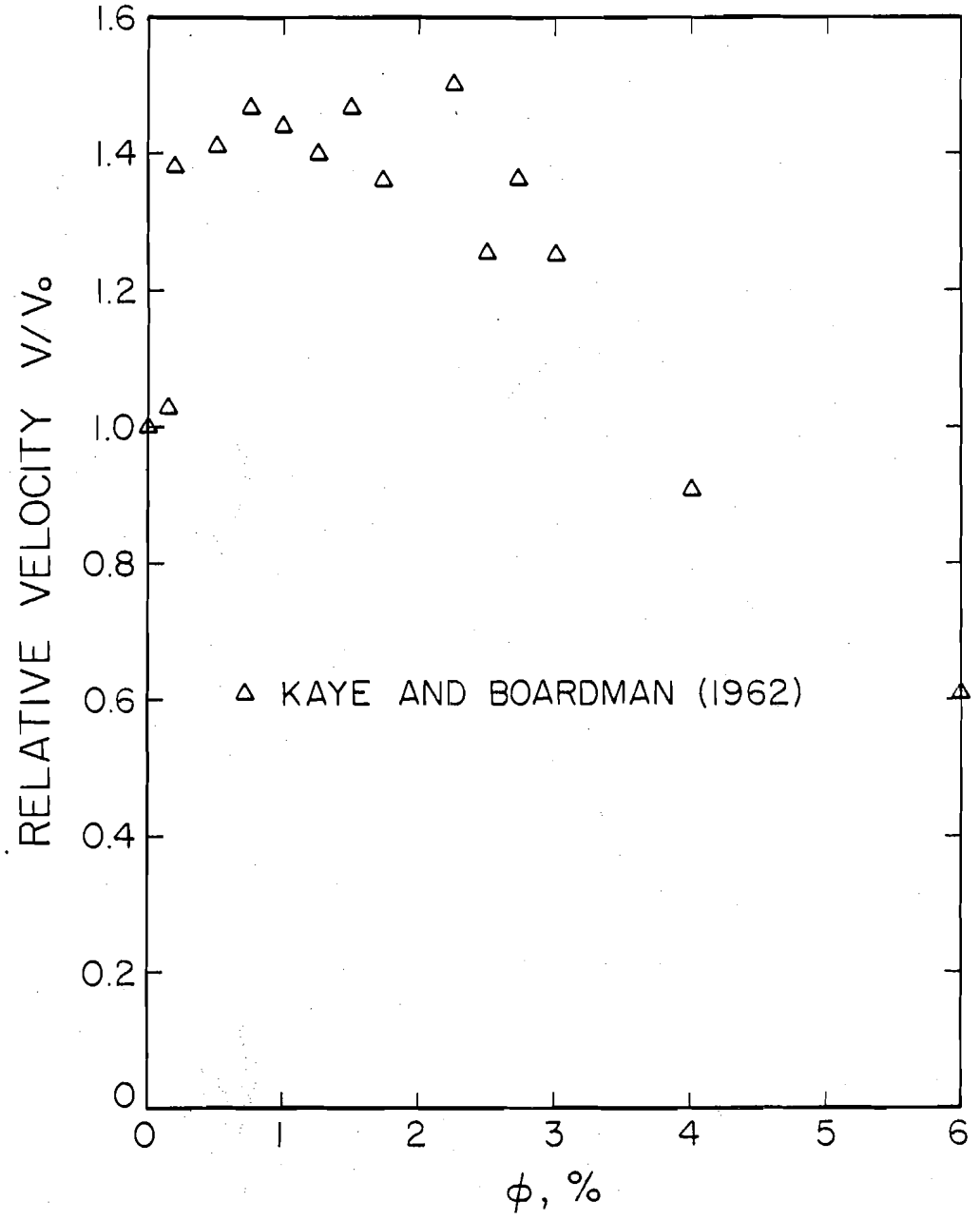

Figure 4.13 Kaye and Boardman (1962) Relative Mean Velocity V/V_0 in Quiescent Flow

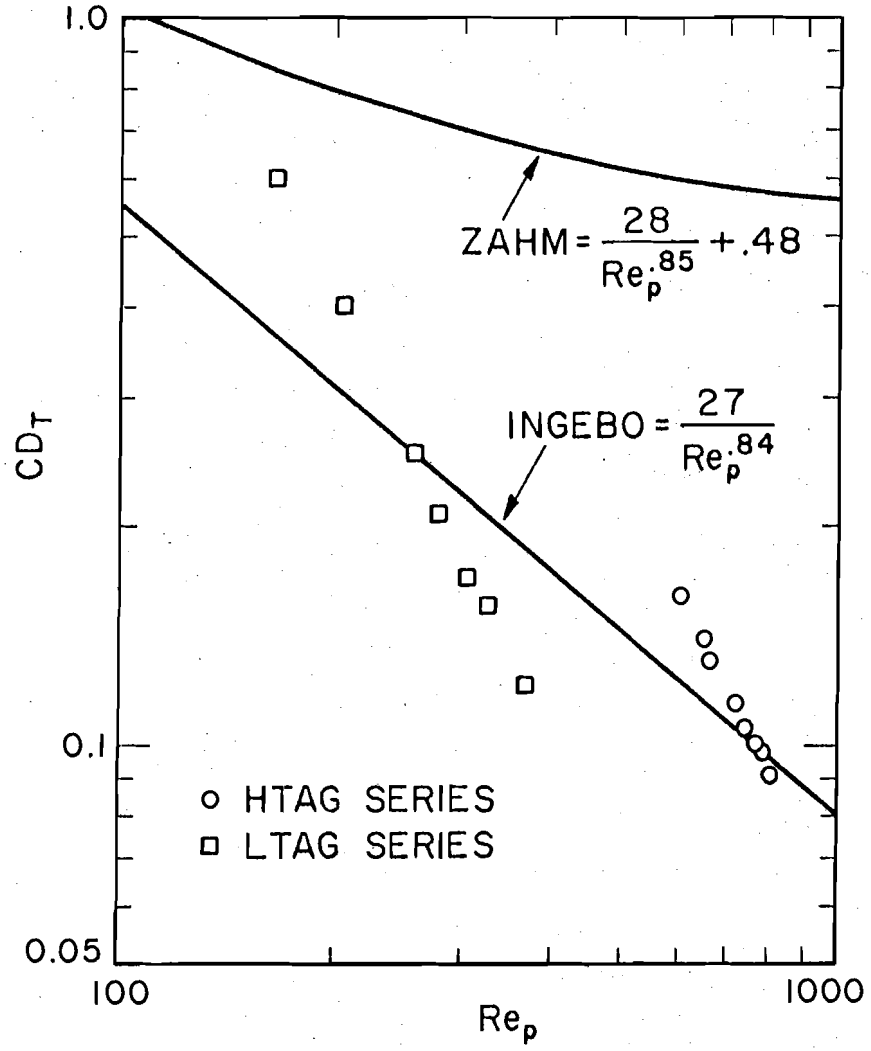

Figure 4.14 Comparison of Experimental Turbulent Drag Coefficients with Theoretical Predictions

were observed for ϕ equal to 1/2, 1, 2 and 3 percent, but not to a large degree. This may explain the smaller relative particle velocities in the present study, as compared to Kaye and Boardman's data for ϕ less than 3 percent.

Happel and Brenner lent theoretical support to the development of Equation 4.8 for the case of cluster formation, but it is imperative to point out that Equation 4.8 is not based on any rigorous theoretical development and caution should be exercised in applying it outside this case.

Figure 4.14 shows the turbulent drag coefficient, C_{D_T} for both series. This was based on the particle Reynold's number, Re_p, defined as:

$$Re_p = \frac{2a\bar{U}_{Rz}(\phi)}{\nu} \tag{4.9}$$

As one can see good agreement exist with Ingebo's (1956) turbulent drag coefficient. The empirical drag curve of Zahm (1926) for spheres in a quiescent fluid is shown to point out the differences in the drag for particle in turbulent fluids.

The effects of particle volume loading becomes evident in light of the particle's rms velocities, $V'_{p,r}$, $V'_{p,\theta}$ and $V'_{p,z}$. Referring to Figure 4.15, the rms velocities for ϕ equal zero are approximately equal, but as ϕ is increased, the rms levels rapidly increase initially, but as ϕ is further increased ($\phi \geq 2\%$) the rms velocities tend to level out; then slowly begin to drop off for higher loadings ($\phi = 10\%$). It is interesting to note several points. The lateral rms velocities, $V'_{p,r}$ and $V'_{p,\theta}$, as demonstrated in both experimental series, are in close agreement. This suggests that the particles are experiencing lateral isotropic fluid behavior. The axial (or longitudinal) rms velocity, $V'_{p,z}$, appears to be slightly higher, but

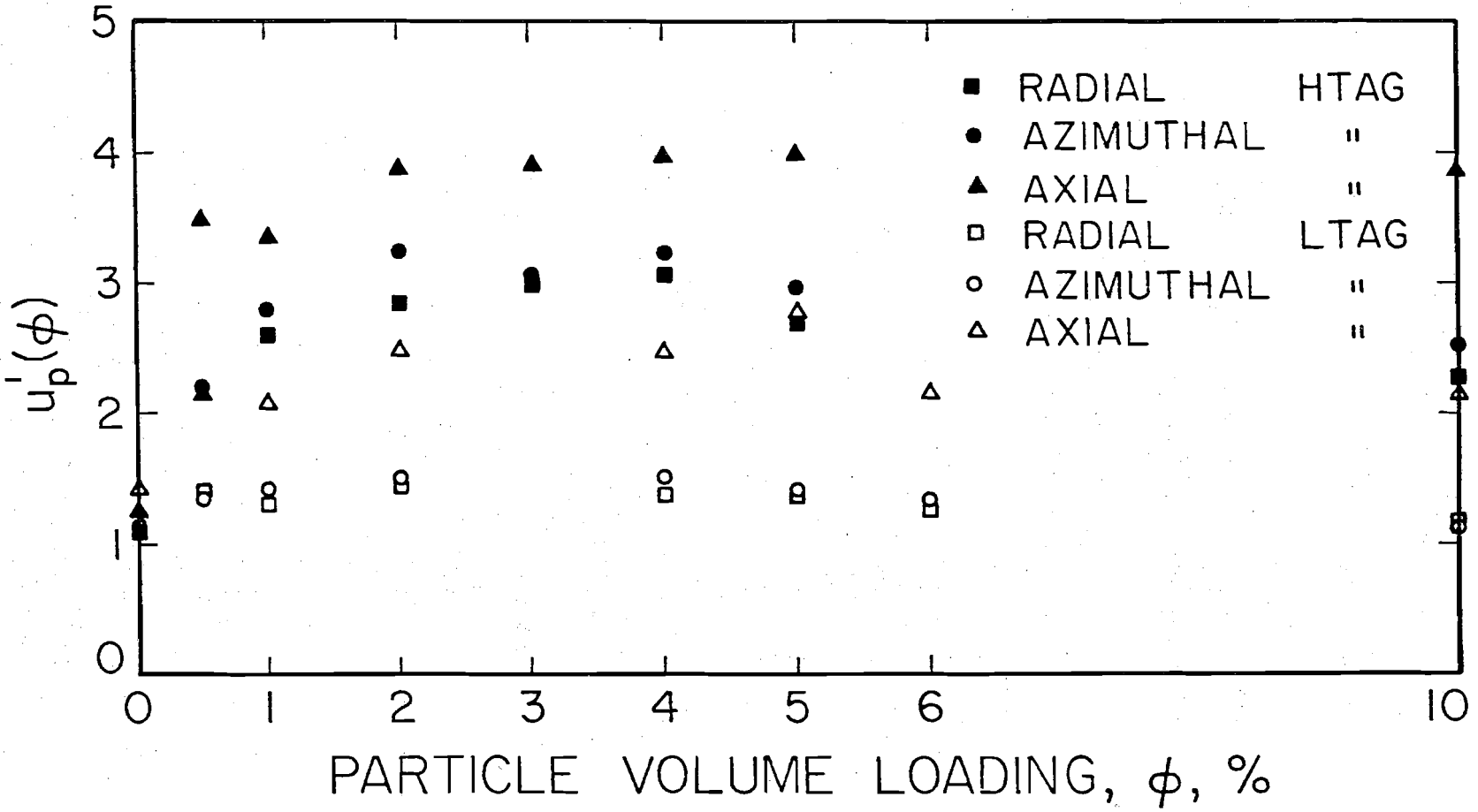

Figure 4.15 Particle rms Velocity $U_p'(\phi)$ at Various Volume Loadings ϕ.%

follows the same trend as the lateral rms velocities. It is interesting to point out that for ϕ greater than zero, the rms velocities for the HTAG series prove to be much higher than the LTAG series. Referring to Figure 4.16, for ϕ greater than 0, the free fall effect on the rms velocities can be removed by normalizing them by the quiescent free fall velocity, f . This indicates the important role that free-fall velocity plays on the turbulent environment. Further discussion of this phenomena is present in the latter portion of this section.

The particle's velocity variance, skewness and kurtosis, shown in Table 4.3, are directly related to the second, third and fourth moment of the velocity's probability density function (p.d.f.). As one can see the magnitude of the skewness is relatively small. The average value of the kurtosis is 3.06. This would indicate a Gaussian behavior of the velocity's p.d.f, the form of which is:

$$p(\omega_p) = \frac{[\omega_p']^{-1}}{\sqrt{2\pi}} e^{-\omega^2/2\omega_p'^2} \qquad (4.10)$$

where $w_p'^2$ is the variance of the instantaneous particle velocity, w_p. P.d.f.'s calculated from the experimental data are shown in Figure 4.17a through 4.17d. As one can see they further support the skewness and kurtosis data. A Gaussian probability density function is generally anticipated for turbulent fluid measurements, and as one can see it's indicative of the particle's behavior as direct consequences of the particle-fluid interactions. Referring to Figure 4.18 and 4.19 , an interesting note as to the effect of the volume loading on the probability density functions. Comparison for each direction at various volume loadings, indicates as a whole, that the p.d.f.'s

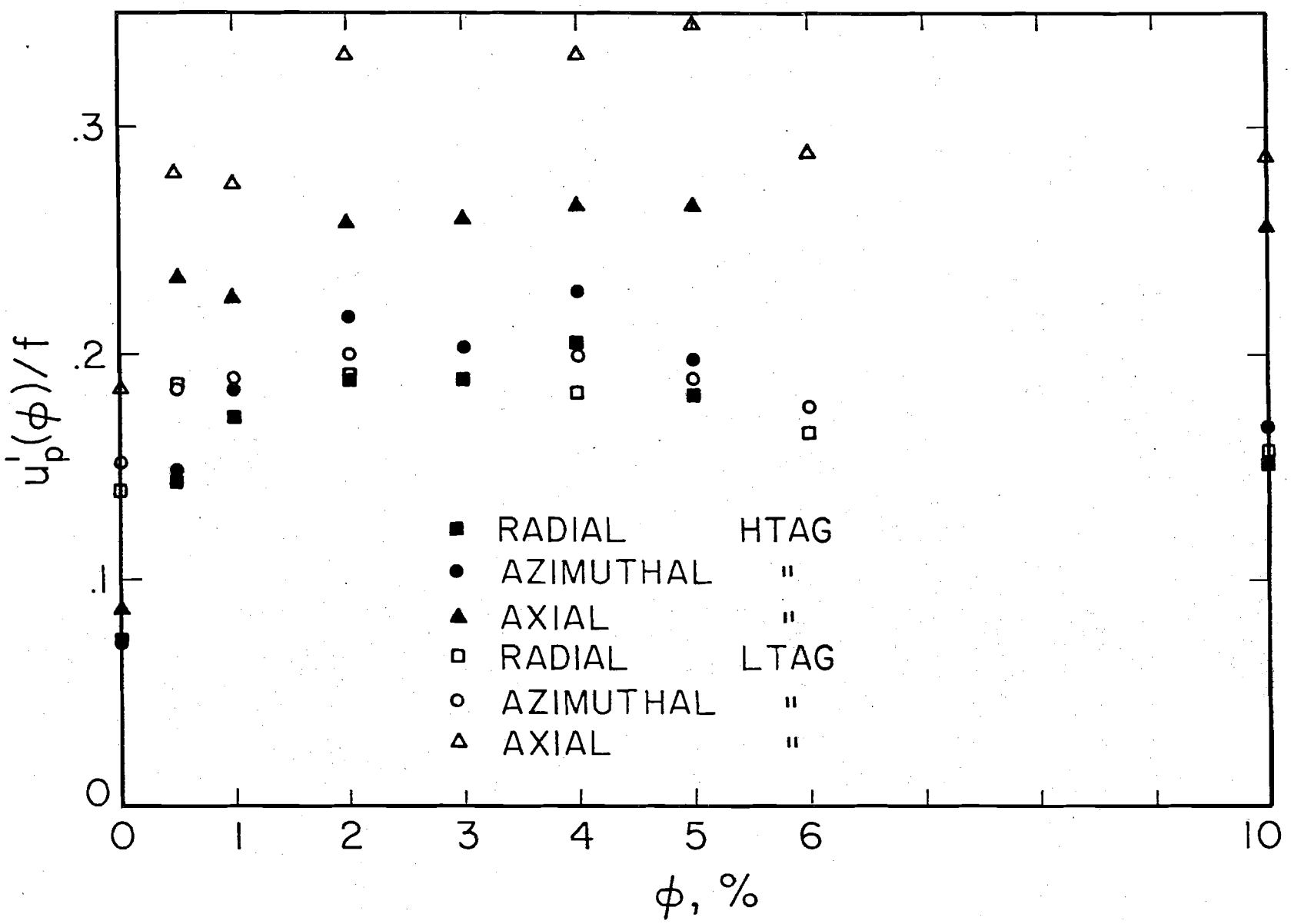

Figure 4.16 Normalized Particle rms Velocity $U_p'(\phi)/f$

Table 4.3 Variance, Skewness and Kurtosis of HTAG and LTAG Series

	VARIANCE						SKEWNESS						KURTOSIS					
Volume Loading	RADIAL		AZIMUTHAL		AXIAL		RADIAL		AZIMUTHAL		AXIAL		RADIAL		AZIMUTHAL		AXIAL	
Series	HTAG	LTAG	HTAG	LTAG	HTAG	LTAG	HTAG	LTAG	HTAG	LTAG	HTAG	LTAG	HTAG	LTAG	HTAG	LTAG	HTAG	LTAG
0.0	1.25	1.13	1.19	1.32	1.63	1.97	-0.168	-0.153	-0.082	0.082	-0.132	-0.047	2.91	3.12	2.75	3.04	2.96	2.97
0.5	4.54	1.94	4.88	1.86	12.23	4.59	-0.013	-0.158	0.036	-0.107	-0.025	0.081	3.28	4.20	3.08	3.22	2.95	2.70
1.0	6.71	1.67	7.76	2.04	11.45	4.28	-0.147	-0.207	-0.149	-0.046	-0.171	-0.088	2.89	3.25	2.75	3.21	2.91	2.93
2.0	8.06	2.09	10.61	2.29	15.11	6.11	-0.03	-0.173	0.130	-0.010	0.076	0.190	2.81	3.19	3.07	3.09	2.75	3.12
3.0	8.78		9.44		15.23		-0.066		-0.133		-0.018		2.97		3.04		2.96	
4.0	9.44	1.87	10.40	2.25	15.80	6.11	-0.076	-0.165	-0.075	-0.111	-0.055	-0.065	2.99	3.41	2.83	3.13	2.68	2.94
5.0	7.31	1.84	8.75	2.02	16.01	7.73	0.01	-0.062	-0.152	0.059	-0.326	-0.065	3.16	3.39	3.66	3.17	3.16	2.99
6.0		1.56		1.79		4.76		0.031		0.021		0.017		3.17		2.92		2.87
10.0	5.20	1.43	6.42	1.42	15.17	4.71	0.137	0.02	-0.110	0.04	-0.10	0.048	2.78	3.38	2.78	3.02	2.68	3.08

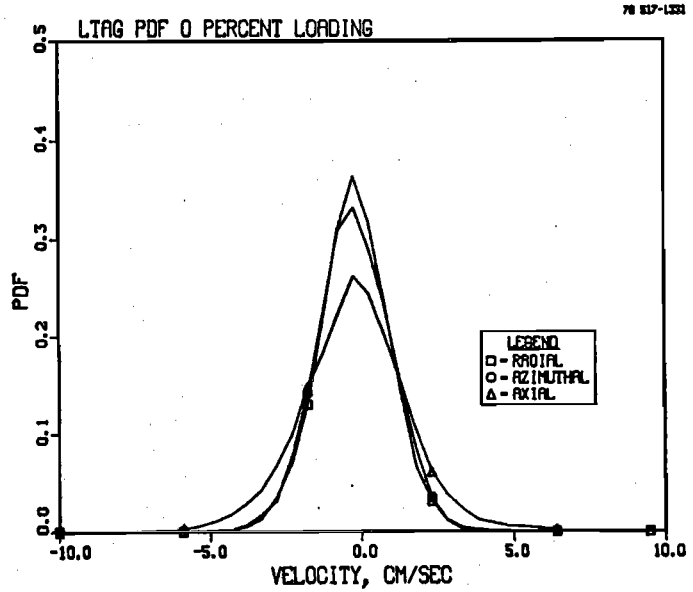

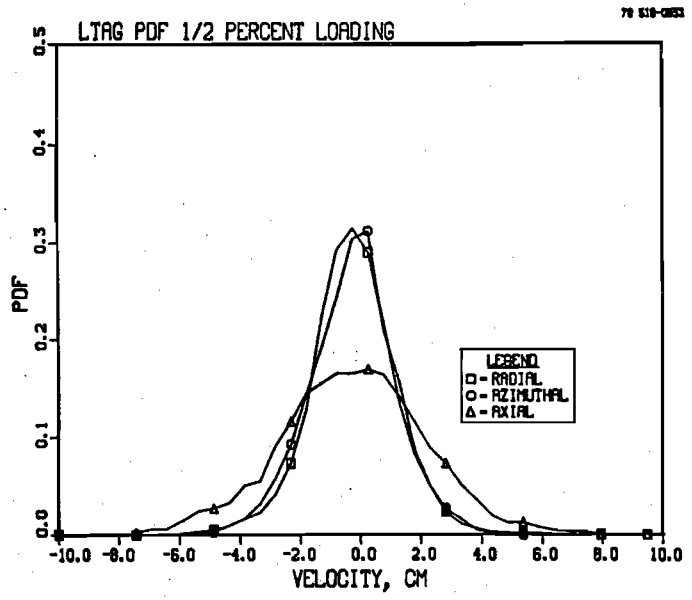

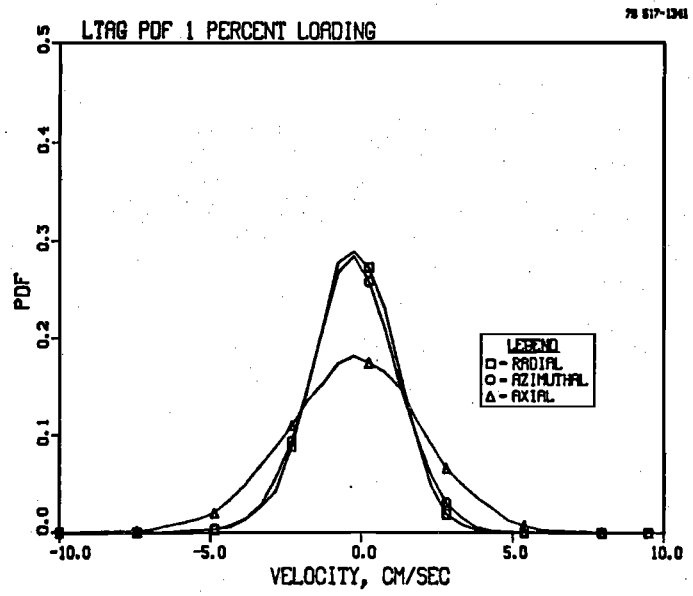

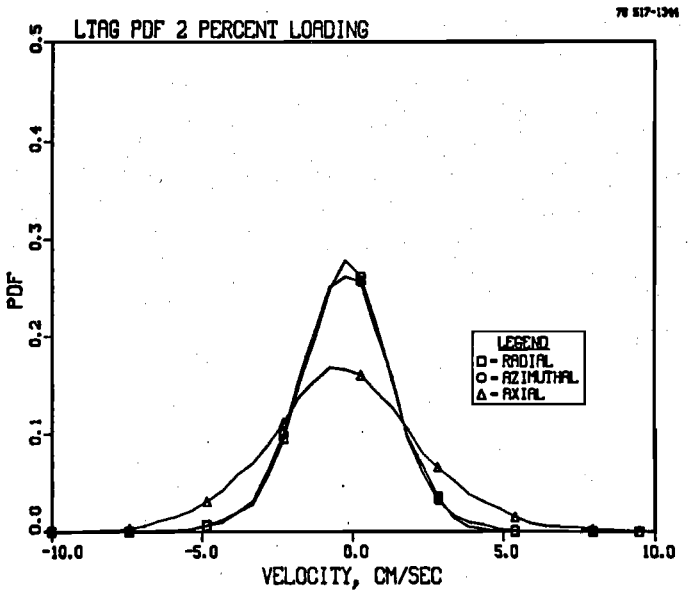

Figure 4.17a LTAG Probability Density Functions for ϕ Equal 0, 1/2, 1, and 2 Percent

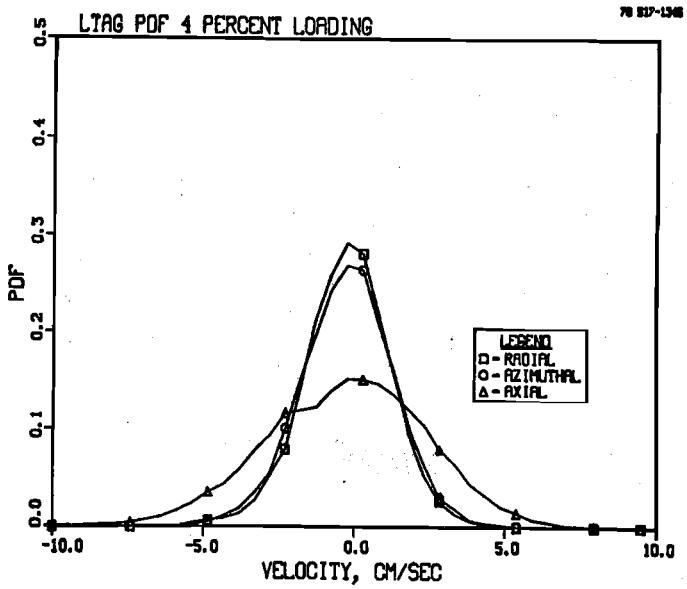

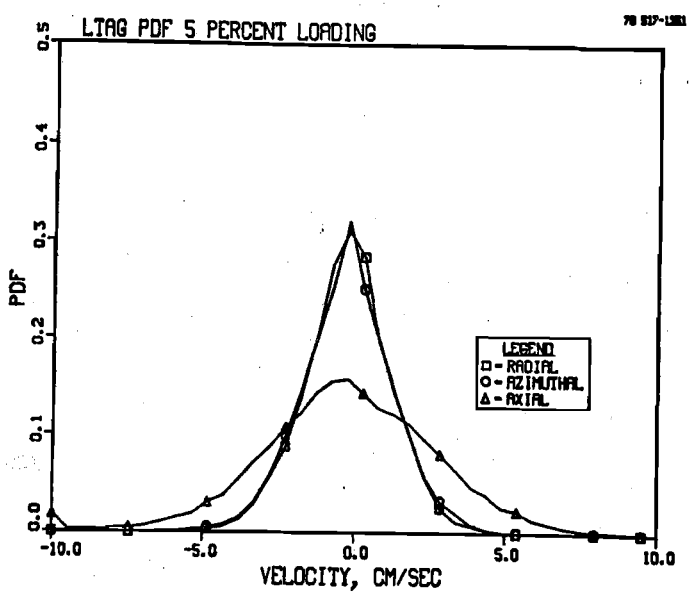

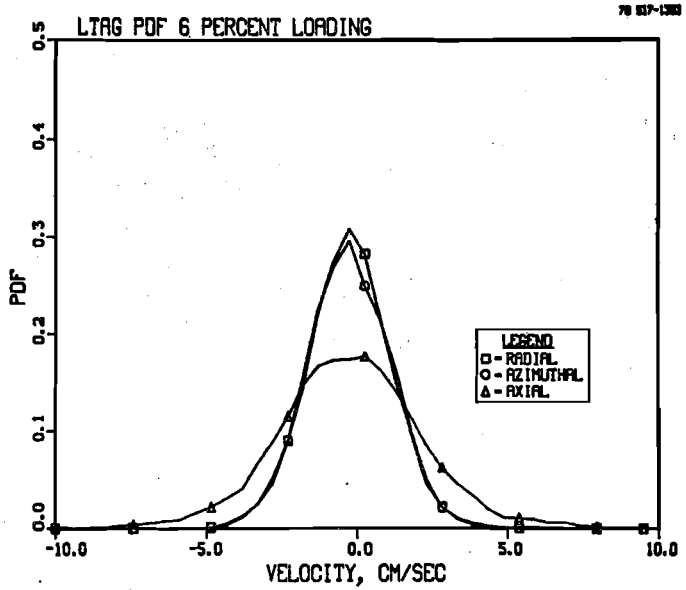

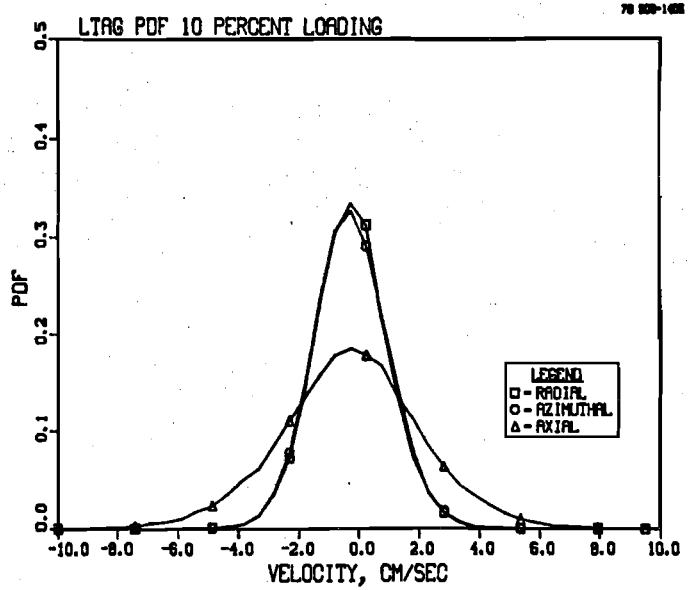

Figure 4.17b LTAG Probability Density Functions for ϕ Equal 4, 5, 6, and 10 Percent

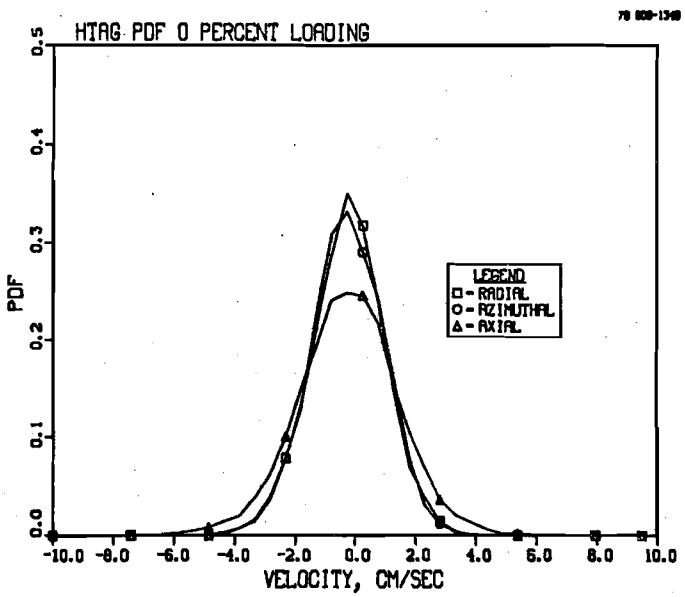

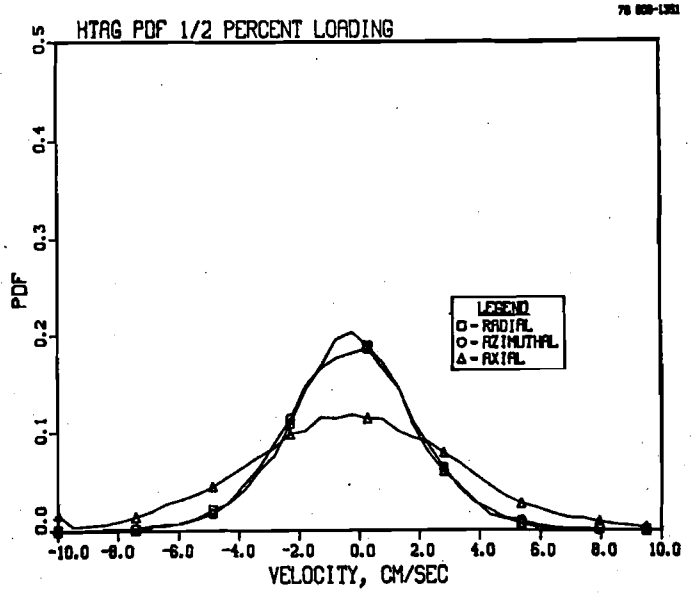

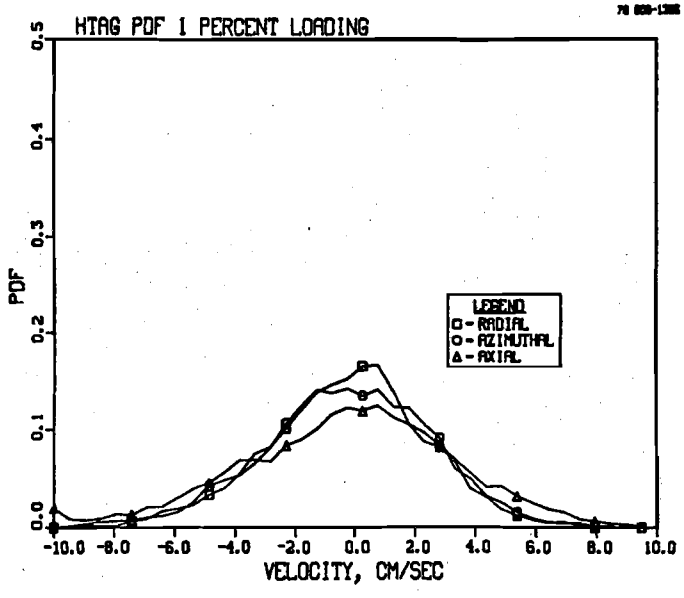

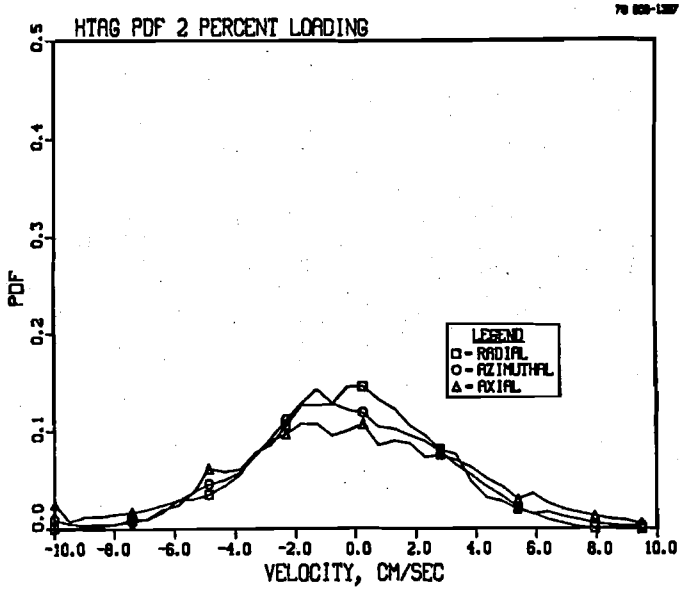

Figure 4.17c HTAG Probability Density Functions for ϕ Equal 0, 1/2, 1, and 2 Percent

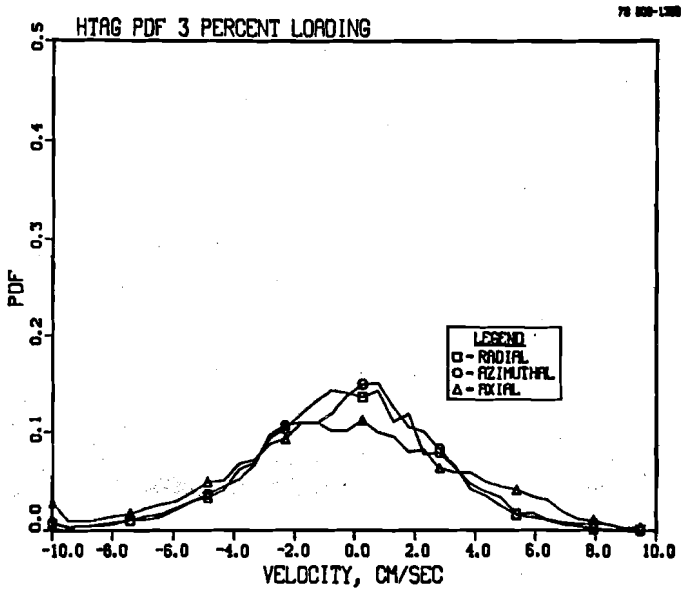

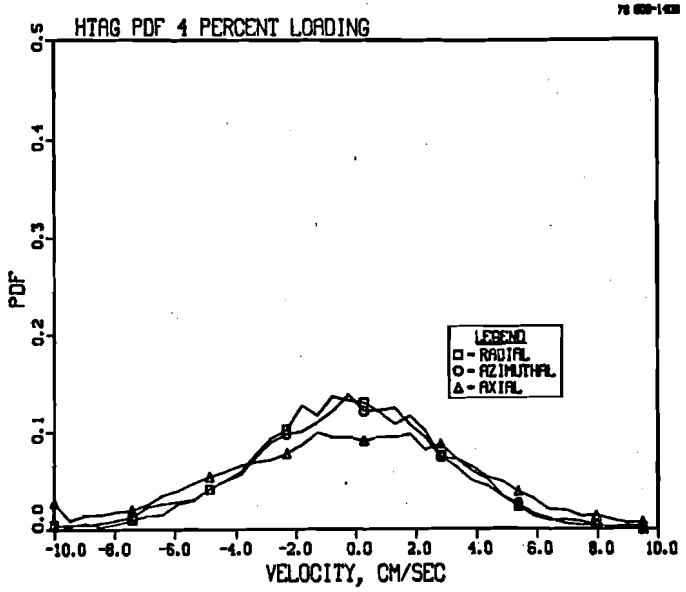

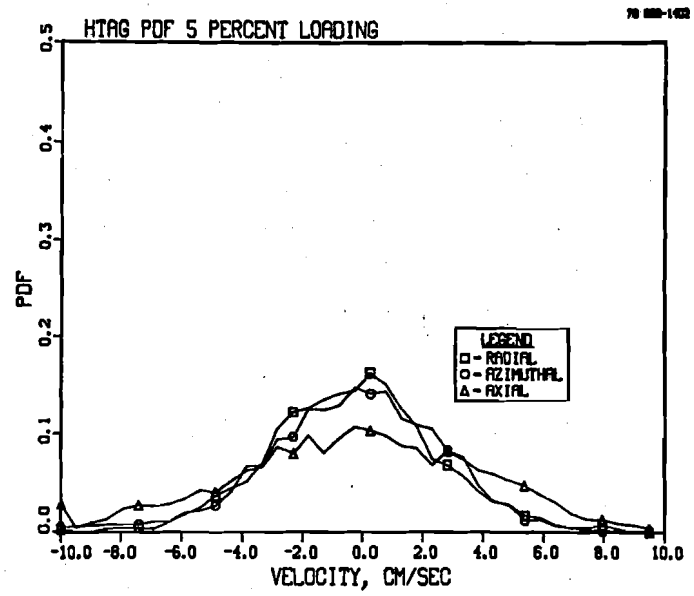

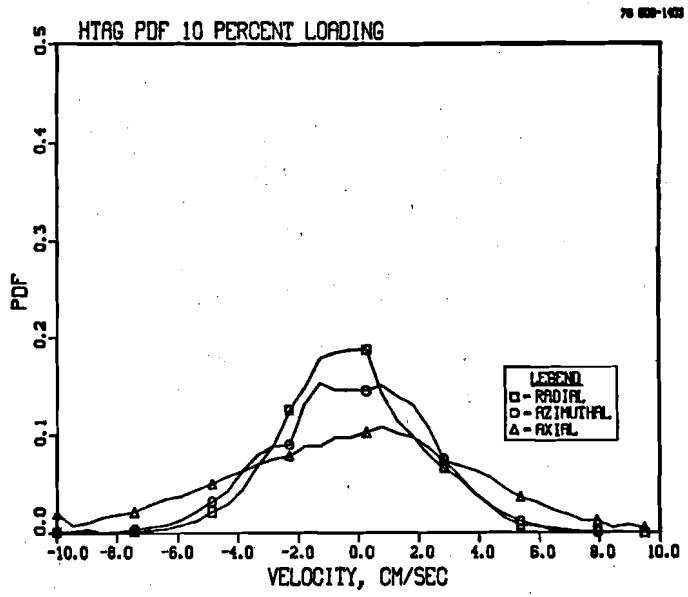

Figure 4.17d HTAG Probability Density Functions for ϕ Equal 3, 4, 5, and 10 Percent

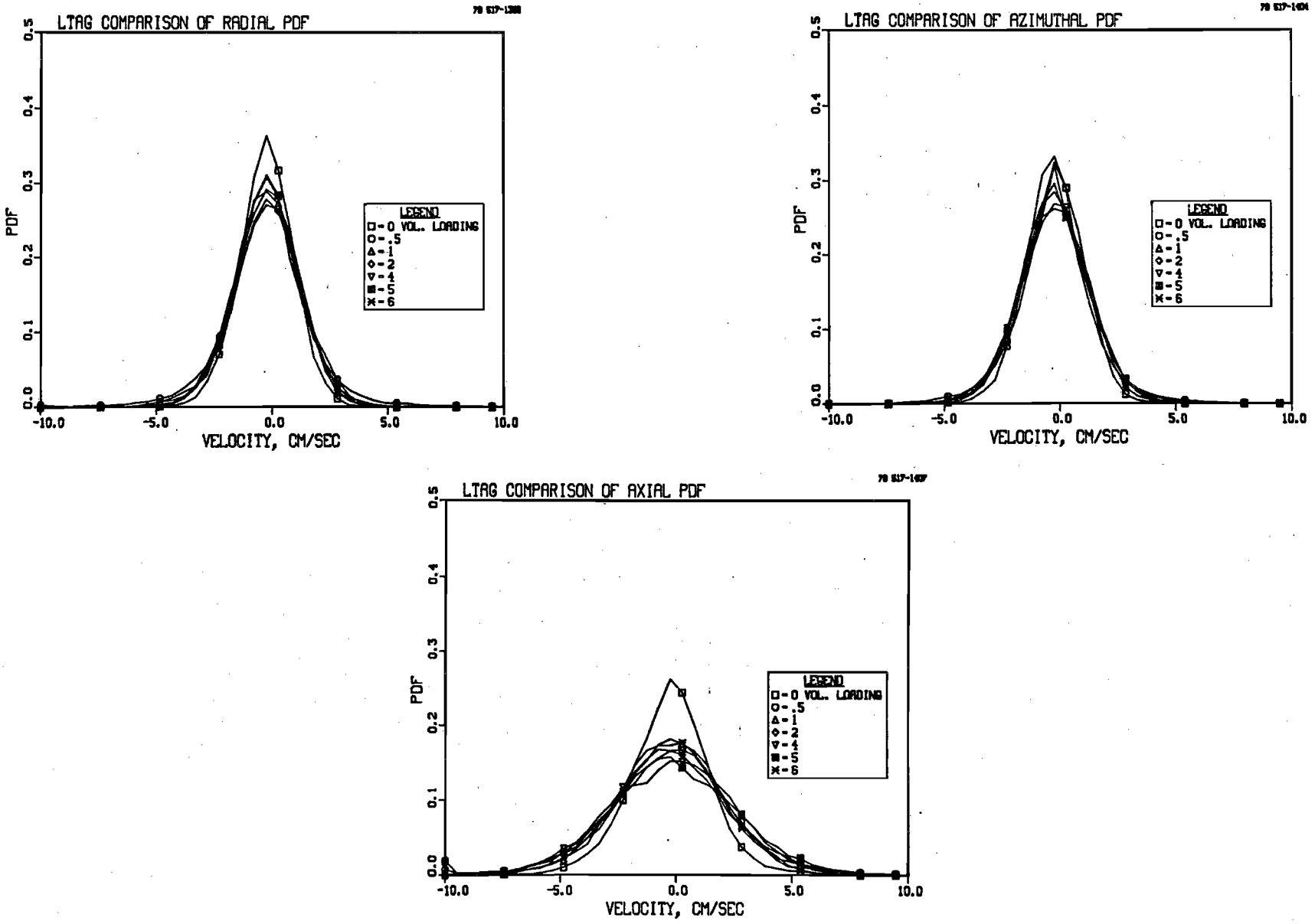

Figure 4.18 LTAG Radial, Azimuthal and Axial Comparisons of Probability Density Functions for Various Volume Loading ϕ,%

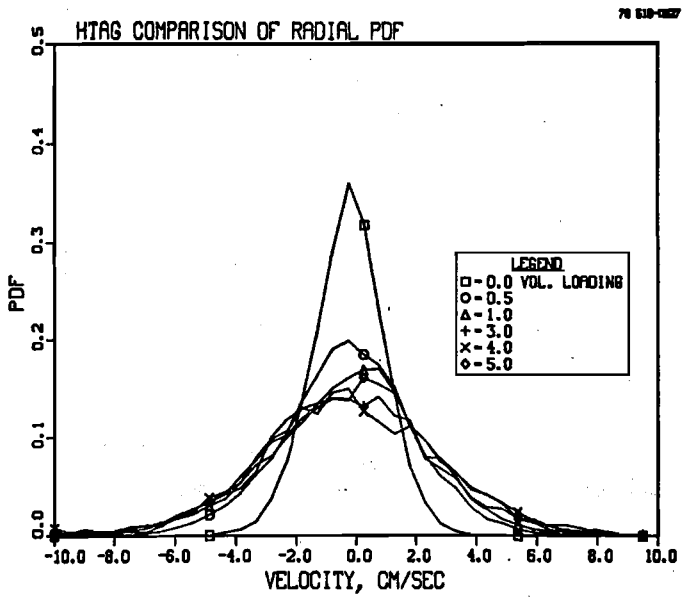

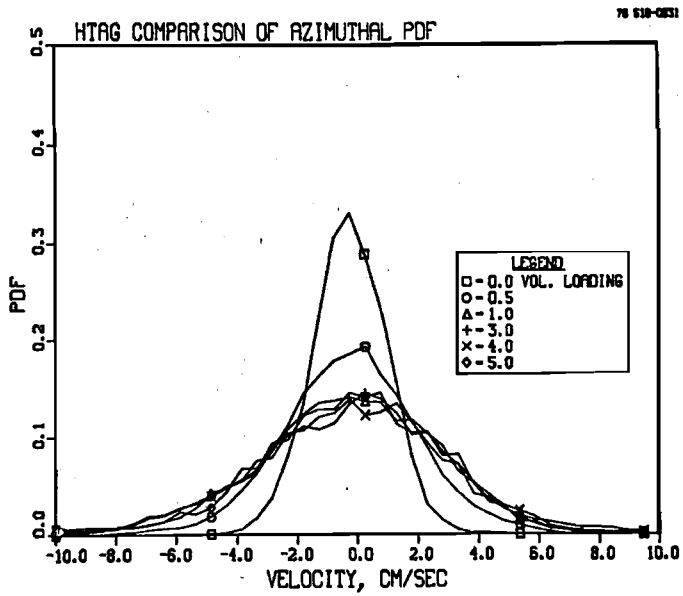

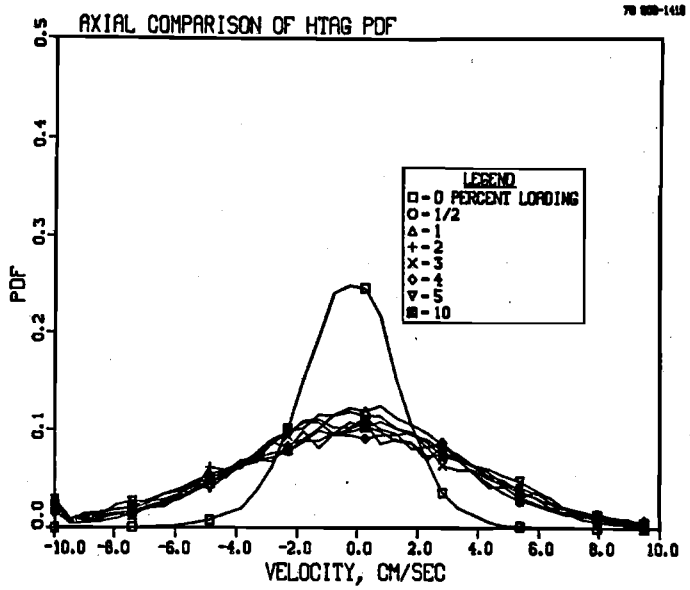

Figure 4.19 HTAG Radial, Azimuthal and Axial Comparisons of Probability Density Functions for Various Volume Loading ϕ,%

become broader as the volume loading is increased. Also the lateral and longitudinal p.d.f.'s are respectively very similar at ϕ =0, but as the loading increases the HTAG p.d.f.'s tend to be more diffuse, indicating a larger HTAG variance. This observation is in agreement with the trend of the previous rms velocity data.

A preliminary look at the velocity autocorrelations for the HTAG and LTAG series, shown in Figures 4.20 and 4.21 generally show the expected form. It was found that the autocorrelations for the LTAG 0.5, LTAG 10, HTAG 10, and HTAG 0.5 experiments showed an external noise problem. An investigation into the source of the noise, indicated that a faulty coaxial cable coming from the tape recorder to the digitizer may have provided a low level 60 Hz signal. Efforts to remove the noise proved to be successful in all but the radial autocorrelation of the LTAG 0.5 experiment.

In general, the radial and azimuthal autocorrelation for each experiment are in good agreement with each other. This once again supports the isotropic lateral behavior observed earlier. The form of the correlations areas one expect for lateral pipe turbulence. Referring to Figure 4.22 to 4.25, a comparison was made of the lateral autocorrelations at the various volume loadings. Notice the slightly lower lateral correlations for the ϕ = 0 percent case. As the volume loading is increased the lateral correlations collapse to a common curve showing little difference between them. This is also indicated by the lateral time macroscale shown in Table 4.4. It's of interest to note the LTAG series particles are correlated for longer times than the HTAG series. The macroscales show a factor of approximately equal to 2 between the LTAG and HTAG series. This is as expected, for it can be shown from Equations 2.90 and 2.94 that:

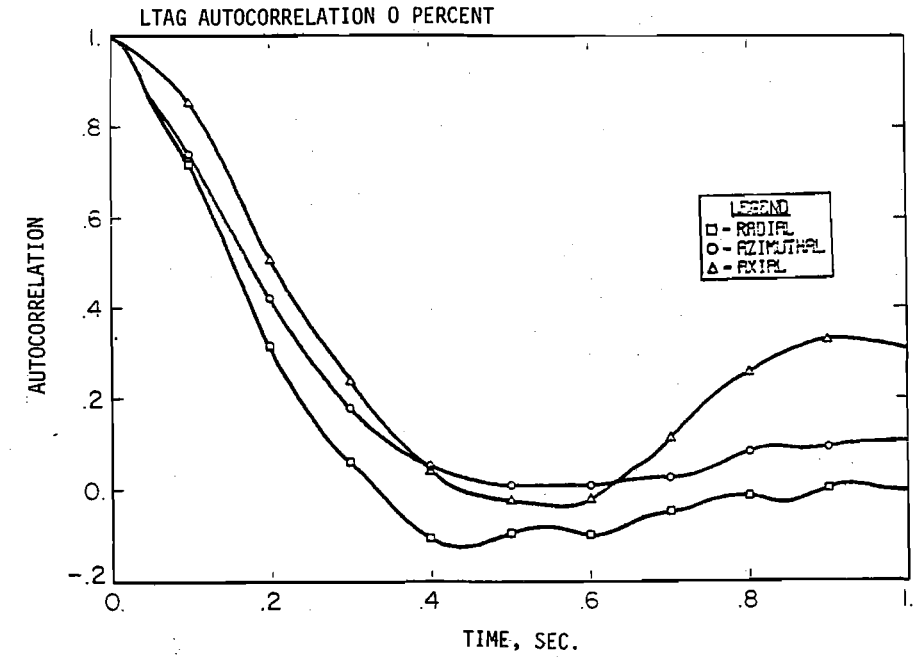

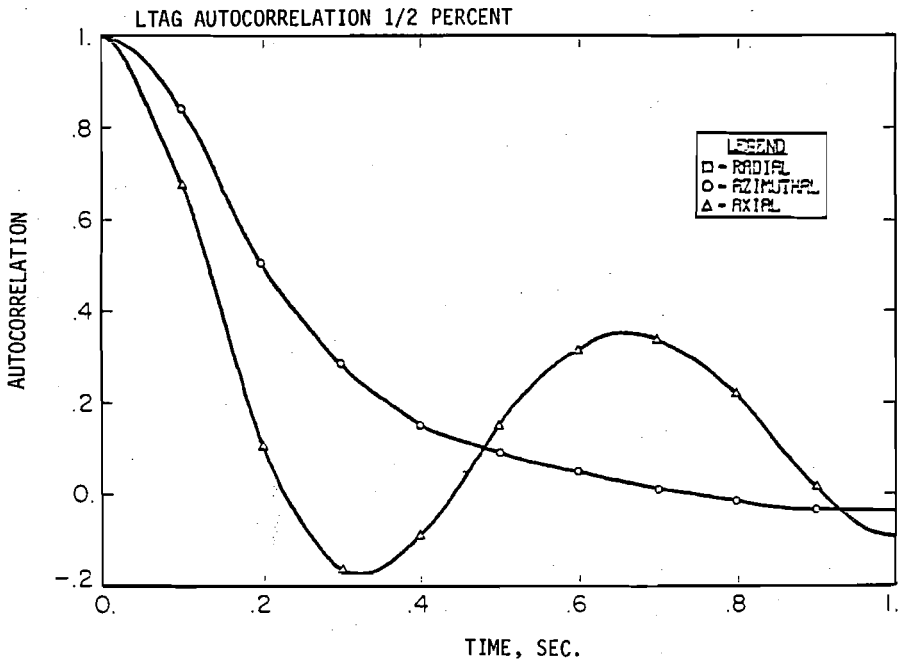

Figure 4.20a LTAG Particle Velocity Autocorrelations for ϕ Equal to 0, 1/2

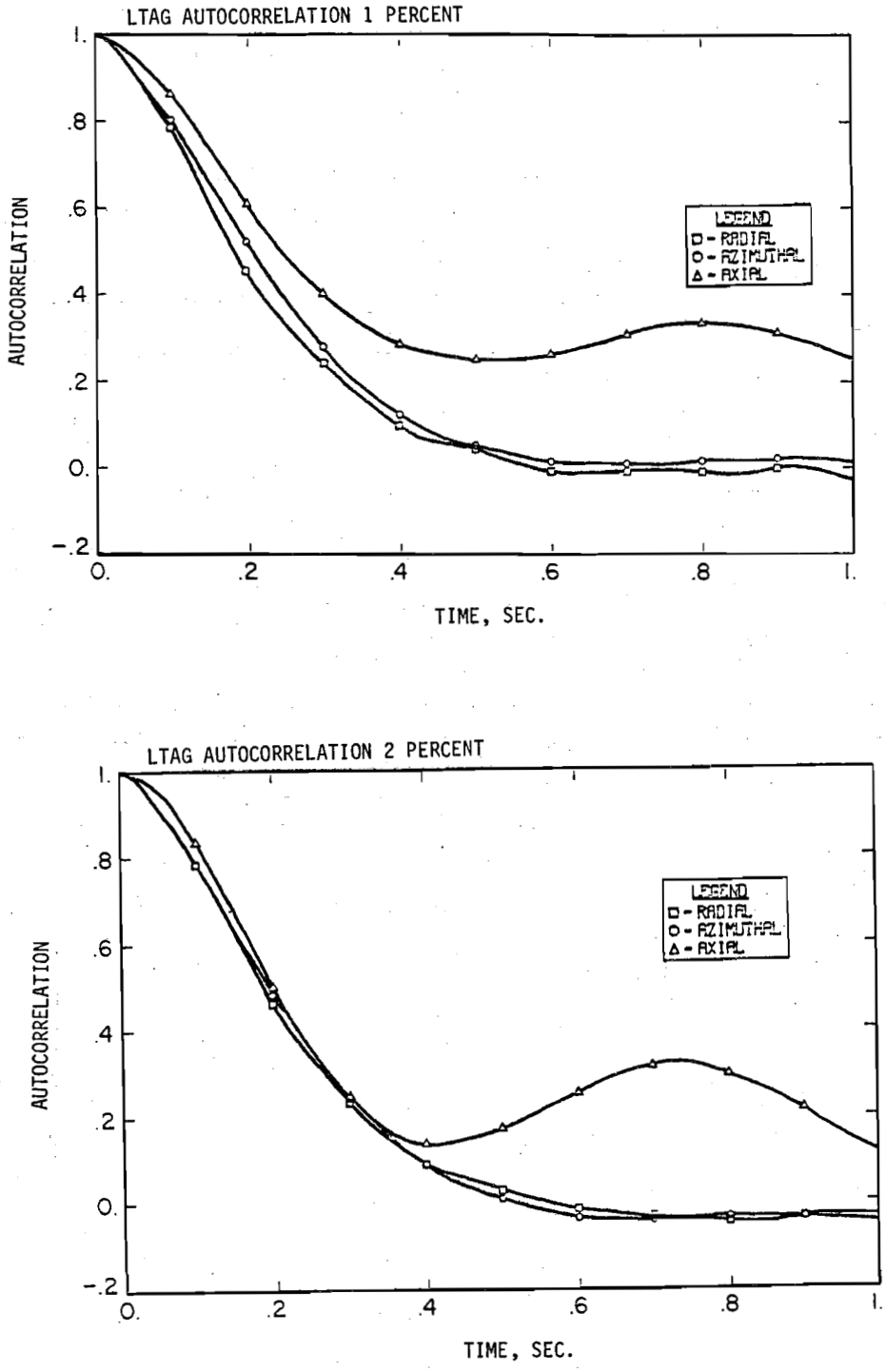

Figure 4.20b LTAG Particle Velocity Autocorrelations for ϕ Equal to 1, 2

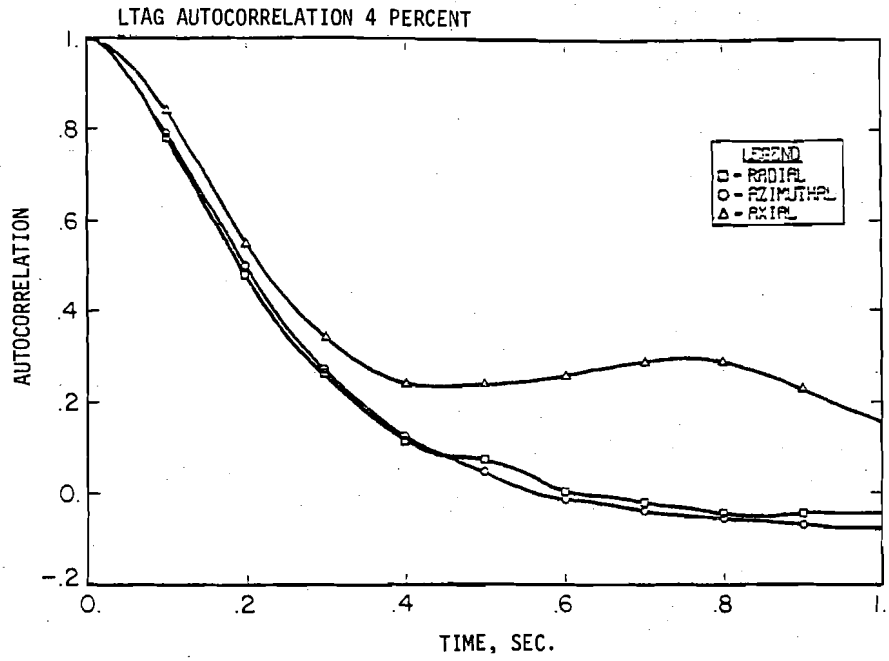

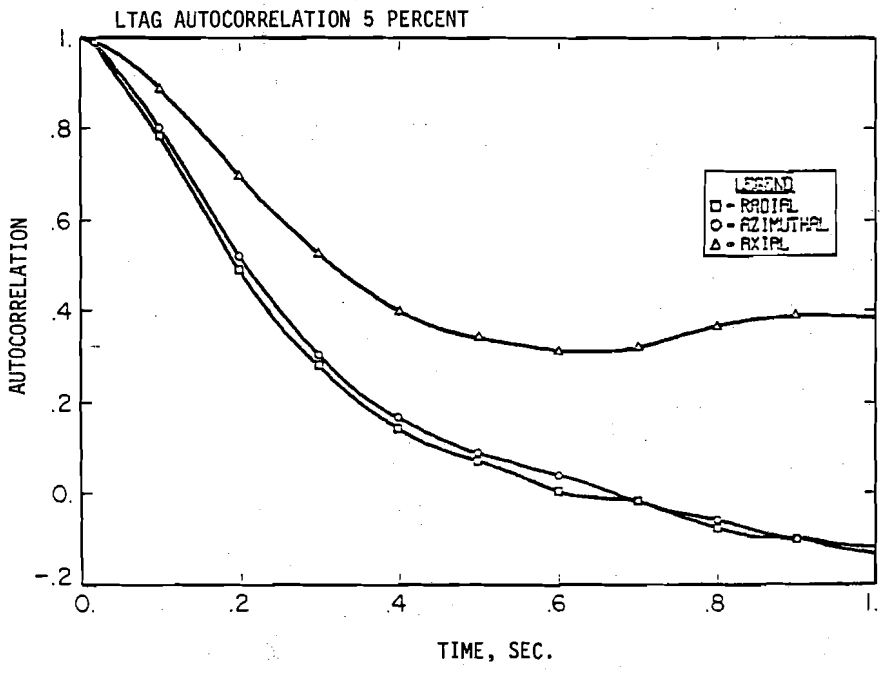

Figure 4.20c LTAG Particle Velocity Autocorrelations for ϕ Equal to 4, 5

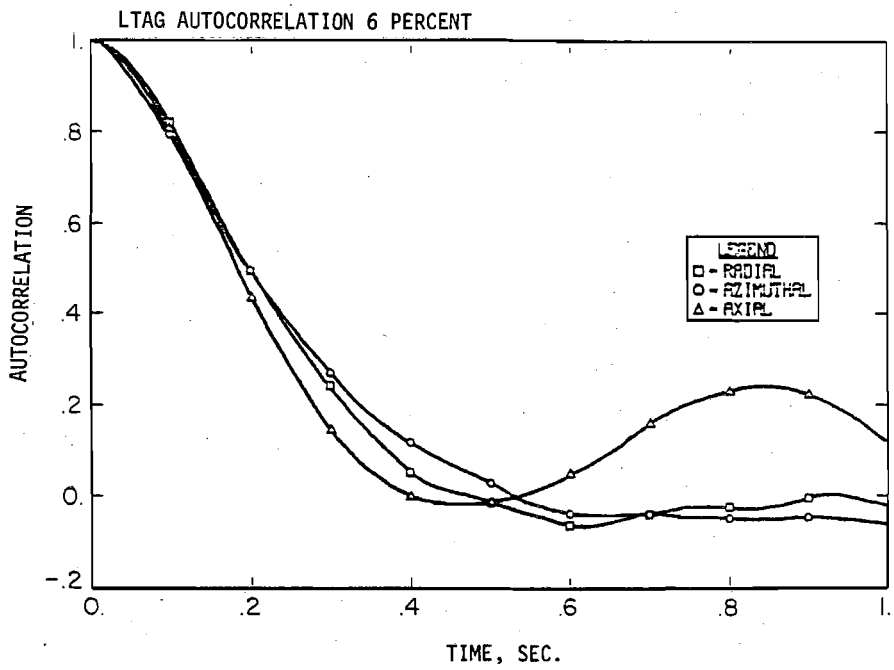

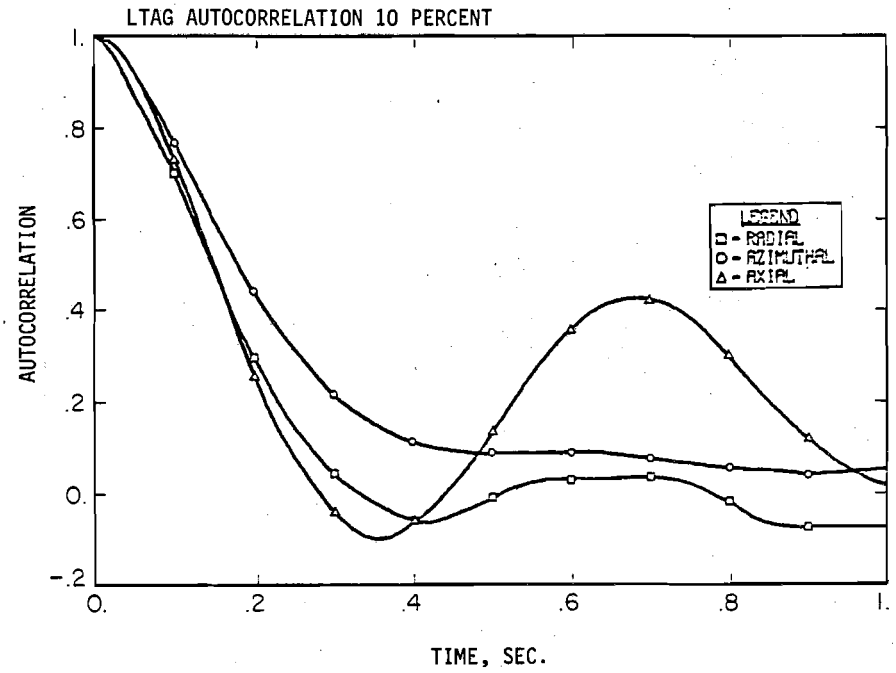

Figure 4.20d LTAG Particle Velocity Autocorrelations for ϕ Equal to 6, 10

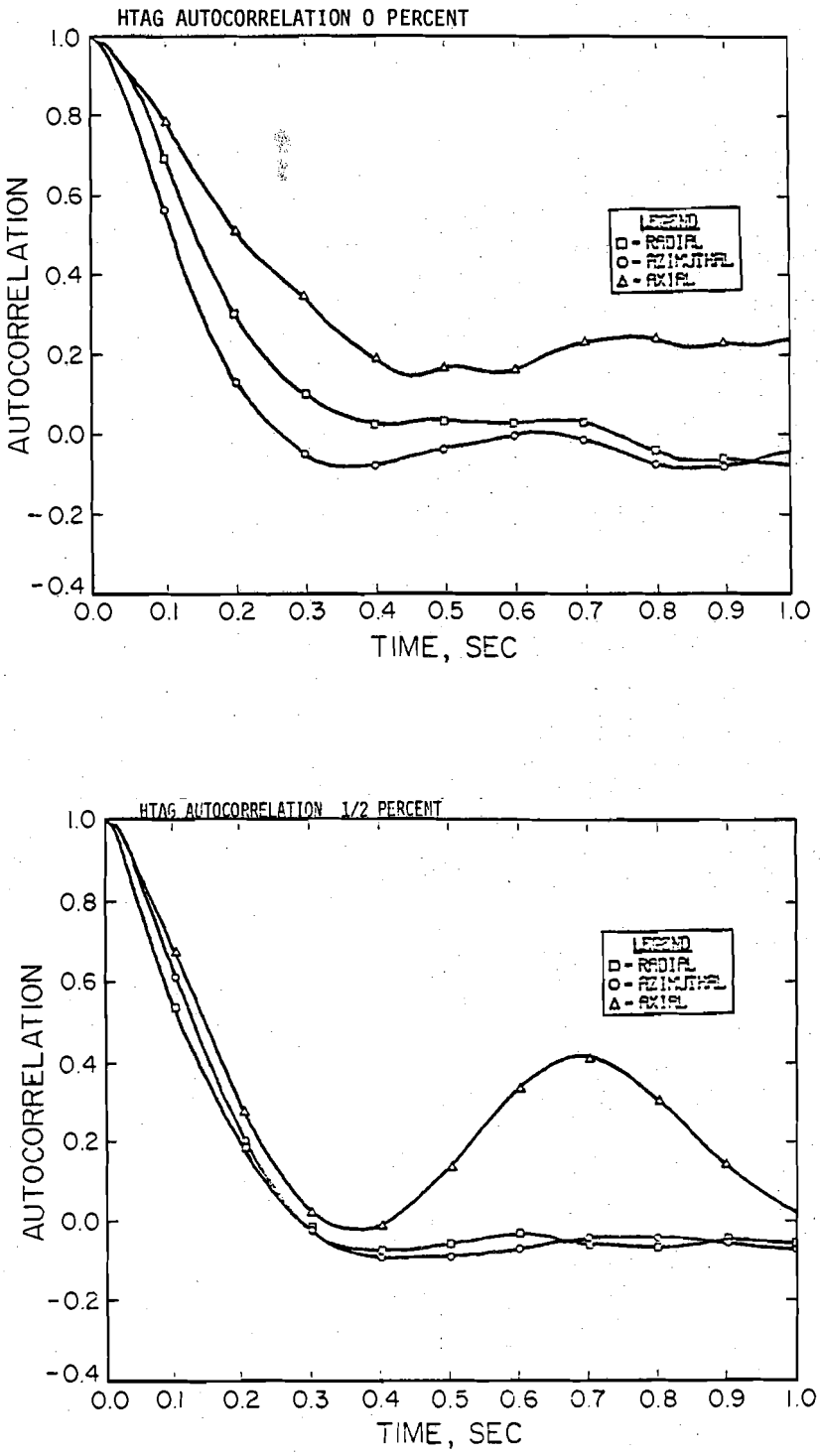

Figure 4.21a HTAG Particle Velocity Autocorrelations for ϕ Equal to 0, 1/2

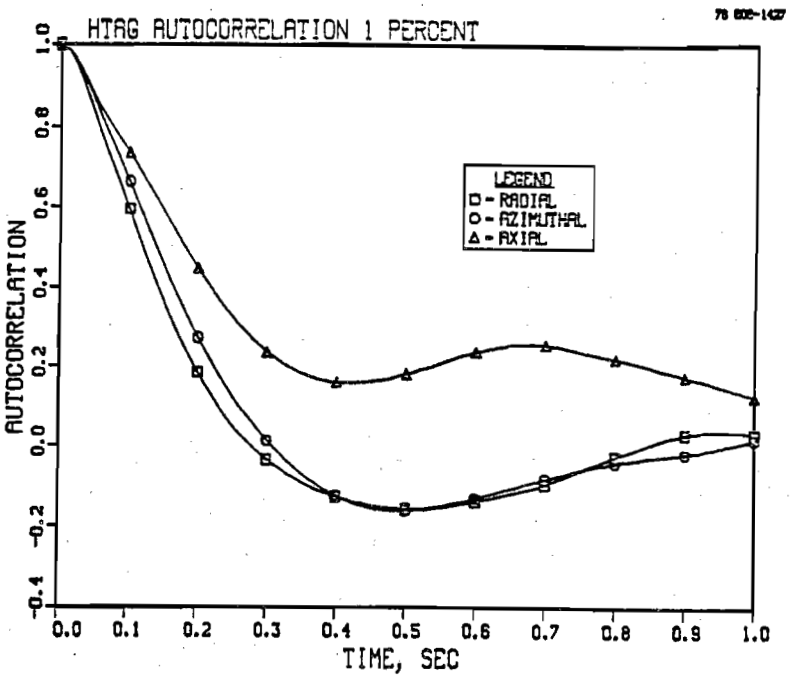

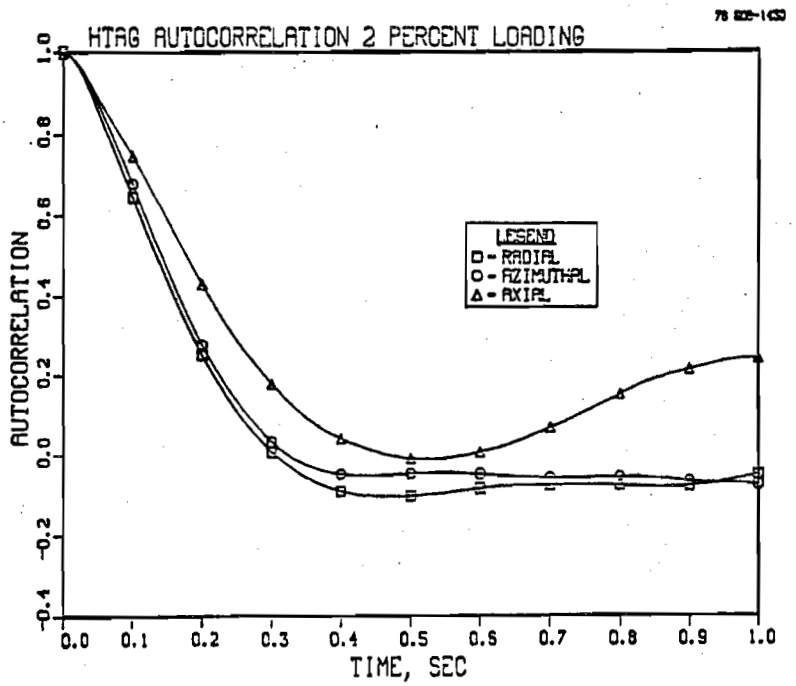

Figure 4.21b HTAG Particle Velocity Autocorrelations for ϕ Equal to 1, 2

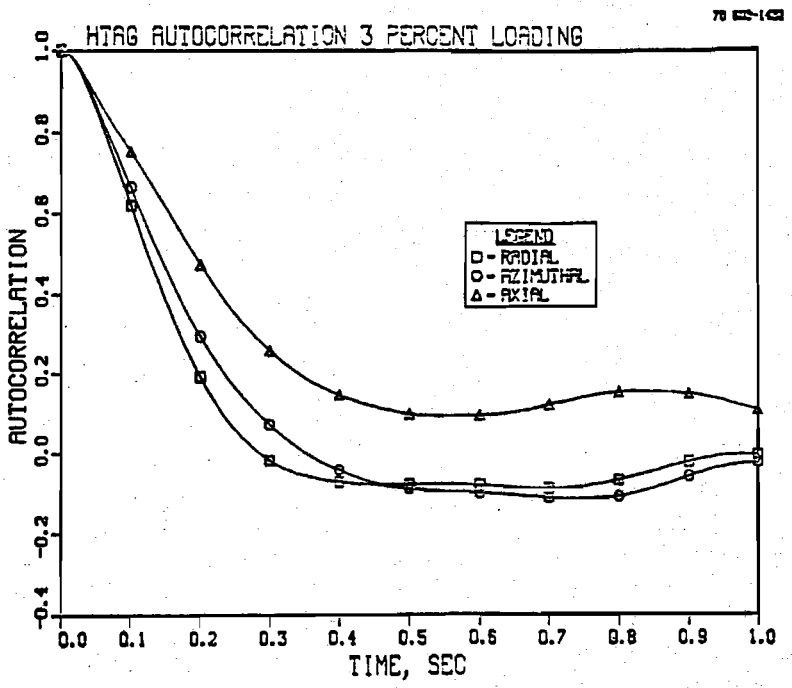

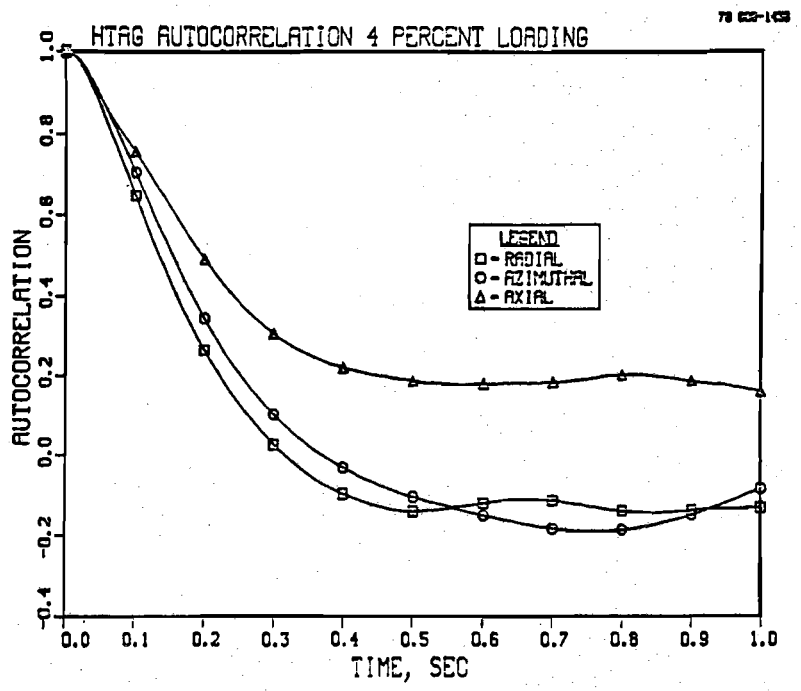

Figure 4.21c HTAG Particle Velocity Autocorrelations for ϕ Equal to 3, 4

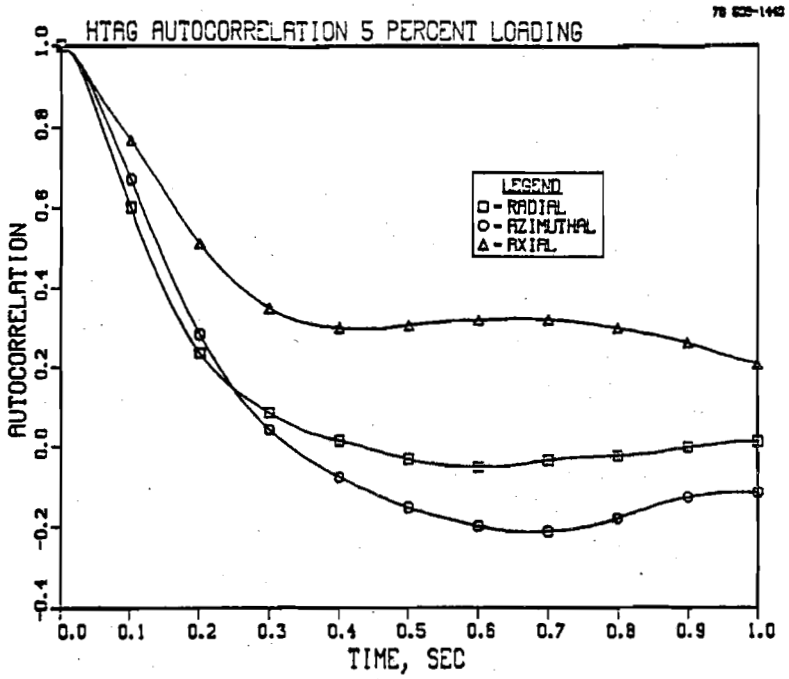

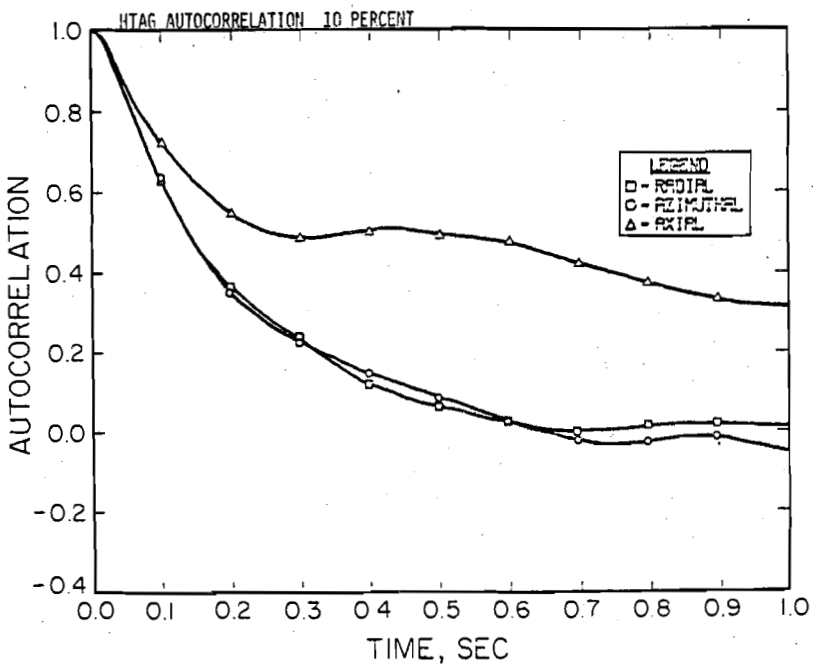

Figure 4.21d HTAG Particle Velocity Autocorrelations for ϕ Equal to 5, 10

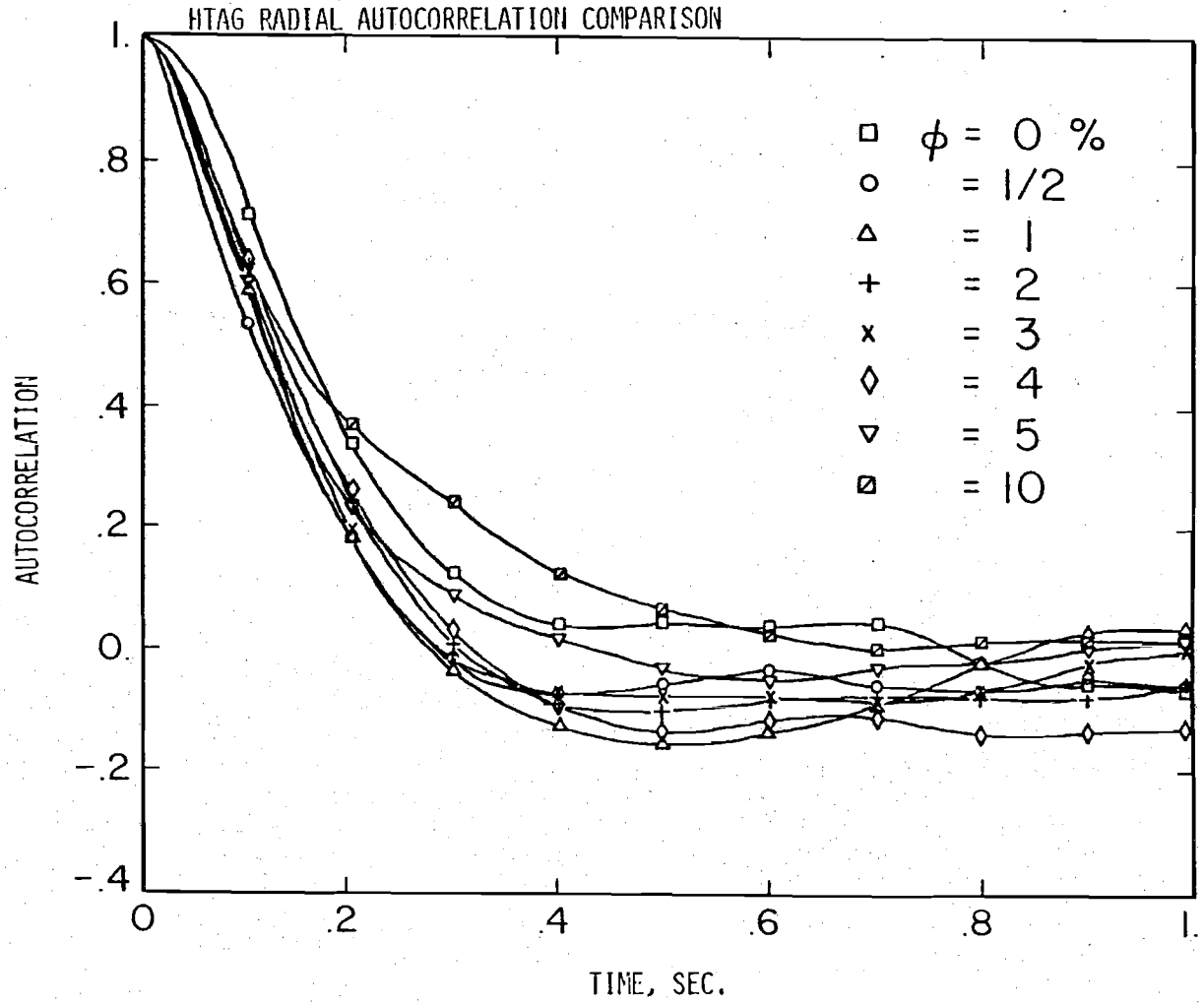

Figure 4.22 Radial Particle Velocity Autocorrelations for HTAG Series

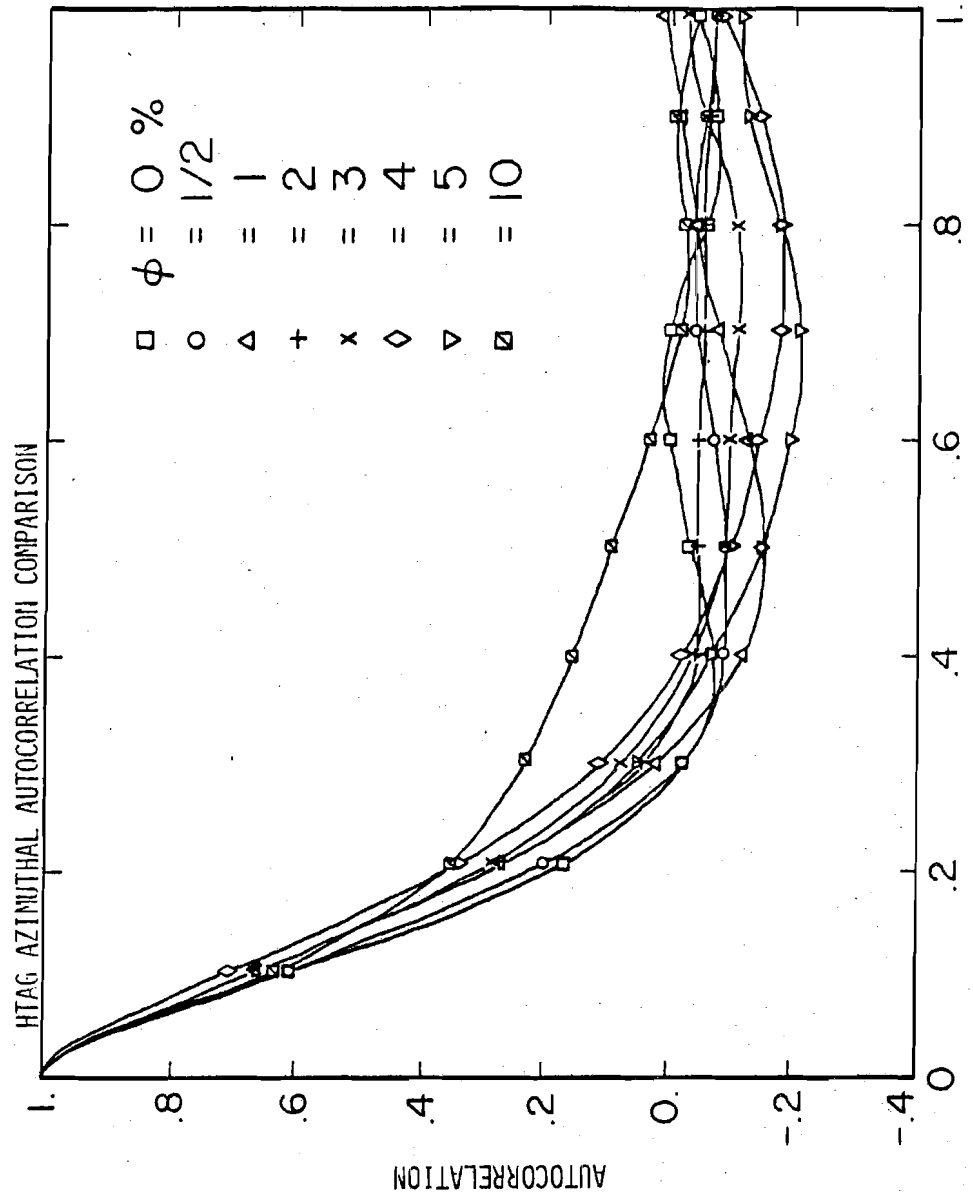

Figure 4.23 Azimuthal Particle Velocity Autocorrelations for HTAG Series

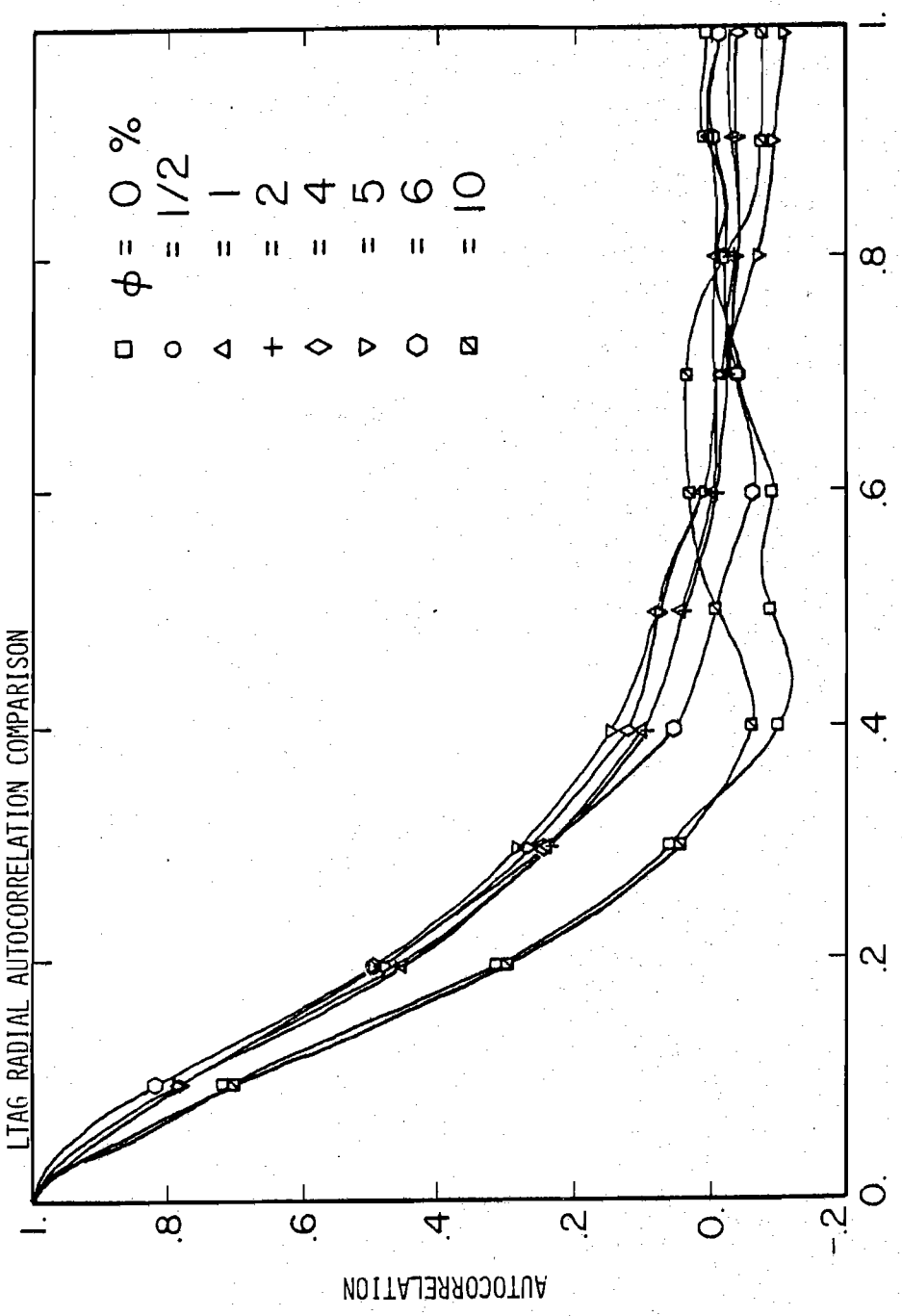

Figure 4.24 Radial Particle Velocity Autocorrelations for LTAG Series

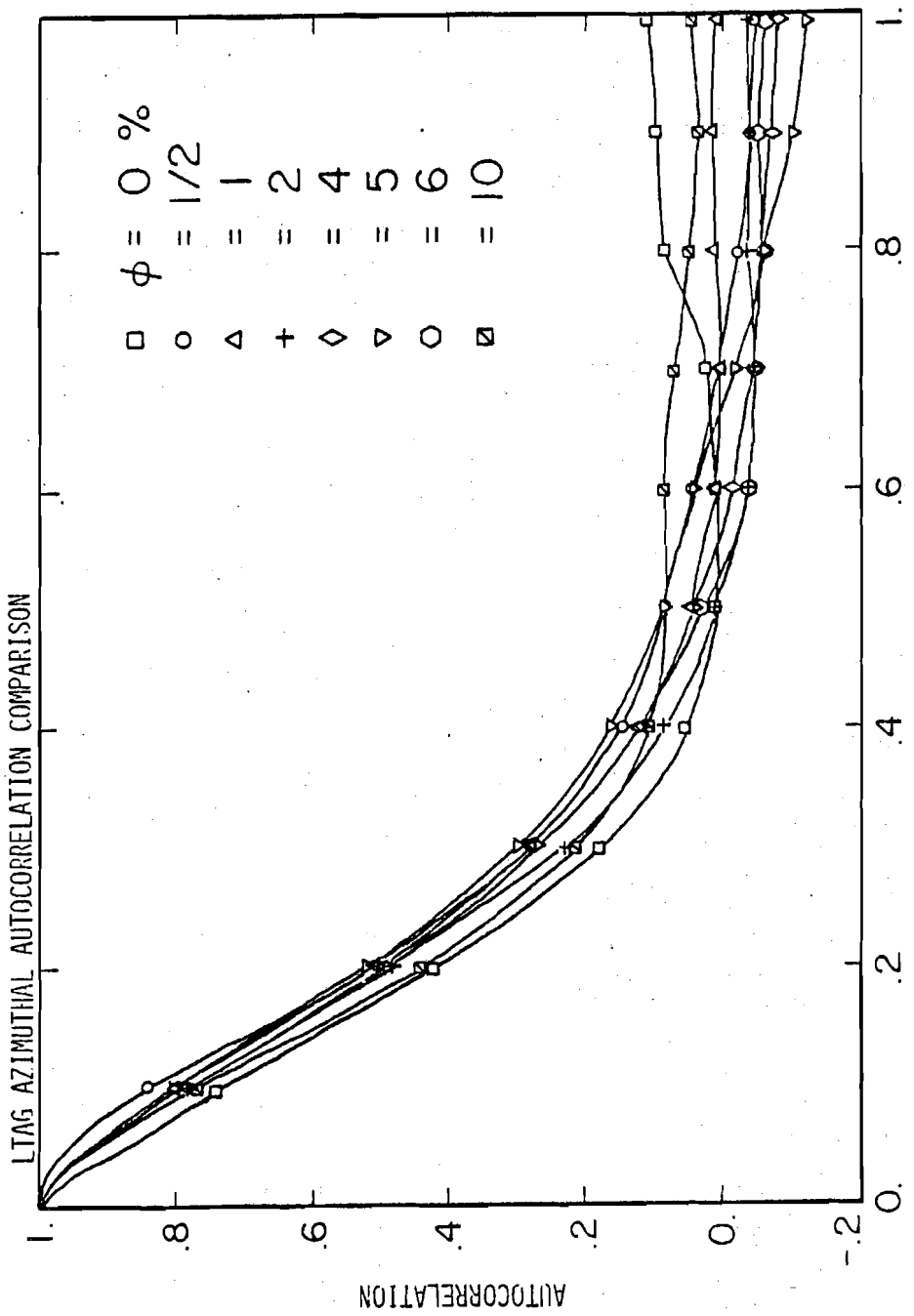

Figure 4.25 Azimuthal Particle Velocity Autocorrelations for LTAG Series

Table 4.4 Microscale and Macroscale of HTAG and LTAG Series

		MICROSCALES						MACROSCALES					
	VOLUME LOADING	RADIAL		AZIMUTHAL		AXIAL		RADIAL		AZIMUTHAL		AXIAL	
Series		HTAG	LTAG	HTAG	LTAG	HTAG	LTAG	HTAG	LTAG	HTAG	LTAG	HTAG	LTAG
	0.0	.104	.108	.091	.123	.118	.128	.134	.098	.076	.188	.276	.232
	0.5	.041	.113	.107	.140	.076	.107	.079	.126	.086	.199	.280	.175
	1.0	.110	.126	.127	.148	.152	.154	.073	.179	.088	.213	.321	.372
	2.0	.119	.133	.127	.143	.145	.157	.085	.175	.1115	.178	.243	.319
	3.0	.114		.125		.160		.0872		.099		.279	
	4.0	.117	.130	.134	.144	.157	.162	.0618	.183	.079	.185	.328	.350
	5.0	.109	.128	.126	.143	.157	.158	.1299	.177	.049	.199	.404	.456
	6.0		.132		.135		.139		.168		.179		.230
	10.0	.116	.100	.116	.122	.142	.116	.196	.107	.1875	.205	.500	.237

$$\hat{V}'_{P,z}\, \mathcal{J}_{P,r}(\Phi) = 1/2 \; \frac{U'^2_{f,r}}{V'^2_{P,r}} \; \Lambda_{f,z}(\Phi) \qquad (4.11)$$

Where $\hat{V}'_{P,z}$ is defined as $(\overline{U}^2_{P,z} + V'^2_{P,z})^{1/2}$. Since $\beta \sim 1.0$, as shown in Table 4.5 for the dynamic characteristics of the particle, it can be shown that $U'^2_{f,r}/V'^2_{P,r} \sim 1.0$ and for a given ϕ and physical system $\Lambda_{f,z}$ is invariant. Also one will note that $V'_{P,z} << \overline{U}_{P,z}$, thus $\hat{V}'_{P,z} = \overline{U}_{f,z}$. Hence we see that $\overline{U}_{P,z}(\phi)\, \mathcal{J}_{P,r}(\phi)$ equals a constant for a given volume loading. Therefore we see as $\overline{U}_{f,z}$ decreases by a factor of 2, which is approximately true between LTAG and HTAG experiments, $\mathcal{J}_{P,r}(\phi)$ is expected to increase by an equal amount.

The axial autocorrelations, shown in Figures 4.20 and 4.21, tend to show the expected form, but upon close examination one will notice a low frequency sinusoidal oscillation. The oscillation is more apparent in all the LTAG series and the HTAG 0.5 experiments. This is shown clearly in Figure 4.26 and 4.27. An intense investigation into the cause of the oscillations showed that the problem lay within the carriage velocimeter's analog signal conditioning. As one will note in Figure 3.6, the analog output from the carriages velocimeter's frequency to voltage (F/V) converter was filtered (cutoff of -36 db/octave at 10Hz). This was done to remove some high frequency ripple produced by the F/V convertor. It was found that the filter caused a phase shift in the input signal. The result of which caused a small apparent velocity to be formed during the axial particle velocity determination. The problem became especially apparent when the carriage was changing velocity. From the experimental logs compiled during the experiments, it was found that the sensitivity of the carriage tracking

Table 4.5 Dynamic Properties of LTAG, HTAG Particles

Experiment	$\overline{U}_{P,z}$	V_P'	$\xi(\phi)$	$\beta(\phi)$	R_{ep}	C_{D_T}	α
LTAG 0	5.70	5.87	.872	.968	312.3	.170	5.26
1/2	6.77	7.10	.835	.967	370.7	.121	7.32
1	6.00	6.35	.408	.966	328.6	.154	6.97
2	5.72	6.23	.453	.964	312.9	.169	7.38
4	5.12	5.68	.397	.956	281.8	.209	7.77
5	3.73	4.65	.393	.952	204.4	.398	6.07
6	4.68	5.16	.593	.948	256.1	.253	8.14
10	3.03	3.72	.730	.930	165.7	.604	6.72
HTAG 0	13.21	13.27	.351	.893	723.2	.114	12.20
1/2	14.13	14.56	.274	.893	773.6	.099	15.29
1	14.76	15.14	.212	.892	808.2	.096	17.14
2	13.67	14.21	.276	.889	749.5	.107	17.64
3	14.28	14.80	.210	.886	782.1	.098	20.07
4	12.31	12.93	.192	.883	674.0	.132	18.68
5	12.04	12.69	.148	.880	659.6	.138	19.60
10	11.12	11.78	.097	.861	608.8	.161	24.64

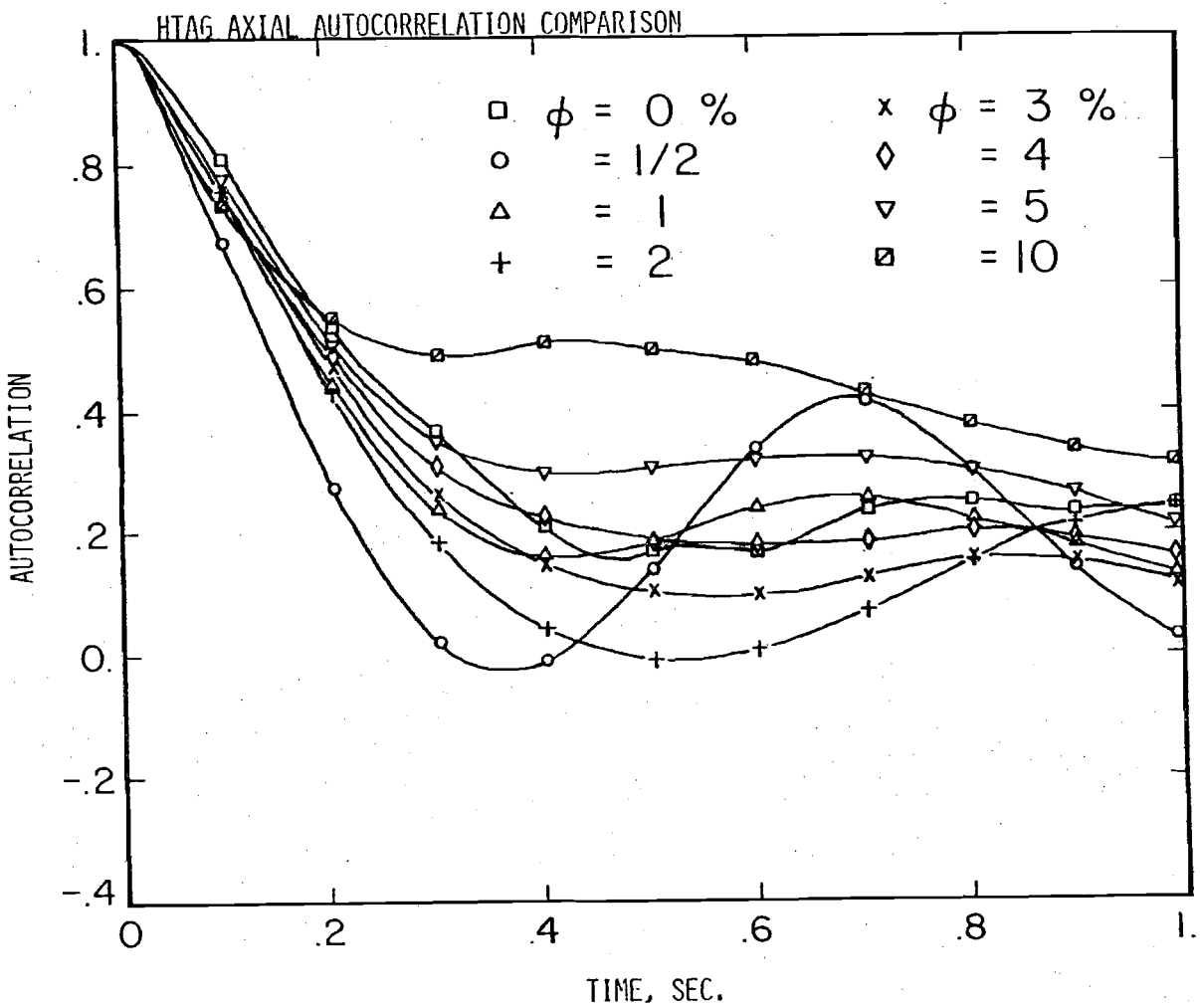

Figure 4.26 Axial Particle Velocity Autocorrelations for HTAG Series

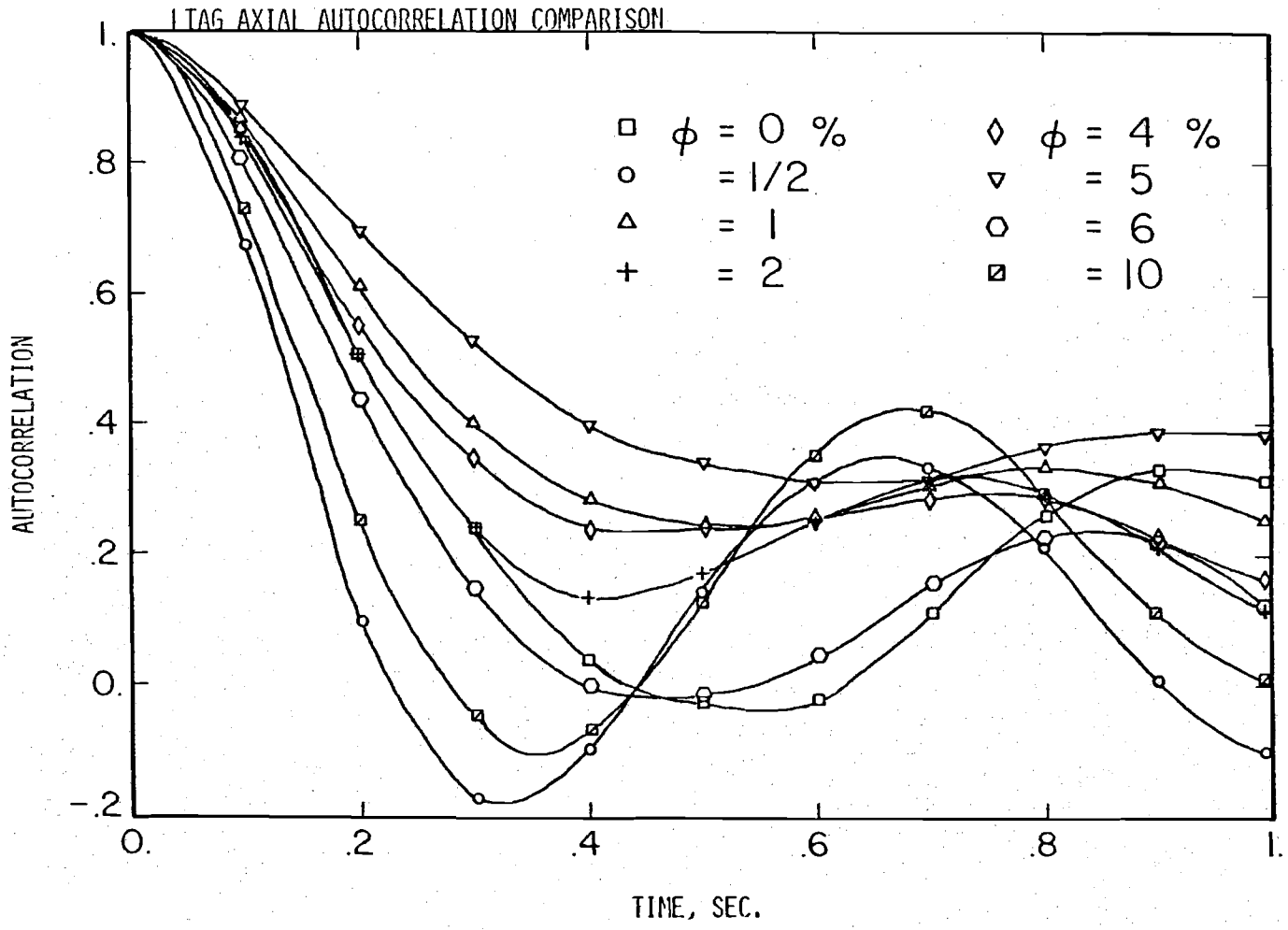

Figure 4.27 Axial Particle Velocity Autocorrelations for LTAG Series

circuits was increased for the LTAG series, HTAG 0.5 and HTAG 10 experiments. This was done to provide a smaller run rejection rate by having the carriage follow the particle closely; this compounded the phase shift problem. It was also noted, that the carriage tended to hunt the particle at a frequency of approximately 1 Hz. As can be seen in the correlations this was close to the oscillations frequency. Although no actual value may be associated with the noise magnitude, it is reasonable to say one must take it into consideration when interpreting the axial data. Qualitatively speaking, due to its cyclic behavior, one would expect the effects of this "noise" to be minimal for averaged axial quantities such as the mean position and velocity, integral scales and dispersion calculations.

With the noise problem in mind several observations may be made. In general the axial correlations for the LTAG series are longer than for the HTAG series, as is evident from the tabulated macroscales. As was shown for the lateral correlations, a similar expression may be found for the particles time macroscale, the form of which is:

$$\hat{V}'_P \, \mathcal{J}_{P,z}(\Phi) = \frac{U'^2_{f,z}}{V'^2_{P,z}} \, \Lambda_{f,z} \qquad (4.12)$$

Once again the same arguments hold for the axial case as they did for the lateral case, and one finds larger correlations for the slower particles. It is interesting to note that the lateral integral scales are smaller than the axial scales. This can be seen directly from Equations 4.11 and 4.12. Solving Equation 4.11 and 4.12 for the fluids spatial scale and equating them we would find:

$$\mathcal{J}_{P,z}(\Phi) = 2 \, \frac{V'^2_{P,z}}{V'^2_{P,r}} \, \frac{U'^2_{f,r}}{U'^2_{f,z}} \, \mathcal{J}_{P,r}(\Phi) \qquad (4.13)$$

Now for an isotropic fluid $U'^2_{f,r}/U'^2_{f,z} = 1$, from experimental results we see $V'^2_{p,z} \sim V'^2_{p,r}$. Thus we find that $\mathcal{J}_{p,z}(\phi) \approx 2\,\mathcal{J}_{p,r}(\phi)$. As shown in Figure 4.28, the actual $\mathcal{J}_{p,z}/\mathcal{J}_{p,r}$ is in general larger than predicted, but one must take into account the axial noise's possible effect in determining the rms axial velocity and axial macroscale.

It is apparent from U'^2_f/V'^2_p, that if the particle variance is known, then the fluid variance may be calculated. Using Howard's (1974) experimental data, Meek (1978) has provided evidence to support this calculation. The particles Howard used in his experiments had a β very close to unity, hence the fluid-particle variance ratio, U'^2_f/V'^2_p, was equal to 1. Meek determined intensities for the lateral particle velocity as

$$I_p = \frac{U'_p}{\overline{U}_{f_c}} \tag{4.14}$$

where $\overline{U}_f$ was the centerline mean fluid velocity, and U'_p, the average lateral rms velocity, defined as:

$$U'^2_p = (V'^2_{p,r} + V'^2_{p,\theta})/2 \tag{4.15}$$

It was assumed that the intensity measurement was made at the mean radial position of the particle. Figure 4.29 shows a comparison between the measured fluid intensity and the lateral particle intensities. As one can see, excellent agreement exists between the fluid and particle intensities.

For the present experiments the lateral particle variances were used to calculate a particle intensity as:

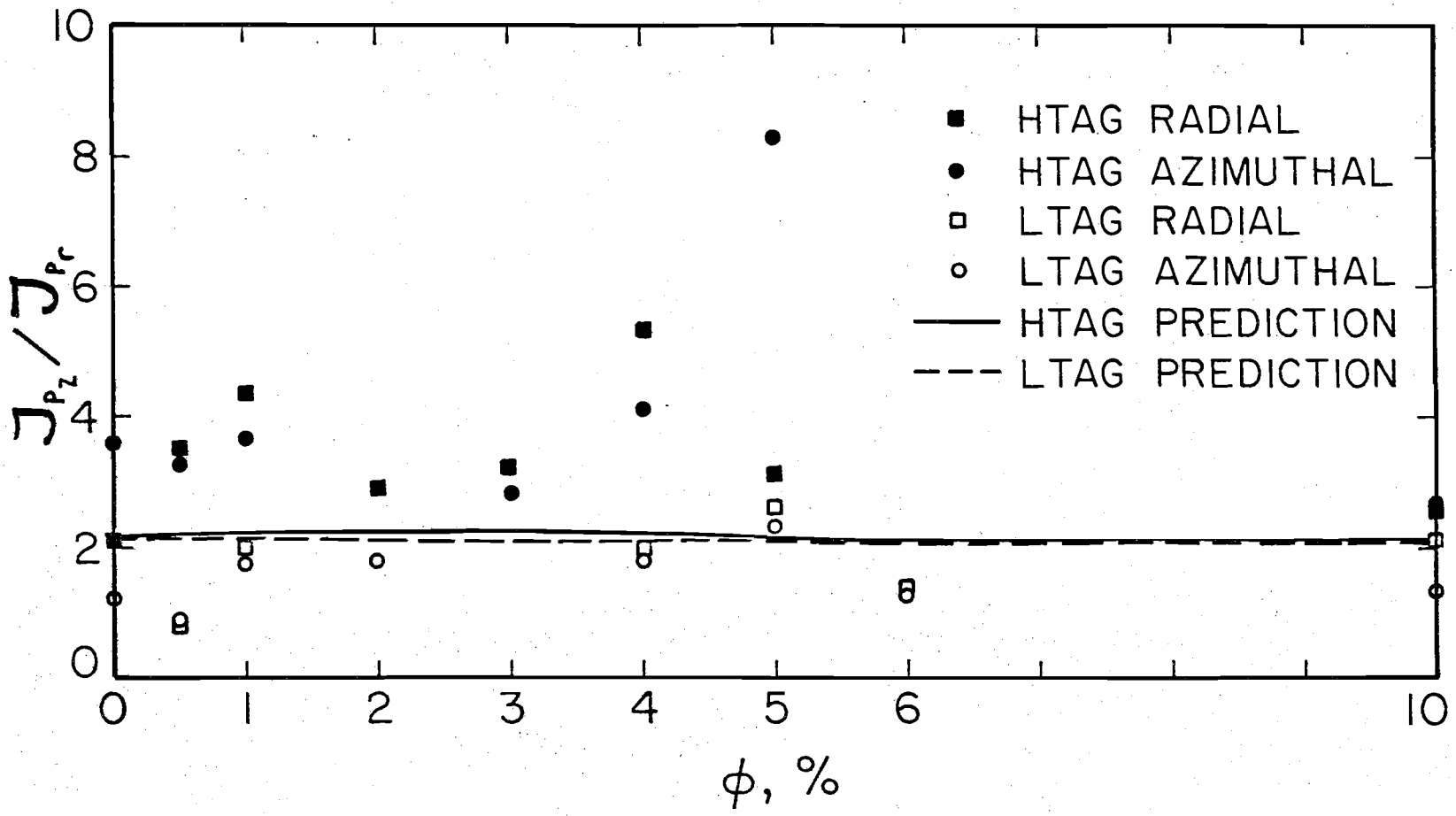

Figure 4.28 Particle Time Integral Scale Ratio, $J_{P,z}(\phi)/J_{P,r}$, for Various Volume Loading ϕ,%

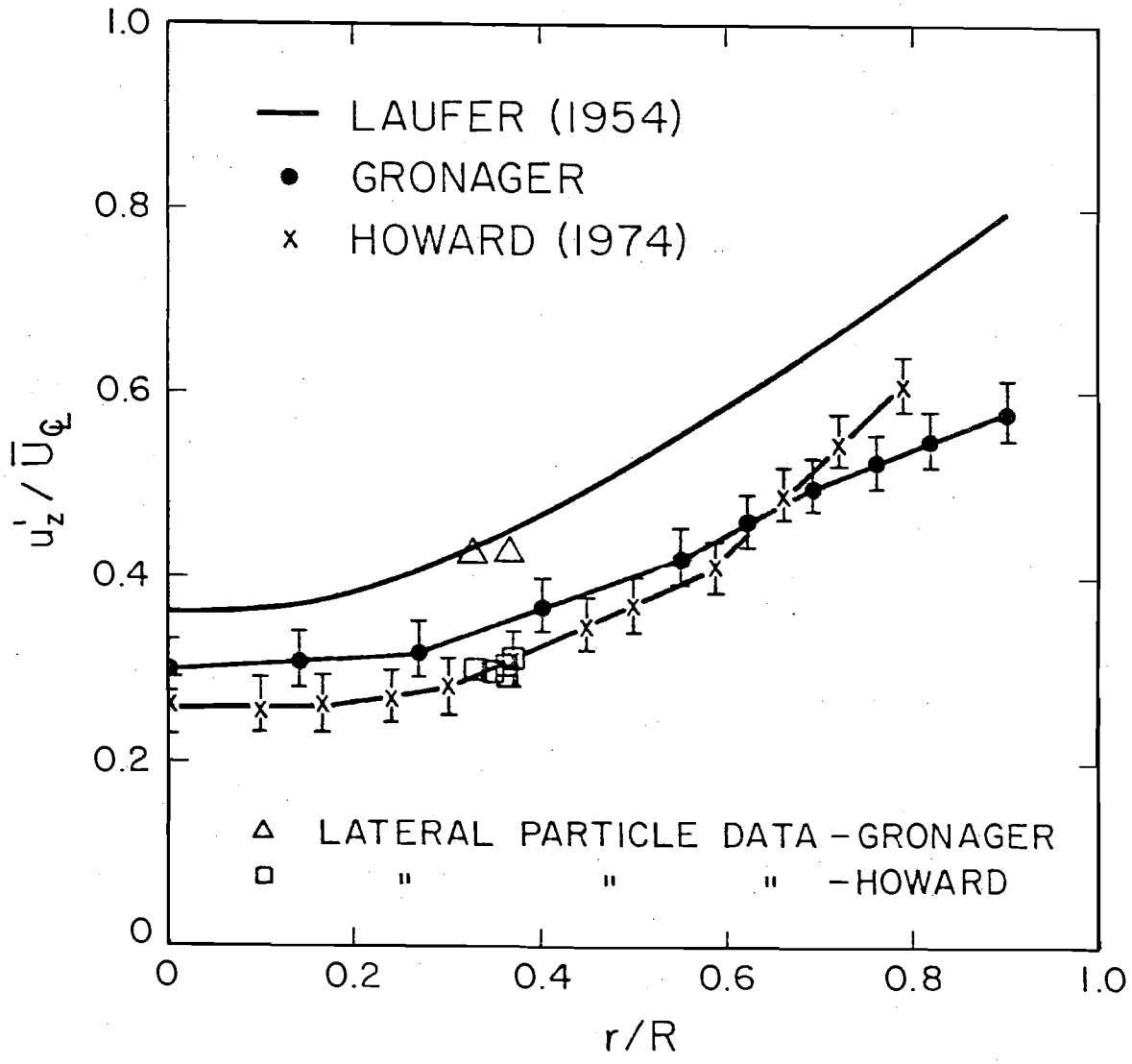

Figure 4.29 Comparison of Lateral Particle and Fluid Intensities for $\phi = 0$

$$I = U_p^{*\prime}(\phi) / \overline{U}_{f_\ell} \tag{4.16}$$

where $U_p^{*\prime}(\phi)$ was determined by:

$$U_p^{*\prime 2}(\phi) = \frac{U_{f,r}^{\prime 2}(\phi)}{V_{P,r}^{\prime 2}(\phi)} \; V_{LAT}^{\prime 2}(\phi) \tag{4.17}$$

where:

$$V_{LAT}^{\prime 2}(\phi) = \left[V_{P,r}^{\prime 2}(\phi) + V_{P,\theta}^{\prime 2}(\phi) \right] / 2 \tag{4.18}$$

Although the same calculation could be performed using the axial particle variance, $U_{P,z}^{\prime 2}$, it was felt that the axial noise, inherent in the particle variance, would not provide the best estimate of the fluid's intensity at various volume loadings. For the case where ϕ equals zero, we see good agreement with the fluid data as shown in Figure 4.29. Extending this concept for non-dilute suspensions yields an estimate for the fluid intensity as a function of ϕ. This is shown in Figure 4.30. It is interesting to note the same trend exists for both experimental series, with the effects of the free fall particle velocity playing an important role in the fluid's turbulent characteristics. It should be pointed out once again that for the very dilute suspensions ($\phi \sim 0$), the intensities are the same, showing the insensitivity of the particle free-fall velocity in determining the fluid's intensities, but as the volume loading is increased the effects of the free fall velocity become apparent. The higher fluid's intensity for the faster free fall particles may be a direct result, as Hinze points out, of a combined effect from the wakes of the spheres and to a lesser extent the shear experienced by the fluid as it passes through the particle suspension.

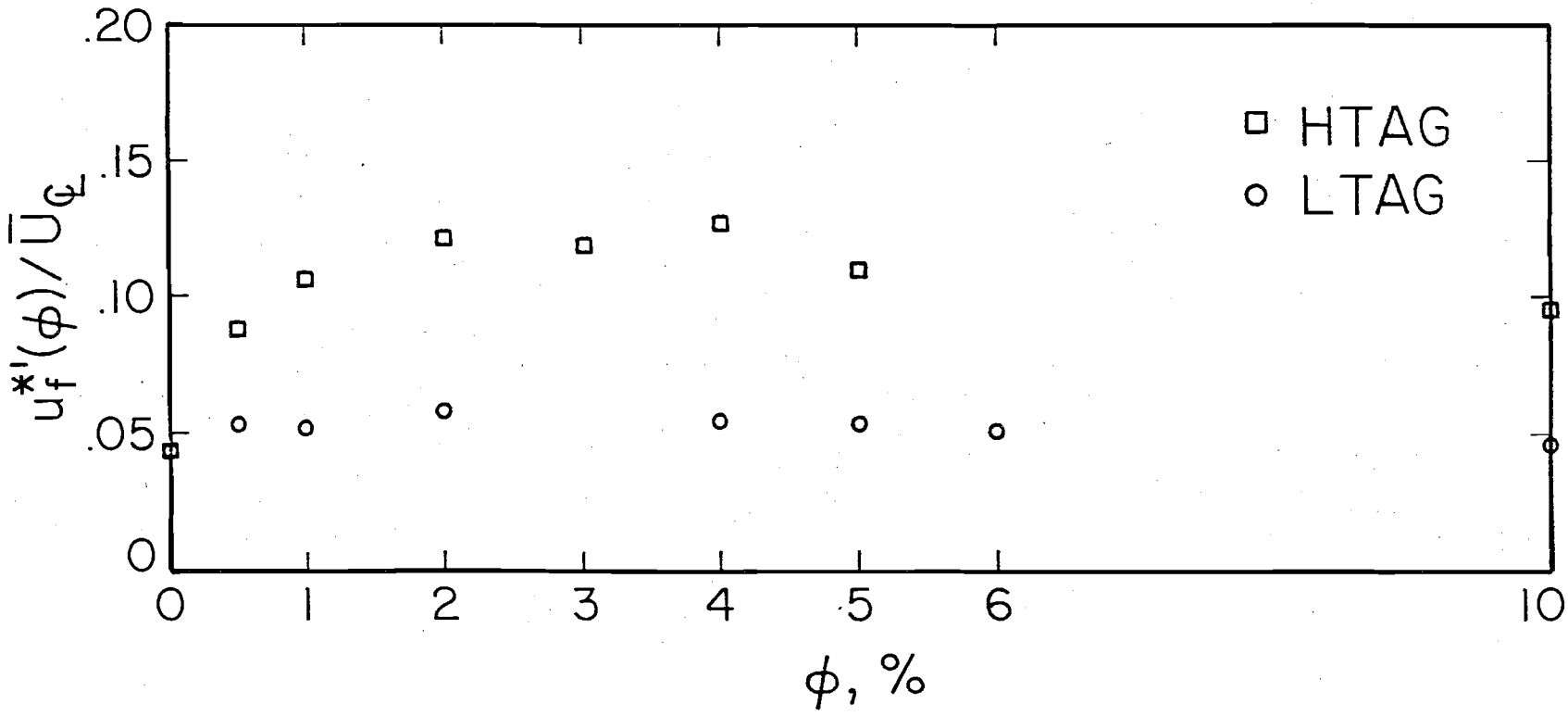

Figure 4.30 Estimated Fluid Intensity at Various Particle Volume Loading ϕ,%

As one would expect, the slower particles have smaller effect on the fluid's characteristic. This can be seen in the limit for neutrally buoyant particles where the wake effects would be negligible.

In addition to the fluid's intensity, an estimate of the fluid's axial integral scales can be made from the particles' data. From Equations 4.11 and 4.12, we see that the axial and lateral particle time macroscale may be used to determine the fluid spatial scales $\Lambda_{f,z}(\phi)$, such that:

$$\Lambda_{f,z}(\phi) = 2\,\hat{V}'_{p,z}\;\mathcal{T}_{p,r,\theta}(\phi)\;\frac{V'^2_{p,r}}{U'^2_{f,r}} \tag{4.19}$$

$$\Lambda_{f,z}(\phi) = \hat{V}'_{p,z}\;\mathcal{T}_{p,z}(\phi)\;\frac{V'^2_{p,z}}{U'^2_{f,r}} \tag{4.20}$$

Once again lateral data, obtained from Howard's experiments, was used to calculate the fluid's spatial scales for ϕ equal to zero. As shown in Figure 4.31, good agreement exists between the calculated scales and the convective scales Λ_z, determined from two point hot film anemometer data by Howard. With this in mind, estimates of the fluid's spatial scales for the non-dilute suspension case were made using both the lateral and longitudinal time macroscale scales. The results of which are shown in Figure 4.32. It is difficult to draw any concrete conclusion from these calculations, other than the scales are widely scattered about the 2.5 cm region, with the HTAG longitudinal scales displaying larger values. As input to the autocorrelation functions presented in Chapter 2, the fluid time macroscale, $T_{f,z}$, properly scaled for the suspended particle is required. Referring to Figure 4.33 one can see in comparison a slightly smoother trend of fluid's integral scale data.

Using the particle's physical characteristics and the input parameters

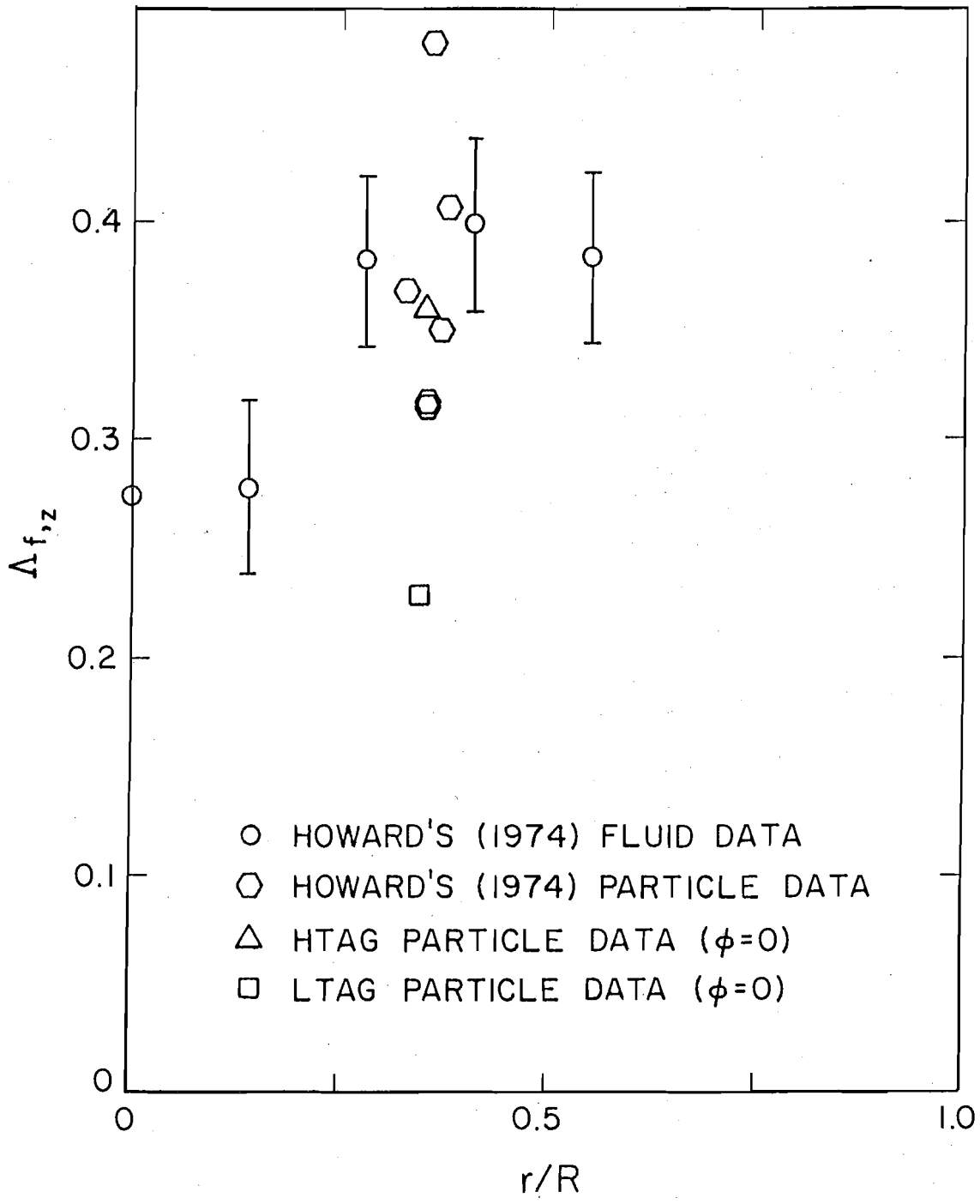

Figure 4.31 Comparison of Lateral Particle Data and Fluid Spatial Integral Scale

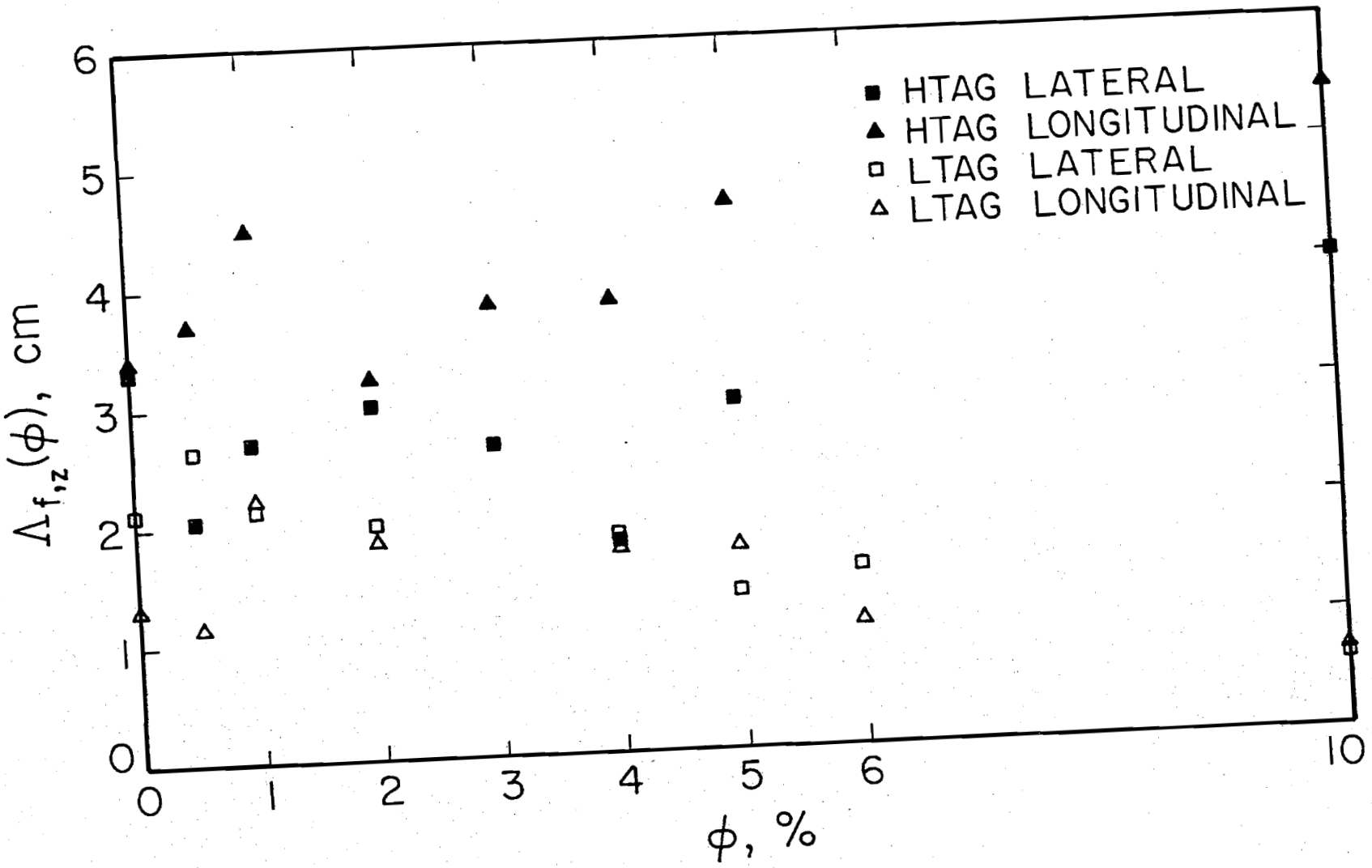

Figure 4.32 Estimated Fluid Spatial Scale for Various Particle Volume Loading ϕ,%

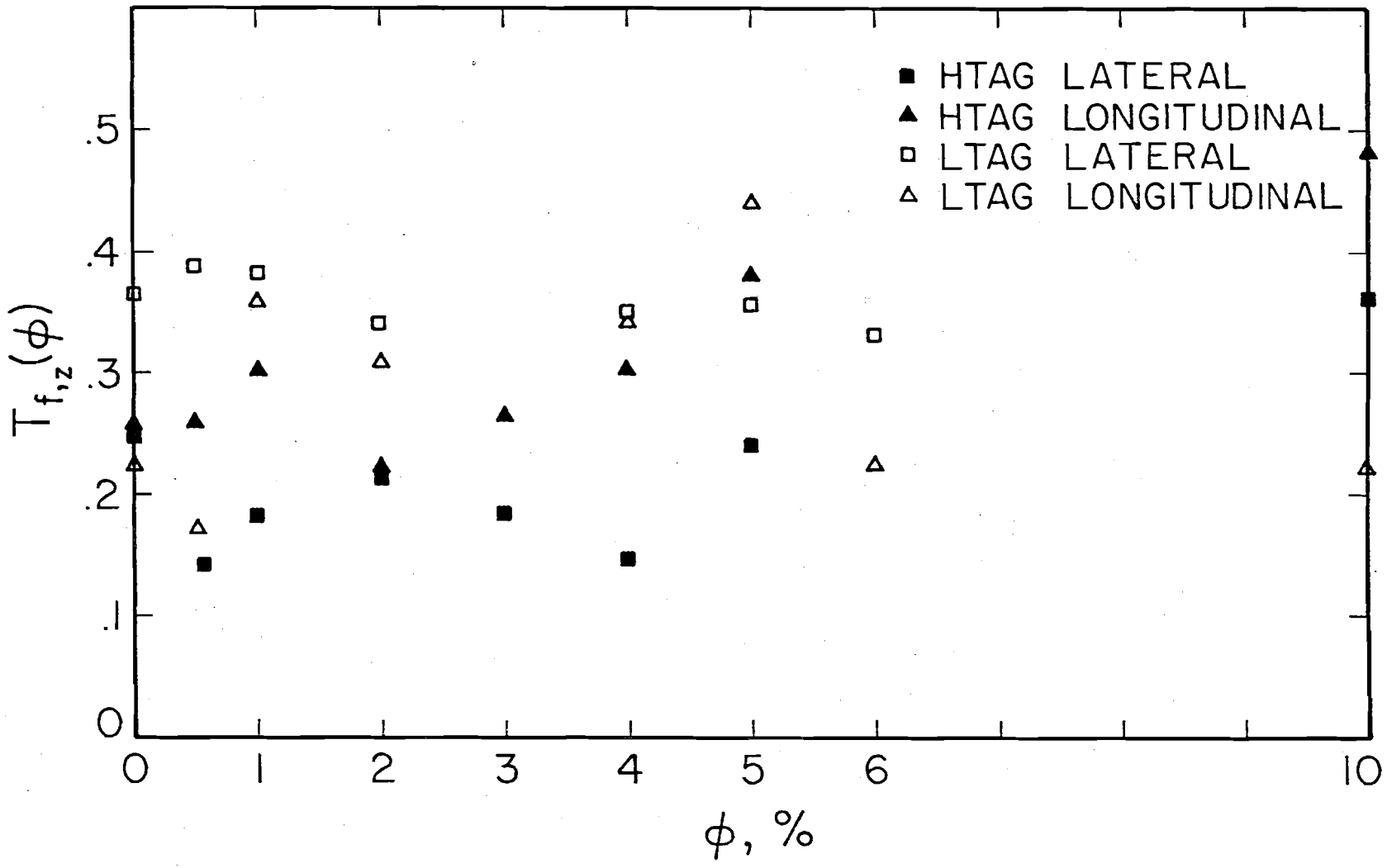

Figure 4.33 Estimated Normalized Fluid Integral Scale $T_{f,z}(\phi)$, at Various Volume Loading ϕ,%

shown in Table 4.6, autocorrelation functions were generated using the Newton's law region model described in Chapter 2. The resultant comparison is shown in Figures 4.34.

In general one can see that the lateral prediction shows reasonable agreement with experiment. Based on the model's assumption of an exponential Lagrangian fluid autocorrelation, poor agreement exists for small lagtime τ. This characteristic is inherent in the model.

Itis difficult to assess the performance of the longitudinal predictions; due to the apparent noise associated with the axial velocity data.

The application of the theory, developed in Chapter 2, was in its ability to predict the dispersion of the particles at various volume loadings. Thus a comparison was made of the particles dispersion $\overline{X_p^2}(t)$, as calculated from experimental data, and that predicted by Equations 2.93 and 2.94. The experimental particle dispersion was calculated, as was the theory, using from the particles autocorrelation in the following manner:

$$\overline{X_p^2}(t) = 2V_p'^2 \int_0^t (t-\tau) R_p(\tau) d\tau \qquad (4.21)$$

This was first shown by Kampé de Fériet (1939) for earlier work by Taylor (1921).

A comparison is shown in Figures 4.35 to 4.38 for several volume loadings of both the LTAG and the HTAG series. In general good agreement is seen for both experimental series. It should be noted that the dispersion is directly related to the autocorrelation functions used by the theory and obtained in the experiment, in that $\overline{X_p^2}(t)$ is an integral quantity of the autocorrelation as demonstrated by:

Table 4.6 Input Parameter in Theory

Experiment	U'_f/U_{ℓ}	$f(\phi)$	$T_{f,z}(\phi)$
LTAG ϕ	.0427	5.70	.225
1/2	.0531	6.77	.170
1	.0525	6.00	.364
2	.0573	5.72	.310
4	.0557	5.12	.339
5	.0543	3.73	.440
6	.0505	4.68	.219
10	.0475	3.03	.219
HTAG 0	.0437	13.21	.261
1/2	.0867	14.13	.267
1	.1065	14.76	.309
2	.1206	13.67	.231
3	.1194	14.28	.268
4	.1261	12.31	.315
5	.1117	12.04	.391
10	.0940	11.12	.487

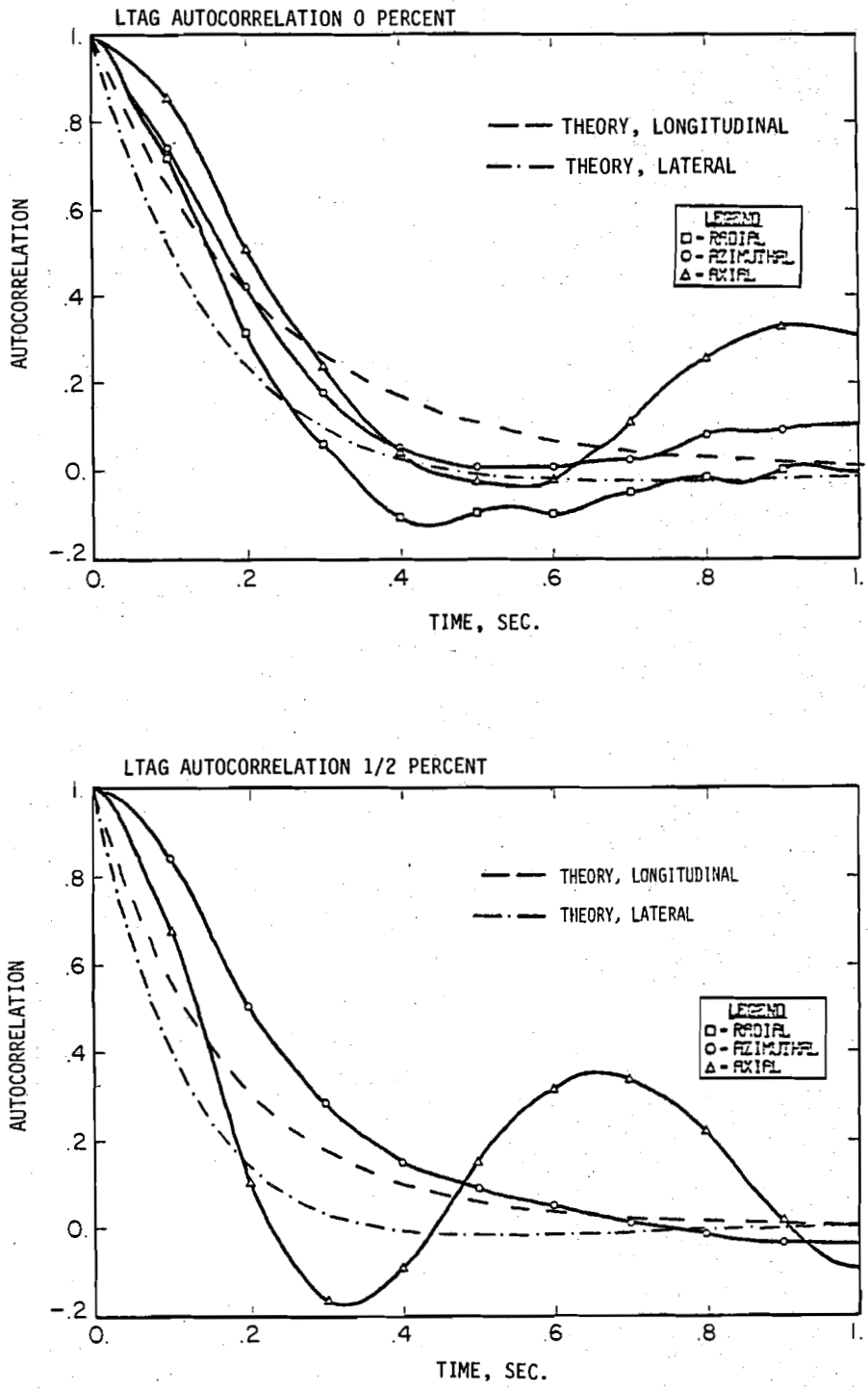

Figure 4.34 Comparison of Experimental Particle Autocorrelations with Theoretical Predictions

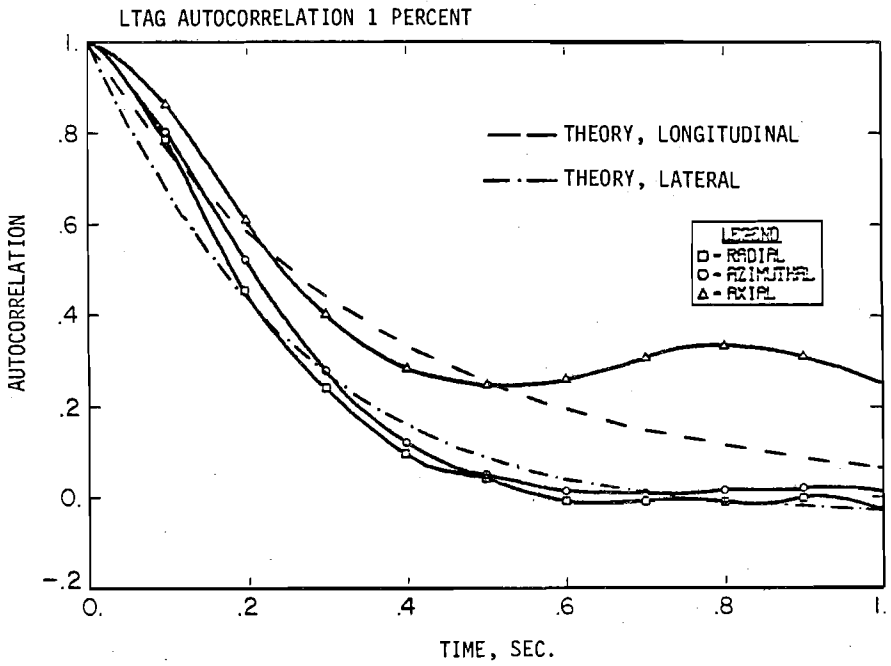

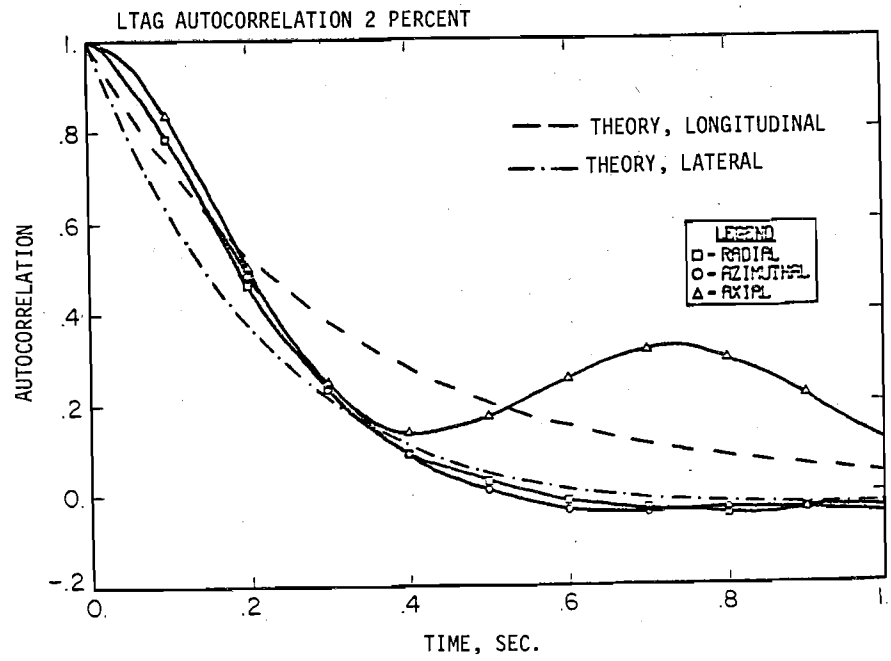

Figure 4.34 Comparison of Experimental Particle Autocorrelations with Theoretical Predictions

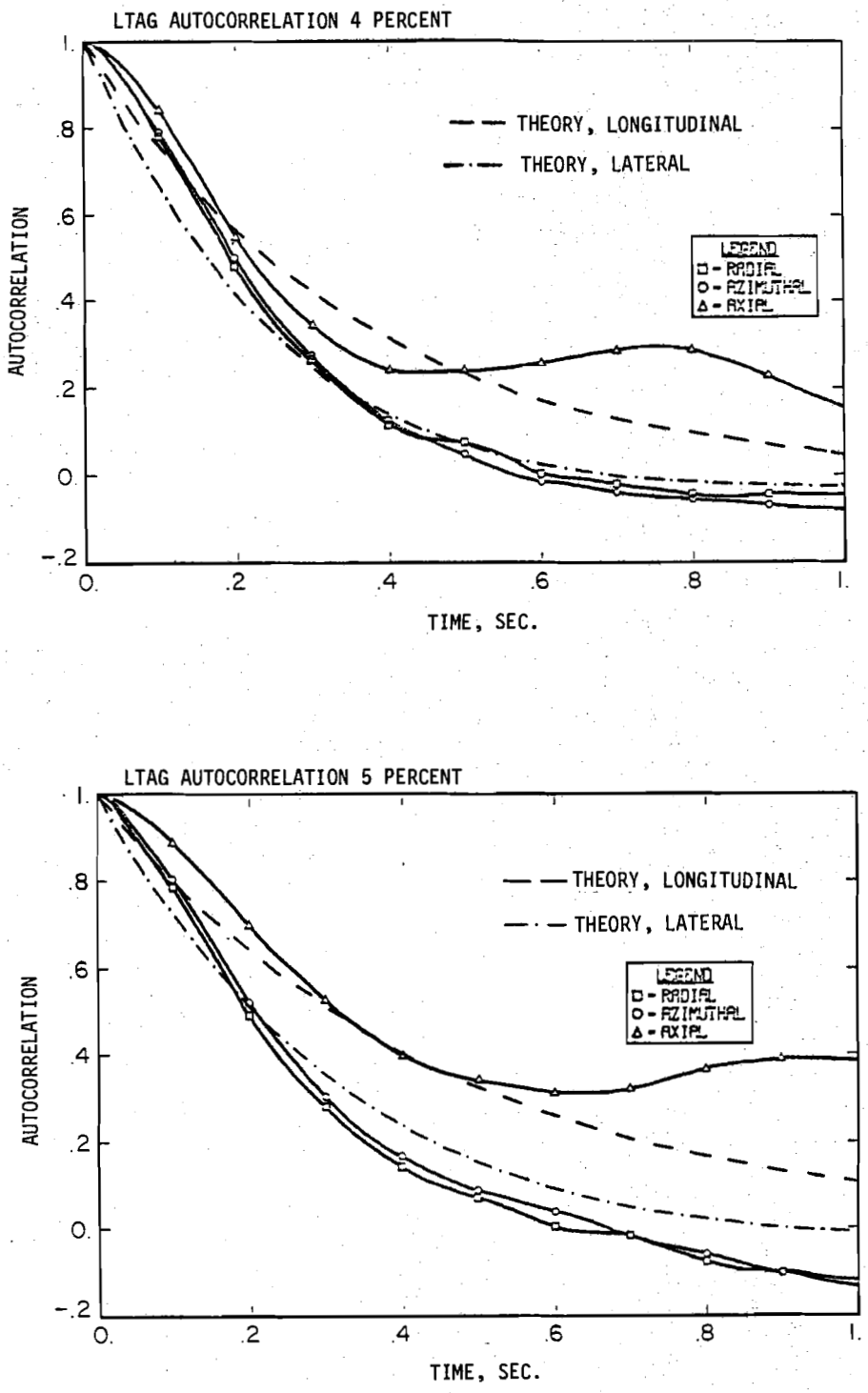

Figure 4.34 Comparison of Experimental Particle Autocorrelations with Theoretical Predictions

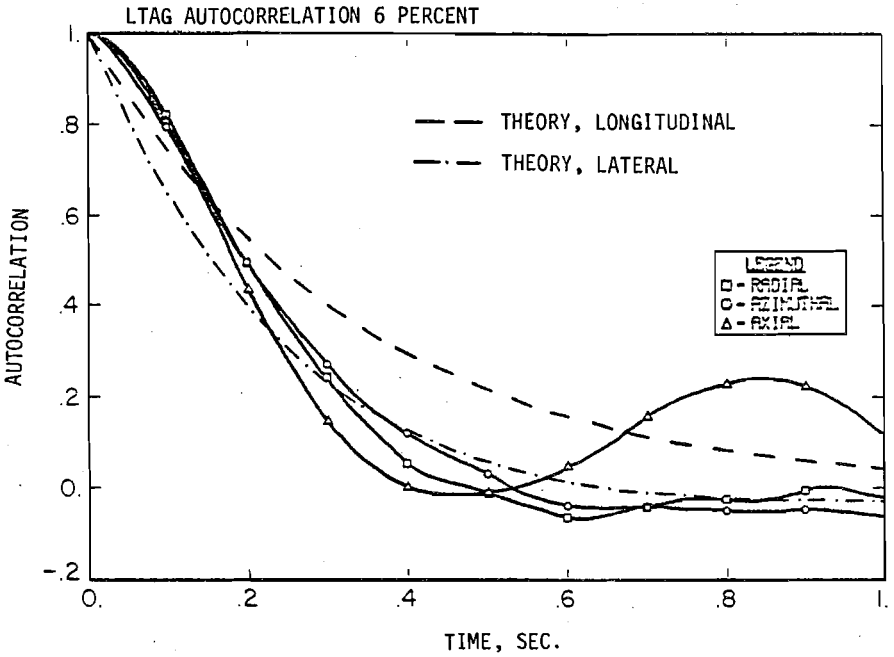

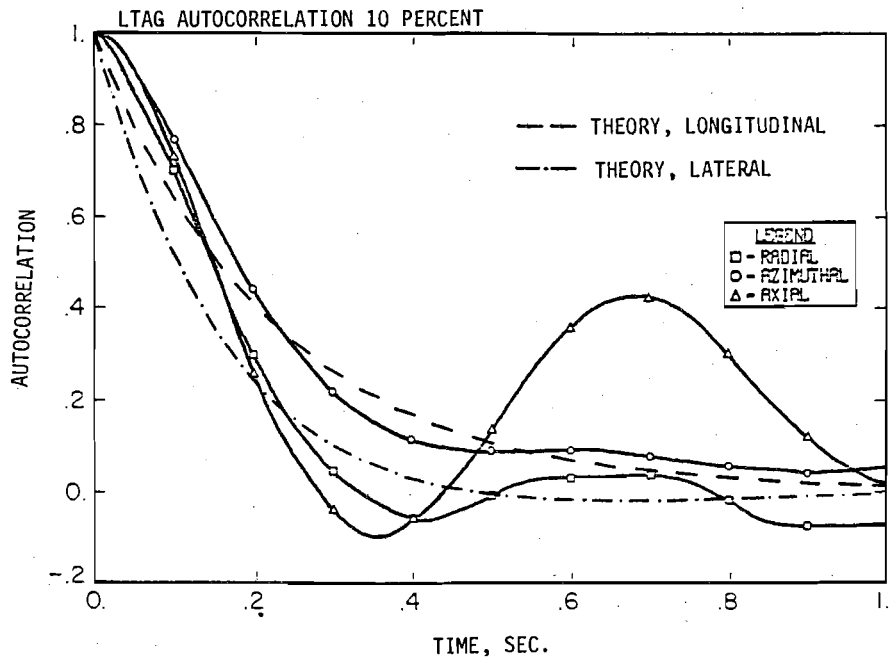

Figure 4.34 Comparison of Experimental Particle Autocorrelations with Theoretical Predictions

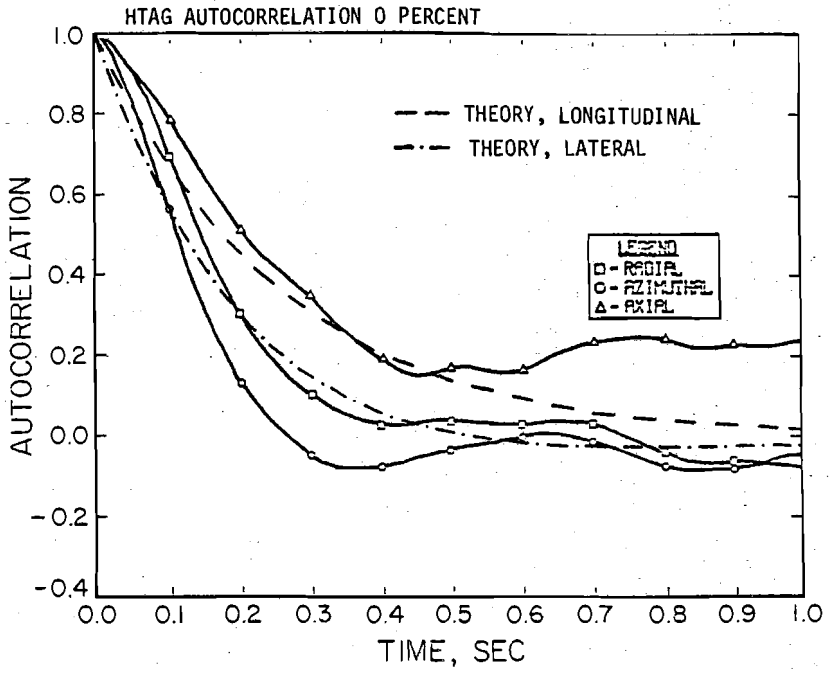

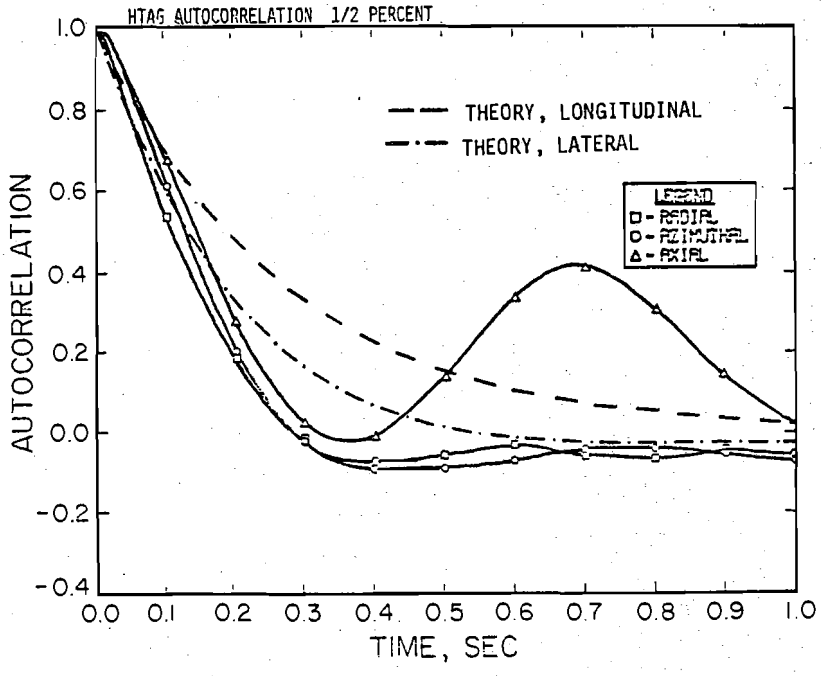

Figure 4.34 Comparison of Experimental Particle Autocorrelations with Theoretical Predictions

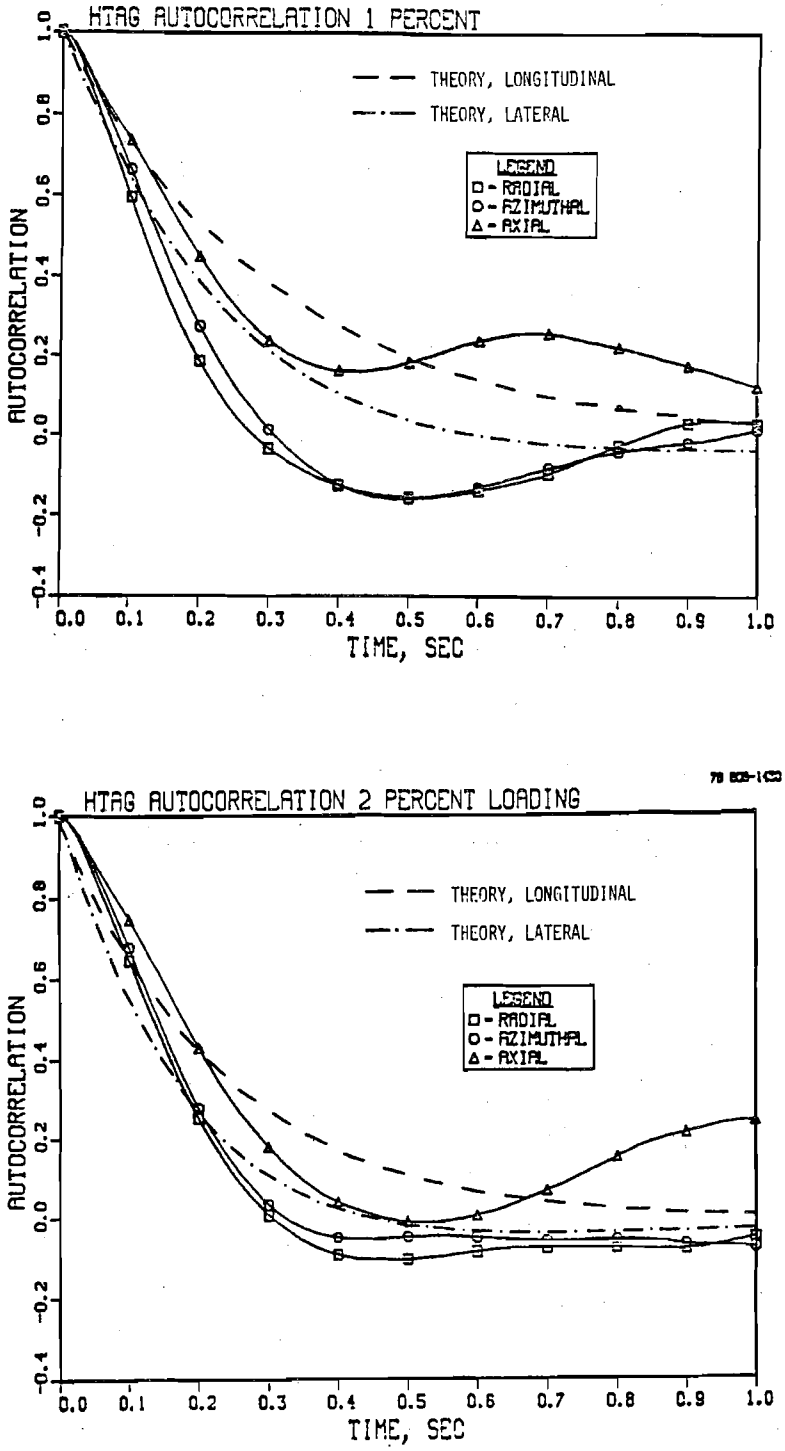

Figure 4.34 Comparison of Experimental Particle Autocorrelations with Theoretical Predictions

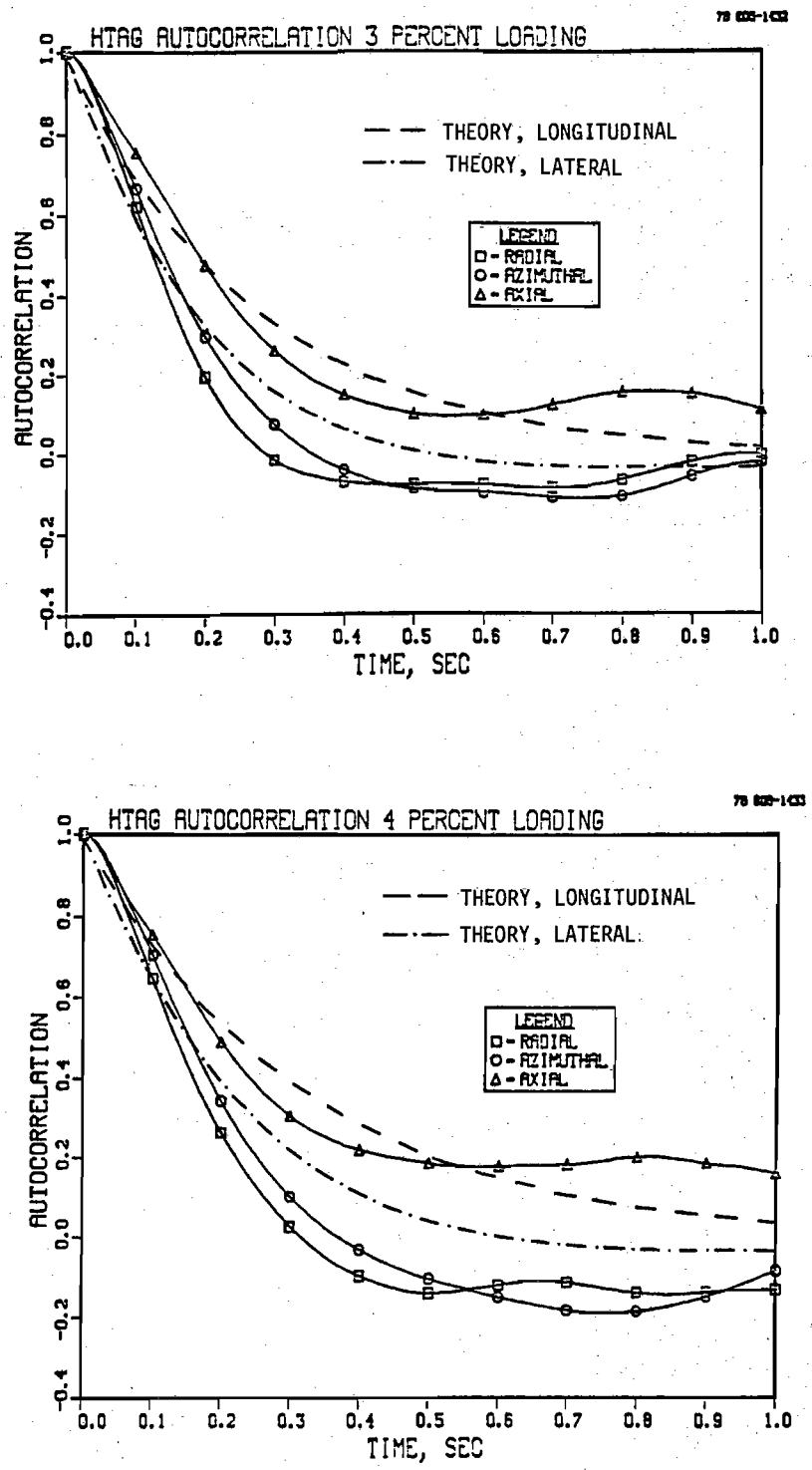

Figure 4.34 Comparison of Experimental Particle Autocorrelations with Theoretical Predictions

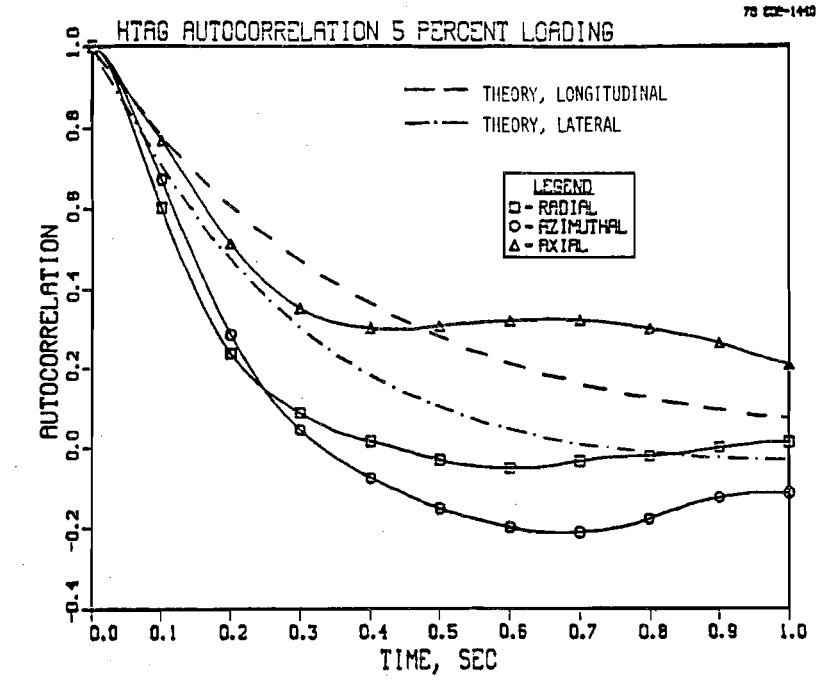

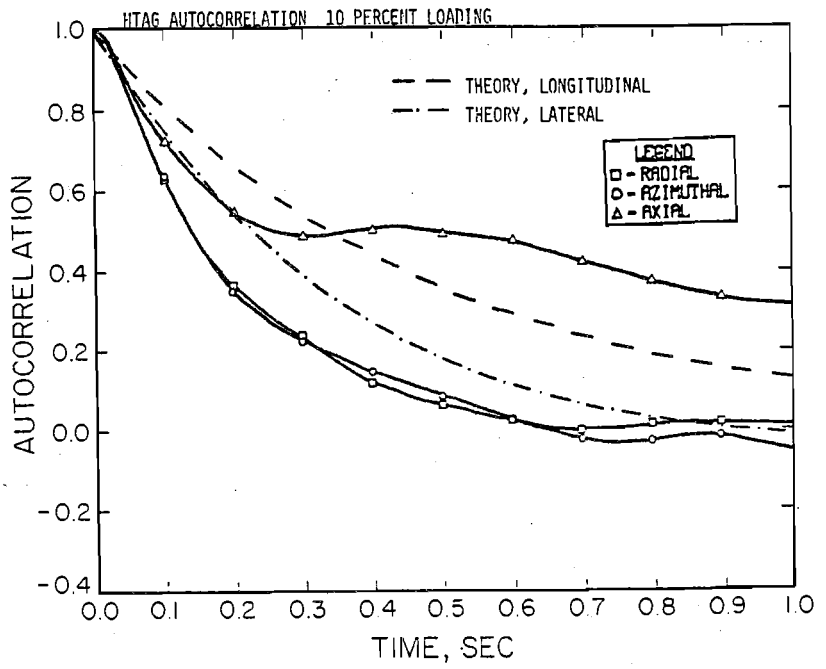

Figure 4.34 Comparison of Experimental Particle Autocorrelations with Theoretical Predictions

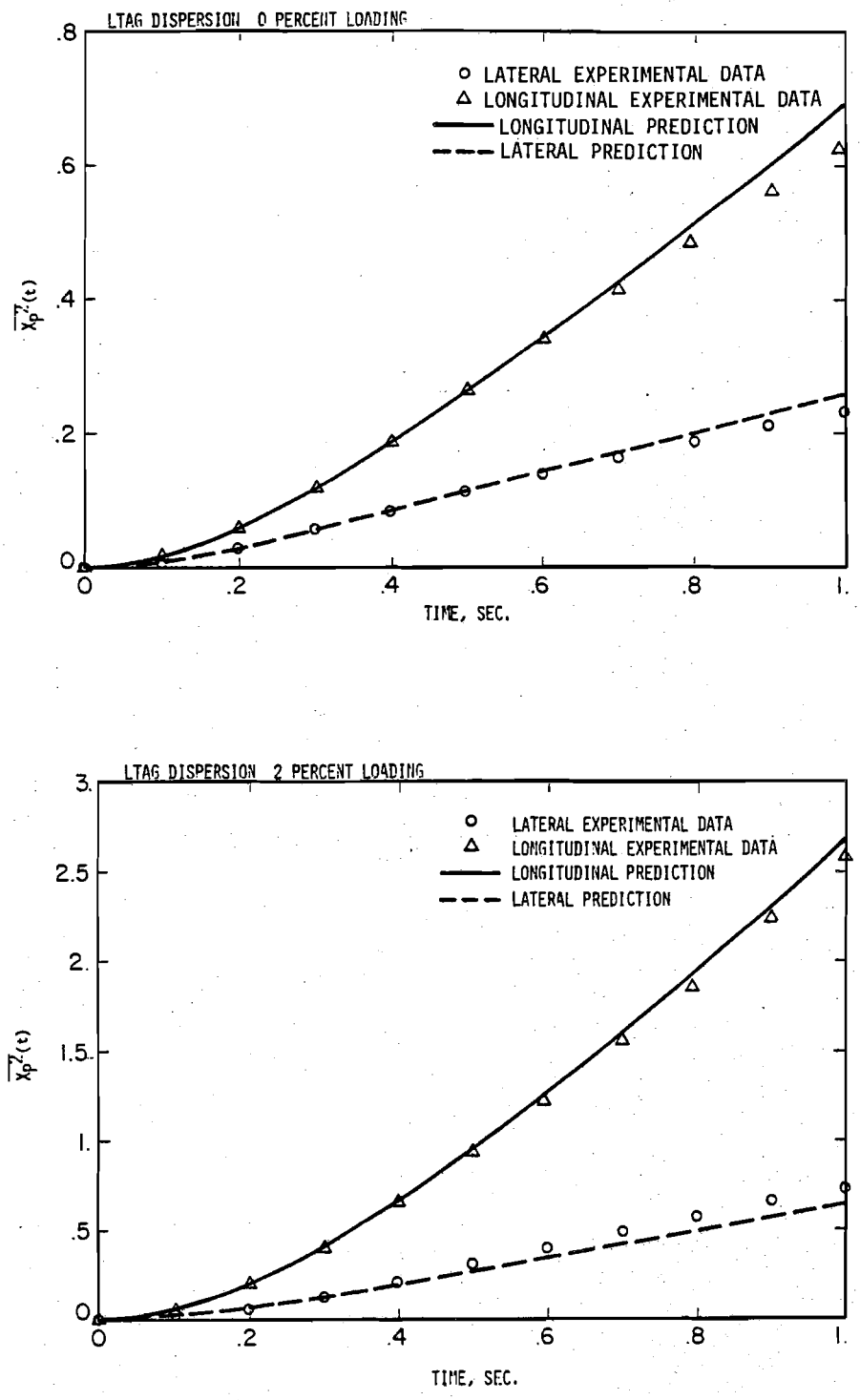

Figure 4.35 Comparison of Experimental Dispersion with Theoretical Predictions for LTAG ϕ and LTAG 2

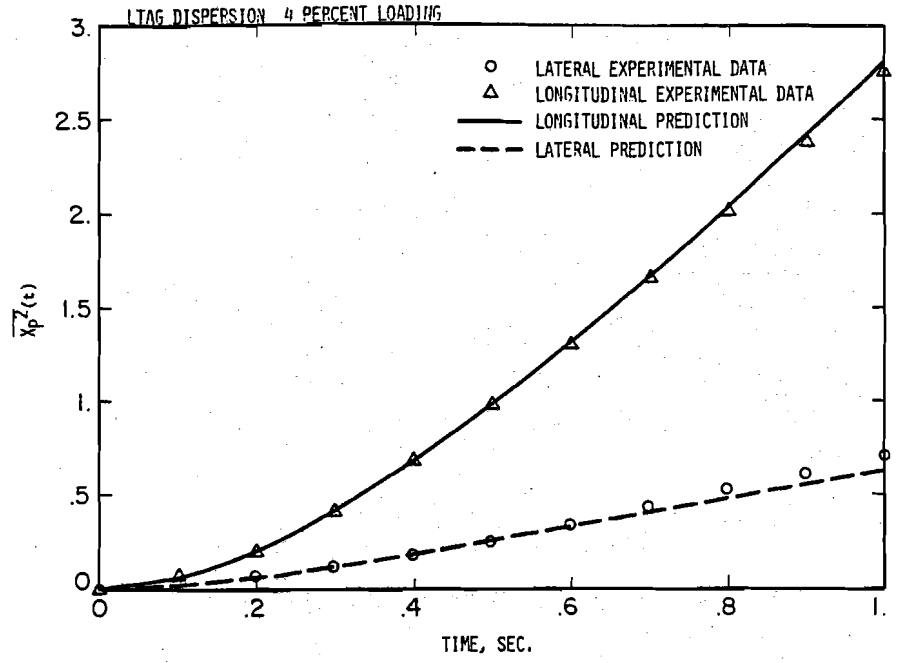

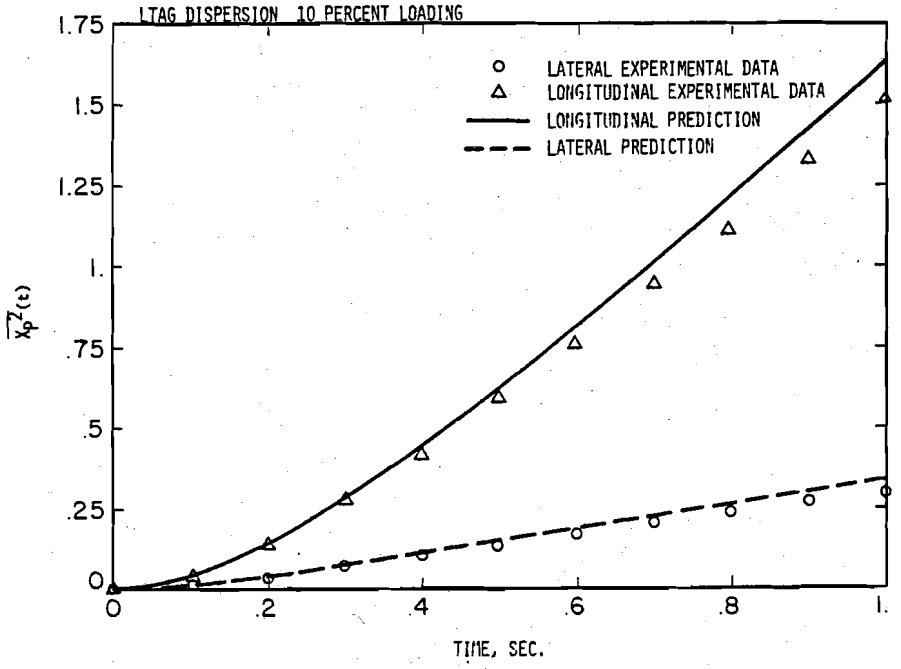

Figure 4.36 Comparison of Experimental Dispersion with Theoretical Predictions for LTAG 4 and LTAG 10

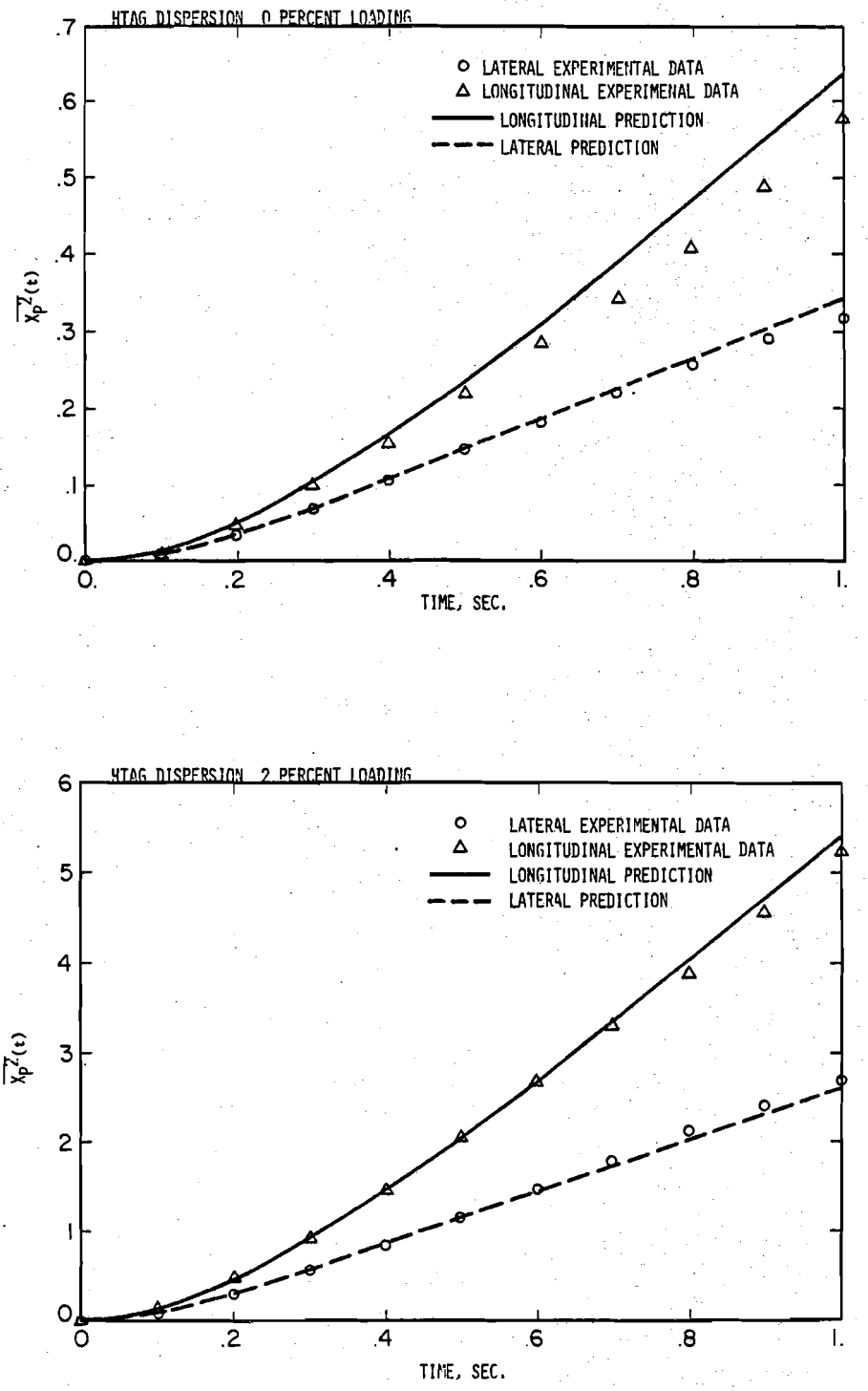

Figure 4.37 Comparison of Experimental Dispersion with Theoretical Predictions for HTAG 0 and HTAG 2

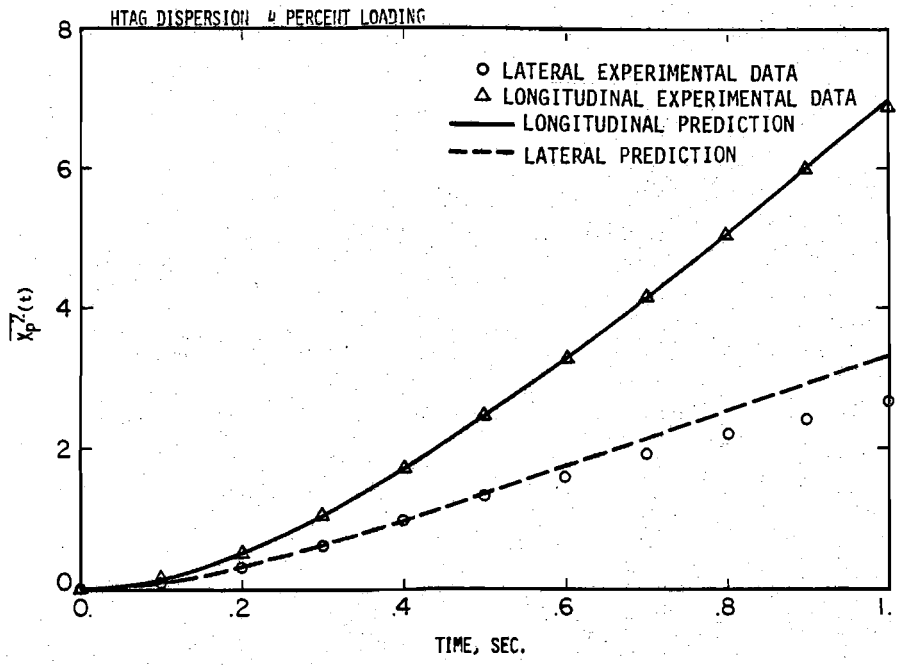

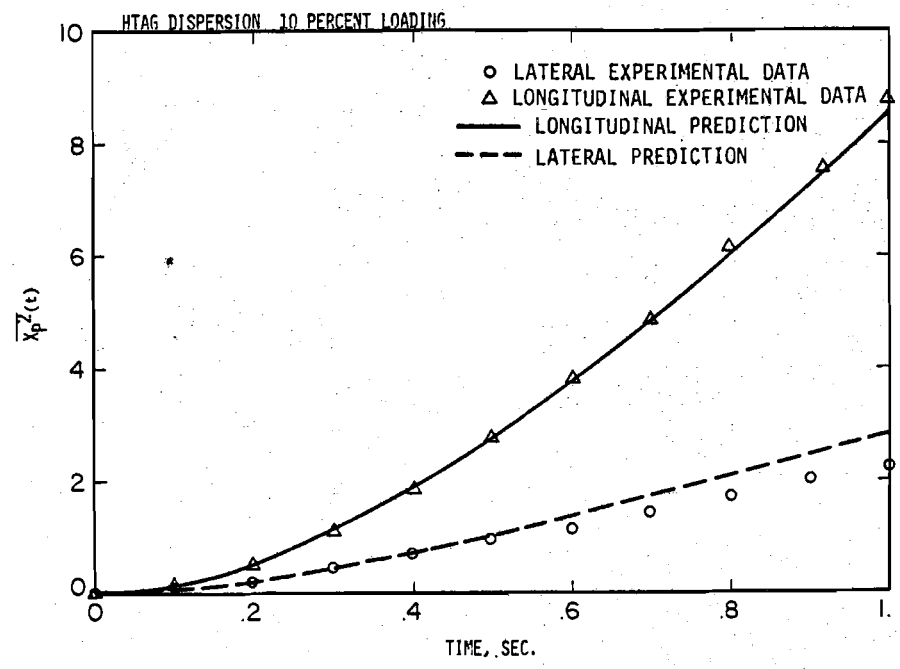

Figure 4.38 Comparison of Experimental Dispersion with Theoretical Predictions for HTAG 4 and HTAG 10

$$\overline{X_p^2(t)} = 2 V_p'^2 T_p t \qquad \text{large } t \qquad (4.22)$$

It is interesting to note the overall effects of the volume loading on particle diffusion coefficient, ϵ,

$$\epsilon = V_p'^2 T_p \qquad (4.23)$$

which is shown in Figure 4.39 for the lateral and longitudinal directions. For the lateral direction there is an initial increase in ϵ for small ϕ. As the volume loading increases, ϵ levels off where at higher loadings (ϕ = 10%), we see a slight decrease. This may be due to the particle's motion being restricted by the close proximity of the other particles. We also note the effects of the particle's free fall velocity, showing higher diffusion for HTAG series. This was also noted by Kada and Hanratty (1960) where the relative velocity between the fluid and the particle played an important role in the diffusion coefficient of the fluid (which is indicative of particle behavior).

The longitudinal diffusion coefficient shows the relative effect of the volume loading. As expected diffusion is greater for the longitudinal direction due to the turbulent fluid structure, but caution must be used in interpreting these results due to the uncertainty in the measured axial macroscale.

4.3 Error Analysis

This section deals with the relative uncertainty of the experimental data presented in the previous section. Howard (1974) compiled a very thorough analysis of error to be expected for the particle data acquisition and analysis systems. Using Howard's analysis as a guide, errors were

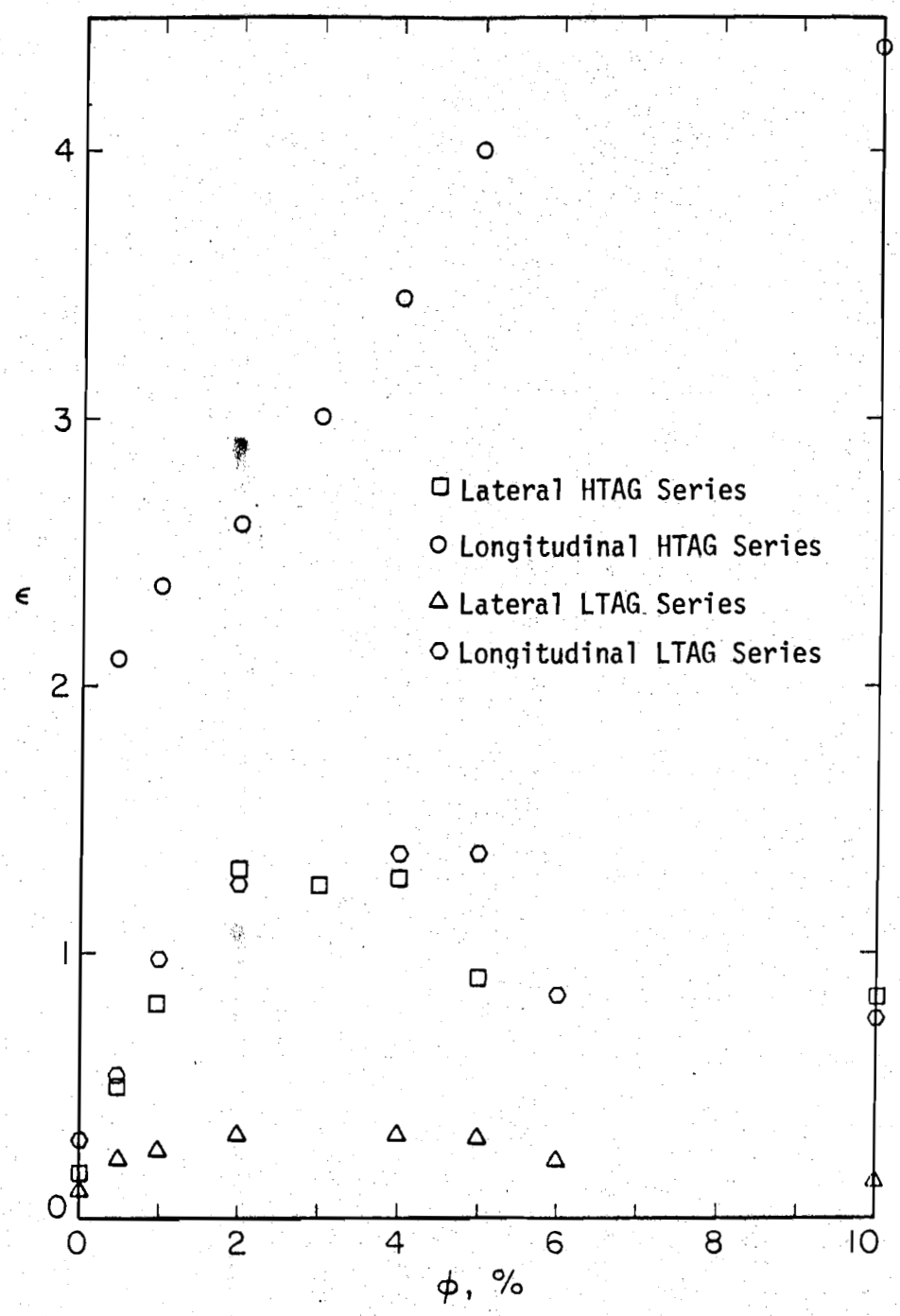

Figure 4.39 Particle Diffusion Coefficients for LTAG and HTAG Series

calculated for the present system. For a detailed discussion of the techniques employed one is referred to Howard's thesis. In an effort to confirm the techniques employed by Howard, static error experiments were conducted, with a comparison shown between predicted errors and those measured in the laboratory. A brief discussion is presented as to the relative efforts of ensembling of a finite number of non-stationary observations.

Howard examined the data acquisition system, shown in Figure 3.6, to ascertain which components were the major contributors of error, and to what degree that error was propogated through the data analysis. He pointed out that the strongest source of noise came from the photomultiplier tubes. This was attributed to the time varying, quantized decay of the Co 60 source used in the particle. As a result of this observation, improvements were made to reduce the problem in the present facility. This consisted of incorporating a more intense radioactive source within the particle. Howard reported a signal to noise ratio of 26.5 db for a 20 millicurie source, the signal to noise ratio was improved to 46.5 db by using a 50 millicurie source in the present system. Table 4.7 outlines the major components of the data acquisition system, their relative characteristics and limitations. If the basis of the error in the present system is restricted to the uncertainty of the time varying decay rate of the source, the expected errors propogated through the data analysis would be smaller than those shown by Howard. Following Howard's development, the errors were calculated for such quantities as the instantaneous relative position, the mean and rms position, the instantaneous velocity, as well as the mean and rms velocity.

Referring to Table 4.8, a comparison is made between the expected errors of the present system, and those of Howard. The relative error, in general, is lower for the present study.

Table 4.7 Data Acquisition System Component Characteristics

Device	Input	Output	S/N	Linear Non Linear	Frequency Limitations
Photomultiplier Tubes	γ rays	Voltage	46 db	Linear	Dead time of NaI Crystal 10^{-6} sec, 1 mHz
Carriage Velocimeter	Digital Voltage	Analog Voltage	54 db	Linear	10 KHz
Active Lowpass Filters	Voltage	Voltage	84 db	Linear	- 1 db at 100 Hz
Differential Amplifier and Filter	Voltage	Voltage	86 db	Linear	- 3 db at 74 Hz
Tape Recorder	Voltage	Voltage	50 db	Linear + 40% of Center Freq.	
Analog to Digital Conversion	Analog Voltage	Digital	90 cb	Linear	1 msec sample rate - 1000 Hz

Table 4.8 Predicted Errors

	HOWARD	GRONAGER
Absolute Position		
r	.52 cm	.283 cm
θ	.75 rad	.73 rad
Z	.24 cm	.41 cm
Instantaneous Relative Position		
r	.053 cm	.031 cm
θ *	.018 rad	.010 rad
Z	.098 cm	.045 cm
Mean Position		
r	.022 cm	.011 cm
θ	.007 rad	.001 rad
Z	.040 cm	.016 cm
Instantaneous Relative Velocity		
r	.42 cm/sec	.194 cm/sec
θ **	.59 cm/sec	.227 cm/sec
Z	.77 cm/sec	.286 cm/sec
Mean Velocity		
r	.001 cm/sec	.005 cm/sec
θ	.001 cm/sec	.005 cm/sec
Z	.002 cm/sec	.008 cm/sec
rms Velocity		
r	.17 cm/sec	.069 cm/sec
θ	.17 cm/sec	.069 cm/sec
Z	.32 cm/sec	.102 cm/sec

* r = 3 cm
** r = 3 cm, θ = 2 radians

Experiments were conducted to establish a direct measure of the error, for comparison with the predicted results. This was done in a similar manner in which the calibration experiments conducted, as described in Chapter 3. With the carriage mounted on a static test section, a particle was placed at selected locations within the calibrated region. With the data acquisition operational, the rms voltage of the T, U, V signals were tabulated as the particle was placed at the selected radial and axial positions. The results, shown in Figure 4.40, for a typical case indicates a constant rms voltage across the region of interest. Thus one can assume that the relative source of error is independent of position.

With the particle located at the origin of the calibrated region, data was recorded for an immobile particle. Thirty runs, typical in length to the particle runs, were recorded and subjected to the same data analysis as the particle data.

The results, shown in Table 4.9, are compared with the predicted error. Agreement between the predicted and experimentally observed error data is generally good. The exception is the instantaneous velocity error. Similar results were found by Howard, in which he attributed the source of the error to be the estimate of the particle's relative position correlation.

In order to estimate the relative noise associated with the autocorrelation, let us assume that the measured velocity time series of the particle $V_s(t)$ contains the velocity corresponding to the true velocity (noise free) plus an additional velocity, $V_n(t)$, from the data acquisition system, due to its inherent noise. That is to say,

$$V_s(t) = V_t(t) + V_N(t) \tag{4.24}$$

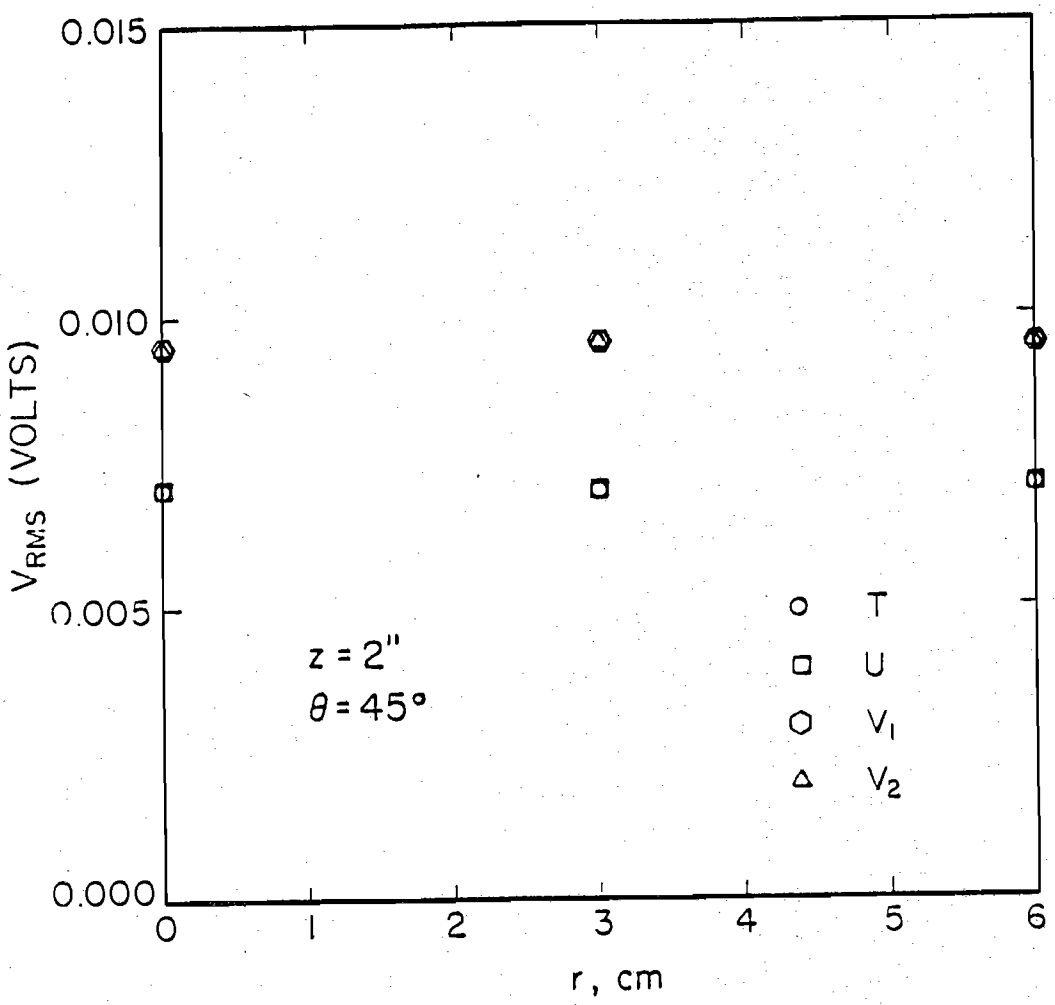

Figure 4.40 Radial Variation of Photomultiplier Tube rms Voltage

Table 4.9 Comparison of Predicted Error with Observed Error

Quantity	Predicted Error	Observed Error
Absolute Position		
$\sigma(r_{abs})$	.283 cm	.160 cm
$\sigma(\theta_{abs})$	.73 rad	.295 rad
$\sigma(Z_{abs})$	.410 cm	.285 cm
Instantaneous Relative Position		
$\sigma(r_i)$	.031 cm	.021 cm
$\sigma(\theta_i)$	.010 rad	.032 rad
$\sigma(Z_i)$	.045 cm	.047 cm
Instantaneous Velocity		
$\sigma(V_{ri})$	.194 cm/sec	.28 cm/sec
$\sigma(V_{\theta i})$	.227 cm/sec	.25 cm/sec
$\sigma(V_{Zi})$	.286 cm/sec	.635 cm/sec

Forming the autocovariance of $V_s(t)$, as done in the data analysis programs,

$$Cov_{V_s}(\tau) = \overline{V_s(t)\, V_s(t+\tau)} \tag{4.25}$$

where the overbar indicates a long time average, substituting for $V_s(t)$ and carrying out the indicated operations gives:

$$Cov_{V_s}(\tau) = \overline{V_t(t) V_t(t+\tau)} + \overline{V_t(t) V_N(t+\tau)} + \overline{V_N(t) V_t(t+\tau)} + \overline{V_N(t)\, V_N(t+\tau)} \tag{4.26}$$

Since the noise signal and the true particle velocity are statistically independent, the crosscovariance terms would vanish yielding:

$$Cov_{V_s}(\tau) = Cov_{V_t}(\tau) + Cov_{V_N}(\tau) \tag{4.27}$$

Solving the above equation for the covariance of the true velocity time series yields:

$$Cov_{V_t}(\tau) = Cov_{V_s}(\tau) - Cov_{V_N}(\tau) \tag{4.28}$$

The covariance of the noise shown in Figure 4.41 was provided by the static error experiments. Referring to Figure 4.42 and 4.43, the improvement to the covariance function by applying this technique is apparent. As indicated in the previous section, a 60 Hz noise was introduced into the LTAG 0.5, LTAG 10, HTAG 0.5, and HTAG 10 experimental data during digitalization. The above technique was used to remove the noise's contribution.

As was pointed out before, the experimental data is non-stantionary due to the relatively short length of data per run. In order to improve the statistical uncertainty of the data, the data were ensembled. The

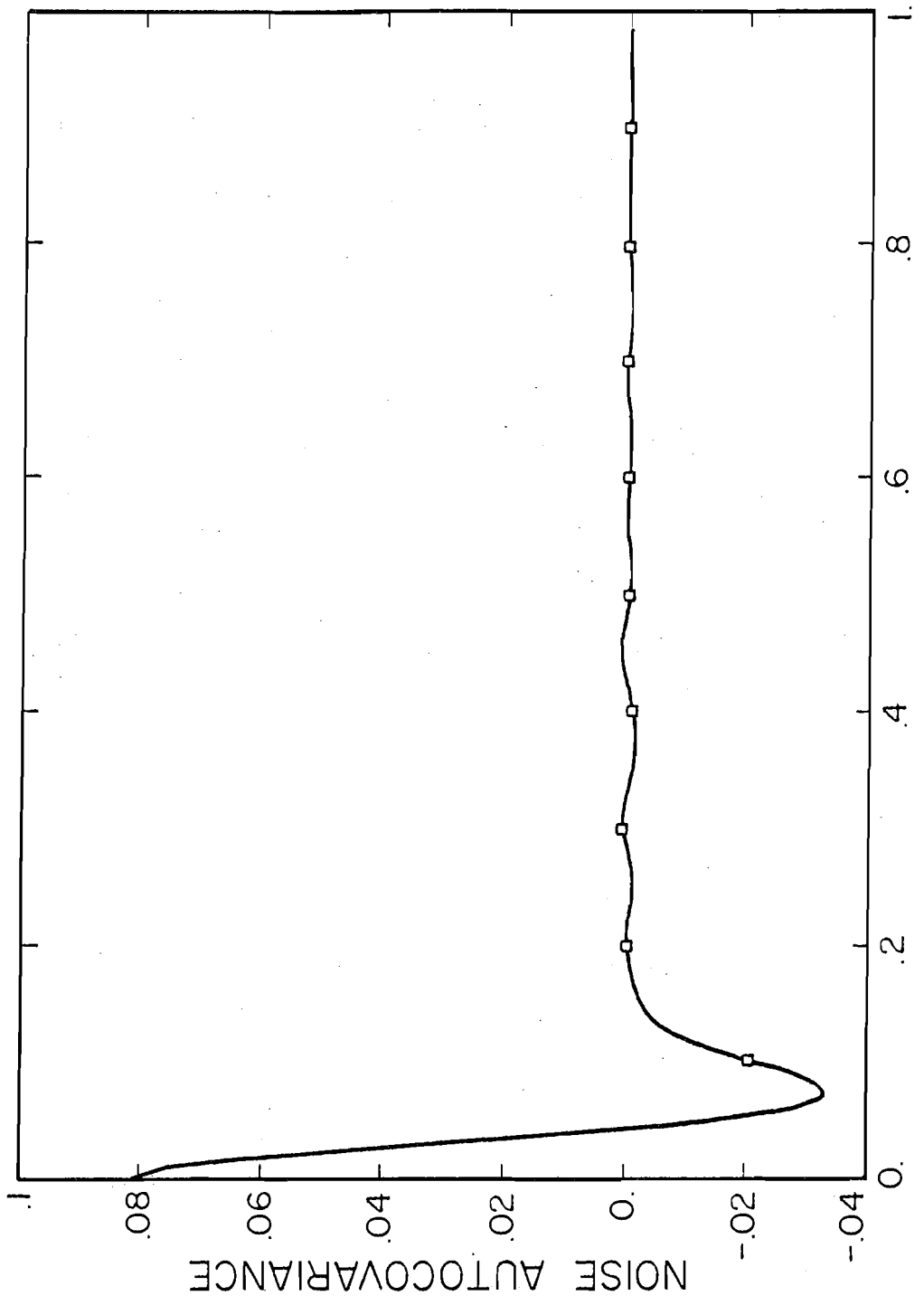

Figure 4.41 Electronic Noise Autocovariance

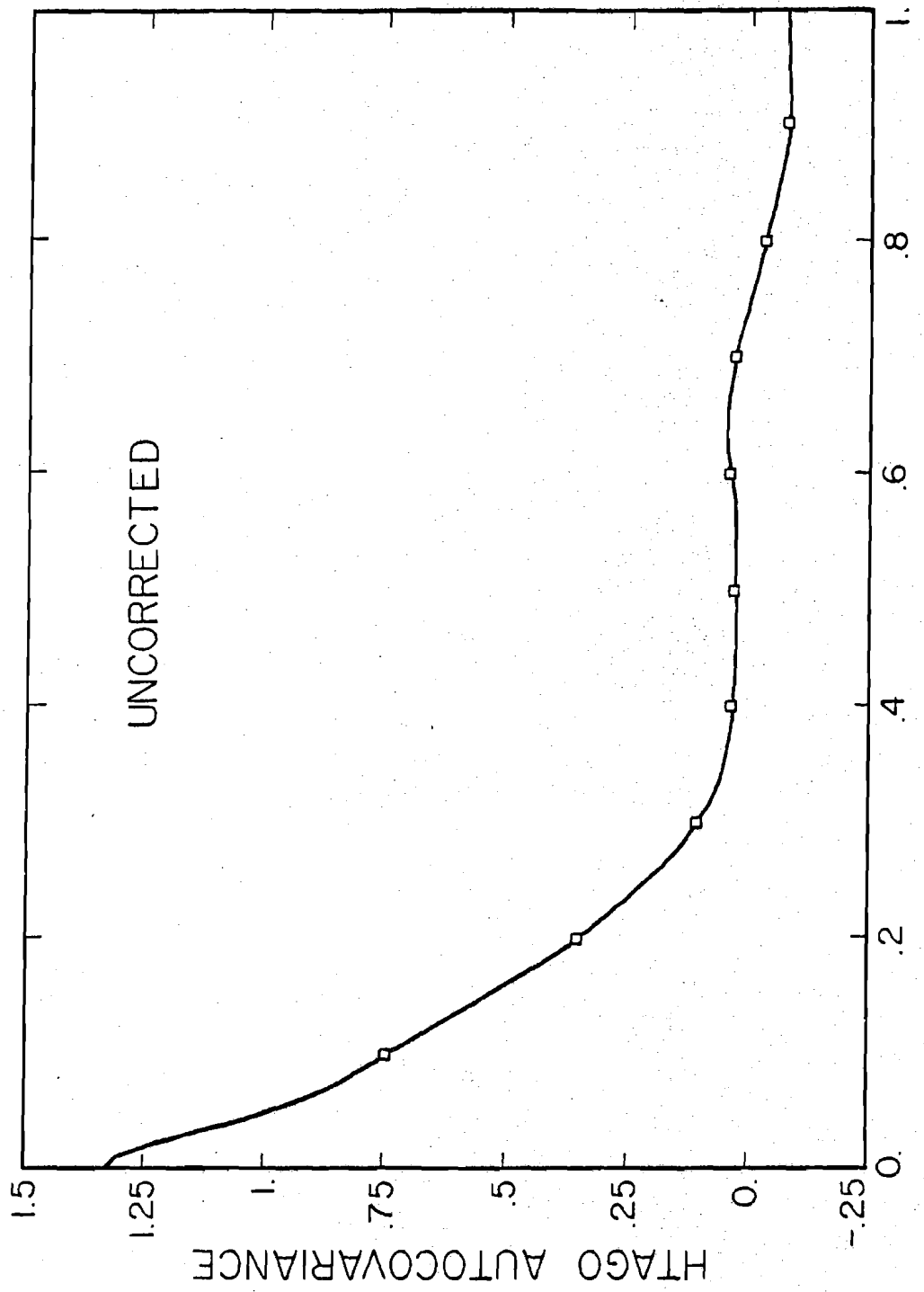

Figure 4.42 Uncorrected HTAG 0 Particle Autocovariance

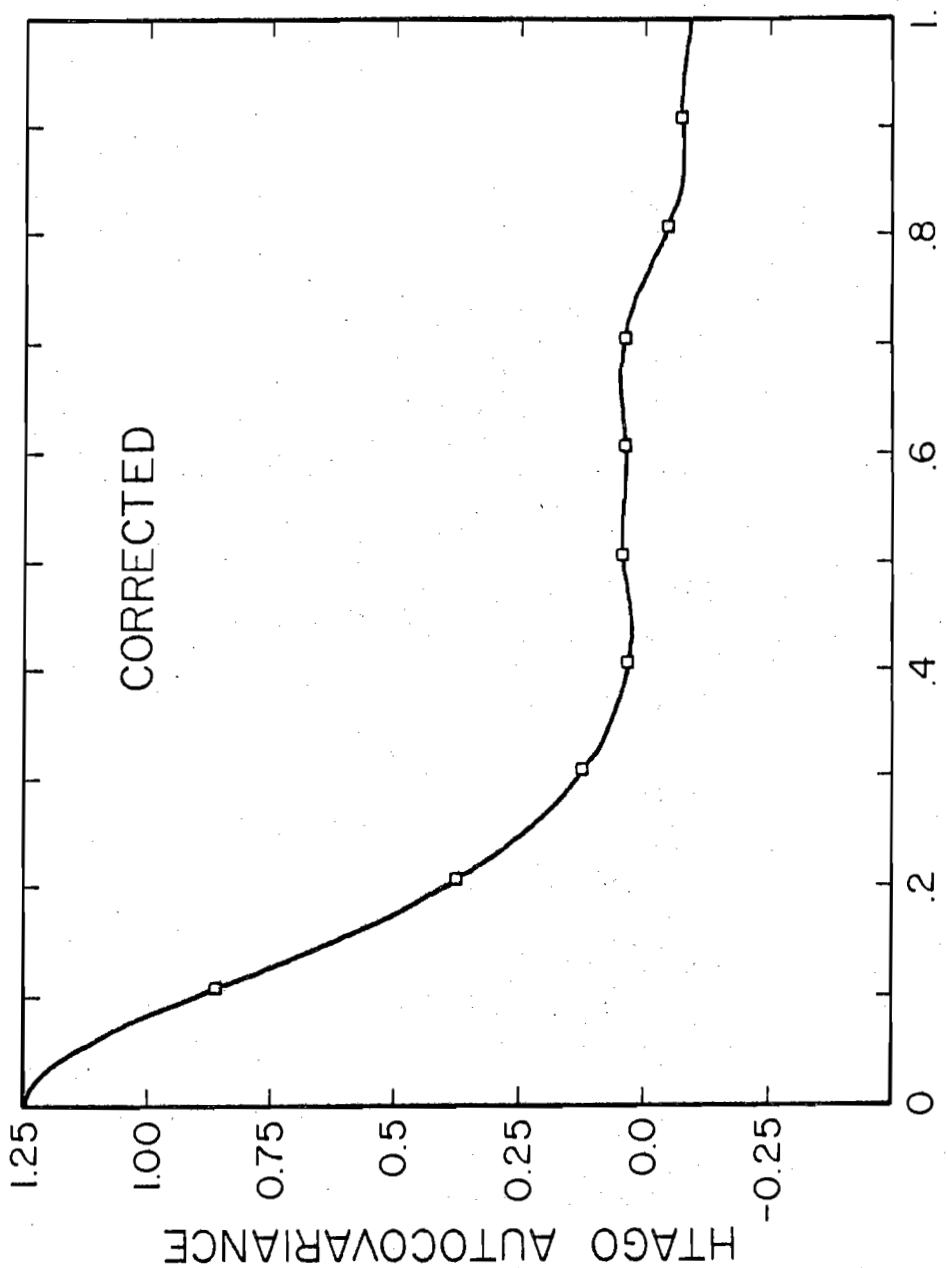

Figure 4.43 Corrected HTAG 0 Particle Autocovariance

procedure is straightforward; the results for each experiment of the analysis program, MAP, produced a set of good runs, N_G. This set of N_G runs were ensembled with equal weight by the program ENSEMBLE. As one can easily show, the errors one would expect for an individual event would be reduced by a factor of $1/\sqrt{M}$ for M independent events. To obtain an estimate as to the effective number of events needed to stabilize a measurement, a comparison was made of a typical measurement as a function of the number of runs ensembled. Referring to 4.44, the radial rms velocity of the HTAG 1 experiment is shown at various number of runs ensembled. It is found that after ensembling 10 runs the data has stabilized. This was found to be true for the other statistical quantities also.

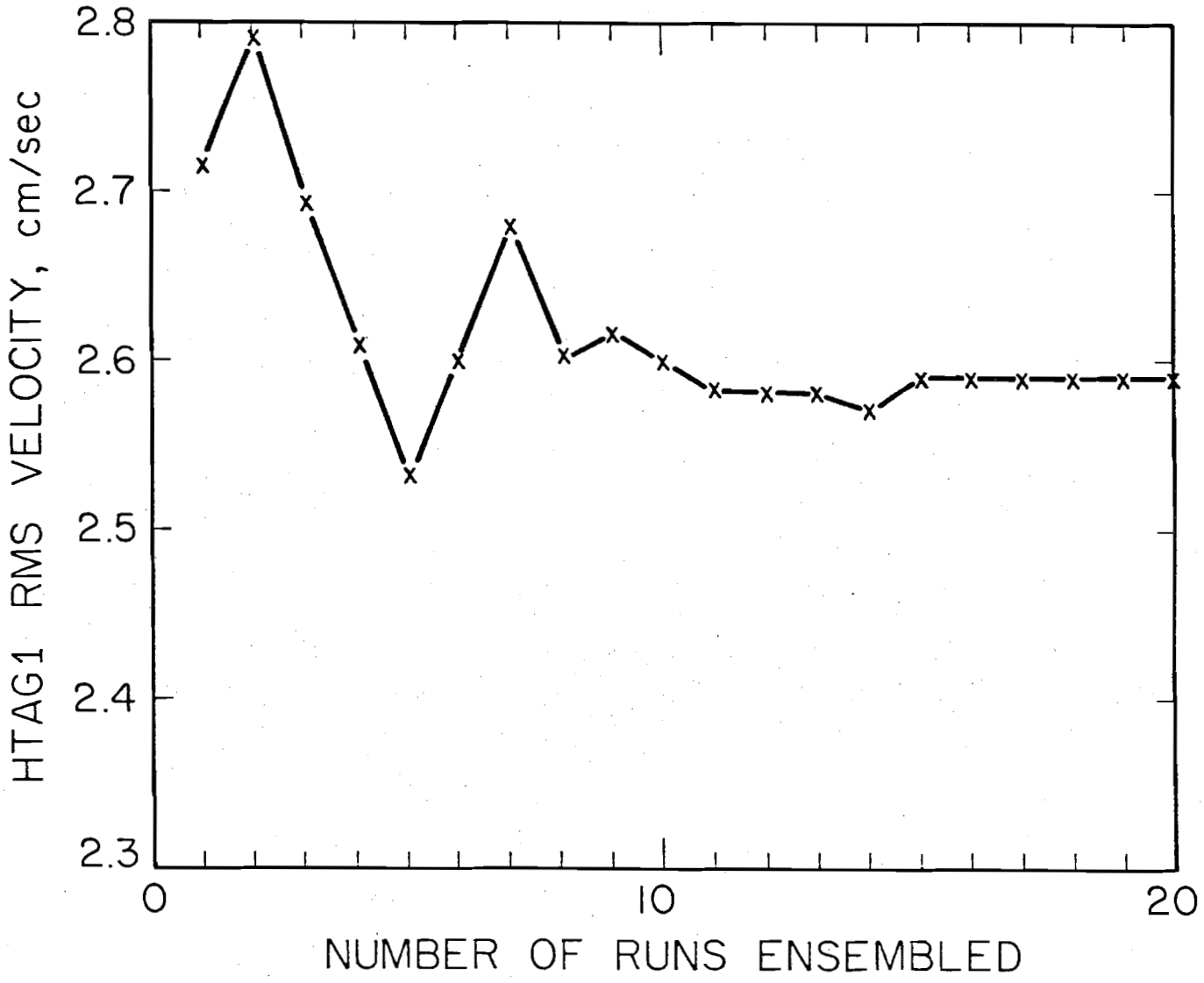

FIGURE 4.44 Convergence of HTAG 1 rms Velocity

CHAPTER 5 SUMMARY, CONCLUSIONS AND RECOMMENDATIONS

5.1 Summary and Conclusions

An investigation was made to determine the effects of particle density and particle volume concentration on the behavior of suspended particles in a turbulent flow field. An analytical model was developed in Chapter 2, as an extension of earlier work by Meek (1972). This model incorporated the hydrodynamic interaction between particles in non-dilute turbulent suspensions. The model was further extended for a large range of particle Reynolds numbers. As shown, good agreement existed between experimental data and the model's prediction for ϕ greater than 0. A complete test of the theory was not realized since an independent experimental observation of the fluid turbulence could not be made in the experiments.

Modifications were made to the experimental facility in order to circulate an increased inventory of particles. Experiments were conducted to determine the influence the modification might have had on the fluid's turbulent structure. The results indicated no observable change in the fluid's behavior, as reported earlier by Howard (1972). The data acquisition system was up-dated in order to improve reliability and accuracy. A more intense radioactive source was employed to improve the signal to noise ratio of the photomultiplier tubes. The statistical uncertainty was found to be less than 8% for the experimental data.

Two techniques were employed in efforts to directly measure the fluctuating fluid velocity at various particle concentrations. An attempt was made to employ standard anemometer techniques, but the reliability of the data was compromised by particle-probe interference. Efforts to utilize

a nearly neutral buoyant tagged particle also proved to be fruitless, due to the inability of the tagged particle to remain within the calibrated region of the flow.

Due to the lack of direct experimental observation of the fluid's structure at various particle concentrations, an estimate of the structure was made based on the lateral behavior of the particle. This was based on results obtained from Howard's (1974) data. It was found for particles with a β close to 1, that lateral particle data compared closely with independent measurements of the fluid's intensity and spatial scales (for $\phi = 0$). Although it has not been experimentally verified, it is reasonable to infer that for particles with $\beta \sim 1$, such a comparison will yield reasonable estimates of the fluid structure for particle loadings in which direct particle-particle collisions are not the dominant factor (e.g., Batchelor, 1972 suggests that $\phi \leq 20\%$).

Two series of experiments were conducted to statistically determine the behavior of non-dilute turbulent suspension, for different particle free fall velocities. The mean velocity of the particles were determined for various particle concentration. A comparison with the previous work by Kaye and Broadman (1962) in quiescent fluids showed that particle gathering in clusters played an important role in the mean velocity of the particles. The effects of particle clusters tend to produce higher free fall velocities.

The effects of the volume loading, as well as, the free fall velocity are clearly brought out in the observed rms velocity of the particles. The rapid rise in the rms velocities indicates that the fluid's turbulent structure changes for small volume loadings. This may be due to the

particle wakes acting as generators of turbulence as they fall through the fluid. As one might expect, the effects are enhanced for particles with large free fall velocities. (Kada and Hanratty, 1960 reported similar particle velocity effects in their measurements of point source fluid diffusion). It was also found that the rms velocities reached a maximum for values of ϕ between 1 and 5 percent. It is not clear which mechanisms come into play within the fluid to cause this rather broad peak. As ϕ is further increased a slight drop in the rms velocities was detected. This might be due to the restricted motion of the particles at higher volume loadings (ϕ = 10%), where particles are in close proximity with one another (approximately 3/4 of a diameter between particles).

The velocity autocorrelation brought to light the relative isotropic behavior of the particle's lateral fluctuating velocities. This observation is supported by the lateral rms velocities. The correlations exhibited a strong relation to the particle mean velocity in which the LTAG series showed longer correlations than the HTAG series due to its slower mean velocity. The lateral experimental autocorrelations showed good agreement with theory. Such a comparison for the axial autocorrelation data was hampered by an inherent noise caused by a phase shift in the carriage velocity time series.

The application of the theory toward engineering problems was demonstrated. The particle's predicted disperson enjoyed good agreement with the experimental data. Due to the averaging characteristics of the dispersion calculation, the axial data was shown to be useful. The turbulent particle diffusion coefficient, ε, indicated a greatly enhanced diffusion for a relatively small volume loading. As ϕ was further increased, ε was observed to level off to a

maximum value, then to reduce for ϕ equals 10 percent (similar to the rms behavior).

5.2 Recommendations for Future Research.

The research undertaken by this project provided experimental data for a relatively small region of the overall turbulent transport of solids in fluids. The following recommendations are made for future research:

1. The behavior of the fluid phase in non-dilute suspensions should be investigated to provide independent data to verify the theory.
2. A variation of particle size and density should be studied to provide a more complete range of parameterized data to compare with the theory. This has not been realized for the non-dilute cases.
3. Larger particle concentrations could also be investigated to determine the overall loading effects for applications of engineering interest.
4. The transport of suspended solids in horizontal pipes is found in many engineering applications. It is suggested that modifications be made to the existing system to utilize the same unique data acquisition system for horizontal turbulent flow.

APPENDIX A

PARTICLE ANALYSIS PROGRAM

A.1 Main Analysis Program

A simplified flow chart of the main analysis program is shown in Figure A.1. The main program generally provides initialization of variables, as well as providing data management for each run.

Analysis of each run begins with a call to the subroutine DATA. The function of which is to read the raw voltage difference signals and carriage velocity voltage from digital magnetic tape. This is performed by Utilizing the TPIOZ system provided by the University of Illinois Computer Services Office.

Once the raw signals are obtained by DATA, main calls the subroutine FILTER to apply a digital Gaussian filter to the data. The filter is applied at every 40th point of the time series. The relationship between the input voltage signal V_K and the output voltage $V_{s,i}$ is:

$$V_{s_i} = \frac{V_K + \sum_{k=1}^{m/2} (V_{i+K} + V_{i-K}) \exp[-(9.68 f_{90} K \Delta t)^2]}{1 + 2 \sum_{k=1}^{m/2} \exp[-(9.68 f_{90} K \Delta t)^2]} \qquad (A.1)$$

where Δt is the time increment between voltage points, M is the total number of points over which the filter is applied, and f_{90} is the frequency at which the voltage signal is attenuated by 0.1. The relationship between f_{90} and M is:

$$m = \frac{0.20664}{\Delta t\, f_{90}} \left(\ln f_{90} + 9.298 \right)^{1/2} \qquad (A.2)$$

For the present study f_{90} was 3 hz, Δt = 0.001 sec. and M equalled 223 points.

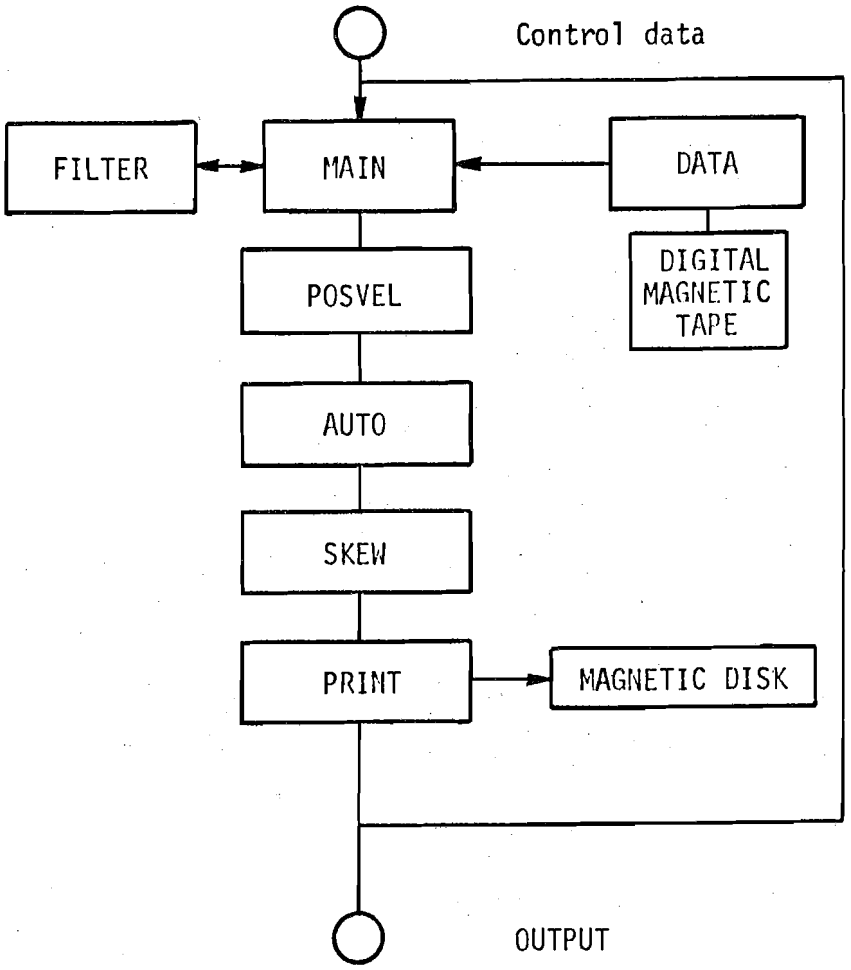

Figure A.1 Main Analysis Program Flow Chart

The filtered data is next manipulated by the subroutine POSVEL, the purpose of which is to calculate the instantaneous position and velocity of the particle. As discussed in Chapter 3, the particle position was determined from:

$$X_i = f(a_j, T, U, V) \tag{A.3}$$

$$Y_i = f(b_j, T, U, V) \tag{A.4}$$

$$Z_i = f(c_j, T, U, V) \tag{A.5}$$

The Cartesian position relative to the carriage are converted to cylindrical position by:

$$r_i = (x_i^2 + y_i^2)^{1/2} \tag{A.6}$$

$$\theta_i = \arctan(y_i/x_i) \tag{A.7}$$

$$z_i = z_i \tag{A.8}$$

The cylindrical velocities, relative to the carriage are calculated as:

$$V_{r,i} = \frac{r_{i+1} - r_i}{\Delta t} \tag{A.9}$$

$$V_{\theta,i} = \frac{r_{i+1} + r_i}{2} \cdot \frac{\theta_{i+1} - \theta_i}{\Delta t} \tag{A.10}$$

$$V_{zrc,i} = \frac{z_{i+1} - z_i}{\Delta t} \tag{A.11}$$

In order to provide the axial particle velocities relative to the fluid velocity the following calculation is performed:

$$V_{z,i} = V_{zrc,i} + V_c - \bar{U}_{f_i}(r_i) \tag{A.12}$$

Where V_C is the carriage velocity and $\bar{U}_f(r_i)$ is the mean fluid velocity at the radial position r_i. They are determined by:

$$V_c = 9.416\, e_c \tag{A.13}$$

$$\bar{U}_{f_i}(r_i) = \bar{U}_{f_t}\left(1 - r_i/9.21\right)^{0.156} \tag{A.14}$$

where e_c is the voltage from the carriage velocimeter.

The subroutine POSVEL also calculates the mean and rms position of particle for each direction as

$$\bar{r} = \frac{1}{N}\sum_{i=1}^{N} r_i \tag{A.15}$$

$$\bar{\theta} = \frac{1}{N}\sum_{i=1}^{N} \theta_i \tag{A.16}$$

$$\bar{z} = \frac{1}{N}\sum_{i=1}^{N} z_i \tag{A.17}$$

and:

$$r_{rms} = \left[\frac{1}{N}\sum_{i=1}^{N}(r_i - \bar{r})^2\right]^{1/2} \tag{A.18}$$

$$\theta_{rms} = \left[\frac{1}{N}\sum_{i=1}^{N}(\theta_i - \bar{\theta})^2\right]^{1/2} \tag{A.19}$$

$$z_{rms} = \left[\frac{1}{N}\sum_{i=1}^{N}(z_i - \bar{z})^2\right]^{1/2} \tag{A.20}$$

A similar method was used to calculate the mean and rms velocities.

The autocovariance functions were calculated in the subroutine AUTO by the method of lagged products:

$$Cov_{V_r}(j) = \frac{1}{N-j}\sum_{i=1}^{N-j} V_{r,i} - V_{r,i+j} \tag{A.21}$$

$$Cov_{V_\theta}(j) = \frac{1}{N-j}\sum_{i=1}^{N-j} V_{\theta,i} - V_{\theta,i+j} \tag{A.22}$$

$$Cov_{V_z}(j) = \frac{1}{N-j}\sum_{i=1}^{N-j} V_{z,i} - V_{z,i+j} \tag{A.23}$$

Statistical parameters such as the skewness and kurtosis were calculated in the subroutine SKEW.

The skewness and kurtosis in the radial direction is determined by:

$$\text{SKEWNESS} = \left[\frac{1}{N}\sum_{i=1}^{N}(V_{r,i})^3\right] \Big/ (V_{r,rms})^3 \tag{A.24}$$

$$\text{KURTOSIS} = \left[\frac{1}{N}\sum_{i=1}^{N}(V_{r,i})^4\right] \Big/ (V_{r,rms})^4 \qquad (A.25)$$

A similar method was used for the azimuthal and axial directions.

The subroutine PRINT provided the probability density function (p.d.f.) calculation, as well as output data for each run. The p.d.f.'s were calculated in a standard manner:

If $V_{MIN} \leq V_i < V_1$ Then BIN 1 = BIN 1 + 1

If $V_1 \leq V_i < V_2$ Then BIN 2 = BIN 2 + 1

. . . .
. . . .
. . . .

If $V_{N-1} \leq V_i \leq V_{MAX}$ Then BIN N = BIN N + 1

Where V_i is the corresponding velocity in the time series, V_{MIN} through V_{MAX} are the minimum and maximum velocities expected in the time series, and the BINs are counters (when V_i is found to reside within interval between V_M and V_{M-1}, the bin M is incremented).

The output data is printed in the brief form shown in Figure A.2 for each run. In addition the calculated statistical information is stored on magnetic disk for future use by ENSEMBLE.

A.2 ENSEMBLE

The program ENSEMBLE provided the ensembling of the statistical data as well as, calculated the INTEGRAL Scales and Taylor Microscales. The ensembling was calculated as:

$$\overline{\omega_K} = \frac{1}{N}\sum_{i=1}^{N}\omega_{K,i} \qquad (A.26)$$

where $W_{K,i}$ is the statistical quantity for each run and $\overline{W}_K$ is the ensembled result, and N is the number of runs ensembled.

J.GRONAGER EXPERIMENT HTAG1 CER=1.18 VOL.=1F RUN=168 MFILE=8Z 2/8/79 NO. OF BLOCKS= 0

DIAMETER OF THE PARTICLE = 0.48 CM

QUIESCENT FREE FALL VELOCITY = 14.50 CM /SEC

QUIESCENT REYNOLDS NUMBER = 799.3

QUIESCENT DRAG COEFFICIENT = 0.5761

DENSITY OF THE PARTICLE = 1.1800 GM/CC

BETA = 0.3929

ALPHA = 0.4608 /SEC

NUMBER OF POINTS IN THE RAW VOL TAGE SERIES = 9000 WITH TIME INCREMENT OF 0.001 SECONDS

NUMBER OF POINTS IN THE POSITION/TIME SERIES = 686 WITH TIME INCREMENT OF 0.010 SECONDS

INCREMENT IN TIME SERIES POINTS BEFORE SMOOTHING = 1 MILLISECONDS

TIME OF SMOOTHING INCREMENT = 0.223 SECONDS

FILTER CHARACTERISTIC = 0.9 3 3.0 HZ

TIME OF RUN = 6.850 SECONDS

STATISTICAL AND REYNOLDS STRESS INFORMATION:

VRSKEW	VTSKEW	VZSKEW	VRKURT	VTKURT	VZKURT	RTSTRESS	RZSTRESS	TZSTRESS
0.0053	-0.1079	-0.5596	2.2792	2.5295	3.5028	-2.1199	-2.9320	0.0309

	RADIAL	AZIMUTHAL	AXIAL	CARRIAGE
MEAN POSITION	3.414 CM	2.044 RAD	-2.195 CM	
RMS POSITION	1.921 CM	0.274 RAD	1.377 CM	
MEAN VELOCITY	-0.685 CM /SEC	-0.035 CM /SEC	12.515 CM /SEC	36.165 CM /SEC
RMS VELOCITY	3.586 CM /SEC	2.183 CM /SEC	2.711 CM /SEC	2.896 CM /SEC

THE TURBULENT PARTICLE REYNOLDS NUMBER IS 689.

THE TURBULENT PARTICLE DRAG COEFFICIENT IS 0.719

AVERAGE MEAN SQUARE ERROR IN MEAN FLUID VELOCITY= 0.3

Figure A.2 Sample Output Data From Subroutine Print

The integral Scale was calculated from the ensembled autocorrelation as:

$$\mathcal{J} = \int_0^\infty \overline{R}(\tau)\, d\tau \tag{A.27}$$

and Taylor's microscales as:

$$\frac{1}{\tau^2} = 2\pi^2 \int_0^\infty f^2 \overline{E}(f)\, df \tag{A.28}$$

where $\overline{E}(f)$ the particle energy spectra, is calculated as:

$$\overline{E}(f) = \int_0^\infty \overline{R}(\tau) \cos(2\pi f \tau)\, d\tau \tag{A.29}$$

ENSEMBLE creates an output file in which the ensembled statistical information is written for further use by the programmer.

REFERENCES

Basset, A.B., "A Treatise on Hydrodynamics," Dover Publications, Inc., New York, 2, Ch. 22, p. 285 (1961).

Batchelor, G.K., "Sedimentation in a Dilute Dispersion of Spheres," Journal of Fluid Mechanics, 52, pp. 245-268 (1972).

Boussinesque, J., "Theorie Analytique de la Chaleur," 2, p. 224, Gauthier Villars, Paris (1903).

Buyevich, Y.A., "Statistical Hydromechanics of Disperse Systems. Part 1," J. Fluid Mech., 49, p. 489 (1971).

Buyevich, YU.A., "Statistical Hydromechanics of Disperse Systems, Part 2. Solution of the Kinetic Elevation for Suspended Particles," Journal of Fluid Mechanics, 52, pp. 345-355 (1972).

Buyevich, YU.A.,"Statistical Hydromechanics of Disperse Systems, Part 3. Pseudo-turbulent Structure of Homogeneous Suspensions," Journal of Fluid Mechanics, 56, pp. 313-336 (1972).

Chao, B.T., "Turbulent Transport Behavior of Small Particles in Dilute Suspension," Osterreichisches Ingenieur-Archiv, 18, pp. 7-21 (1964).

Cheng, P.Y. and H.K. Schaehman, J. Ploymer Sci. 16, p. 19 (1955).

Corrsin, S. and J.L. Lumley, "On the Equation of Motion for a Particle in Turbulent Fluid," Applied Scientific Research, Sec. A, 6, pp. 114-119 (1956).

Elata, C. and A.T. Ippen, "The Dynamics of Open Channel Flow with Suspensions of Neutrally Bouyant Particles," TECHNICAL REPORT NO. 45, Hydrodynamics Laboratory, M.I.T., Cambridge, MA (1961).

Happel, J. and Brenner, H., Low Reynolds Number Hydrodynamics, Englewood Cliffs, NJ (1965).

Happel, J. and Epstein, N., "Cubical Assemblages of Uniform Spheres," Ind. and Engng. Chem. 46, pp. 1187 (1954).

Hinch, E.J., "An Averaged-Equation Approach to Particle Interactions in a Fluid Suspension," Journal of Fluid Mechanics, 83, pp. 695-720 (1977).

Hino, M., "Turbulent Flow with Suspended Particles," Proceedings of ASCE, NY4, p. 161 (1963).

Hinze, J.O., Turbulence, McGraw Hill Co., Inc., New York, p. 357 (1959).

Hinze, J.O., "Turbulent Fluid and Particle Interaction," Reprint from Progress in Heat and Mass Transfer, Pergamon Press, New York (1972).

Howard, N.M., "Experimental Measurements of Particle Motion in a Turbulent Pipe Flow," Ph.D. Thesis, University of Illinois (1974).

Ingebo, R.D., "Drag Coefficients for Droplets and Solid Sphere in Clouds Accelerating in Airstreams," NACA-TN3762 (1956).

Jones, B.G., "An Experimental Study of the Motion of Small Particles in a Turbulent Fluid Field Using Digital Techniques for Statistical Data Processing," Ph.D. Thesis, University of Illinois (1966).

Jones, B.G., R.J. Ostensen and C.C. Meek, "Linearized Non Stoksian Drag in Turbulent Flow," Proceedings of the ASCE, 99 EM1, p. 233, February (1973).

Kada, H. and T.J. Hanratty, "Effects of Solids on Turbulence in a Fluid," A.I.Ch.E. Journal, 6, No. 4, pp. 624-630 (1960).

Kampé de Fériet, J., "Les Fonctions Aleatoires Stationaires et la Theorie Statistique de la Turbulence Homogene," Ann. Soc. Sci. de Bruxelles, 59, p. 59 (1939).

Kaye, B.H. and R.P. Boardman, Proc. Symposium Interaction Between Fluids and Particles, London, Brit. Inst. Chem, Engrs. (1962).

Laufer, J., "The Structure of Turbulence in Fully Developed Pipe Flow," NACA Report 1174, pp. 417-434 (1954).

Lumley, J.L., "Some Problems Connected With the Motion of Small Particles in Turbulent Fluid," Ph.D. Thesis, The Johns Hopkins University (1957).

McNown, J.S. and P.N. Lin, "Proc. Second Midwestern Conf. Fluid Mechanics," Reprint in Eng. No. 109, Iowa State University (1952).

Meek, C.C., "Statistical Characterization of Dilute Particulate Suspensions in Turbulent Fluid Fields," Ph.D. Thesis, University of Illinois (1972).

Meek, C.C. and Jones, B.G., "Studies of the Behavior of Heavy Particles in a Turbulent Fluid Flow," accepted for publication in the Journal of Atmospheric Sciences (March, 1973).

Meek, C.C., Private Communications (1978).

Milne-Thomson, C.B.E., Theoretical Hydrodynamics, MacMillan Company, New York, p. 499 (1960).

Oseen, C.S., Hydrodynamik, p. 132, Leipzig (1927).

Pismen, L.M. and Nir, A., "On the Motion of Suspended Particles in Stationary Homogeneous Turbulence," Journal of Fluid Mechanics, 84, pp. 193-206 (1978).

Reeks, M.W., "On the Dispersion of Small Particles Suspended in an Isotropic Turbulent Fluid," Journal of Fluid Mechanics, 83, pp. 529-546 (1977).

Shirazi, M.A., "On the Motion of Small Particles in a Turbulent Field," Ph.D. Thesis, University of Illinois (1967).

Tam, C.K.W., "The Drag on a Cloud of Spherical Particles in Low Reynolds Number Flow," J. Fluid Mechanics, 38, p. 537 (1969).

Taylor, G.I., "Diffusion by Continuous Movements," Proc. London Math Society, 151, pp. 196-211 (1921).

Tchen, C.M., "Mean Value and Correlation Problems Connected with the Motion of Small Particles Suspended in a Turbulent Fluid," Martinus Nijhoff, The Hague, Ch. 4, p. 72 (1947).